Universidad del País Vasco Euskal Herriko Unibertsitatea

Euskal Herriko Unibertsitatea
Facultad de Ciencia y Tecnología
Departamento de Química Inorgánica

GRAPHENE-RELATED MATERIALS FOR ELECTROCHEMICAL CAPACITORS

A dissertation Submitted to the University of the Basque Country

In partial fulfilments of the requirements for the degree of

Doctor of Philosophy

by

Adriana M. Navarro-Suárez

Thesis Advisors:

Dr. Javier Carretero-González

Prof. Dr. Teófilo Rojo Aparicio

International Reviewers

Encarnación Raymundo-Piñero

Olivier Crosnier

Yury Gogotsi

Examination Panel

David Ávila-Brande

David Mecerreyes

Francesca Soavi

Idoia Ruiz de Larramendi

Pedro Gómez-Romero

18th November 2016

A Copito de Nieve… Obviamente.

“What I need now... is a strong drink and a peer group.”

— Douglas Adams and Adriana Navarro-Suárez

ACKNOWLEDGEMENTS

First of all, I would like to thank the funding by the Graphene Flagship (Grant agreement no: 604391. Call: FP7-ICT-2013-FET-F), the Etortek Program (ENERGIGUNE12), the Basque Government Scholarship for pre-doctoral formation (PRE_2014_1_62), the Egonlabur Traveling Grant (EP_2016_1_0030), and the CIC energiGUNE fellowship and traveling help.

I am grateful to the international reviewers of this thesis and members of my examination panel for agreeing to be part of the team. Your insights are greatly appreciated.

Jesús, Nuria & José: Thank you for taking care of business while we were trying not to blow the lab up.

Thanks to the people in charge of the administrative stuff: Elena, Sara, Begoña O., Leire, Marco, Cristina (x2), Lola, Silvia, Iñaki & Asier at CIC energiGUNE, Danielle & Wendy at Drexel University and Professors Idoia Ruiz de Larramendi, Izaskun Gil de Muro, Luis Lezama, Luis León and Pascual Ramón at Euskal Herriko Unibertsitatea. You guys made my life so much easier.

Yury, Javi & Teo, thank you for taking me into your groups and hearts. I have enjoyed discussing ideas, results, manuscripts and life with the three of you.

To all the collaborators through the development of this work: Supercaps team, Polymat people, AJ Drexel Nanomaterials Institute guys, Damien, Paula, Eli, and Michel. Working with you was a fun activity that expanded my perspectives. Here's to many more collaborations to come!

Scientific help from Alex, Vladimir, Nuria G., Begoña A., Aitor V., Yan, Ibai, Naira, Anabel, Cristina L. (the second), Zalditxu, and Egoitz is greatly appreciated.

To Diana Farías & Marco F. Suárez, you guys helped to shape my scientific mind a decade ago, and instilled a love of learning that has kept me going even through the intricate path of a PhD.

When I arrived in Europe, I couldn't imagine that an Amiens girl would be keeping me company for the next five years. Thank you Morgane, for being a great team mate and bringing along Lucy and Emilie. French girls rule!

Being the party planner of the pintxo pote group brought me amazing stories and memories. I appreciate every single member who has joined at one point or another. I should also thank the participants of “The Kutxi Challenge”, “The Kutxi Challenge: The revenge in costume” and the Welcome/Farewell/Halloween/Carnival/Birthday parties. A loud group of obnoxious drunk people is always fun to hang out with.

Lisset & Danny, you guys always managed to move me away from my scientific side and brought out the clown in me, you guys rock! Keep up the good work!

Thank you to all the people at CIC energiGUNE (present and former members) for not being extremely angry at my loudness, bad jokes and inappropriate behavior. Special thanks to: Cris L. (the first) for all the party experiences and Euskera advice. Little Anna for all the hugs, recommendations and for trying to bring my dance-y side out. Nebilo, the fact that you were my boss’ best friend during his studies and now kind of mine, makes me think that if I ever have a student I should introduce her/him/them to you. The three of you were amazing companions in completely different moments, I’m gonna miss you guys.

Termin-Aitor & Iron-Maider, you were first-row witnesses of the “Oh my goodness, Adriana is being serious now… oh wait, she is writing her thesis while wearing sun glasses” phase. I can’t emphasize enough how appreciated your jokes/stories/comments are. As Maider said “Maidrianaitor” will be back!

The people at Drexel University were great to me and their help and random conversations are greatly appreciated. Next time we see each other I won’t be writing my thesis so I promise we will have more fun!

Natalie, Cedric, Liz & Taron, you are amazing. We should quit our jobs and start organizing social activities, we rock at that!

To the new (Laura, Jay & Andrés) and old (Amir, M.J., Fred, Gene, Foggy spy, Lucy, Juli “the bro-in-law”, Silvia, Seth) friends who I met/saw/visited in the US. You made a huge country feel like my little neighborhood, thank you!

My scientific parents, Eli & Javi: I learnt so much from both of you, it’s hard to believe we spend such a small timeframe actually together. Thank you for all the advice, jokes, comments, instructions, dinners, drinks, skype meetings… I will keep calling you mom & dad until the end.

My Dumb Family: Matz, Manolito & Thambi. I connected with you through alcohol, language and weirdness (in that order). Five years later, our logical conjunction (or

illogical in our case) keeps being alcohol and weirdness (I'm sorry Manolo, we don't speak the same language). Love you guys.

Matz, you are the greatest person ever (mainly because we share THE mind). Even when we were thousands of kilometers away, I felt you right by my side. Our amazing adventures, travels, stories mean everything to me. Keep being the most supportive gf the world would ever know; I promise I will keep appearing with random plans for us to do. Just remember, at the end of the road, you are the only one who really knows where home is… Let's talk to strawberries together!

Now, let's switch languages randomly!

Esker handi bat Euskal Herriari azken urte hauetako harreragaitik; Euskal Herria beti bigarren aberri bezala sentituko dut. Baita, esker anitz María Arnaiz, Eider, Cristina L. (x2) (Luengo eta Loreak), Jokin, Ane, Nuria, Zalditxu, Begoña (x3), Laida, Aitor V., Maider, Naira, Javi R. "the King" eta Edurne-ri eukal hizkuntzan eta kulturan murgiltzeko emandako laguntza eta prestakuntzagaitik.

Pour mes parents et ma grand-mère Français, qui m'ont donné une famille loin de la mienne. Il n'y a pas assez de mots pour remercier cette famille qui a décidé qu'adopter une Colombienne étrange bien qu'adulte, n'était pas une perte de temps et un bon investissement. Je chéris chaque moment que nous avons passé ensemble. Encore et toujours à vos côtés pour de très longues années!

Gracias infinitas a Ainhoa (Aitor's wife) y los padres de Maider por alimentarme durante el proceso de escritura de esta tesis.

Silvia, Sonia, Lina, Lucy, Karen, D. Peña & Carlos, básicamente los he conocido desde siempre, y los he tenido a mi lado cuando más los he necesitado. Tal vez no lo han notado, pero ustedes han sido un sistema de apoyo muy importante, mantenerme medianamente cuerda nunca habría sido posible sin ustedes.

Las mujeres de mi familia son fundamentales en mi vida: Mi abuelita, mi madre, mis tías, mis primas, Anita y Peluca. Ustedes han sido un ejemplo y un motivo a seguir adelante. El camino es "culebrero" pero nunca se hace especialmente difícil cuando se cuenta con semejante club de fans. Mi madre se merece todo en este mundo, a pesar de que sólo tiene una hija loca sin ideas coherentes, la ha apoyado en todo momento. Cuando crezca le voy a hacer una estatua.

Gracias a los tíos y primos por todas las cervezas, rones, whiskeys compartidos desde tiempos inmemoriales. El entrenamiento al que me han sometido fue fundamental durante el desarrollo de este trabajo. Gracias especiales a Javier N.

por ayudarme a traer esta tesis al siglo XXI.

Por último, pero no menos importante: Hace unos meses, el ser más importante en mi vida hizo su última presentación en este planeta. Mi abuelita fue una mujer fuerte, valiente, segura de sus convicciones, pero siempre dispuesta a escuchar, con un sentido del humor inigualable y un corazón gigante. Son zapatos enormes los que nos dejó, pero esperando ser el cambio que quiero ver en el mundo, intentaré seguir sus pasos. Copito de nieve: este trabajo doctoral y el título (que esperemos llegue) son suyos.

ABSTRACT

The research described throughout this doctoral thesis has been carried out at CIC energiGUNE, an Energy Cooperative Research Centre, located in Miñano (Alava, Spain).

Doctor Javier Carretero-González and Professor Teófilo Rojo Aparicio have been the supervisors of this work. During the development of this thesis and as part of the doctoral training, Miss Adriana M. Navarro-Suárez, the PhD candidate, has carried out a 6-month stay at A.J. Drexel Nanomaterials Institute (Philadelphia, USA). Professor Yury Gogotsi is the founder and director of this institute.

In the development of this doctoral thesis, the PhD candidate has explored the potential applications of graphene-related materials for electrochemical energy storage (EES), specifically in supercapacitors. Supercapacitors are expected to find many forthcoming applications in hybrid electric vehicles and other load-levelling applications. In order to achieve that end, their energy density must be maximized while the power capability continues intact. In the constantly changing technological landscape, it is relevant to face new strategies and mechanisms to achieve high energy density materials. Hence, in this thesis, the preparation of innovative redox active materials along with their nanostructuration with graphene or other nanomaterials to lead a high energy and high power density electrode in supercapacitors were our main goal.

Graphene has a large theoretical specific surface area and a very high intrinsic

electrical conductivity in plane as well as high mechanical strength and chemical stability. Because of these characteristics, graphene has been projected to provide better means for storing electricity. In this thesis, we explored and evaluated new electrode materials that either showed graphene-type structure or contained directly graphene layers. By using these materials, we expected to develop supercapacitors that exhibit double-layer capacitance, redox pseudo-capacitance, extrinsic redox pseudo-capacitance, or intercalation pseudo-capacitance.

To this end, this Doctoral Thesis has four defined objectives.

1. Synthesis of a nanoporous carbon with graphene-like structure to use it as double-layer capacitors.
2. Design, characterization and development of novel polymer-graphene cells with enhanced redox-pseudocapacitive behaviour.
3. Synthesis of an electrochemically active polymer as electrode material and the nanostructuration of the electrode by introducing low-dimensional carbon nanostructures.
4. Development of an asymmetric supercapacitor with two 2D nanomaterials showing intercalating pseudocapacitance.

LABURPENA

Doktorengo tesi honetan deskribatzen den ikerkuntza lana CIC energiGUNEn, Energiaren Ikerkuntza Zentro Koperatiboan, Miñaon (Araba) garatu da.

Lan honen gainbegiraleak Javier Carretero González doktorea eta Teófilo Rojo katedraduna izan dira. Doktorego tesiaren garapenean, Adriana M. Navarro-Suárez PhD kandidatuak, A.J. Drexel Nanomaterials Institutuan (Philadelphia, EEBB) 6 hilabeteko egonaldia egin du. Yury Gogotsi katedraduna da institutu honen zuzendari eta sortzailea.

Doktoretza tesi honetan grafenoa eta bere deribatuak energia elektrokimikoaren metaketa sistematan, zehazki superkondentzadoreetan, izan ditzaketen erabilera aztertu da. Izan ere, etorkizunean gailu hauek ibilgailu hibridoetan eta bestelako karga-balaztatze aplikazioetan berezko lekua izatea espero da. Hala ere, helburu hau lortzeko ezinbestekoa da energia dentsitatea maximizatzea potentzia-ahalmena bere horretan mantentzen delarik. Etengabeko aldaketak jasaten dituen teknologia baten testuinguruan, estrategia eta mekanismo berriei aurre egiteak berebiziko garrantzia du energia dentsitatea altuko materialak lortu nahi baldin badira. Hori horrela izanik, Tesi honen helburu nagusia propietate elektrokimikoei dagokionez berriak diren grafeno-deribatu nanoegituratuak edo bestelako nanomaterialak prestatzea izan da, beti ere energia eta potentzia dentsitate balio altuak lortzeko xedearekin.

Grafenoaren gainazal azalera espezifiko teorikoak eta planoko konduktibitate

elektriko intrintsekoak oso balio altuak dituzte. Era berean, bere erresistentzia mekanikoa eta egonkortasun kimikoa ere oso onak dira. Propietate hauek direla eta, grafenoa kargak biltegiratzeko etorkizuneko materialtzat hartu izan ohi da. Ildo horri jarraituz, grafeno motako egitura edo zuzenean grafeno geruzak dituzten elektrodo material berriak aztertu eta ebaluatu dira lan honetan. Material horiek erabiliz, geruza bikoitzeko kapazitantzia, erredox-pseudokapazitantzia, erredox-pseudokapazitantzia estrintsekoa edo pseudokapazitantzia tartekatua erakusten duten superkondentsadoreak garatu dira.

Laburbilduz, Doktorego Tesi honen helburu zehatzak lau izan dira:

1. Grafeno motako egitura duten ikatz nanoporotsuaren sintesia geruza bikoitzeko kondentsadoreetan erabiltzeko.
2. Polimero-grafeno gelaxka berrien diseinua, karakterizazioa eta garapena erredox-pseudokapazitantzia ekarpen hobetuarekin.
3. Elektrokimikoki aktiboa den polimero baten sintesia eta bere nanoegituraketa dimentsio baxuko karbono egiturak gehituz.
4. Superkondentsadore asimetriko baten garapena pseudokapazitantzia tartekatua aurkezten duten bi dimentsiotako nanomaterial ezberdinak erabiliz.

RESUMEN

La investigación llevada a cabo durante el desarrollo de esta tesis doctoral ha sido realizada en CIC energiGUNE, un centro de Investigación Cooperativa dedicado a la investigación en Energía, localizado en Miñano (Álava, España).

El doctor Javier Carretero González y el Profesor Teófilo Rojo Aparicio han sido los supervisores de este trabajo. Durante el desarrollo de esta tesis y como parte de su entrenamiento doctoral, la señorita Adriana Milena Navarro Suárez, ha llevado a cabo una estancia de 6 meses en el A.J. Drexel Nanomaterials Institute (Filadelfia, Estados Unidos de América). El profesor Yury Gogotsi es el director y fundador de este instituto.

Durante el desarrollo de esta tesis doctoral, la candidata ha explorado las posibles aplicaciones de materiales relacionados con grafeno para almacenamiento de energía electroquímico, específicamente en supercondensadores. Se espera que los supercondensadores encuentren futuros usos en vehículos eléctricos híbridos y otras aplicaciones relacionadas con balance de carga energética. Para lograr este objetivo, la densidad energética de los supercondensadores debe ser maximizada

mientras su potencia se mantiene intacta. En el cambiante panorama tecnológico, es importante utilizar nuevas estrategias y mecanismos para lograr materiales con una alta densidad energética. Por lo tanto, el principal objetivo de esta tesis es la preparación de materiales novedosos con propiedades electroquímicas capacitivas y su nanoestructuración con grafeno u otros nanomateriales que conlleven a una alta densidad de energía y potencia.

El grafeno tiene alta área superficial teórica y alta conductividad eléctrica intrínseca en plano, así como alta fuerza mecánica y estabilidad química. Gracias a estas características, el grafeno se ha proyectado como un material superior para almacenar electricidad que los materiales tradicionales. En esta tesis, exploramos y evaluamos nuevos materiales para electrodos que o mostraban una estructura tipo grafeno o que contenían menos de 30 capas de grafeno. Al usar estos materiales, esperamos desarrollar supercondensadores que muestren capacitancia de doble capa, pseudocapacitancia intrínseca o extrínseca causada por reacciones de reducción-oxidación y pseudocapacitancia de intercalación.

En esta tesis doctoral se han definido cuatro objetivos:

1. Síntesis de un carbón nanoporoso con estructura tipo grafeno para su uso como electrodo en un supercondensador de doble capa.
2. Diseño, caracterización y desarrollo de una novedosa celda basada en un polímero y óxido de grafeno reducido con un pronunciado comportamiento pseudocapacitivo causado por reacciones de reducción-oxidación.
3. Síntesis de un polímero electroquímicamente activo como material para electrodo y la nanoestructuración de dicho electrodo introduciendo nanoestructuras de carbono de baja dimensionalidad.
4. Desarrollo de un supercondensador asimétrico usando dos nanomateriales con estructura bidimensional que muestran pseudocapacitancia de intercalación.

Teniendo en cuenta los objetivos determinados anteriormente, esta tesis doctoral se ha dividido en seis capítulos:

Capítulo 1: Introducción

En este capítulo se hace una revisión de los mecanismos capacitivo y farádico de almacenamiento de energía. Se da una vista global de los diferentes tipos de supercondensadores. Esta sección describe los métodos de fabricación de estos dispositivos y de algunos materiales para electrodos. Este capítulo atrae la atención a los principales retos de los materiales usados tradicionalmente para aplicaciones en supercondensadores.

Capítulo 2: Electrodos basados en carbones nanoporosos con estructura similar al grafeno para supercondensadores.

El efecto de las temperaturas de carbonización y activación, así como la proporción entre el hidróxido de potasio y el carbón (KOH/C) en la estructura nanoporosa de los carbones derivados de lignina se estudió empleando TGA (en inglés *Thermogravimetric Analysis*), Adsorción/desorción de Nitrógeno gaseoso y SAXS (en inglés *Small Angle X-ray Scattering*). La información estructural, como es la distribución del tamaño de poros y área superficial, fueron extraídas mediante un programa de análisis de la adsorción de gas basado en NLDFT (en inglés *Non-Local Density Functional Theory*). Está información fue contrastada con la obtenida mediante un programa de análisis de dispersión de rayos X llamado IRENA. La presencia de regiones ordenadas en el material fue analizada por espectroscopia Raman, SEM y TEM (en inglés *Scanning Electron Microscopy* y *Transmission Electron Microscopy*). La relación entre el tamaño de poro, el área superficial y el tamaño del cristalito de las regiones ordenadas con la capacitancia de doble capa en electrólitos acuosos y orgánicos fue discutida en detalle.

Capítulo 3: Electrodos multi-redox para supercondensadores basados en óxido de grafeno parcialmente reducido y un biopolímero

El monómero 3,4-etilendioxitiofeno es polimerizado en presencia de lignina; de esta manera PEDOT (poli-3,4-etilendioxitiofeno), un polímero

conductor de electrones, ayuda a aumentar el comportamiento capacitivo de la lignina, un biopolímero con procesos electroquímicos controlados por difusión. Este aumento fue confirmado estudiando los biopolímeros lignina y lignina/PEDOT con un microelectrodo a diferentes velocidades de barrido y calculando las contribuciones capacitivas y farádicas a la corriente. El biocomposite fue caracterizado mediante FTIR (en inglés *Fourier Transform Infrared*) y análisis termogravimétrico. Por otro lado, un óxido de grafito fue reducido térmicamente a baja temperatura para incrementar su conductividad mientras mantenía su solubilidad en agua y conservaba algunos grupos funcionales para tener un comportamiento pseudocapacitivo causado por las reacciones reversibles de reducción/oxidación de dichos grupos. El prGrO (en inglés *partially reduced Graphite Oxide*) fue caracterizado por FTIR (en inglés *Fourier Transform Infrared Spectroscopy*), adsorción/desorción de nitrógeno gaseoso, Difracción de rayos X y XPS (en inglés *X-ray Photoelectron Spectra*). Estos dos materiales, el biopolímero Lignina/PEDOT y el prGrO, fueron estudiados en un electrólito acuoso en configuraciones de 3-electrodos, simétricas y asimétricas y finalmente en una configuración simétrica usando un composite de los dos materiales.

Capítulo 4: Estudio de polímeros derivados de quinonas y aminas que presentan reacciones de reducción/oxidación para dispositivos de almacenamiento energético

Dos biopolímeros basados en monómeros con grupos funcionales quinona y amina fueron sintetizados. Sus propiedades electroquímicas fueron evaluadas en una configuración de tres electrodos en un electrólito acuoso. En diferentes estados de carga, los electrodos fueron analizados por FTIR (en inglés *Fourier Transform Infrared Spectroscopy*), difracción de rayos X y espectroscopia de Raman; basados en estos resultados un mecanismo de almacenamiento de carga fue propuesto. Para mejorar la procesabilidad de los materiales para electrodo, un conector PEO (en inglés *Polyethylene oxide*) fue introducido durante la polimerización. Pruebas de solubilidad de los nuevos materiales fueron realizadas para determinar la mejor ruta de preparación de los electrodos. Los nuevos ter-polímeros fueron analizados en una configuración de tres electrodos en un

electrólito acuoso para cuantificar la cantidad de carga almacenada en estos materiales. Una evaluación de los valores capacitivos como función de las densidades de corriente también fue llevada a cabo.

Capítulo 5: Desarrollo de supercondensadores en configuración asimétrica usando como electrodos carburo de titanio bidimensional (MXene) y óxido de grafeno reducido

En este capítulo se describe la preparación y estudio de cuatro materiales de electrodo diferentes: i) Carburo de Titanio bidimensional (MXene), ii) Un composite preparado a partir de Carburo de Titanio bidimensional (MXene) y Nanotubos de carbono multi-pared, iii) óxido de grafeno reducido químicamente, y iv) óxido de grafeno reducido térmicamente. Estos materiales fueron caracterizados por espectroscopia Raman, difracción de rayos X y microscopía electrónica de barrido. Todos los materiales fueron estudiados electroquímicamente en configuraciones de tres electrodos y simétrica. A partir de estos resultados, el Carburo de Titanio bidimensional (MXene) y el óxido de grafeno reducido químicamente fueron escogidos como la pareja electroactiva de electrodos para supercondensadores en configuración asimétrica en un electrolito acuoso. Siguiendo el mismo procedimiento, el composite preparado a partir de Carburo de Titanio bidimensional (MXene) y Nanotubos de carbono multi-pared y el óxido de grafeno reducido térmicamente fueron usados como electrodos en un supercondensador en configuración asimétrica en un electrolito orgánico y un líquido iónico. La retención de capacitancia con el número de ciclos y su eficiencia coulombica durante el ciclado también fueron evaluadas.

Capítulo 6: Conclusiones & Perspectivas

Las principales conclusiones del trabajo realizado durante el desarrollo de esta tesis son presentadas en esta sección. También delineamos futuros métodos para la mejora de las propiedades de los materiales desarrollados en esta tesis.

TABLE OF CONTENTS

LIST OF TABLES

LIST OF FIGURES

Introduction

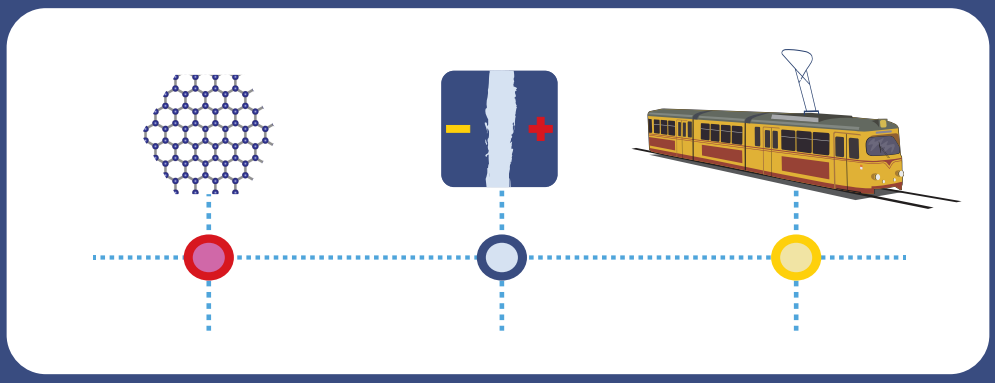

1 INTRODUCTION

World energy consumption is projected to double in the next fifty years, making the research in energy storage and conversion a priority. Particularly in energy storage, researchers focus especially on the development of electrochemical energy storage (EES) systems that should meet market requirements such as low cost, efficiency and safety.[1–4] There is a full spectrum of energy-storage applications with varying storage times, volumes and rates of charging and discharging, creating market opportunities for advanced batteries, fuel cells, flywheels, pumped water, compressed air, supercapacitors and other technologies. The importance of electrical energy storage will continue to grow as markets for consumer electronics and electrification of transportation expand. Due to the intermittent character of renewable energy sources, there is also a need, particularly with transportation and grid storage applications, for devices where large amounts of energy is delivered or accumulated quickly (within seconds or minutes).[5]

Scheme 1-1 depicts the different kinds of electrochemical energy storage devices. Electrochemical energy storage technology is based on devices capable of exhibiting high energy density (batteries) or high power density (electrochemical capacitors). Batteries store energy in chemical bonds that follow reduction-oxidation (redox) reactions in which a phase transformation is involved. Capacitors store energy electrostatically in electric fields, and in the case of electrochemical capacitors (ECs or supercapacitors) between ions in solution and an electrode material.[6]

Scheme 1-1. Classification of electrochemical energy storage.[6]

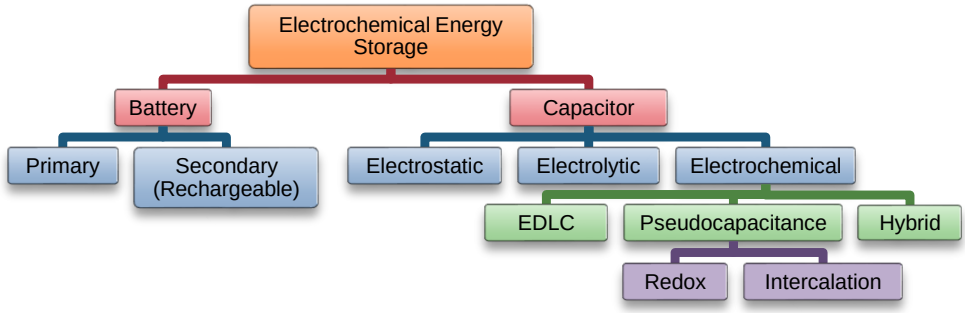

ECs have attracted interest because of their high pulse power (5 – 10 $kW.kg^{-1}$), long cycle life (because of their high reversibility), fast rate capability. The use of low cost and renewable precursors to prepare electrode materials and the possibility of using them in aqueous media,[7,8] in the absence of harmful chemicals make of this system also a desired option.[1–3] Because of the differences in the charge storage mechanisms in ECs and batteries, the energy density exhibited by the former (5 $Wh.kg^{-1}$)[9] is at least one order of magnitude lower than the one presented by the latter. Thus, batteries are used in applications requiring a higher energy while supercapacitors in those demanding high power output within a few seconds; otherwise, combinations of both devices are used when both high energy and high power are needed.

1.1 Principle of Capacitors

Capacitors can be explained using a simple model consisting of two conductive plates separated by a dielectric material. By applying an electric field, the two plates are positively and negatively charged respectively.

The ability to store charge, also called Capacitance ($\boldsymbol{C}$ in farads), is determined by the ratio between the charge stored ($\boldsymbol{Q}$ in coulombs) at each conductor plate and the voltage difference ($\boldsymbol{V}$ in volts) across the capacitor:

$$\boldsymbol{C = Q \times V} \qquad \textbf{Equation 1-1}$$

In a capacitor with electrodes of equal area, in parallel configuration and separated by a determined distance and a dielectric medium, the capacitance will also be determined by Equation 1-2

$$C = \varepsilon_0 \times \varepsilon_R \times \frac{A}{d} \qquad \textbf{Equation 1-2}$$

where ε_0 and ε_R are the vacuum permittivity (8.854×10^{-12} F.m^{-1}) and the dielectric constant of the material between the plates (for vacuum ε_R = 1), respectively, A is the area of the plates in m^2, and d stands for the distance between the two parallel plates in m.

1.2 Faradaic and Capacitive Energy Storage

The development of high energy density devices with optimum performance is based on first understanding of the chemistry and electrochemistry of the materials used as electrodes to develop new ones with improved properties. Figure 1-1 illustrates the characteristic behaviour of these electrochemical energy storage materials and summarizes the features that distinguish them from each other.[10]

Similar to dielectric capacitors, electrical double-layer capacitance (EDLC) originates from the formation of an electrical double layer upon device polarization. The ions of the electrolyte adsorb onto the electrode surface or inside the pores of opposite charge. When charged, the anions in the electrolyte will move towards the positive electrode while cations will diffuse towards the negative. This can be assimilated to a series connection of two unequal parallel plate capacitors, one being made up of one carbon electrode (one plate) and the cations (the other plate) while the other is composed of the other carbon electrode and the anions.[11] Thus, the best performing EDLC materials should have a high specific surface area (SSA), making nanostructured carbons the materials of choice, since they can easily deliver high SSA at low price and possess good electrical conductivity. Generally, EDLCs offer great cyclability and power densities and are characterized by nearly rectangular cyclic voltammograms (CVs) and linear galvanostatic charge–discharge profiles (Figure 1-1 (a)).

Pseudocapacitive materials present a continuous, highly reversible change in the oxidation state during charge/discharge. Redox pseudocapacitance occurs when ions are electrochemically adsorbed onto the surface or near surface of a material with a concomitant faradaic charge-transfer.[5] Intercalation pseudocapacitance occurs when ions intercalate into the tunnels or layers of a redox-active material accompanied by a faradaic chare transfer with no crystallographic phase change.[5]

Pseudocapacitive materials present a continuous, highly reversible change in the oxidation state during charge/discharge, characterized by CVs with almost perfectly rectangular CVs or little separation in peak position on charge/discharge (surface

redox, Figure 1-1 (b)) or significantly broadened peaks (intercalation, Figure 1-1 (c)).[10]

Pseudocapacitance can be intrinsic or extrinsic to a material, in that the property can emerge through material engineering. Intrinsic pseudocapacitive materials display the characteristics of capacitive charge storage for a wide range of particle sizes and morphologies. On the other hand, extrinsic materials do not exhibit

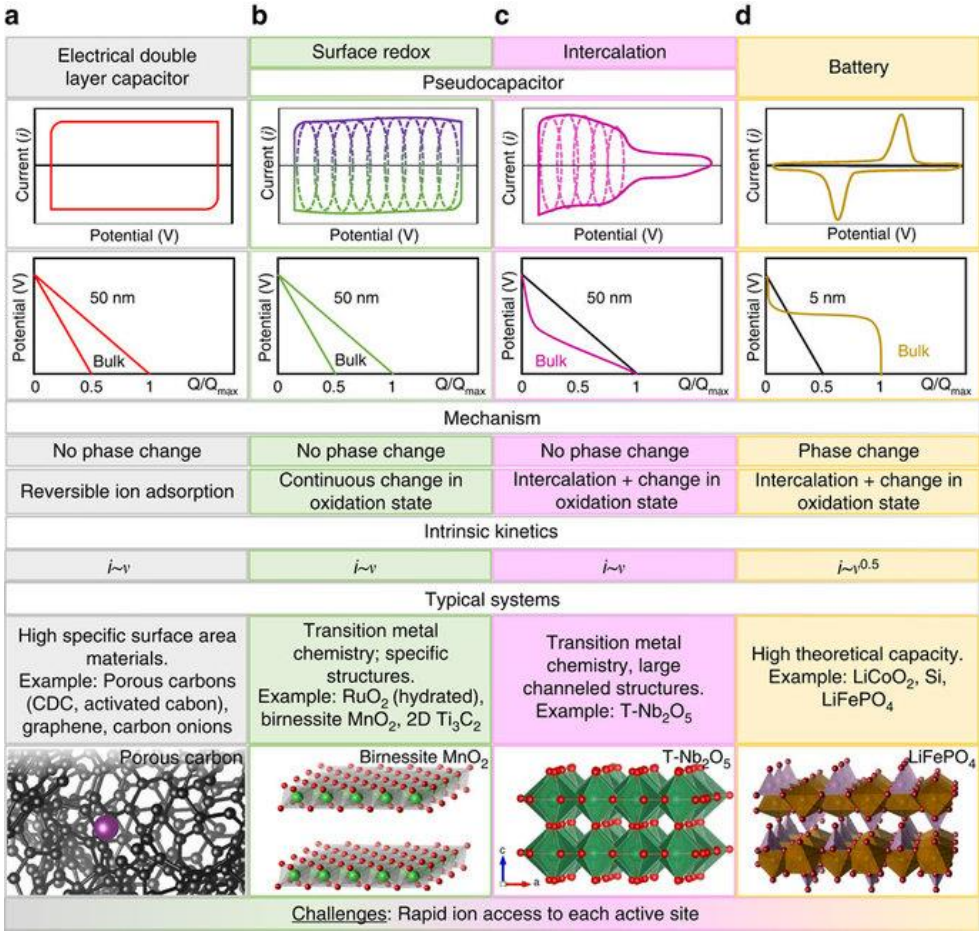

Figure 1-1. Faradaic and capacitive energy storage. Summary of the characteristic metrics such as cyclic voltammetry, galvanostatic profiles, key mechanism descriptions and typical systems that are known to utilize the mentioned charge storage mechanisms: double-layer capacitor[12–16] (a), surface redox pseudocapacitance due to adsorption and/or fast intercalation of ions [17–19] (b), intercalation pseudocapacitance[20] (c) and batteries[4,21,22] (d). *i* = current, *v* = sweep rate. Different colours in the plots indicate different storage mechanisms.[10]

pseudocapacitance in the bulk state due to phase transformations during ion storage. With these materials, increasing the surface area through nanostructuring leads to improved high rate behaviour due to a decrease in diffusion distances and in some cases, the suppression of a phase transformation.

A capacitive charge storage mechanism is not diffusion limited and follows Equation 1-3.

$$\boldsymbol{i = C_d A v} \qquad \textbf{Equation 1-3}$$

where, $\boldsymbol{i}$ is the current (A), $\boldsymbol{C_d}$ is the areal capacitance (F.m^{-2}), $\boldsymbol{A}$ is the surface area (m^2) and $\boldsymbol{v}$ is the scan rate (V.s^{-1}).[23]

Charging in batteries is often accompanied by a phase transformation in the host material. This process is characterized by distinct peaks in the CV and plateaus in the galvanostatic charge/discharge profiles (Figure 1-1 (d)).[10] The change of the maximum current peak with the potential scan rate for a reversible diffusion-controlled reaction is given by the Randles–Sevcik equation:

$$\boldsymbol{I_{peak} = 0.4463(nF)^{3/2} AC \left(\frac{D}{RT}\right)^{1/2} \times v^{1/2}} \qquad \textbf{Equation 1-4}$$

where, $\boldsymbol{I_{peak}}$ is the maximum peak current (A), $\boldsymbol{n}$ the number of electrons involved, $\boldsymbol{F}$ the Faraday constant (A.s), $\boldsymbol{C}$ the concentration of the diffusing species (mol.cm^{-3}), $\boldsymbol{D}$ the diffusion coefficient of the diffusing species (cm^2.s^{-1}) and $\boldsymbol{v}$ the potential scan rate (V.s^{-1}).[23]

Materials exhibiting a hybrid charge mechanism can be described as the combination of two separate mechanisms, namely capacitive effects ($\boldsymbol{k_1 v}$) and diffusion-controlled insertion ($\boldsymbol{k_2 v^{1/2}}$) according to:

$$\boldsymbol{i(v) = k_1 v + k_2 v^{1/2}} \qquad \textbf{Equation 1-5}$$

where, $\boldsymbol{v}$ is the sweep rate. By determining both $\boldsymbol{k_1}$ and $\boldsymbol{k_2}$, it is thus possible to distinguish the fraction of the current arising from diffusion-limited and that from capacitive processes at specific potentials.[24]

Table 1-1. Comparison of the properties of battery and supercapacitor.

	Battery	Supercapacitor
Discharge time	0.3-3 h	0.3-30 s
Charge time	1-5 h	0.3-30 s
Energy Density (Wh.kg-1)	10-100	1-10
Specific Power (W.kg-1)	50-200	~1000
Charge/Discharge Efficiency (%)	70-85	85-98
Cycle life (# cycles)	500-2000	>100000

Table 1-1 summarizes the differences expected between batteries and ECs.[25] Due to their different electrochemical behaviour, their properties are also different. The supercapacitor has high power density, short charge-discharge time, high charge-discharge efficiency and long cycle life compared with battery.

The Ragone plot (energy density vs power density) has been widely employed to evaluate the overall performance of an energy storage device. The energy density values ($\boldsymbol{E}$) of a device can be calculated by using Equation 1-6:

$$E = \frac{1}{2} C V^2 \qquad \textbf{Equation 1-6}$$

where, $\boldsymbol{C}$ is the capacitance and $\boldsymbol{V}$ is the specific voltage window for device.

The power density values of a supercapacitor device can be calculated according to

$$P = \frac{V^2}{4R_s} = \frac{E}{t} \qquad \textbf{Equation 1-7}$$

where, $\boldsymbol{P}$ is the power density (W.kg^{-1}), $\boldsymbol{R_s}$ is the equivalent series resistance, $\boldsymbol{E}$ is the energy density (Wh.kg^{-1}) and $\boldsymbol{t}$ is the discharge time (h).[24]

A Ragone plot is shown in Figure 1-2, it can be seen that supercapacitors occupy a region between conventional capacitors and batteries.[26]

It should be noted that the energy/power density can only be used to characterize the electrochemical profile of a supercapacitor device, rather than a single electrode. In addition, the energy/power density is critically dependent on the mass loading of electrode-active materials. It is clear that a low mass loading of the

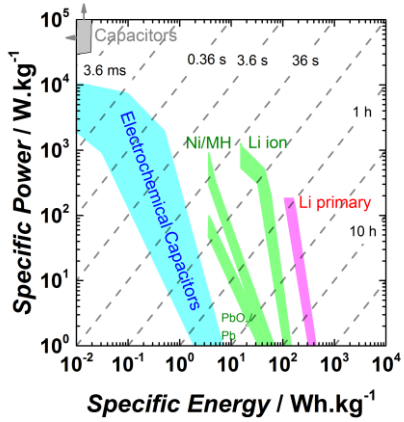

Figure 1-2. Specific power against specific energy, also called a Ragone plot, for various electrical energy storage devices.[11]

electrode always results in a better electrochemical performance, due to its low relative current. However, the low mass loading of electrode materials also results in the energy/power density calculated from the mass of active materials being far form that of the practical supercapacitor device.[27]

1.3 Best Methodology for Electrode Performance Testing

The key factor that reflects the performance of supercapacitors is the capacity of the electrodes to store and release energy. In this section, different cell configurations for electrode testing are reviewed. The goal is to find the optimal configuration that would allow the best electrode performance.

1.3.1 Test cell configuration

The test cell configuration for electrode performance testing typically consists of either 2 or 3 electrodes. These two different test-cell configurations yield distinctively different results and should only be used to test electrodes in the appropriate setting.[28]

A typical 3 electrode cell consists of a reference electrode, a working electrode and a counter electrode. Only the working electrode would contain the material that is being tested for its electrochemical properties. In addition, the voltage potential

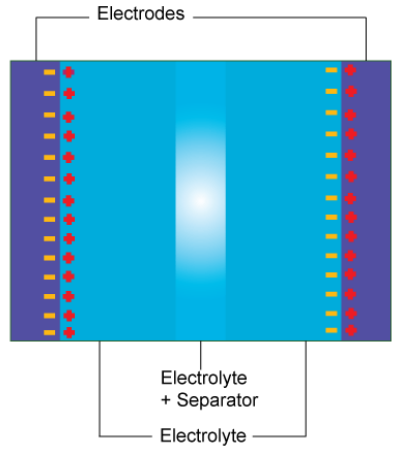

Figure 1-3. Schematic diagram of mechanism of a supercapacitor.

applied to the working electrode is highly dependent on the reference electrode and would yield more capacitance compared to a 2-cell electrode configuration.[29] As a result, these attributes make the 3-cell electrode configuration especially sensitive and this could result in significant errors when estimating the energy storage capacity for electrode performance in supercapacitance applications. Despite the limitations, the 3-cell electrode configuration does allow users to study the electrochemical properties of the active material in the working electrode. In addition, the electrolyte and solvent stability can also be investigated.[30] Nevertheless, as commercial supercapacitors consist of a 2-electrode configuration, tests using this configuration should also be performed. In most of the cases of this work, the materials are first studied in a 3-electrode configuration to study the stability of the material in the electrolyte and then in a 2-electrode configuration.

Figure 1-3 shows the schematic diagram of a 2-electrode configuration. The electrodes are immersed in an electrolyte solution, with a separator between them. The separator is placed between the electrodes to prevent electrical contact, but allows ions from the electrolyte to pass through. When charged, the anions in the electrolyte will move towards the positive electrode while cations will diffuse towards the negative. This can be assimilated to a connexion in series of the capacitors.

According to the composition of electrode materials, supercapacitor devices in a 2-electrode configuration can be classified in symmetric, asymmetric and hybrid supercapacitors.

- Symmetric supercapacitors are typically composed of two identical supercapacitor-type electrodes (Figure 1-4 (a)), including EDLCs and

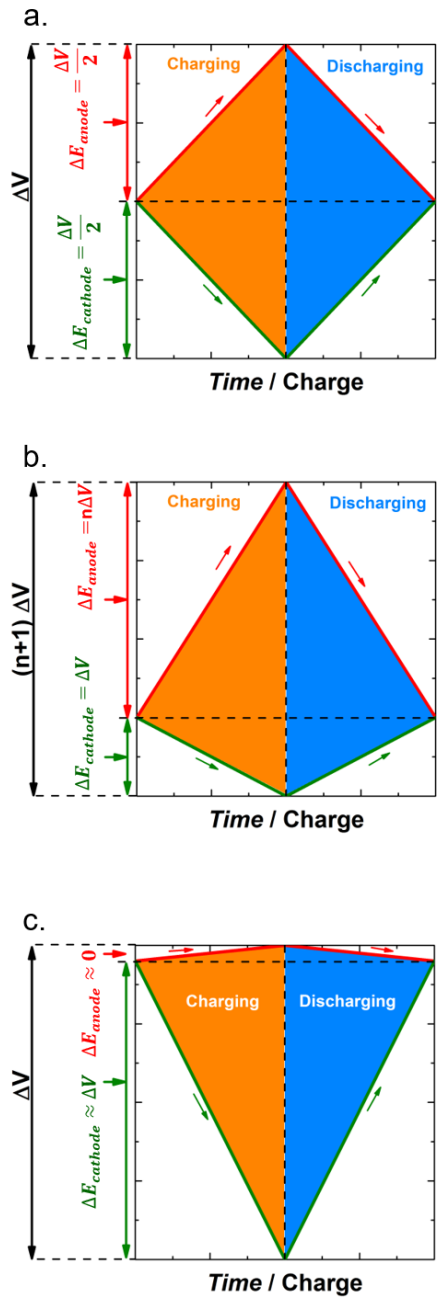

Figure 1-4. Schematic potential profiles of a symmetric (a), asymmetric (b), and hybrid (c) system.[31]

pseudo-capacitive materials.[24] During this thesis, we will refer to *capacitance* when the electrode capacitance was calculated and to *cell capacitance* to the value of the whole device. This distinction will be specifically important when comparisons between symmetric and asymmetric cells are made.

- Asymmetric supercapacitor refers to every combination of positive and negative electrodes whenever there is any difference between the two electrodes (weight, thickness, material, etc.). Due to the asymmetry in the electrochemical behaviour for the cations and anions (Figure 1-4 (b)), unequal specific capacitances for positive ($\boldsymbol{C_{SP+}}$) and negative ($\boldsymbol{C_{SP-}}$) electrodes occur. Therefore, in order to maintain the stable voltage conditions of $\boldsymbol{V_-} = \boldsymbol{V_+}$, the weight of the electrodes ($\boldsymbol{m_-}$ and $\boldsymbol{m_+}$) should be unequal to compensate for the different specific capacitance values[10]:

$$\boldsymbol{m_-} = \frac{\boldsymbol{C_{SP+}}\boldsymbol{m_+}}{\boldsymbol{C_{SP-}}} \qquad \textbf{Equation 1-8}$$

- Hybrid supercapacitors constitute a special case of asymmetric supercapacitors. They are typically composed of two electrodes with different charge storage mechanisms, *i.e.* a supercapacitor-type electrode and a battery-type electrode (Figure 1-4 (c)).[24]

1.3.2 Choice of electrolyte

Energy and power densities are affected by the kind of electrolyte used. The energy density is affected by the voltage window and ion concentration of the electrolyte (Equation 1-7). The power density is impacted by the resistance of the electrolyte (Equation 1-8). Three types of electrolytes are usually used: aqueous, organic and ionic liquid electrolytes. Usually, salts are added to both, aqueous and organic electrolytes, to provide additional ionic conductivity in the full specified temperature range. The salts must be added in sufficient quantities (typically 1M) to prevent any depletion at high voltage. Ionic liquid electrolytes may be mixed with a solvent to reduce its viscosity and consequently increase its conductivity while reducing the series resistance.[32] When choosing an electrolyte, four parameters should be taken into account: low ionic resistance, high capacitance, simple synthesis and wide potential window in which the electrolyte will remain stable.[28]

- Aqueous electrolytes: Compared to organic electrolytes, can provide the highest ionic concentration and lowest resistance. These characteristics

cause aqueous-based supercapacitors to display the highest capacitance of the three electrolyte types. Common aqueous electrolytes include Na_2SO_4, KOH, H_2SO_4, and KCl salts. They are most commonly used in lab-scale testing.[28] The most important disadvantage of aqueous electrolytes is their small voltage window as low as about 1.2 V.

- Organic electrolytes: The most common type of organic electrolyte is tetraethylammonium tetrafluoroborate (Et_4NBF_4) in propylene carbonate or acetonitrile. They are mostly used in real-world applications because of their large electrochemical window (as high as 3.5 V). However, the water content should be kept below 3 - 5 ppm or the voltage window will be reduced. Drawbacks are depletion of the electrolyte upon charging, small operating temperature range, poor conductivity (2 - 56 $mS.cm^{-1}$)[33], and safety issues.[34]

- Ionic liquid electrolytes are non-volatile molten salts that can exist in liquid form at the desired temperatures. They are rarely used but recent research suggests that their use may increase in the near future because of their favourable properties such as excellent thermal stability (up to 500 ºC),[35] conductivity, large electrochemical window (about 4.5 V) and recyclability. Additionally, the physical and chemical properties of the electrolyte can be managed by substituting its cations or anions.[34]

1.4 Strategies for Improving the Energy Density of Supercapacitors

Now that portable electronic devices such as smartphones have become ubiquitous, one major problem remains: battery technology has not kept up with the demands placed on them. Moreover, the lack of a reliable battery still holds back electric vehicles from being readily adopted over vehicles using an internal combustion engine.[36] Supercapacitors have several useful features, such as high power density, excellent performance at low temperatures and a large number of charge and discharge cycles. However, the low energy density of current supercapacitors is the main impediment to realizing the full commercial potential of this technology in high energy density applications.

It is important to think outside the box when developing new storage solutions utilizing supercapacitors (Scheme 1-2). On the one hand, design of new electrolytes with bulky ions or with multi-electron redox reactions has been predicted to be the new research direction in the electrolyte area.[10] On the other hand, further

Scheme 1-2. Diagram showing the different strategies to improve the performance of supercapacitors.[37]

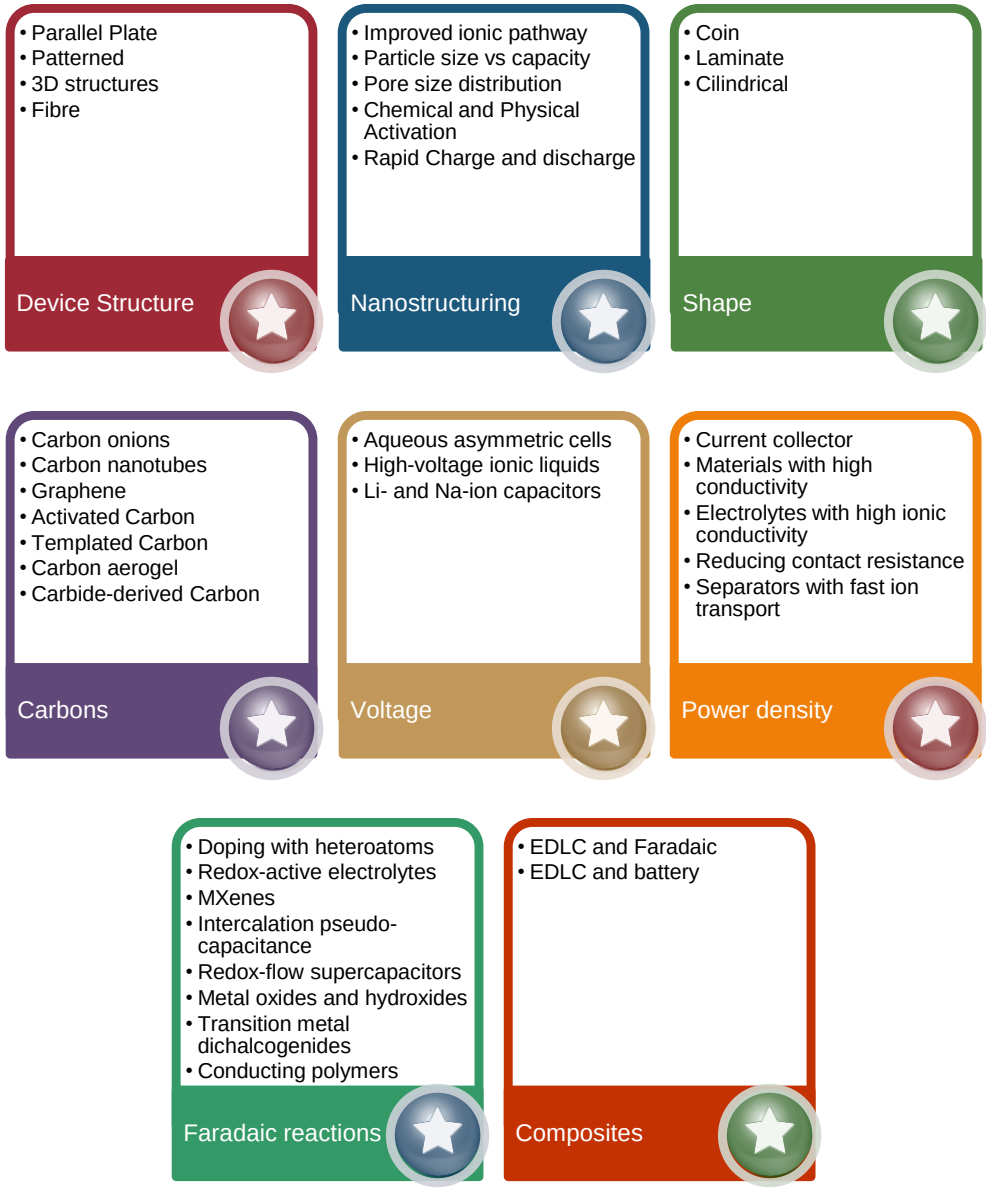

developing new materials with high capacitance and improved performance relative to existing electrode materials is the most important method to improve the energy density of supercapacitors.[38]

1.5 Electrode Materials

Understanding the charge storage mechanisms and the development of high-quality materials have allowed great progress in the recent years. Nevertheless, to achieve high energy density without sacrificing the high power density is still a major bottleneck in establishing supercapacitors as the primary power source.[39] Amongst all the components of a full supercapacitor device (electrodes, separator and electrolyte), electrodes are key components which greatly affect the performance of supercapacitors.[36] Hence, designing and fabricating high quality electrode materials play a decisive role in developing next-generation high performance supercapacitors. As seen in Figure 1-1, the electrode materials of ECs can present three storage mechanisms: double-layer capacitance, surface redox pseudocapacitance and intercalation pseudocapacitance. In this thesis, materials related to these three mechanisms are studied for supercapacitor applications.

1.5.1 Double-Layer Capacitive Materials

The conventional electrode materials for EDLCs are porous activated carbons (AC) (Figure 1-5) with large specific surface areas (1000 – 2000 $m^2.g^{-1}$) which can deliver capacitances of 200 $F.g^{-1}$ and 100 $F.g^{-1}$ in aqueous and organic electrolytes,

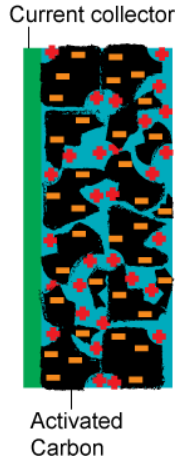

Figure 1-5. Double-layer capacitance mechanism.

respectively.[24] The advantages of carbon materials include abundance, low cost, easy processing, non-toxicity, good electronic conductivity, high chemical stability, and wide operating temperature range.[40] Normally, carbon materials store charges mainly in an electrochemical double-layer formed at the interface between the electrode and the electrolyte, rather than storing them in the bulk of the capacitive material. Therefore, the charge accumulation capability of carbon materials at the electrode/electrolyte interface is increased with their specific surface area.[41]

Activated carbons can be produced by chemical or physical methods. In physical activation, the carbon precursor is pyrolyzed at temperatures in the range 600 – 900 ºC, in absence of oxygen, to remove non-carbon species and cross-link carbon atoms, and subsequently, oxidized (mainly under CO_2 or steam) at temperatures between 600 – 1200 ºC, in order to remove carbon atoms and create pores. In chemical activation, a carbon precursor or amorphous carbon is impregnated with certain chemicals (such as KOH, NaOH, H_3PO_4, ZnCl, H_2SO_4) and then heat-treated at temperatures between 450 – 900 ºC with chemical reactions finally producing pores.[42] Chemical activation offers some advantages over physical activation such as: lower temperatures, faster heat treatment, usually simultaneous carbonization/activation steps and higher carbon yields.[43]

Activated carbon materials produced from different precursors like fossil coals or renewable low cost precursors (biomass) are the most frequently used in commercial EDLC systems. The double layer capacitances of ACs from natural renewable materials reach 35 – 166 $F.g^{-1}$ in organic electrolytes, and more than 300 $F.g^{-1}$ in aqueous electrolytes. The highest specific capacitances of ACs from natural renewable materials can reach the values for ACs from fossil fuels and even exceed them.[44] This indicates that ACs from natural, renewable, low-cost and environmental-friendly materials will likely replace the more conventional ACs from fossil fuels and dominate the future AC market.

Graphene, a two dimensional defect free carbon monolayer, has recently enabled the dramatic improvement of portable electronics and electric vehicles by providing optimum means for storing electricity.[37]

1.5.2 Surface Redox Pseudocapacitance

Materials based on an electrical double-layer mechanism have limited specific capacitance, typically in the range of 10 – 50 $\mu F.cm^{-2}$ for a real electrode surface. As pseudocapacitance may be 10 – 100 times greater, supercapacitors made of redox-active materials are highly desirable as the next generation of ECs.[40]

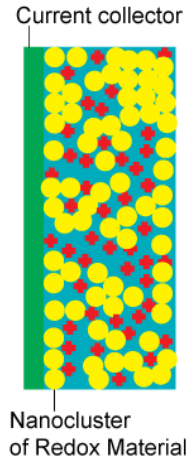

Figure 1-6. Redox pseudocapacitive mechanism.

Conducting polymers (CPs), including polyacetylene (PA), polypyrrole (PPy), polyaniline (PANI), and poly(3,4-ethylenedioxythiophene) (PEDOT) have been considered as promising pseudo-capacitive electrode materials for supercapacitors (Figure 1-6) due to their prominent properties.[24] Conducting polymers are rendered conductive through a conjugated bond system along the polymer backbone. They offer capacitive behaviour through redox reactions that occur not only on the surface, but also throughout the entire bulk. The redox processes are highly reversible because no structural changes, such as phase transformation, happen during the redox reactions. Early researchers termed the oxidation-reduction processes of these polymers as 'doping'. The positively-charged polymers, introduced by oxidation on the repeating units of polymer chains, are termed as 'p-doped', while negatively-charged polymers generated by reduction are termed as 'n-doped'. The potentials of these doping processes are determined by the electronic state of π electrons.[40]

CPs can only supply charges within a strict potential window. Beyond this strict potential range, the polymer may be degraded at more positive potential, and as the potential is too negative, the polymer may be switched to an insulated state (un-doped state). Hence, the selection of a suitable potential range for ES performance is crucial.[45]

PEDOT has been explored as a candidate material for ECs because of is high stability. Capacitance values from 60 to 160 $F.g^{-1}$ were achieved by using ultrasonic radiation on the CP[46] or mixing it with multiwalled carbon nanotubes.[47] Unfortunately, swelling and shrinking of CPs may occur during the

intercalating/deintercalating process. These problems often lead to mechanical degradation of the electrode and fading electrochemical performance during cycling, and then compromise CPs as electrode materials.[40]

1.5.3 Intercalation Pseudocapacitance

Another type of charge storage mechanism has been recently discovered, intercalation pseudocapacitance depends on the intercalation/de-intercalation of cations (*e.g.* Li^+, Na^+, K^+, and H^+) in the bulk of active materials, but is not limited by the diffusion of cations within the crystalline framework of active materials (Figure 1-7). In cation-intercalated pseudocapacitance, the advantage of batteries (*i.e.* charge storage in the bulk of the electrode materials) is combined with the advantage of supercapacitors (*i.e.* charge storage without diffusion control).

Properties such as diffusion ion length or contact area with electrolyte for utilization of active material in the performance of the ECs are of utmost importance. Due to their high surface area (with no bulk volume), 2-dimensional (2D) nanomaterials have attracted substantial interest for supercapacitor applications. Moreover, 2D materials have the ability to intercalate ions and thus can provide intercalation pseudocapacitance.[48]

Recently, MXene, a new family of 2D carbides with metallic conductivity, hydrophilicity, and capability for ion intercalation has emerged. MXenes have shown high volumetric capacitance values in microsized binder-free and mechanically strong electrodes for supercapacitors.[19]

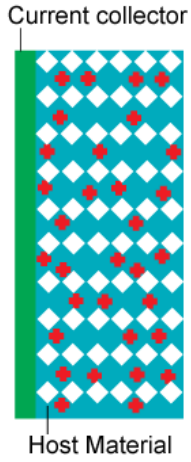

Figure 1-7. Intercalation pseudocapacitive mechanism.

MXenes derive from the layered hexagonal MAX phases, where M represents an early transition metal, A stands for and A-group element and X represents C or N. The A-group element is removed by selective etching, yielding 2D MXene sheets.[49]

Most research on MXenes has been focused on Ti_3C_2. Upon immersion into aqueous solutions, Ti_3C_2 shows spontaneous intercalation of Na^+, K^+, Li^+, Al^{3+}, Mg^{2+} with sulphates, hydroxides and nitrates as anions.[19] When tested in 1 M H_2SO_4, Ti_3C_2 free standing films show high volumetric and gravimetric capacitance (900 $F.cm^{-3}$ and 246 $F.g^{-1}$, respectively). However, the main issue for MXene use as pseudocapacitive materials is finding a matching positive electrode with equally high capacitance and conductivity, as they can only operate under negative potentials in aqueous electrolytes.[48]

1.6 Graphene for Supercapacitors

In the 20th century, a significant number of graphene and graphite related studies were conducted. However, it was not until 2004 when the article "Electric Field Effect in Atomically Thin Carbon Films"[50] was published in the Science journal that graphene finally gained worldwide attention. This report constituted the first study on the electrical properties of graphene and showed the potential of graphene and its future use in electronics (Scheme 1-3).

The fundamental properties of graphene make it promising for a multitude of applications (Figure 1-8). In particular, graphene has attracted great interest for supercapacitors because of its extraordinarily theoretical high surface area of up to 2630 $m^2.g^{-1}$. Recently, the intrinsic capacitance of single layer graphene was reported to be ~21 $\mu F.cm^{-2}$; this value sets the upper limit for electric double-layer capacitance for all carbon-based materials.[51] Thus, supercapacitors based on graphene could, in principle, achieve an EDLC as high as ~550 $F.g^{-1}$ if the entire surface area can be fully utilized.

Graphene is also interesting as electrode material for supercapacitors due to its unique properties: high conductivity,[50] good chemical and thermal stability,[52] wide potential window,[53] and excellent mechanical flexibility[54].

Currently, graphene is the most studied material for charge storage and the published results confirm its potential to change today's energy storage landscape. Specifically, graphene could present several new features for energy storage devices, transparent batteries, and high capacity and fast-charging devices.[37]

Over the past few years, some low cost and high yield two-dimensional carbon

Scheme 1-3. Flowchart showing the history of graphite/graphene research.[28]

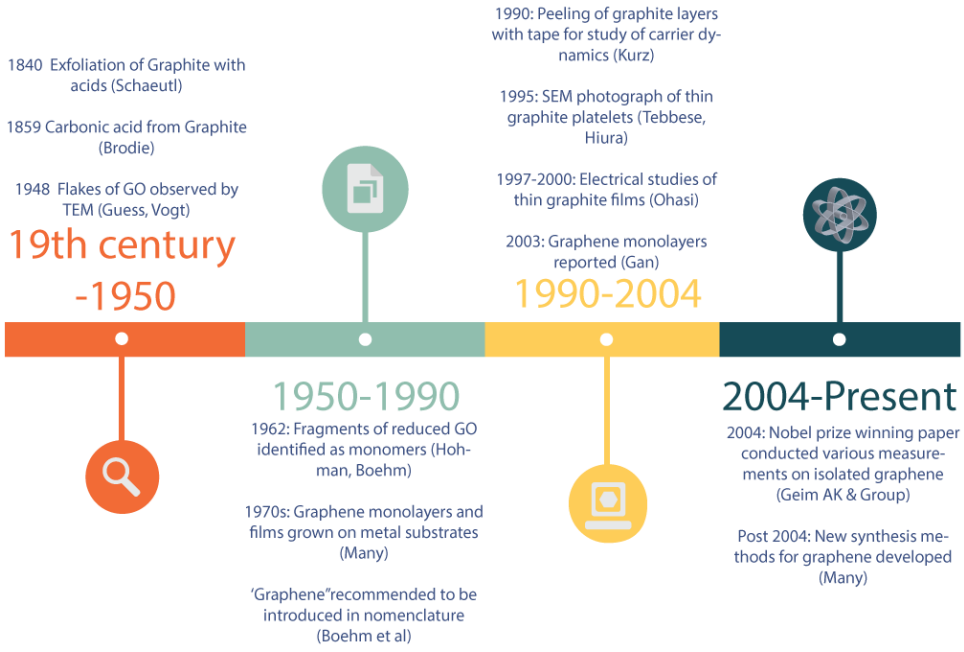

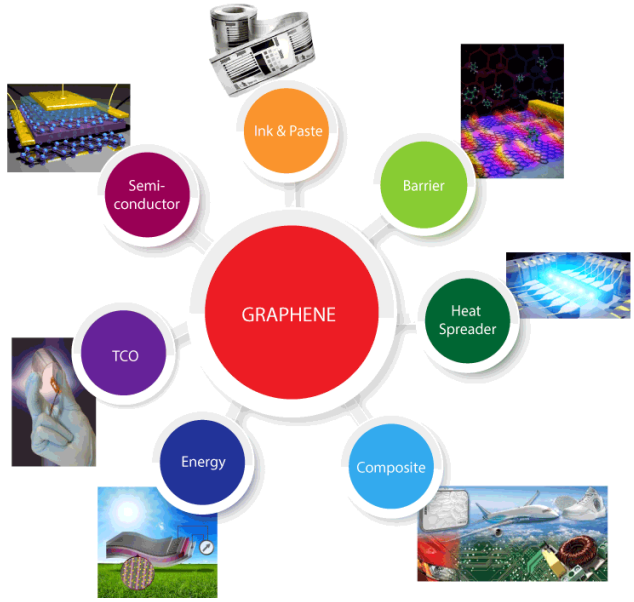

Figure 1-8. Overview of Applications of Graphene in different sectors ranging from conductive ink to chemical sensors, light emitting devices, composites, energy, touch panels and high frequency electronics.[55]

forms, such as reduced graphene oxide (rGO), have been developed as members of the graphene family.[56] rGO are commonly produced by reduction of graphene oxide (GO) with chemical, thermal or electrochemical methods.[57–59] These materials can be only classified as moderate quality graphene materials according to their defects (residual oxygen-containing groups, vacancy defects, edges and deformations) even after reduction.[37] Nevertheless, the rGO allows for continuous large-scale production with low cost and effective functionalization for further enhancement of the electrochemical performance of supercapacitors.

A variety of chemical reducing agents have been considered to restore the graphene network and its conductivity in the GO sheets.[60] Hydrazine is the most commonly reported reducing agent for GO reduction. Chemically modified graphene by reduction of suspended graphene oxide in water using hydrazine hydrate has been reported. The resulting sheets showed a surface area of 705 $m^2.g^{-1}$ and provided specific capacitances of 135 and 99 $F.g^{-1}$, respectively, in aqueous and organic electrolytes.[61]

Thermal treatment of GO suspension from 150 – 200 °C has also been shown to produce rGO by removing the oxygen from GO thus enabling high conductivity up to 5230 $S.m^{-1}$. A specific capacitance of 122 $F.g^{-1}$ at 5 mA could be achieved after thermal treatment at 200 °C, corresponding to a charge/discharge rate of 1000 $mA.g^{-1}$.[62] The advantage of this approach is its potential for scalable green production of carbon-based supercapacitor electrode materials.

The full potential of energy-storage devices built from graphene has yet to be realized. Many challenges remain, particularly with regard to feasible techniques for the low-cost mass production of graphene with controlled microstructure and low residual oxygen content. Further understanding of the interaction of graphene sheets at the nanoscale to form self-assembled structures of different shapes and dimensionalities will drive more potential applications for graphene.[37]

1.7 Scope of this Thesis

In this thesis, materials with different capacitive mechanisms will be developed and studied as electrode materials for supercapacitor applications. Four approaches are presented in this thesis.

- The first one is the study of the effect of the synthesis temperature and KOH/C ratio on the structural and textural properties of activated nanoporous carbons and their posterior use as electrode materials for double-layer capacitors.

- For the second path, two materials are developed; the first one is a partially reduced Graphite Oxide, while the second is a copolymer based on a biopolymer and PEDOT. Both materials are studied as electrodes for supercapacitors separately, then in an asymmetric configuration and finally as a self-assembly composite.
- In the third strategy, the nanostructuring process of a redox active polymer electrode with different types of nanocarbons is studied. The optimum synthesis conditions are determined to provide the best match between the electrochemical properties of the redox active polymer and the dimensionality of the conductive filler.
- In the last chapter, two asymmetric supercapacitors based on two different 2D materials (*i.e.* reduced Graphene Oxide and MXene) with applications in aqueous and organic electrolytes are developed.

1.8 References

(1) Winter, M.; Brodd, R. J. *Chem. Rev.* **2004**, *104* (10), 4245–4269.

(2) Burke, A. *J. Power Sources* **2000**, *91* (1), 37–50.

(3) Miller, J. R.; Simon, P.; Patrice, S. *Science (80-.).* **2008**, *321* (5889), 651–652.

(4) Armand, M.; Tarascon, J.-M. *Nature* **2008**, *451* (7179), 652–657.

(5) Augustyn, V.; Simon, P.; Dunn, B. *Energy Environ. Sci.* **2014**, *7* (5), 1597–1614.

(6) Miller, J. M. *Ultracapacitor Applications*; The Institution of Engineering and Technology: London, 2011.

(7) Rufford, T. E.; Hulicova-Jurcakova, D.; Zhu, Z.; Lu, G. Q. *Electrochem. commun.* **2008**, *10* (10), 1594–1597.

(8) Rufford, T. E.; Hulicova-Jurcakova, D.; Fiset, E.; Zhu, Z.; Lu, G. Q. *Electrochem. commun.* **2009**, *11* (5), 974–977.

(9) Conway, B. E. *Electrochemical Supercapacitors*; Springer US: Boston, MA, 1999.

(10) Lukatskaya, M. R.; Dunn, B.; Gogotsi, Y. *Nat. Commun.* **2016**, *7*, 12647–12660.

(11) Simon, P.; Gogotsi, Y. *Nat. Mater.* **2008**, *7* (11), 845–854.

(12) Chmiola, J.; Yushin, G.; Gogotsi, Y.; Portet, C.; Simon, P.; Taberna, P.-L. *Science (80-.).* **2006**, *313* (5794), 1760–1763.

(13) Shi, H. *Electrochim. Acta* **1996**, *41* (10), 1633–1639.

(14) Zhu, Y.; Murali, S.; Stoller, M. D.; Ganesh, K. J.; Cai, W.; Ferreira, P. J.;

Pirkle, A.; Wallace, R. M.; Cychosz, K. A.; Thommes, M.; Su, D.; Stach, E. A.; Ruoff, R. S. *Science (80-.).* **2011**, *332* (2011), 1537–1541.

(15) Pech, D.; Brunet, M.; Durou, H.; Huang, P.; Mochalin, V.; Gogotsi, Y.; Taberna, P.; Simon, P. **2010**, *5*, 651–654.

(16) Frackowiak, E.; Metenier, K.; Bertagna, V.; Beguin, F. *Appl. Phys. Lett.* **2000**, *77* (15), 2421.

(17) Zheng, J. P.; Cygan, P. J.; Jow, T. R. *J. Electrochem. Soc.* **1995**, *142* (8), 2699–2703.

(18) Ghodbane, O.; Pascal, J.-L.; Favier, F. *ACS Appl. Mater. Interfaces* **2009**, *1* (5), 1130–1139.

(19) Lukatskaya, M. R.; Mashtalir, O.; Ren, C. E.; Dall'Agnese; Rozier, P.; Taberna, P. L.; Naguib, M.; Simon, P.; Barsoum, M. W.; Gogotsi, Y. *Science (80-.).* **2013**, *341* (6153), 1502–1505.

(20) Augustyn, V.; Come, J.; Lowe, M. A.; Kim, J. W.; Taberna, P.-L.; Tolbert, S. H.; Abruña, H. D.; Simon, P.; Dunn, B. *Nat. Mater.* **2013**, *12* (6), 518–522.

(21) Okubo, M.; Hosono, E.; Kim, J.; Enomoto, M.; Kojima, N.; Kudo, T.; Zhou, H.; Honma, I. *J. Am. Chem. Soc.* **2007**, *129* (23), 7444–7452.

(22) *Nanomaterials for lithium-ion batteries : fundamentals and applications*; Yazami, R., Ed.; Taylor & Francis Group: Boca Ratón, 2014.

(23) Bard, A. J.; Faulkner, L. R. *Electrochemical methods : fundamentals and applications*; Wiley, 2001.

(24) Wang, Y.; Song, Y.; Xia, Y. *Chem. Soc. Rev.* **2016**, *451*, 652–657.

(25) Pandolfo, A. G.; Hollenkamp, A. F. *J. Power Sources* **2006**, *157* (1), 11–27.

(26) Kötz, R.; Carlen, M. *Electrochim. Acta* **2000**, *45* (15–16), 2483–2498.

(27) Gogotsi, Y.; Simon, P. *Science (80-.).* **2011**, *334* (6058), 917–918.

(28) Tan, Y. Bin; Lee, J.-M. *J. Mater. Chem. A* **2013**, *1* (47), 14814–14843.

(29) Stoller, M. D.; Ruoff, R. S. *Energy Environ. Sci.* **2010**, *3* (9), 1294.

(30) Staiti, P.; Lufrano, F. *Electrochim. Acta* **2007**, *53* (2), 710–719.

(31) Roldán, S.; Barreda, D.; Granda, M.; Menéndez, R.; Santamaría, R.; Blanco, C. *Phys. Chem. Chem. Phys.* **2015**, *17*, 1084–1092.

(32) Zheng, J. P.; Jow, T. R. *J. Electrochem. Soc.* **1997**, *144* (7), 2417–2420.

(33) Ue, M.; Ida, K.; Mori, S. *J. Electrochem. Soc.* **1994**, *141* (11), 2989–2996.

(34) Fu, C.; Kuang, Y.; Huang, Z.; Wang, X.; Yin, Y.; Chen, J.; Zhou, H. *J. Solid State Electrochem.* **2011**, *15* (11–12), 2581–2585.

(35) Maton, C.; De Vos, N.; Stevens, C. V. *Chem. Soc. Rev.* **2013**, *42* (13), 5963–5977.

(36) Wang, G.; Zhang, L.; Zhang, J. *Chem. Soc. Rev.* **2012**, *41* (2), 797–828.

(37) El-Kady, M. F.; Shao, Y.; Kaner, R. B. *Nat. Rev. Mater.* **2016**, *1*, 16033.

(38) Aricò, A. S.; Bruce, P.; Scrosati, B.; Tarascon, J.-M.; van Schalkwijk, W. *Nat. Mater.* **2005**, *4* (5), 366–377.

(39) Shehzad, K.; Xu, Y.; Gao, C.; Duan, X. *Chem. Soc. Rev.* **2016**, *306*, 666–669.

(40) Wang, G.; Lei, Z.; Jiujun, Z. *ChemsucChem* **2012**, *41*, 797–828.

(41) Frackowiak, E. *Phys. Chem. Chem. Phys.* **2007**, *9* (15), 1774–1785.

(42) Marsh, H.; Rodríguez-Reinoso, F. *Activated Carbon*; Elsevier, 2006.

(43) Lozano-Castelló, D.; Lillo-Ródenas, M. A.; Cazorla-Amorós, D.; Linares-Solano, A. *Carbon N. Y.* **2001**, *39* (5), 741–749.

(44) Wei, L.; Yushin, G. *Nano Energy* **2012**, *1* (4), 552–565.

(45) Frackowiak, E.; Khomenko, V.; Jurewicz, K.; Lota, K.; Béguin, F. *J. Power Sources* **2006**, *153* (2), 413–418.

(46) Li, W.; Chen, J.; Zhao, J.; Zhang, J.; Zhu, J. *Mater. Lett.* **2005**, *59* (7), 800–803.

(47) Lota, K.; Khomenko, V.; Frackowiak, E. *J. Phys. Chem. Solids* **2004**, *65* (2–3), 295–301.

(48) Mendoza-Sanchez, B.; Gogotsi, Y. *Adv. Mater.* **2016**, *28* (29), 6104–6135.

(49) Naguib, M.; Kurtoglu, M.; Presser, V.; Lu, J.; Niu, J.; Heon, M.; Hultman, L.; Gogotsi, Y.; Barsoum, M. W. *Adv. Mater.* **2011**, *23* (37), 4248–4253.

(50) Novoselov, K. S.; Geim, A. K.; Morozov, S. V; Jiang, D.; Zhang, Y.; Dubonos, S. V; Grigorieva, I. V; Firsov, A. A. *Science* **2004**, *306* (5696), 666–669.

(51) Xia, J.; Chen, F.; Li, J.; Tao, N. *Nat. Nanotechnol.* **2009**, *4* (8), 505–509.

(52) Vivekchand, S. R. C.; Rout, C. S.; Subrahmanyam, K. S.; Govindaraj, A.; Rao, C. N. R. *J. Chem. Sci.* **2008**, *120* (1), 9–13.

(53) Chen, D.; Tang, L.; Li, J. *Chem. Soc. Rev.* **2010**, *39* (8), 3157–3180.

(54) Lee, C.; Wei, X.; Kysar, J. W.; Hone, J. *Science* **2008**, *321* (5887), 385–388.

(55) Ferrari, A. C.; Bonaccorso, F.; Falko, V.; Novoselov, K. S.; Roche, S.; Bøggild, P.; Borini, S.; Koppens, F.; Palermo, V.; Pugno, N.; Garrido, J. a.; Sordan, R.; Bianco, A.; Ballerini, L.; Prato, M.; Lidorikis, E.; Kivioja, J.; Marinelli, C.; Ryhänen, T.; Morpurgo, A.; Coleman, J. N.; Nicolosi, V.; Colombo, L.; Fert, A.; Garcia-Hernandez, M.; Bachtold, A.; Schneider, G. F.; Guinea, F.; Dekker, C.; Barbone, M.; Galiotis, C.; Grigorenko, A.; Konstantatos, G.; Kis, A.; Katsnelson, M.; Beenakker, C. W. J.; Vandersypen, L.; Loiseau, A.; Morandi, V.; Neumaier, D.; Treossi, E.; Pellegrini, V.; Polini, M.; Tredicucci, A.; Williams, G. M.; Hong, B. H.; Ahn, J.

H.; Kim, J. M.; Zirath, H.; van Wees, B. J.; van der Zant, H.; Occhipinti, L.; Di Matteo, A.; Kinloch, I. a.; Seyller, T.; Quesnel, E.; Feng, X.; Teo, K.; Rupesinghe, N.; Hakonen, P.; Neil, S. R. T.; Tannock, Q.; Löfwander, T.; Kinaret, J. *Nanoscale* **2014**, *7* (11), 4598–4810.

(56) Bianco, A.; Cheng, H. M.; Enoki, T.; Gogotsi, Y.; Hurt, R. H.; Koratkar, N.; Kyotani, T.; Monthioux, M.; Park, C. R.; Tascon, J. M. D.; Zhang, J. *Carbon N. Y.* **2013**, *65*, 1–6.

(57) Zhu, Y.; Murali, S.; Cai, W.; Li, X.; Suk, J. W.; Potts, J. R.; Ruoff, R. S. *Adv. Mater.* **2010**, *22* (35), 3906–3924.

(58) Dreyer, D. R.; Park, S.; Bielawski, C. W.; Ruoff, R. S. *Chem. Soc. Rev.* **2010**, *39*, 228–240.

(59) Zhu, Y.; James, D. K.; Tour, J. M. *Adv. Mater.* **2012**, *24* (36), 4924–4955.

(60) Yu, Z.; Tetard, L.; Zhai, L.; Thomas, J. *Energy Environ. Sci.* **2015**, *8* (3), 702–730.

(61) Stoller, M. D.; Park, S.; Zhu, Y.; An, J.; Ruoff, R. S.; Stoller, M. D.; Park, S.; Zhu, Y.; An, J.; Ruoff, R. S. *Nano Lett.* **2008**, *8* (10), 3498–3502.

(62) Zhu, Y.; Stoller, M. D.; Cai, W.; Velamakanni, A.; Piner, R. D.; Chen, D.; Ruoff, R. S. *ACS Nano* **2010**, *4* (2), 1227–1233.

NANOPOROUS CARBON ELECTRODES WITH GRAPHENE-LIKE STRUCTURE FOR SUPERCAPACITORS

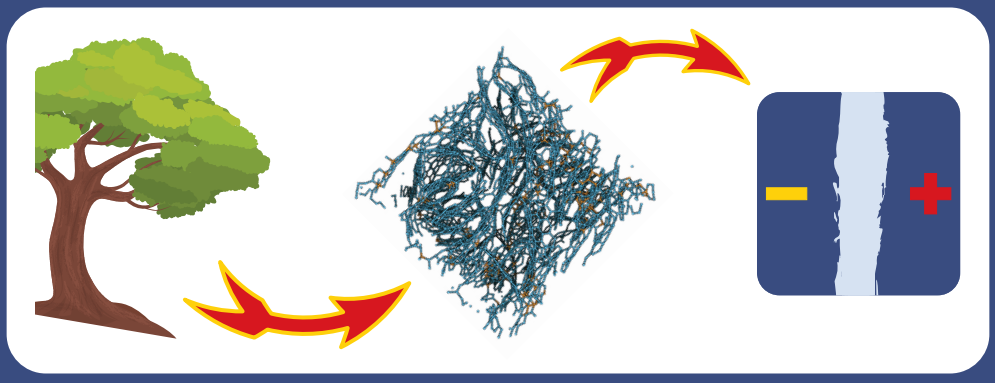

2 NANOPOROUS CARBON ELECTRODES WITH GRAPHENE–LIKE STRUCTURE FOR SUPERCAPACITORS

2.1 Introduction

Carbon materials are widely used for supercapacitor applications because of their unique combination of chemical and physical properties, namely: high conductivity, high surface-area, good electrochemical stability over a wide potential range, high temperature stability, controlled pore structure, processability and compatibility in composite materials, and relatively low cost.[1]

In particular, activated carbon (AC) is a group of porous materials with high surface area (1000 – 2000 $m^2.g^{-1}$). The most frequently used in commercial EDLC systems are produced from different precursors like fossil coals or renewable low cost precursors (biomass).

Lignin is an industrial by-product of cellulosic ethanol, pulp and paper industries. Kraft pulping is currently the most common method used for removal of the

unwanted components from wood during the manufacture of paper products, these residues are extracted in an aqueous solution called Black Liquor, which contains around 25 % of lignin. The thermo-chemical conversion of lignin into value added products is of interest because of its huge availability and its potential to produce higher value products. Extensive research has been done to expand the use of lignin in various sectors, given that currently the largest amount of lignin is burned to cover the energy needs. Minor applications of lignin are in adhesives and polymer composites.[2]

Johnson *et al.*[3] and Baker[4] have shown that lignin fibres synthesized above 1000 °C present ordered inclusions of a highly graphitic nature. These same inclusions are observed in lignin-derived carbons produced at 1800 °C[5] and also when potassium hydroxide (KOH) is used as activating agent at 1000 °C.[6]

Graphene is a promising electrode material for EDLCs because of its high electrical conductivity, large theoretical specific surface area and easy modification.[7–9] However, the effect of graphene insertions on activated carbons on their electrochemical performance has not been studied so far.

The aim of this work is to obtain low-cost and high-surface-area nanoporous carbons with inclusions of ordered regions to study the effect of these zones in the electrochemical performance. The approach is to use chemical activation of a renewable precursor (*i.e.* Lignin) at different temperatures and further implement the derived carbons as electrode materials for EDLCs in both aqueous- and organic-based electrolytes. The impact of the carbonization and subsequent activation conditions of lignin, on the textural properties (surface area and porosity) of the activated nanoporous carbons and their correlation with the electrochemical properties are carried out. Lignin is characterized by Thermogravimetric Analysis (TGA), and Optical and Scanning Electron Microscopy (SEM). The carbons are characterized by Nitrogen adsorption/desorption at 77 K, Small Angle X-Ray Scattering (SAXS), Raman Spectroscopy, X-Ray Diffraction (XRD), and Scanning and Transmission Electron Microscopy (SEM and TEM respectively), cyclic voltammetry and galvanostatic and impedance measurements.

2.2 Methodology

2.2.1 Lignin Isolation from Black Liquor Samples

The black liquor (BL) sample used in this study is produced during a Kraft pulping process and comprise ~17 wt.% of solids by weight, being 30 – 55 wt.% inorganic

and 45 – 70 wt.% organic. The inorganic substances are reported to be sodium hydroxide (NaOH, 5 – 6 $g.L^{-1}$), sodium sulphide (Na_2S, 14 – 16 $g.L^{-1}$) and sodium carbonate (Na_2CO_3, 25 – 30 $g.L^{-1}$).[10] These compounds are chemicals added during the Kraft process to convert wood into wood pulp and then separate cellulose compounds from lignin.

Natural lignin is isolated from BL after treatment at room temperature by adding 125 ml of 1 M sulphuric acid (H_2SO_4, Fisher Chemical, A.R.) to 20 ml of BL. After lignin precipitation, a solid biopolymer is collected by filtration under vacuum by using polytetrafluoroethylene membranes (Sartorius, pore size 0.45 µm and 4.5 cm diameter). Natural lignin is washed with deionized water and then centrifuged at least 5 times before drying at 80 °C under vacuum.

2.2.2 Activation Process

Prior to activation, the carbonization process of the natural lignin is studied by thermogravimetric analysis in a NETZSCH STA 449F3 Jupiter thermal analyser under an argon stream (Praxair, purity 99.9 %) at a heating rate of 5 $°C.min^{-1}$ up to 900 ºC.

Natural lignin is kept under vacuum at 80 ºC prior to the activation process. This procedure consists of an initial carbonization under argon flow of the isolated natural lignin at a heating rate of 5 $°C.min^{-1}$ up to the chosen temperature (400 °C or 900 °C) and kept for 2 hours, cooled down and stored for later activation.

For the activation, the carbon powders are mixed homogenously in an agate mortar with the desired KOH/Carbon ratio. The mixture is pressed to prepare a pellet and then heated at a heating rate of 5 $°C.min^{-1}$ up to the desired temperature for 2 hours. The samples will be referred from now on as BL_CT_#_AT, where CT and AT correspond to the carbonization and activation temperatures respectively and # to the KOH/C ratio. For example, a sample carbonized at 900 °C and activated at 600 °C with a KOH/Carbon ratio of 4 will be referred as BL_900_4_600 and a sample just carbonized at 400 °C with no activation step will be BL_400. On the first section, the experiments are dedicated to analyse the effect of the carbonization and activation temperatures on the final carbon, so we maintain the KOH/C ratio equal to four. On the second section, the effect of the KOH/C ratio is evaluated and the carbonization and activation temperatures are set on 900 ºC. The different samples are shown on Scheme 2-1.

After the activation process, the products are cooled down under argon flow to

Scheme 2-1. Samples synthesized from lignin to evaluate the effect of carbonization, activation and KOH/C ratio on the nanoporous carbon.

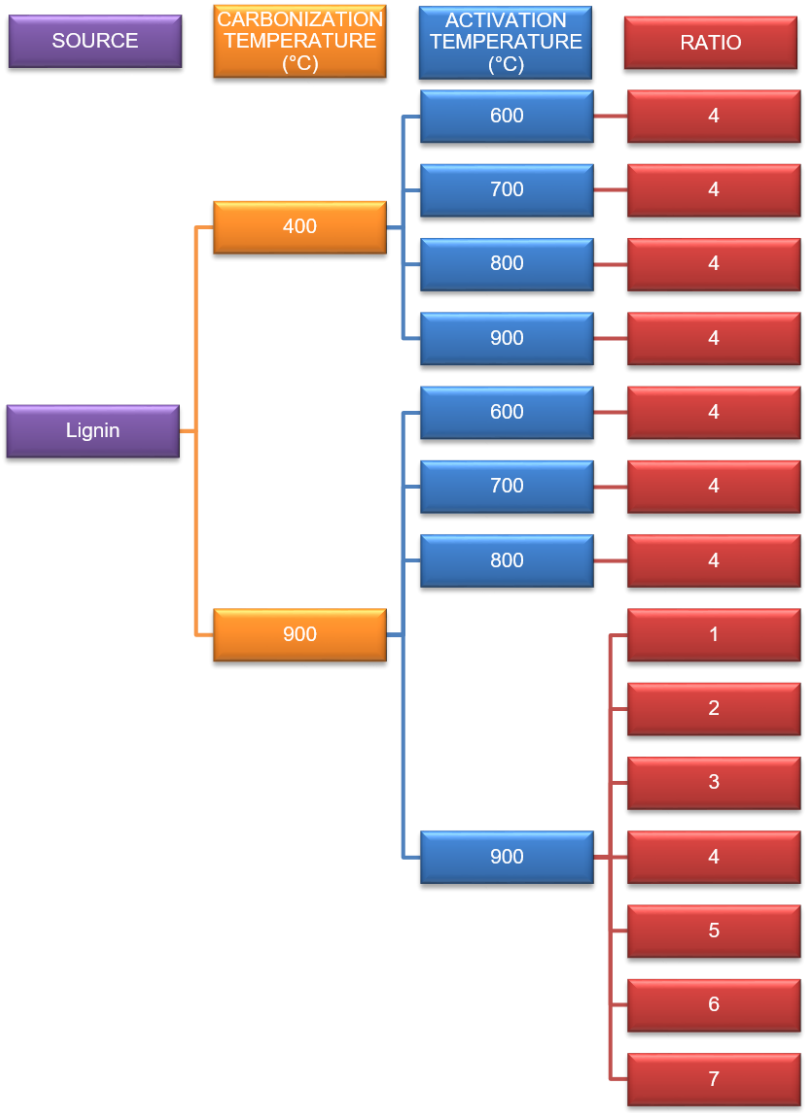

room temperature and washed with 1 M hydrochloric acid (HCl, Scharlau, A.R.) and deionized water (10.1 mΩ.cm) until neutral pH is evidenced, and then filtered off under vacuum to remove any remaining chemical impurity. The final carbonaceous material is dried at 120 ºC under vacuum before electrode preparation.

2.2.3 Characterization Methods

The materials are analysed by SEM, TEM, N_2 sorption, Raman and XRD as explained in Appendix I. Other special characterization techniques for carbon nanomaterials such as SAXS and Raman spectral imaging are used in this chapter.

Small Angle X-Ray Scattering is used to investigate the internal porosity of the carbons and to confirm the results from N_2 sorption. The measurements are performed using a Nanostar U (Bruker, Germany) equipped with microfocus Cu source, evacuated beam path and Vantec 2000 detector, using 107 cm, 28 cm and 4.8 cm sample-detector distances. The incident beam has been carefully calibrated in order to obtain absolute intensities in cm^{-1} with a perfect overlap of the measurements made at the three distances. Intensities are then normalized in $cm^2.g^{-1}$ by the macroscopic density of the powder samples.

Particle size distributions are extracted using the IRENA tool package,[11] using globules form factor (aspect ratio equal to 1) and maximum entropy algorithm. The total specific surface, SSA_{PSD}, is obtained by integrating the whole particle surface distribution.

Mesoscopic specific surface, SSA_{Porod}, in $m^2.g^{-1}$, has been extracted from low $\boldsymbol{Q}$ limit using the Porod's law of scattering by sharp interfaces:[12,13]

$$\boldsymbol{I\ (cm^2.g^{-1}) = 2\pi(\Delta\rho)^2 SSA_{Porod} Q^{-4}} \qquad \textbf{Equation 2-1}$$

For the Raman spectral imaging, a 50X objective lens and 10 seconds of exposition time of the laser beam to the sample are used in areas of at least 600 μm^2. To obtain the Raman images, the sample is moved with a step size of 1 µm and a Raman spectrum is recorded at every point.

The D and G bands are fitted with 2 symmetric Lorentzian functions;[14] the $\boldsymbol{I_D/I_G}$ ratio is calculated from the maximum intensities of the simulated peaks. Crystallite size is calculated from Tuinstra and Koenig (Equation 2-1)[15] model, where $\boldsymbol{I_D}$ and $\boldsymbol{I_G}$ correspond to the intensities of the simulated peaks *D* and *G* respectively, $\boldsymbol{C_{532\,nm}}$ is 4.95[16] and $\boldsymbol{L_a}$ is the cluster diameter.

$$\frac{\boldsymbol{I_D}}{\boldsymbol{I_G}} = \frac{\boldsymbol{C_\lambda}}{\boldsymbol{L_a}} \qquad \textbf{Equation 2-2}$$

The spectra are analysed and Raman images are then constructed using the integrated peak intensity by means of the Origin Lab® software.

2.2.4 Electrodes Preparation

In order to study the electrochemical behaviour of the carbons, electrodes are prepared by mixing 95 wt.% of lignin-derived activated carbon with a 5 wt.% of polytetrafluoroethylene (PTFE solution 60 %, Sigma-Aldrich) as the polymer binder. The mixture is hand-mixed with few millilitres of ethanol until viscous slurry is obtained. The slurry is laminated with the help of a glass test tube until the final thickness is within the micrometre range. Then, the film is dried and kept at 120 ºC under vacuum for 12 hours prior to each measurement. Electrodes of comparable mass (up to 15 mg) with 11 mm diameter and a thickness ranging between 200 µm – 250 µm are studied.

2.2.5 Electrochemical Analysis Conditions

Electrochemical studies are carried out by using a 6 M KOH solution for voltage between 0 and 1 V or in 1.5 M tetraethylammonium tetrafluoroborate (Et_4NBF_4, Acros Organics, 99 %, stored under Argon) in acetonitrile (ACN, 99.9 %, extra dry, Acros Organics, stored under Argon) in a voltage window range of 0 to 2.5 V.

To study their cycling life, two samples are aged by the application of constant voltage at 1 V or 2.5 V, for aqueous or organic electrolyte, respectively, for 140 hours. Every 2 hours, galvanostatic charge/discharge curves at 1 $A.g^{-1}$ are recorded. Before and after the ageing experiments, electrochemical impedance spectroscopy is measured for the two-electrode test cells within the ac frequency region from 10 mHz to 1 MHz at different fixed ΔV with ac voltage amplitude of 10 mV.

2.3 Results and Discussion

2.3.1 Extraction of Lignin from Black Liquor

Images of the Lignin after isolation from the black liquor suspension are taken using an optical and Scanning Electron microscope. Figure 2-1 (a - b) shows optical microscope images at different magnification for the biopolymer particles of natural lignin. The final amount of lignin per volume of black liquor is 120 $g.L^{-1}$.

Figure 2-1 (c - d) shows a SEM image with its corresponding EDX analysis. Sodium and sulphur impurities are present in the lignin, which are the product of the Kraft process used in the paper industry to remove black liquor.

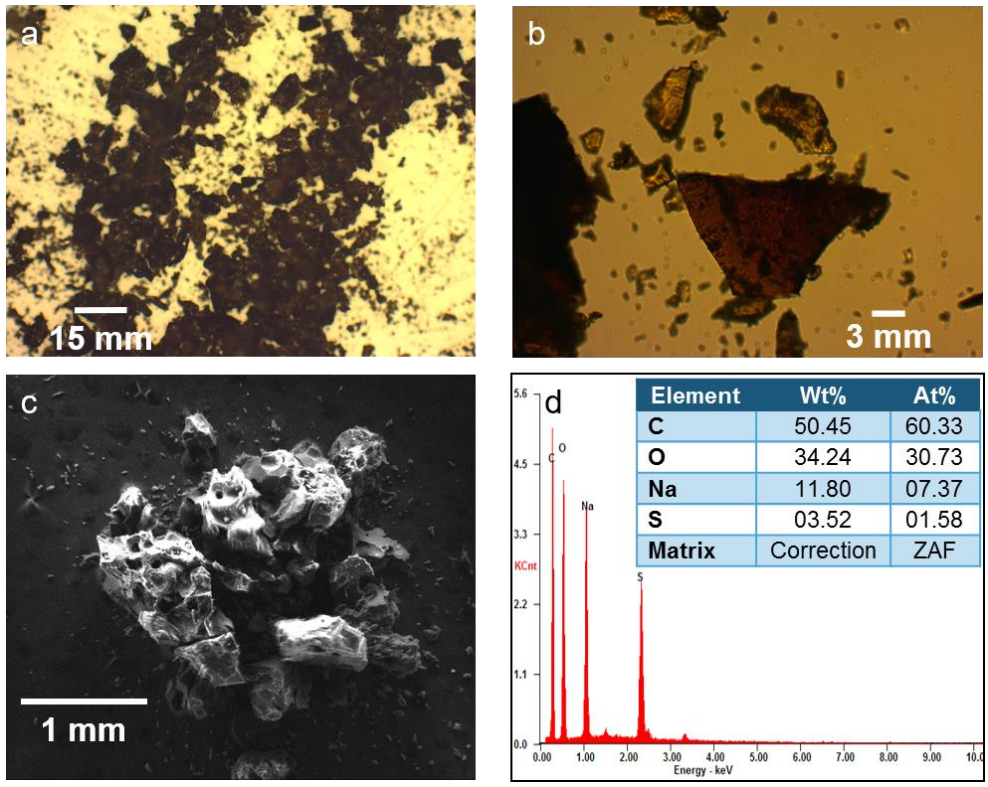

Figure 2-1. Images of the polymer particles of lignin after extraction taken by optical microscope at 5X (a) and 20X (b). SEM image (c) of the same particles and EDX analysis from SEM (d).

2.3.2 Activation Process and Characterization of the Nanoporous Carbons

2.3.2.1 Thermogravimetric Analysis

The formation of the porous structure is as complex as the structure itself. In order to understand the physical phenomenon taking place during the carbonization process of lignin, the sample is studied by thermal gravimetric analysis coupled with mass spectrometry (Figure 2-2). Mass spectrometry identifies the products of the thermal process by using m/z, where m stands for mass and z stands for charge number of ions. The thermal degradation study under argon gas shows a first loss of mass at a temperature lower than 200 ºC corresponding mainly to the loss of water molecules (m/z = 18), above 200 ºC the mass loss is caused by water and carbon dioxide molecules (m/z = 18 and 44, respectively) being produced. The

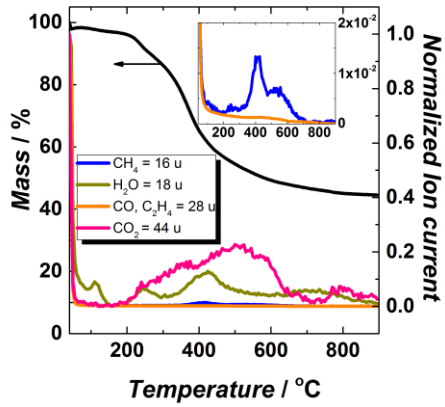

Figure 2-2. Thermogravimetric/mass analysis of a sample of lignin extracted from Black Liquor.

carbon monoxide and ethylene (m/z = 28) molecules are mainly observed below 600 ºC. Between 350 ºC and 700 ºC release of methane (m/z =16) is observed. According to several studies, in the carbonization step a char low pore volume is formed,[17] to increase the porosity in the carbon, an activation step is required. In order to see the effect of methane losses in the final structure of the carbons 400 °C and 900 °C are chosen as carbonization temperatures. At these temperatures, the remaining carbon content is approximately 65 and 45 wt.%, respectively.

During activation with KOH the following reaction takes place:

$$6KOH + C \leftrightarrow 2K + 3H_2 + 2K_2CO_3 \qquad \textbf{Reaction 2-1}$$

Below 400 °C, the KOH would diffuse and intercalate into the carbon. Above 400 °C the removal of water and redistribution of potassium increase the net volume of the sample and lower its density. Above 650 °C, metallic potassium would be liberated, creating the microporosity of a new structure.[18]

2.3.2.2 Effect of the Synthesis Temperature on the Porosity

2.3.2.2.1 N_2 Adsorption-Desorption

Textural properties are analysed by N_2 adsorption-desorption experiments. Figure 2-3 and Table 2-1 show the main results from these analyses. It can be seen that

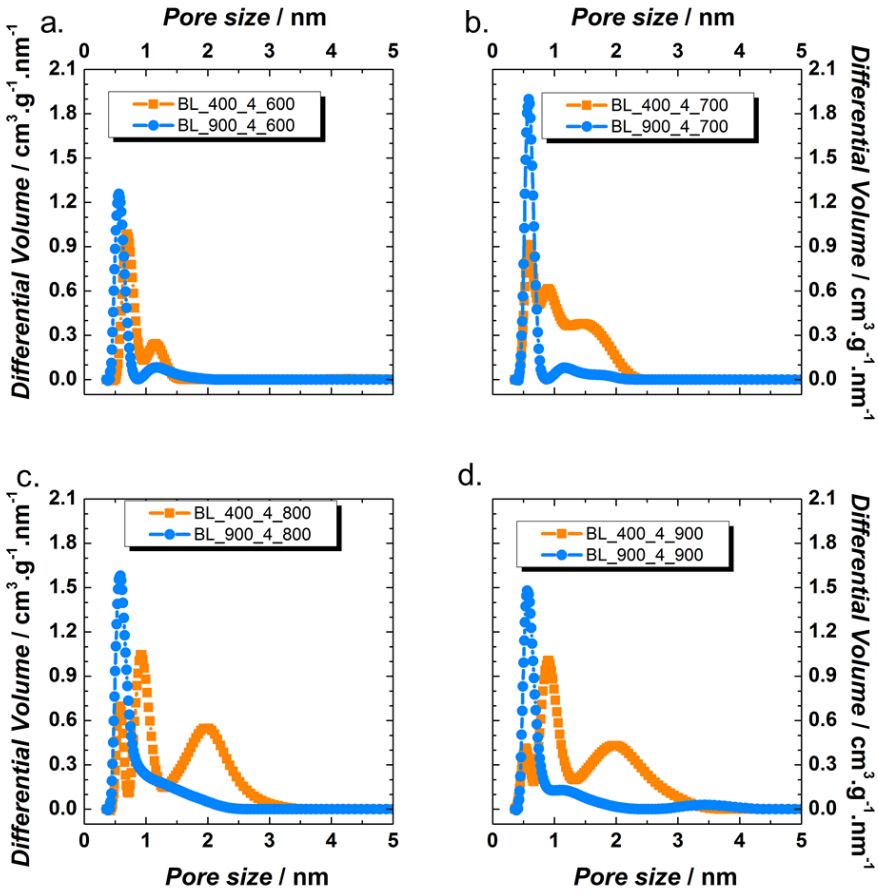

Figure 2-3. Pore size distributions by NLDFT method for samples activated at 600 ºC (a), 700 ºC (b), 800 ºC (c) and 900 ºC (d).

the activated samples previously carbonized at 900 ºC have narrow pore size distribution (PSD) with most of the pores belonging to the ultramicroporous range (< 0.7 nm). By contrast, the activated samples previously carbonized at 400 ºC display broader PSD encompassing both ultramicropores and large micropores with some mesoporosity (< 3 nm).

Table 2-1 shows the values for some of the main textural properties calculated from the N_2 adsorption isotherms by using the NLDFT method. It is evident that as the activating temperature increases, the surface area also increases in both sets of samples accomplishing NLDFT specific surface areas up to ~1500 $m^2.g^{-1}$. For the sample carbonized first and then activated at 900 ºC (BL_900_4_900), the surface area is not increased most probably because at this temperature a

Table 2-1. Textural properties of the activated carbon samples produced from naturally occurring lignin.

Name	S_{NLDFT} ($m^2.g^{-1}$)	$S_{micro-NLDFT}$ ($m^2.g^{-1}$)	$S_{meso-NLDFT}$ ($m^2.g^{-1}$)	$L_{o-NLDFT}$ (nm)	L_{o-DR} (nm)
BL_400_4_600	766	762	4	0.84	1.23
BL_400_4_700	1479	1461	18	1.09	1.34
BL_400_4_800	1510	1303	207	1.21	1.52
BL_400_4_900	1534	1298	236	1.18	1.50
BL_900_4_600	897	897	0	0.69	0.67
BL_900_4_700	1186	1184	2	0.70	0.67
BL_900_4_800	1500	1491	9	0.84	0.94
BL_900_4_900	1272	1254	18	0.76	0.81

competition between the activation process and the C-C bond reorganization takes place, as it will be explained in Section 2.4.2.4. In the case of the samples carbonized at 400 ºC the contribution of the mesoporosity to the surface area is higher than for those samples carbonized at 900 ºC in which, a larger contribution from the micropores to the final value of the surface area is observed.

2.3.2.2.2 Small Angle X-Ray Scattering

In order to understand the nanostructure of the material and to correlate the microporosity differences between the carbons with the carbonization step, all the samples are further analysed by SAXS as can be seen in Figure 2-4. Unlike adsorption measurements, scattering techniques detect a total surface area, including that of pores that may be inaccessible to the adsorbate with a given geometry. In general, the SAXS profiles of the lignin-derived carbons can be described by the following regions: the slope of the form factor at small angles (Guinier region) is primarily determined by the overall size and the final slope at large angles (Porod region) bears the information of the surface. The information about the shape and the internal density distribution of the carbon lies in the oscillating part in the middle section of the form factor (Fourier region).[19] For BL_400 (Figure 2-4 (a)), the Porod law scattering from the micropores lies beyond the maximum observable scattering vector, indicating that these samples do not present micropores. For BL_900 (Figure 2-4 (b)) a fast decrease in the intensity while the scattering angle increases for 0.12 nm^{-1} < Q < 0.8 nm^{-1} is observed. A

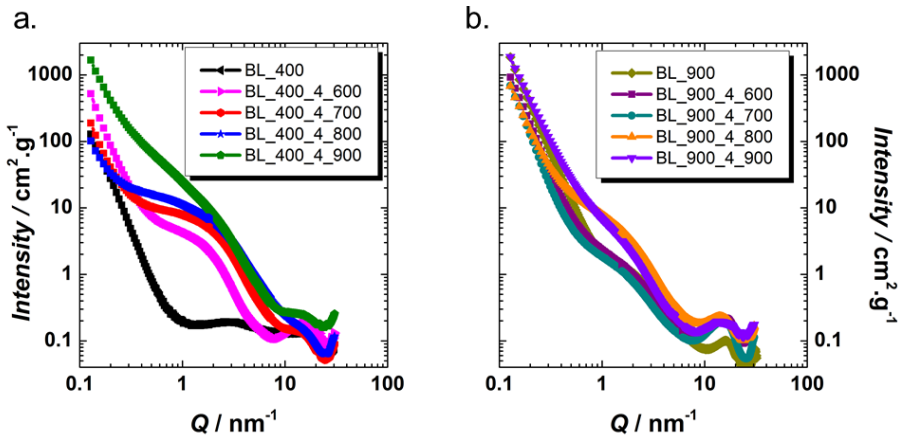

Figure 2-4. SAXS intensity versus scattering angle of the carbonized and the activated samples carbonized at 400 °C (a) and 900 °C (b).

decrease in the slope followed by another drop (0.9 nm^{-1} < Q < 2.9 nm^{-1}), indicating a scattering caused by the presence of micropores in this sample, is also observed. The difference between the samples carbonized at 400 °C (no microporosity evidenced) and 900 °C (presence of microporosity after carbonization) might be caused by the release of methane, which occurs above 350 °C. When the carbonized samples are activated, the presence of micropores is evidenced by the existence of the Fourier and Porod regions in all the SAXS profiles. For both set of samples, it can be seen that as the activation temperature increases, the intensity in the Fourier region increases as well, evidencing an enlargement in the average micropore size. Scheme 2-2 shows a *picture* for the different porous carbon microstructures that might be developed from the different carbonization-activation routes of lignin.

A carbonization process usually approaches completion at 600 °C, therefore the pyrolysis of a polymer below this temperature yields a reticulated product of polymer/carbon.[20] During the activation step of the samples carbonized at 400 ºC, the carbonization and activation process are occurring at the same time. Then, at high temperatures (*i.e.* above 800 ºC), internal microporosity is developed which causes a difference in the Specific Surface Areas calculated by IRENA and NLDFT, as seen in Figure 2-5.

Scheme 2-2. Development of the internal and external porosity during the carbonization and activation processes.

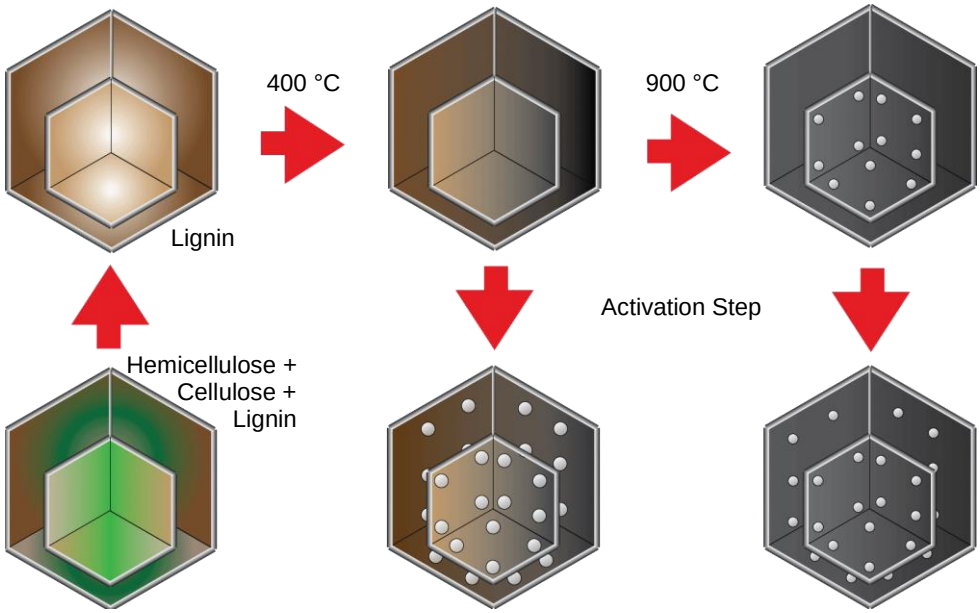

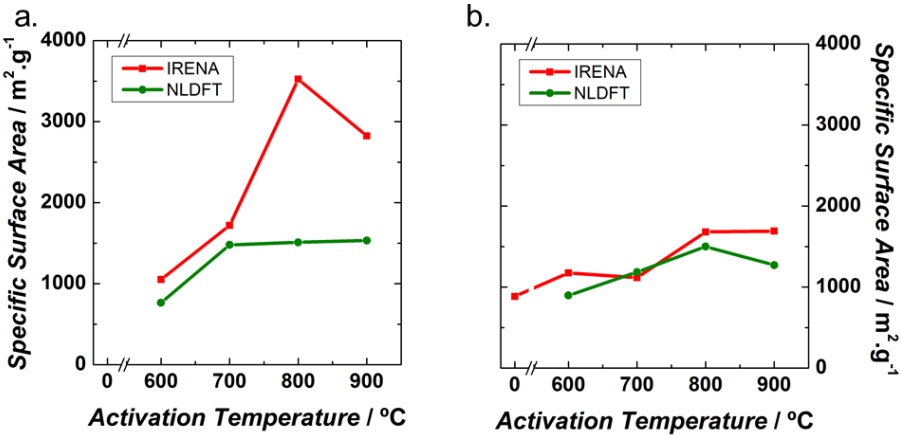

Figure 2-5. Evolution of the Specific Surface Areas with activation temperature of samples previously carbonized at 400 ºC (a) 900 ºC (b) calculated by IRENA and NLDFT.

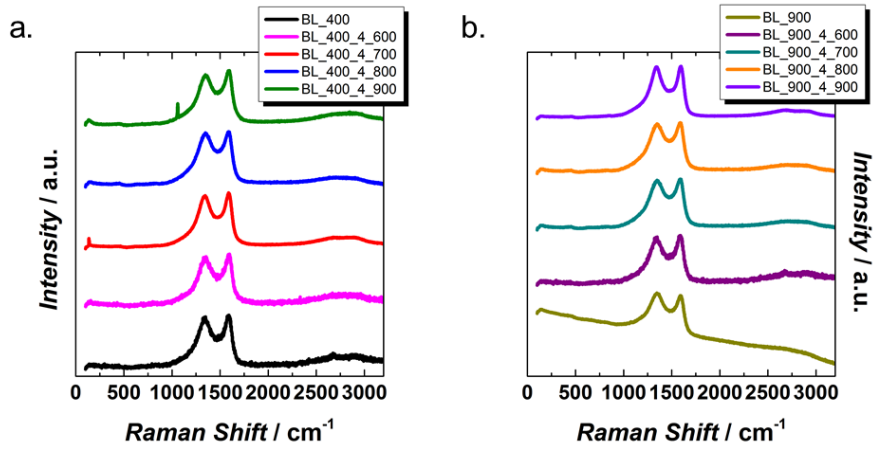

Figure 2-6. Normalized Raman spectra of activated samples after carbonization at 400 °C (a) and 900 °C (b).

2.3.2.2.3 Raman Spectroscopy

Raman spectroscopy is widely used for the characterization of carbonaceous materials because it can provide key information about the properties and characteristics of the sp^2-hybridized carbon bond.[21] Figure 2-6 shows the normalized Raman spectra for the carbonized (non-activated) and the activated samples. The major features of the Raman spectra of all samples include the defect-induced D band (at ~1340 cm^{-1}); the G band (at ~1580 cm^{-1}), which is related to the in-plane vibration of sp^2 carbons and, the 2D band (at ~2705 cm^{-1}), which is the second order of the D band.

2.3.2.2.4 X-Ray Diffraction

Structural ordering of the lignin-derived carbons is studied by X-Ray Diffraction. Figure 2-7 shows the XRD patterns of the activated samples studied here as well as that of the carbonized (non-activated) samples for comparison. All the samples show a remarkable diffraction peak centred around $2\theta = 25.5$ º reminiscent of peak (002) in hexagonal graphite although very broad, pointing to small crystallite size. This is typical of amorphous carbons.[22] The narrow peaks at 29.5 º and 30.5 º correspond to compounds formed by Sodium, Potassium and Sulphur, remnants from the Kraft process.

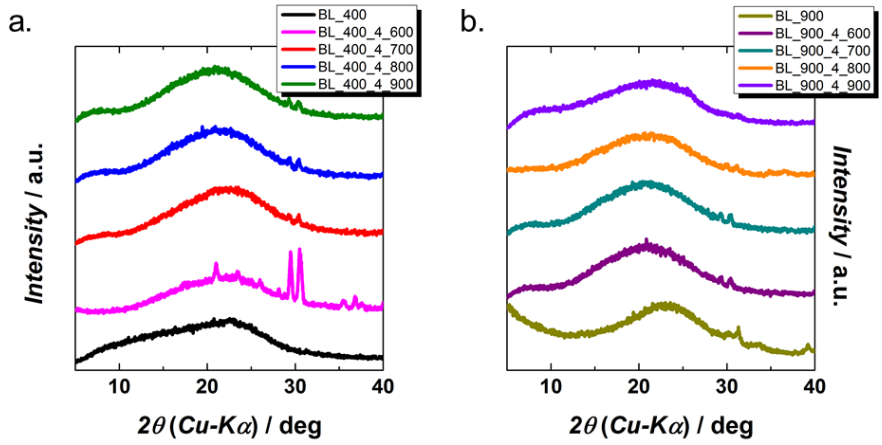

Figure 2-7. XRD patterns corresponding to the nanoporous carbon materials prepared from natural lignin and activated using KOH. The pyrolyzed samples from natural lignin are also included for comparison. Samples initially carbonized at 400 °C (a) and at 900 °C (b).

2.3.2.3 Effect of the Synthesis Temperature on the Electrochemistry

Because the final microstructure of the nanoporous carbons prepared from natural lignin will have a strong impact on the electrochemical properties, we study them as electrode material for supercapacitors applications at room temperature. Figure 2-8 shows the main results of the electrochemical analysis performed on the activated carbon samples in aqueous 6 M KOH electrolyte. Figure 2-8 (a) shows the cyclic voltammograms performed at a constant scan rate of 10 $mV.s^{-1}$ for samples BL_400_4_900 and BL_900_4_700. Both curves exhibit the typical EDLC rectangular shape during the electrosorption of ions. At high scan rates, sample BL_900_4_700 retains its rectangular shape, which proves good electrical conductivity and ion diffusion inside the pores (Figure 2-8 (b)). The highest specific capacitance values (Figure 2-8 (c)) among all the different porous lignin-derived carbons are reached by samples BL_400_4_900 and BL_900_4_700 (~200 $F.g^{-1}$ at 0.1 $A.g^{-1}$), which correspond to the samples with the highest specific surface area (1534 $m^2.g^{-1}$) and the smallest pore size (0.67 nm), respectively.

Figure 2-8 (d) shows the volumetric values for the capacitance calculated taking into account the densities of each electrode (including the polymer binder). The highest value, 107 $F.cm^{-3}$ at 0.1 $A.g^{-1}$, is evidenced by the sample BL_900_4_700, proving that this sample can be used in applications where high gravimetric and/or volumetric capacitance are desired. The high volumetric capacitance value of sample BL_900_4_700 is without any doubt related to its small average pore size,

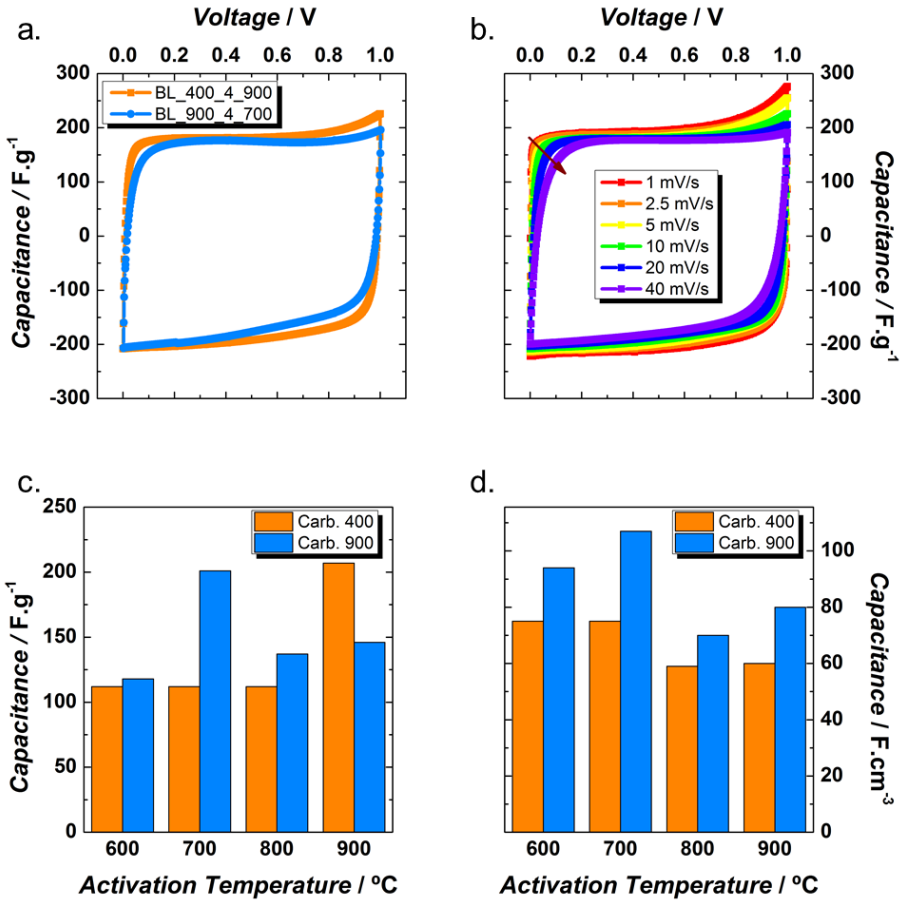

Figure 2-8. Cyclic voltammetry of BL_400_4_900 and BL_900_4_700 at 10 mV.s^{-1} (a). Cyclic voltammetry of BL_900_4_700 at different scan rates (b). Gravimetric (c) and Volumetric (d) capacitance values exhibited by the samples in an aqueous-based electrolyte.

which is a direct consequence of the internal microporosity developed in the carbonization step and observed by SAXS.

In the present work, the electrochemical tests in organic electrolyte are conducted by using a 1.5 M solution of tetraethylammonium tetrafluoroborate salt in acetonitrile. By using organic-based electrolytes, the voltage window will be increased and the energy density enhanced. As shown in Figure 2-9, the CV curves of almost all the samples carbonized at 400 ºC show a symmetric and rectangular shape at 5 mV.s^{-1}, revealing a nearly ideal electrical "double-layer" behaviour, suggesting a non-hindered interaction between the nanopores and the

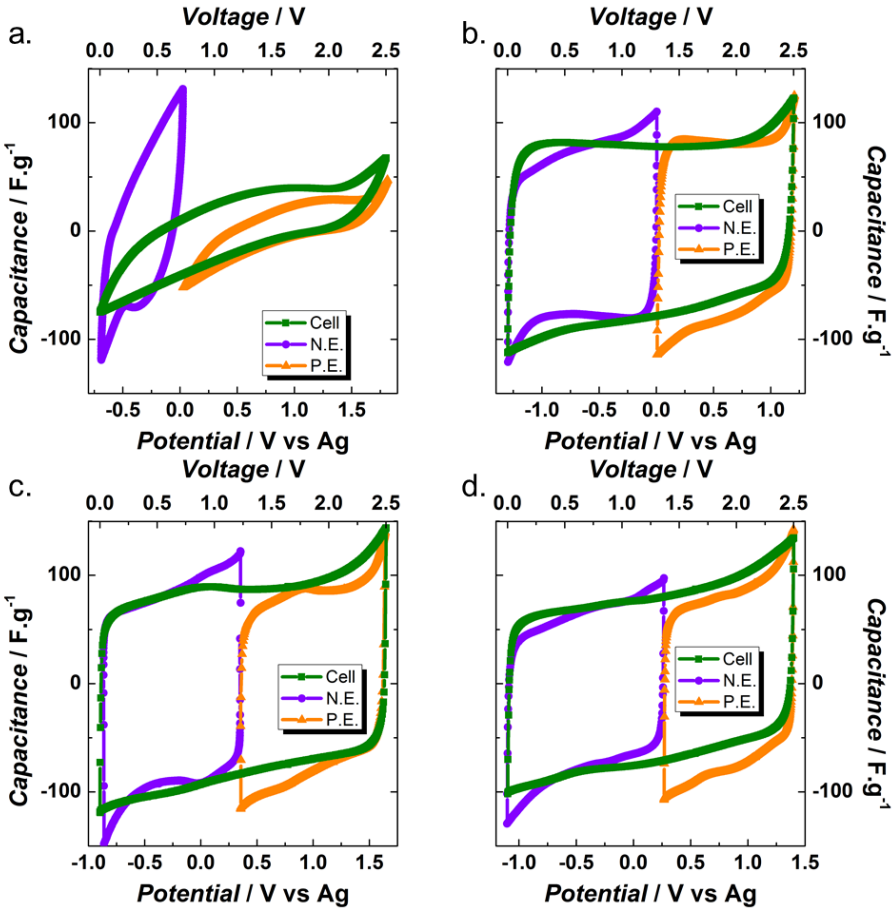

Figure 2-9. Cyclic Voltammetry in a two-electrode cell configuration with a pseudo-reference electrode in an organic electrolyte of BL_400_4_600 (a), BL_400_4_700 (b), BL_400_4_800 (c) and BL_400_4_900 (d).

electrolyte ions as well as no faradaic side reactions. By contrast, sample BL_400_4_600 exhibits distorted CV shapes, most probably due to the intricate interaction between the ions and the nanopores. For the other samples, the right interaction between ions and pores is also proved by the fact that both electrodes, the positive and the negative, achieve the same capacitance values in similar voltage windows. The highest capacitance value, 97 $F.g^{-1}$, is shown by sample BL_400_4_700.

The distorted shape of the CV for the samples carbonized at 900 ºC (Figure 2-10) may be due to the particular porous texture (pore size, shape, tortuosity)[23] of the material. All these samples present a low average micropore size (< 1 nm)

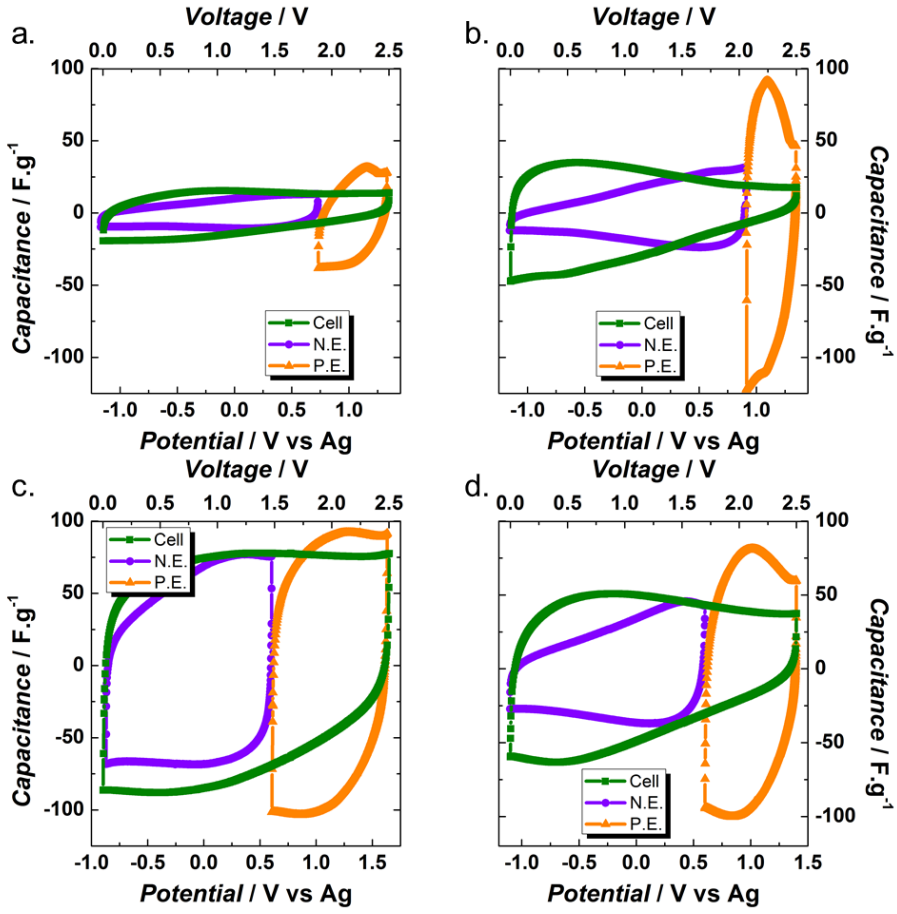

Figure 2-10. Cyclic Voltammetry in a two-electrode cell configuration with a pseudo-reference electrode in an organic electrolyte of BL_900_4_600 (a), BL_900_4_700 (b), BL_900_4_800 (c) and BL_900_4_900 (d).

compared to the effective ion size (*i.e.* the size of the ion inside the pore) leading to the ion sieving effect.[24–26] More precisely, the sizes of the ions in ACN vary in the following way: BF^{4-} bare anion is 0.48 nm while solvated > 1 nm; for the Et_4N^+ bare cation is 0.67 nm and solvated = 1.3 nm.[27] This effect is avoided in the samples carbonized at 400 ºC given that most of them have an average micropore size above 1.3 nm, allowing the unrestricted access of the ions to the pores of the carbon.

In the case of the samples carbonized at 900 ºC, the electrochemical potential window for the negative electrode is larger than for the positive electrode, due to their small average pore size. This way, the restrictive effect of the organic cations (Et_4N^+) to enter into the pores because of the larger molecular shell size in

comparison with the anions (BF^{4-}) is confirmed. The gravimetric capacitance values of the negative electrodes are lower than the positive electrode ones due to the larger potential window of the negative electrodes. These measurements clearly confirm the importance of matching the pore and ion size to optimize capacitive performance.

As the cycle life of supercapacitors is inherently long (due to absence of redox reactions), aging acceleration tests are of primary importance. In this study, we use floating tests[28] to evaluate the behaviour in aqueous and organic electrolytes of samples BL_900_4_700 and BL_400_4_700, respectively. To understand the

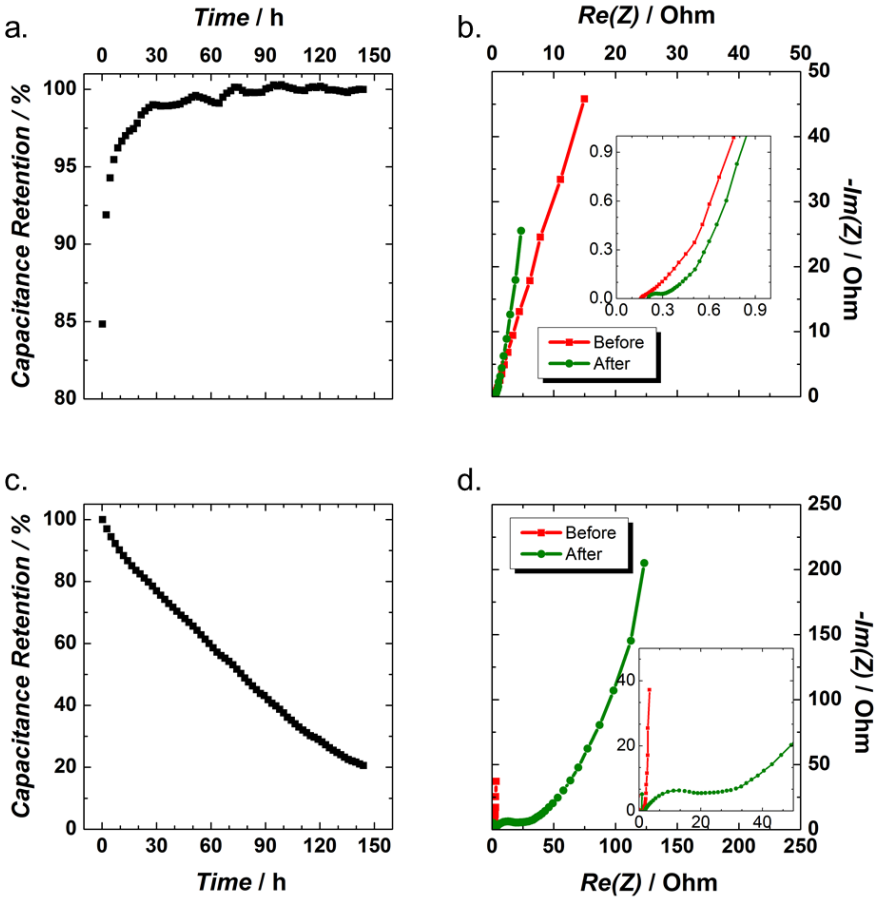

Figure 2-11. Capacitance retention (a) and Nyquist plot (b) of sample BL_900_4_700 in an aqueous electrolyte. Capacitance values (c) and Nyquist plot (d) of sample BL_400_4_700 in an organic electrolyte.

changes in the cell by this aging method, electrochemical impedance spectroscopy is measured before and after the floating test. The result of floating at 1 $A.g^{-1}$ for 150 h for BL_900_4_700 in an aqueous electrolyte is shown in Figure 2-11 (a). No capacitance fading during cycling is observed. The small increase observed in the capacitance, might be caused by the slow diffusion of electrolyte in the carbon. From the Nyquist plot shown in the inset in Figure 2-11 (b), it can be observed that the equivalent series resistance (ESR) for sample BL_900_4_700 in aqueous electrolyte increases from 0.05 Ohm to 0.10 Ohm after the floating test. This is probably due to dimensional changes of the carbon's pores during cycling.[29] However, the time constants (RC) before and after cycling are 0.3 s and 0.4 s, respectively, showing an optimum charge propagation in the electrochemical capacitor.

In the case of sample BL_400_4_700 in an organic electrolyte, the floating test (Figure 2-11 (c)) shows that even though the pores are well adapted to the ions, a drastic capacitance fading as well as a large increase of the electrolyte resistance (from 0.6 Ohm to 1.9 Ohm) and of the ESR (from 0.17 Ohm to 21 Ohm) (Figure 2-11 (d)), are observed. The fading in the capacitance and the increase in both, the electrolyte and the equivalent series resistances suggest the presence of surface oxygen-containing groups, which is probable due to the low carbonization and activation temperatures, that results in instability of the electrode and increase of series resistance.[1]

2.3.2.4 Effect of the KOH/C Ratio on the Porosity

After studying the effect of the carbonization and activation temperatures, the KOH/C ratio effect is studied. For this, a carbonization and activation temperature of 900 ºC is selected to avoid presence of functional groups that can affect the electrochemical performance of the materials.

2.3.2.4.1 Yield

Figure 2-12 shows the yield (% burn off) for the different activated carbons studied in this section. Carbonized lignin (sample BL_900, carbonization yield ~45 wt.%) is used as starting material during the activation step and then also as a reference for the calculation of the activation yields. Although a drastic drop in the yield can be seen from BL_900_1_900 to BL_900_2_900 (~37 wt.%), a more progressive yield decrease from BL_900_2_900 to BL_900_5_900 is observed. Activation by using larger amounts of KOH provokes a further decrease in the final content of carbon rendering a yield of ~25 wt.% for sample BL_900_7_900.

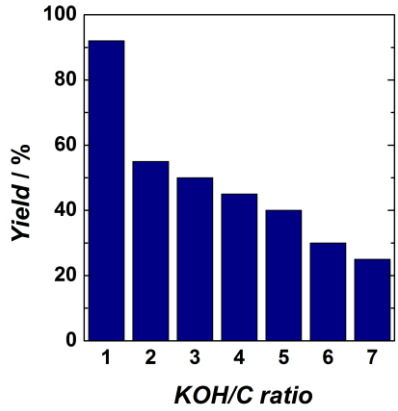

Figure 2-12. Effect of the KOH/C ratio on the yield of the activated carbons.

2.3.2.4.2 N_2 Adsorption/Desorption

Textural properties of the carbon samples are studied by N_2 adsorption/desorption experiments. All these samples present a type I isotherm testifying that lignin-derived carbons are microporous materials. Moreover, the well discernible hysteresis loop at high relative pressure is associated with capillary condensation in mesoporosity (Figure 2-13 (a)).[30–32] After applying the corresponding analysis method to the adsorption isotherms, the surface areas, average pore sizes and micropore volumes are calculated (Table 2-2). Figure 2-14 (b) shows the variation of the specific surface area and the average micropore size determined by the NLDFT method versus the KOH/C ratio. The observed dependence suggests that there is no trend between the KOH/C ratio and the final porosity of the carbon, as distinct from activated carbons based on fossil fuels.[33] The SSA and the average micropore size values show a non-linear trend as the chemical activation of the char proceeds by increasing the KOH/C ratio from 1 to 7. For samples BL_900 and BL_900_1_900 (as for BL_400 in the previous section), the porosity is weakly developed and thus stronger activation is required to achieve practically significant values of specific surface area. As the amount of KOH increases the SSA and the average pore size also increases, but further activation gives rise to a minimum in both values at a KOH/C ratio between 4 and 5. Higher KOH/C ratios provoke the development of an extra porosity with the resulting raise in the SSA and the pore size reaching maximum values of ~1406 $m^2.g^{-1}$ and 0.96 nm for sample BL_900_6_900 and ~1262 $m^2.g^{-1}$ and 0.98 nm for sample BL_900_7_900, respectively.

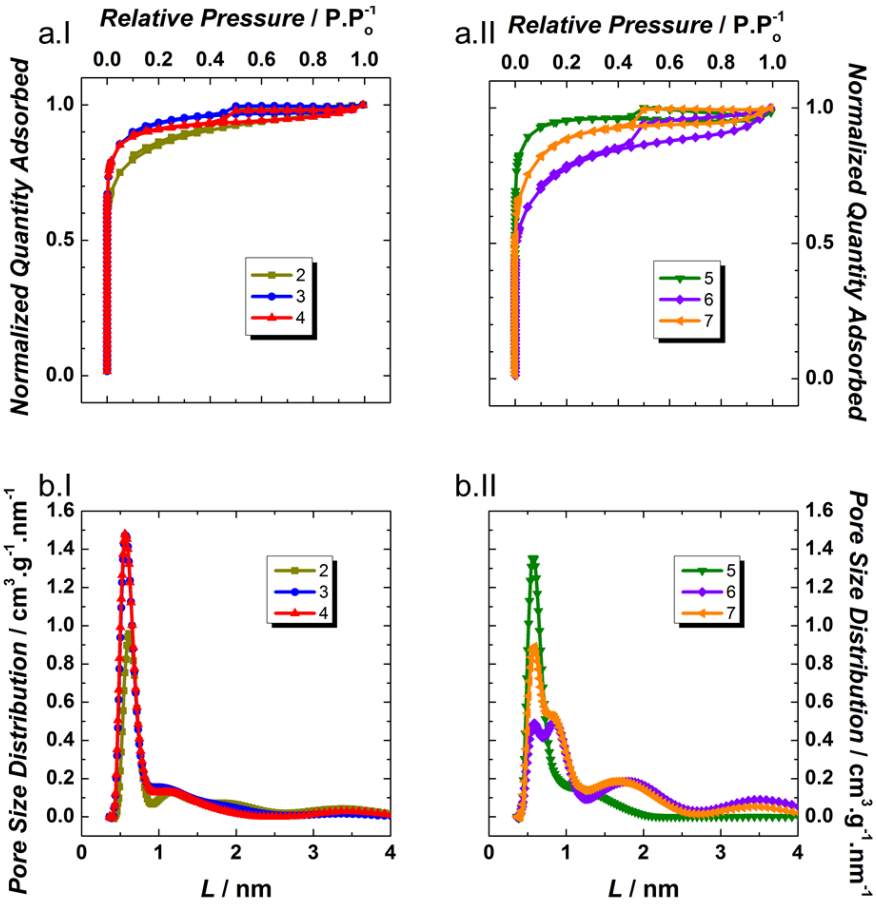

Figure 2-13. Textural analysis for samples 2, 3 and 4 (I) and 5, 6 and 7 (II). Normalized isotherms of the activated carbon samples (a) and differential pore volume calculated by NLDFT method (b).

2.3.2.4.3 Small Angle X-Ray Scattering

The textural properties of the materials are further studied by Small Angle X-Ray Scattering. SAXS profiles for all the samples can be seen in Figure 2-15. They all present the Guinier, Porod and Fourier regions described in the previous section. The major differences are observed during activation of the first four samples, where the activation of the carbon allows the opening of the internal porosity and some mesoporosity appears as well. Samples with KOH/C ratios between 4 and 7, present similar SAXS profiles as their areas and average micropore sizes are fairly similar.

Table 2-2. Textural properties of the activated carbon samples produced from naturally occurring lignin.

Name	S_{NLDFT} ($m^2.g^{-1}$)	$S_{micro-NLDFT}$ ($m^2.g^{-1}$)	$S_{meso-NLDFT}$ ($m^2.g^{-1}$)	$L_{o-NLDFT}$ (nm)	L_{o-DR} (nm)
BL_900_1_900	9	5	4	1.80	--
BL_900_2_900	845	797	48	0.90	1.07
BL_900_3_900	1280	1259	21	0.80	0.87
BL_900_4_900	1272	1254	18	0.76	0.81
BL_900_5_900	1236	1234	2	0.79	0.87
BL_900_6_900	1406	1311	95	0.96	1.24
BL_900_7_900	1262	1196	66	0.98	1.22

In order to see the differences in specific surface area and porosity between the samples by SAXS, the data are analysed with the IRENA tool package and the results are compared to the ones acquired by N_2 sorption in Figure 2-16 and Figure 2-17.

Specific Surface Areas calculated by both methods follow the same trend (Figure 2-16). At KOH/C equal to five, the difference in SSA is more notorious, this can be explained by the structure inhomogeneity of the sample as it will be explained with the Raman experiments.

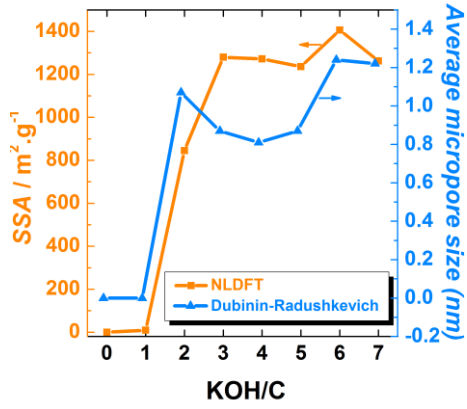

Figure 2-14. Textural properties: specific surface area and average micropore size of the pyrolyzed and activated carbon samples determined by NLDFT method.

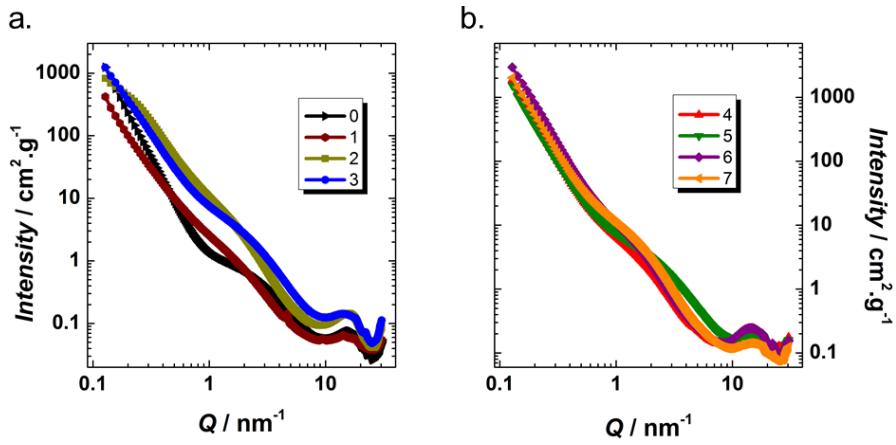

Figure 2-15. SAXS intensity versus scattering angle of the carbonized and the activated samples at different KOH/C ratios: 0, 1, 2, and 3 (a) and 4, 5, 6, and 7 (b).

Comparison of the pore size distribution of the activated carbons with the one from sample BL_900, calculated by IRENA, allows us to confirm that the microporosity observed in all the activated carbons comes from the internal microporosity developed in the carbonization step (Figure 2-17).

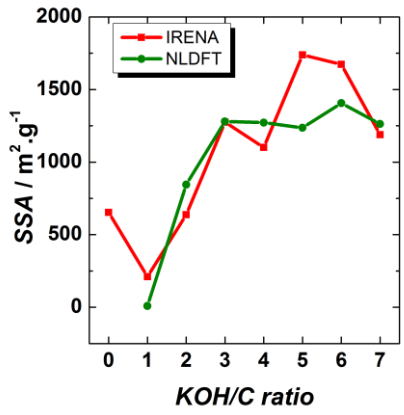

Figure 2-16. Comparison of the Specific Surface Area calculated by SAXS/IRENA (red dots) and NLDFT method (green circles).

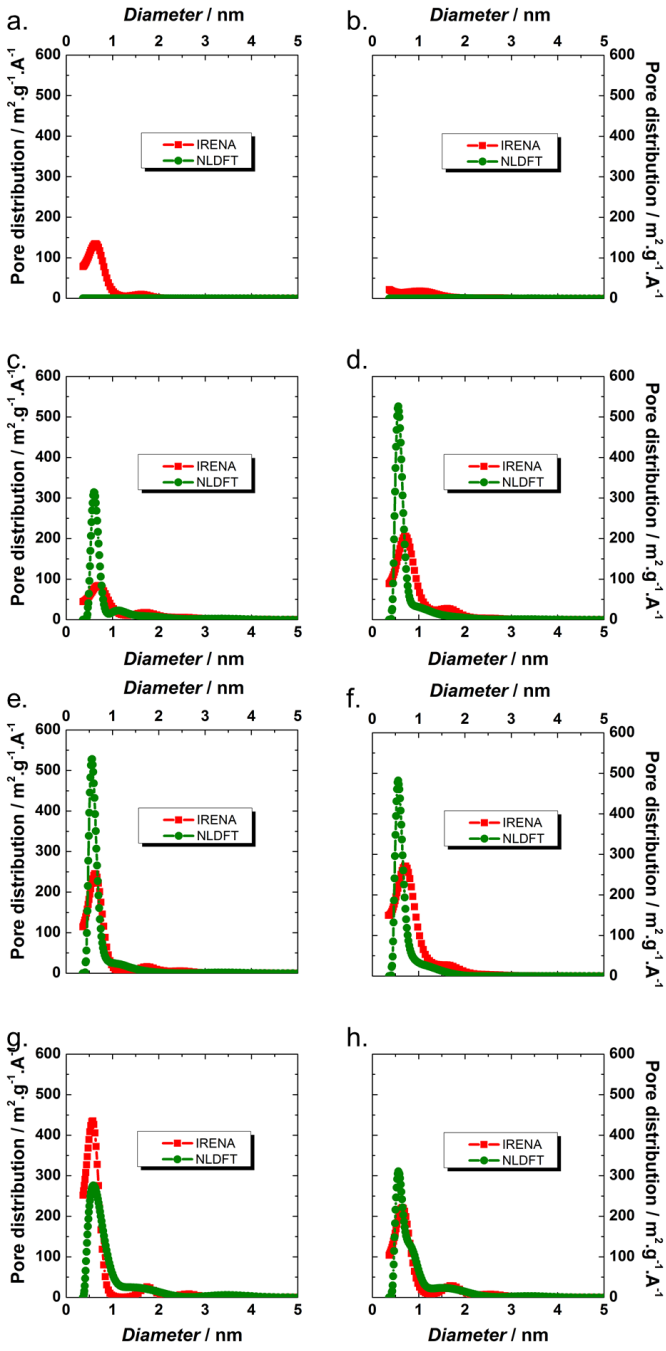

Figure 2-17. Comparison of the pore size distributions calculated by SAXS/IRENA (orange line) and NLDFT method (blue line). KOH/C equal to 0 (a), 1 (b), 2 (c), 3 (d), 4 (e), 5 (f), 6 (g), and 7 (h).

2.3.2.4.4 Raman Spectroscopy

In order to study the ordering of the carbons, acquisition of a single Raman spectrum is performed on several particles of the same specimen for the whole series of carbons prepared in this section. A minimum of 10 spectra are taken on different points of the sample particle. Figure 2-18 shows the typical Raman spectrum of each sample, the samples activated with a KOH/C ratio ≥ 2, clearly show two different zones, ordered (blue line) and disordered (orange line). For all the carbon samples derived from lignin, the low frequency region shows the two characteristic bands for carbonaceous materials; the graphite (G) band between 1570 cm^{-1} and 1600 cm^{-1} and the disorder–induced (D) band between 1330 cm^{-1} and 1360 cm^{-1}. The presence of graphene domains produces the appearance of a weak but well defined band at ~2450 cm^{-1} which is due to a non–dispersive overtone mode of an in–plane optical phonon.[34] The G mode has E_{2g} symmetry and involves the in–plane bond–stretching motion of pairs of C sp^2 atoms; while the D peak is a breathing mode with an A_{1g} symmetry involving phonons near the *K* zone boundary, which only becomes active in the presence of disorder.[14] At the second-order region, the 2D band (2670 – 2760 cm^{-1}) appears. This band is due to two phonon with opposite momentum in the highest optical branch near the *K* point of the Brillouin zone (A'_1 symmetry at *K*).[35]

A Raman spectral imaging study (Figure 2-19) in at least 600 different points of a representative single particle is performed. In order to observe the morphology of these materials, the deconvolution and the ratio between the I_D and I_G peaks (~1340 and ~1580 cm^{-1} respectively) are calculated.

The analysis shows that lignin-derived carbons have a complex structure comprising a distribution of ordered ($I_D/I_G < 0.5$) and disordered ($I_D/I_G > 0.5$) zones. In Figure 2-19 Raman maps are shown coloured according to the ratio of the peaks intensities, showing the distribution of ordered as well as disordered areas.

For sample BL_900_2_900, the formation of ordered regions seems to be in the initial stages. The presence of more ordered areas increases as the KOH/C ratio increases obtaining almost completely organized zones for ratios 4, 5, 6 and 7.

The probability distribution of I_D/I_G in a particle in the different samples is shown in Figure 2-20 (a - g); the area of each rectangle represents the frequency of points with an I_D/I_G ratio corresponding to each interval and the total area is equal to the number of spectra taken in each sample. Figure 2-20 shows the percentile distribution of the samples in ordered and disordered zones. KOH/C ratios equal to 1, 4 and 7 show almost no deviation from the main peaks and the carbons appear either completely disordered (BL_900_1_900) or ordered (BL_900_4_900

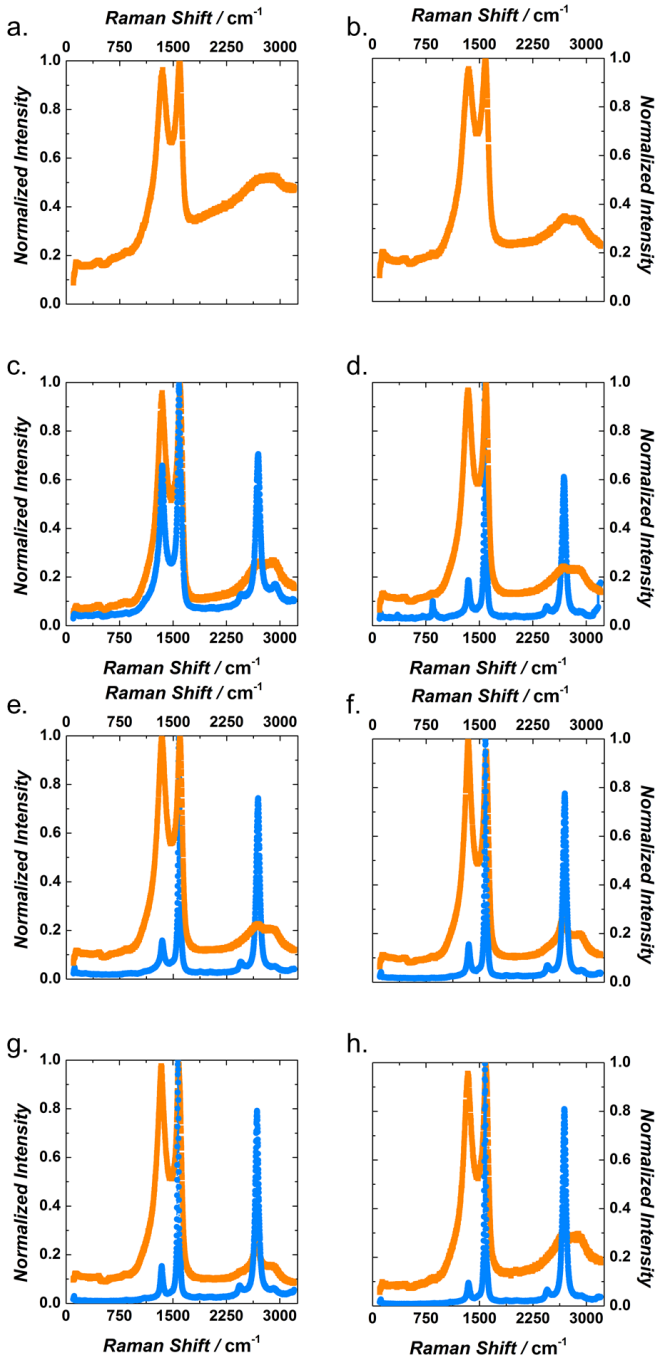

Figure 2-18. Normalized Raman spectra of samples with KOH/C ratio of 0 (a), 1 (b), 2 (c), 3 (d), 4 (e), 5 (f), 6 (g) and 7 (h); depicting the two different spectra observed in different particles.

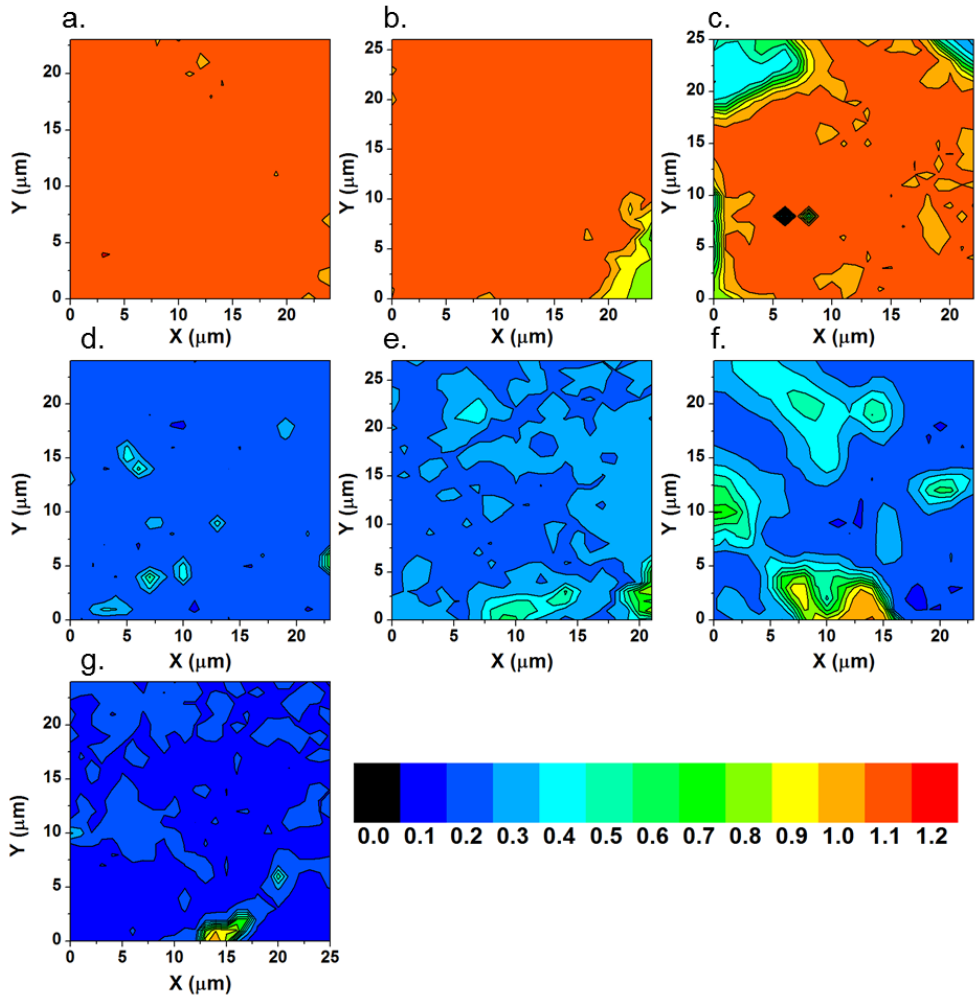

Figure 2-19. Distribution obtained by Raman spectral imaging of the ordered and disordered areas inside a particle for KOH/C ratio 1 (a), 2 (b), 3 (c), 4 (d), 5 (e), 6 (f), 7 (g). Colour scale on the right bottom varies with the I_D/I_G values from 0.0 (dark blue) to 1.2 (dark red).

and BL_900_7_900). At KOH/C equal to 2, 3, 5 and 6, the presence of outliers of low frequency indicates that for these ratios the morphology of the carbon is more heterogeneous, even though the majority of the structure is disorganized (BL_900_2_900 and BL_900_3_900) or organized (BL_900_5_900 and BL_900_6_900). This heterogeneity causes discrepancies in the calculations of Specific Surface Areas by NLDFT and IRENA.

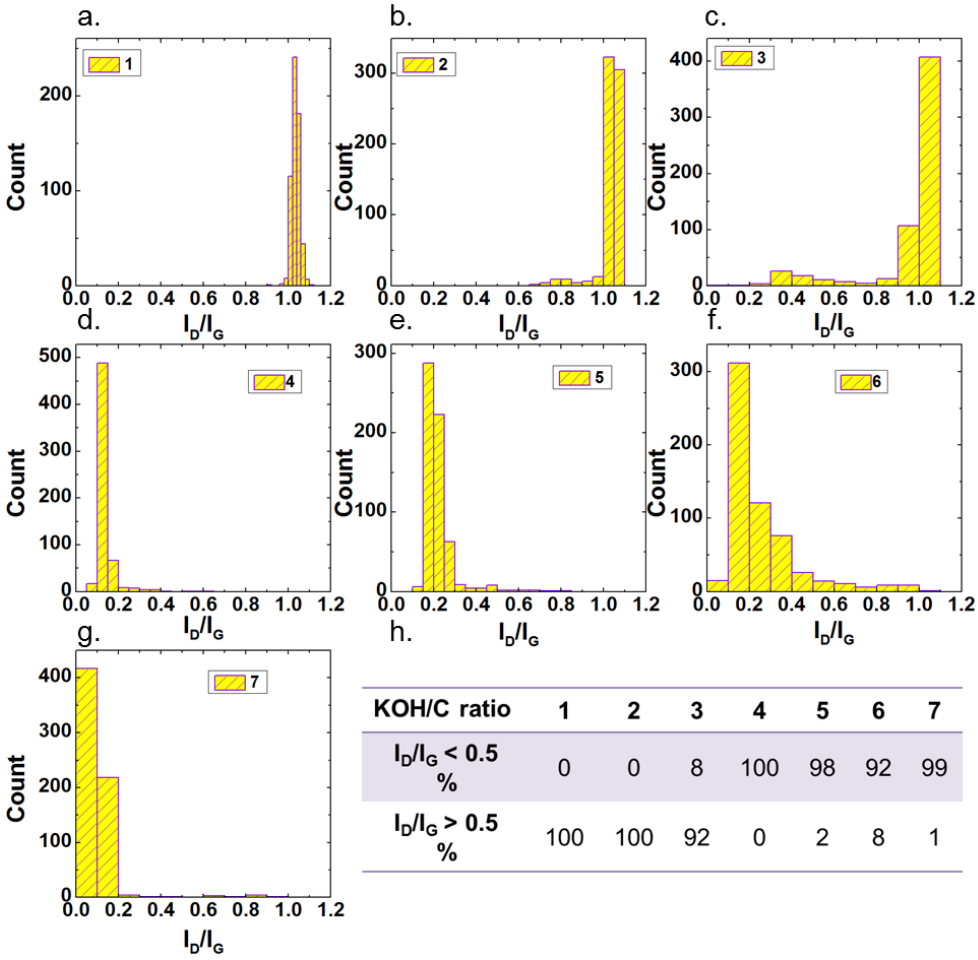

KOH/C ratio	1	2	3	4	5	6	7
I_D/I_G < 0.5 %	0	0	8	100	98	92	99
I_D/I_G > 0.5 %	100	100	92	0	2	8	1

Figure 2-20. Histogram of KOH/C ratio calculated from the Raman spectral imaging for KOH/C ratio 1 (a), 2 (b), 3 (c), 4 (d), 5 (e), 6 (f), 7 (g) and percentile distribution of the samples (h).

2.3.2.4.5 X-Ray Diffraction

Figure 2-21 (a - h) shows the diffraction profiles for the set of samples studied in the present work. The XRD measurements did not show any remarkable difference among the samples. All of them presented a prominent and broad peak at ~2θ = 26 º corresponding to the (002) diffraction in graphite (Figure 2-21 (i)).

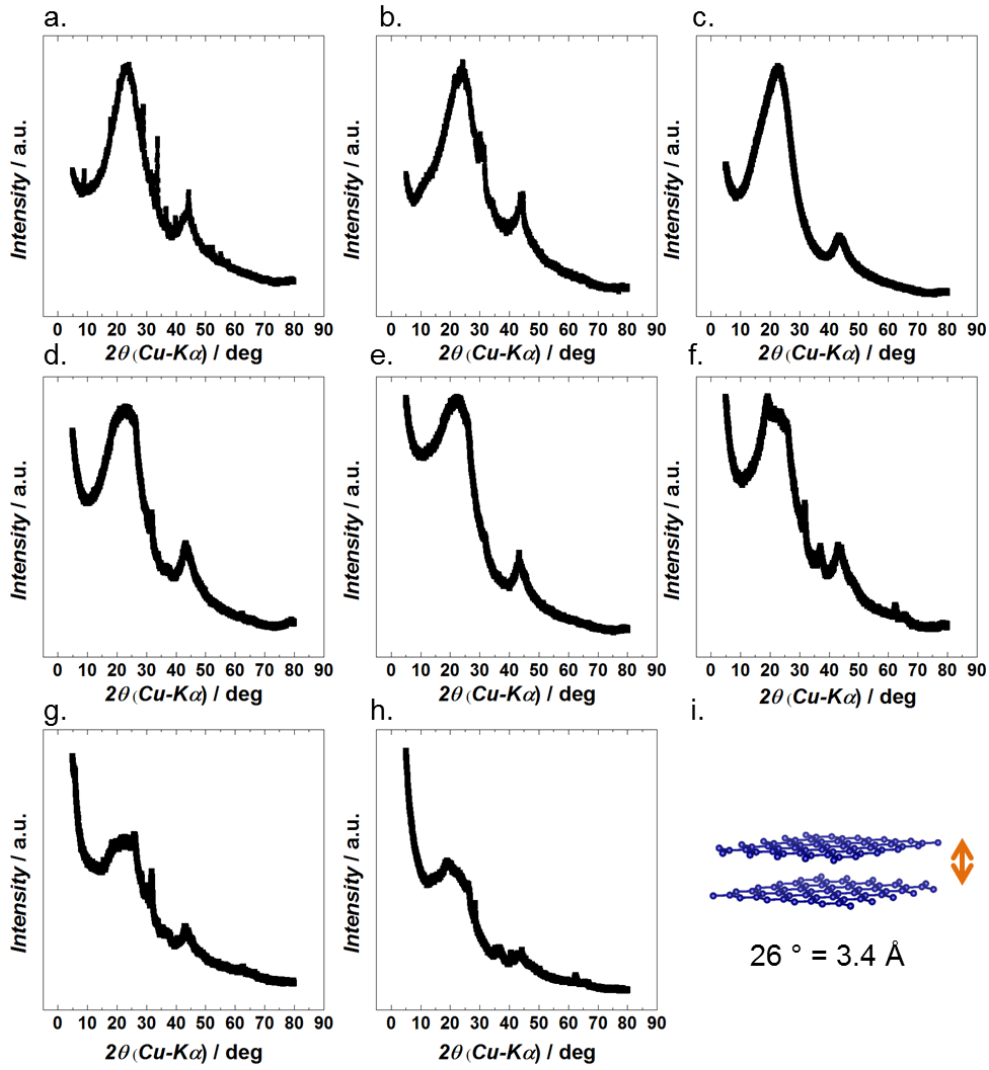

Figure 2-21. X-Ray Diffraction patterns of the lignin-derived carbons, by KOH/C ratio equal to 0 (a), 1 (b), 2 (c), 3 (d), 4 (e), 5 (f), 6 (g) and 7 (h). Image illustrating the interlayer distance causing the 26 ° peak (i).

2.3.2.4.6 Scanning and Transmission Electron Microscopy

Four samples (BL_900, BL_900_2_900, BL_900_4_900, BL_900_6_900) are selected to analyse their morphology and microstructure by SEM (Figure 2-22 (a - d)) and TEM (Figure 2-22 (e – h)). Sample BL_900 in Figure 2-22 (a and e) has a typical microstructure of low-ordered carbon produced by thermal carbonization.

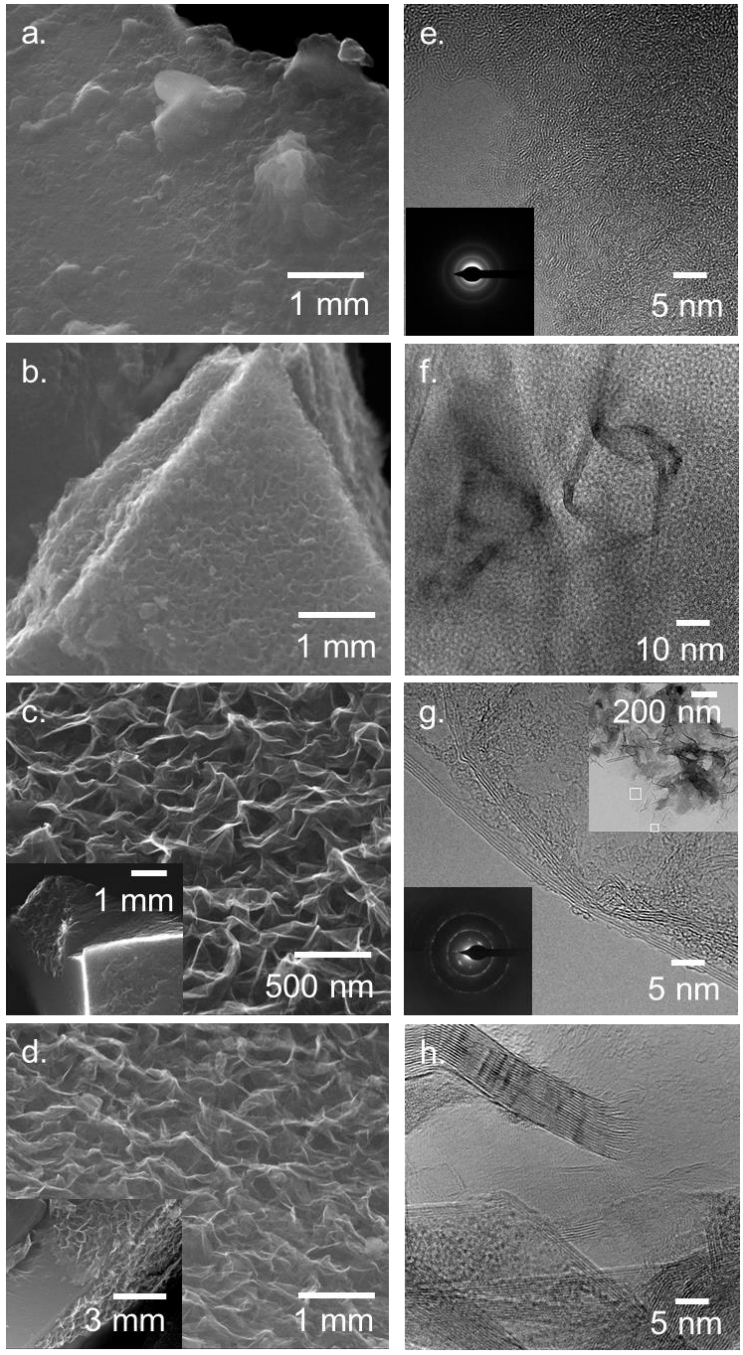

Figure 2-22. SEM (left) and HRTEM (right) images of the samples 0 (a and e), 2 (b and f), 4 (c and g) and 6 (d and h). Inset images: electron diffraction of the samples 0 (e) and 4 (g) and TEM image of a particular area in sample 4 (g).

SAD pattern (inset in Figure 2-22 (e)) shows only continuous uniform rings. After activation at 900 °C by using a KOH/C ratio above 2, the material shows not solely typical amorphous microstructure of activated carbons but also ordered regions. Figure 2-22 (b) shows the corrugation produced on the surface of the material due to the development of well-defined graphene layers during the activation process. The presence of few-layer graphene (FLG) embedded into the amorphous carbon matrix is confirmed by HRTEM (Figure 2-22 (f)). This phenomenon becomes more noticeable on the more strongly activated carbon specimens BL_900_4_900 (Figure 2-22 (c)) and BL_900_6_900 (Figure 2-22 (d)). The top-right inset in Figure 2-22 (g) shows an agglomerate of carbon particles being mostly made up of few-layer graphene (see the HRTEM image of a selected area in Figure 2-22 (g)). A curved few-layer graphene structure, similar to the one obtained from delamination of highly graphitized carbon materials, is observed. The electron diffraction (ED) analysis (the bottom-left inset in Figure 2-22 (g)) also confirms the crystallinity of the material.

Figure 2-22 (h) shows an HRTEM image of sample BL_900_6_900, in which nanoparticles exhibiting a larger number of stacked graphene layers than for sample BL_900_4_900 along with less ordered carbon are observed; the maximum number of graphene layers is estimated to be up to 30. As the amount of KOH/C ratio increases, the presence of both FLG along with less ordered areas is identified by SEM and TEM, this appearance of well-defined graphene layers occurs after carbonization and corresponds to a solid-state rearrangement.[36]

Lignin-derived carbon can graphitize at temperatures above 2100 °C by the catalytic effect of sodium and sodium compounds present in lignin.[3,4] Therefore, the C–C bond reorganization observed in these lignin-derived carbons might be due to a catalytic effect caused by presence of metals in the material, *e.g.* metallic impurities (ash content) from the biopolymer as well as metallic potassium produced during chemical activation.

Actually, potassium hydroxide has been proved to be a catalytic agent in the reconstruction of closed-shell graphitic carbon[37] and during the rearrangement of carbon nanofibers.[38] More recently, activated carbon prepared from graphite oxide exhibited both the typical breakdown of the C–C bond network and a re-structuring process during the chemical activation with KOH.[22] Thus, the final microstructure of lignin-derived carbon might be the result of two competitive processes: the chemical oxidation and the re-organization of the C–C bond mainly induced by metallic particles. The detailed mechanism of chemical activation still requires elucidation although the overall process can be described by Reaction 2-1, followed by side reactions amongst the different by-products ($K/K_2CO_3/CO_2$) with carbon.[22]

2.3.2.5 Effect of the KOH/C Ratio on the Electrochemistry

Figure 2-23 shows the cyclic voltammetry results at 5 $mV.s^{-1}$ of the series BL_900_#_900 (where # denotes de KOH/C ratio), indicating gravimetric (Figure 2-23 (a)) and volumetric (Figure 2-23 (b)) capacitance values. The almost purely capacitive behaviour of the nanoporous materials with KOH/C > 2, is evidenced in their cyclic voltammetry measurements (Figure 2-23) at 5 $mV.s^{-1}$, in which a rectangular shape demonstrates the lack of faradaic charge transfer processes. Moreover, the profiles are quite symmetric meaning that these novel nanoporous carbon electrodes have good electrochemical reversibility and coulombic efficiency in 6 M KOH. Sample BL_900_1_900 shows a more resistant shape because of its low porosity.

Figure 2-24 shows how the gravimetric and volumetric capacitance follow the same trend as the specific surface area, confirming that capacitive storage is strongly dependent on the available surface.

Figure 2-25 shows the variation of the capacitance with the current density. Sample BL_900_6_900 exhibits the highest capacitance (144 $F.g^{-1}$) at 0.1 $A.g^{-1}$ and the largest retention (75 % at 10 $A.g^{-1}$), this is a direct result of this sample having the largest SSA and second largest micropore average size from this set of samples. Samples BL_900_5_900 and BL_900_7_900 show lower capacitance values than their counterparts and poorer retention because of their low S_{micro} (Table 2-2).

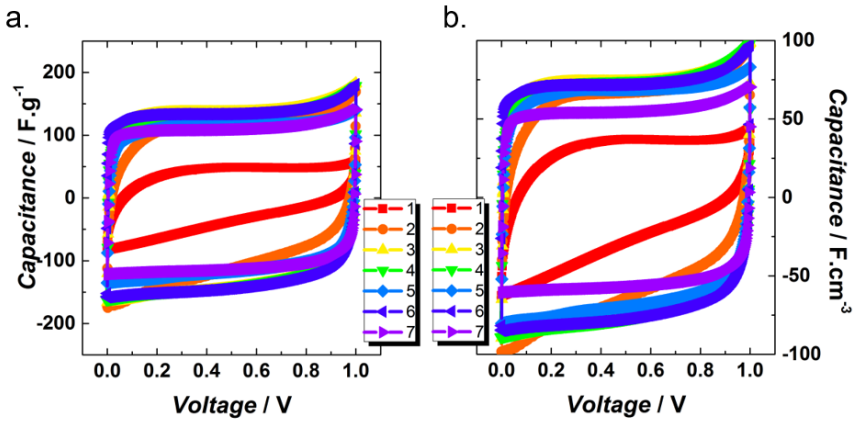

Figure 2-23. Gravimetric (a) and Volumetric (b) capacitance values in function of the voltage exhibited by the samples in aqueous electrolyte.

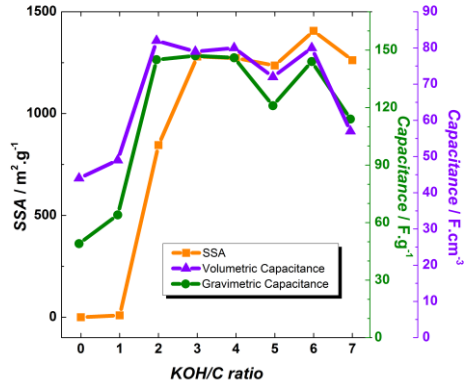

Figure 2-24. Specific surface area and gravimetric and volumetric capacitance in an aqueous electrolyte in function of the KOH/C ratio.

The main results of the electrochemical analysis performed on the activated carbon samples in Et_4NBF_4/ACN electrolyte are shown in Figure 2-26. CVs for samples BL_900_2_900 and BL_900_4_900 (see results for a constant scan rate of 5 $mV.s^{-1}$ in Figure 2-26 (a - b)) show distorted CV shapes most probably due to the intricate interaction between the ions and the nanopores.[23] Sample BL_900_4_900 exhibits a gradual decrease in capacitance as the voltage increases up to 2.5 V, most likely due to the low average micropore size (0.76 nm)

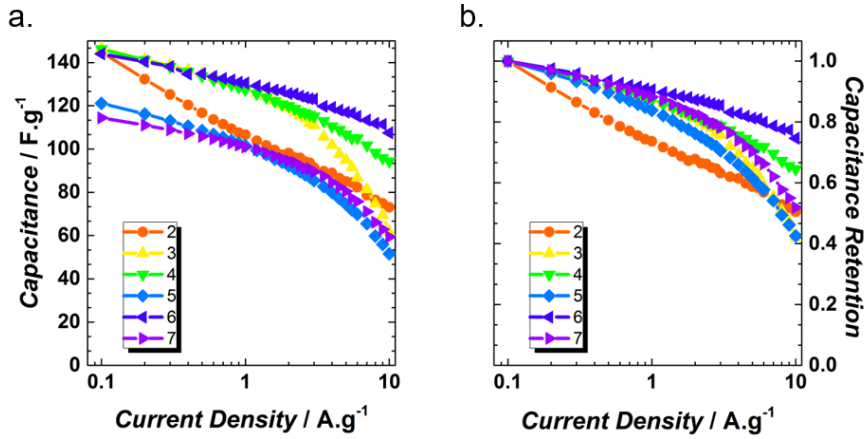

Figure 2-25. Evolution of the capacitance with current density (a) and comparison of capacitance retention with current density (b).

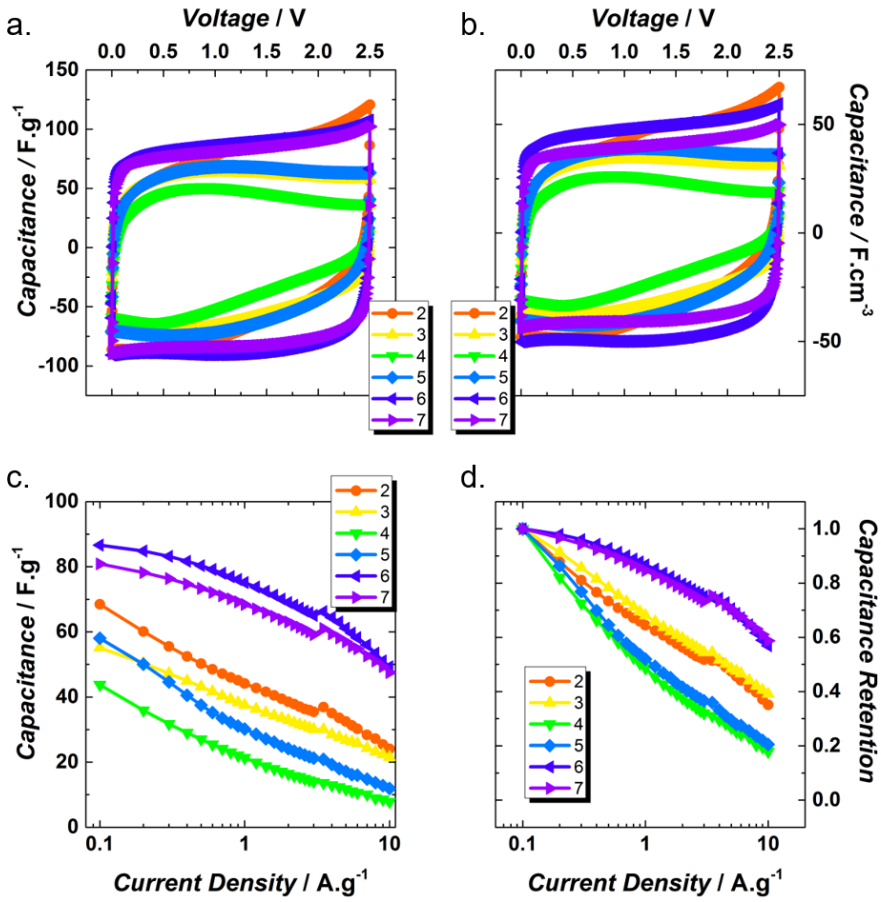

Figure 2-26. Cyclic voltammetry (a), rate capability (b), and normalized rate capability (c) of the samples in organic electrolyte.

compared to the effective ion size (*i.e.* the size of the ion inside the pore), leading to the ion sieving effect.[25] A similar behaviour is observed during the discharge from 2.5 V to 0 V. The rest of the samples have pores large enough for fitting the organic ions (the size of the largest ion, Et_4N^+, is about 0.67 nm and 1.30 nm for the bare and solvated ions, respectively).[27]

Figure 2-26 (c - d) shows the evolution of the specific capacitance as a function of the current density ranging between 0.1 $A.g^{-1}$ and 10 $A.g^{-1}$. Sample BL_900_6_900 presents the highest capacitance value (89 $F.g^{-1}$) and samples BL_900_6_900 and BL_900_7_900 achieve the highest rate capability at 10 $A.g^{-1}$, 59 %, in Et_4NBF_4/ACN.

Additional information about the capacitance and the real working potential range of each electrode in 1.5 M Et_4NBF_4/ACN is studied by measuring the charge/discharge curves using a 2-electrode cell configuration, where a silver rod is additionally used as a pseudo-reference electrode.[39,40] Figure 2-27 shows the galvanostatic curves for all the samples at 0.1 $A.g^{-1}$. KOH/C ratios from 2 to 5 show non-symmetric charge/discharge curves, while samples BL_900_6_900 and BL_900_7_900 show a linear dependence of the voltage on time, indicating non-restricted access of ions into porosity. The asymmetry in the potential range is more notorious in sample BL_900_4_900, confirming the difficulty of the organic cations (Et_4N^+) to enter into the pores as a consequence of their larger size in comparison with the anions (BF^{4-}). Because of the lower gravimetric capacitance exhibited by the negative electrode (*i.e.* 32 $F.g^{-1}$) compared to the positive electrode (*i.e.* 67 $F.g^{-1}$), its potential window increases remarkably (*i.e.* 1.7 V compared to 0.8 V for the positive electrode) in order to satisfy the equivalence of charges stored in each electrode. Thus, the negative electrode restricts the overall cell performance. Considering that the pore size of 0.76 nm is lower than the size of solvated ions, it can be reasonably supposed that at least partially solvated Et_4N^+ ions are electrosorbed. Nevertheless, for the rest of the samples, this effect is less drastic because the average pore size is closer to the size of the solvated ions. As a result, the ion-sieving effect is not discernible.

The relationship between the KOH/C ratio, the microstructure and the capacitance values in an organic electrolyte is depicted in Figure 2-28. The in-plane crystal size averaged out separately for the disordered and ordered areas is calculated on the basis of the Raman data using the Tuinstra–Koenig equation, widely used for the characterization of amorphous and graphitic materials.[41] The in-plane crystal size shows an opposite tendency when compared to the textural properties depicted in Figure 2-14. A local maximum is observed at the KOH/C ratio equal to 4, corresponding to an ordered in-plane crystal size of 37 nm. The reason for this interplay between the crystallite and the pore size might be related to the pore shrinking when the size of the carbon cluster increases. However, this is not observed for sample BL_900_7_900 which shows the highest crystal size as well as the largest pore size. This behaviour can be explained by the presence of isolated ordered regions, and/or the consumption of more KOH for the reorganization of C–C bonds rather than for the creation of porosity. Remarkably, the increase in the crystal size of the ordered regions does not improve the capacitive properties in 1.5 M Et_4NBF_4/ACN. In this way, samples BL_900_4_900 and BL_900_6_900, with ordered crystallite sizes of 37 and 24 nm, achieve capacitance values of 44 and 87 $F.g^{-1}$, respectively.

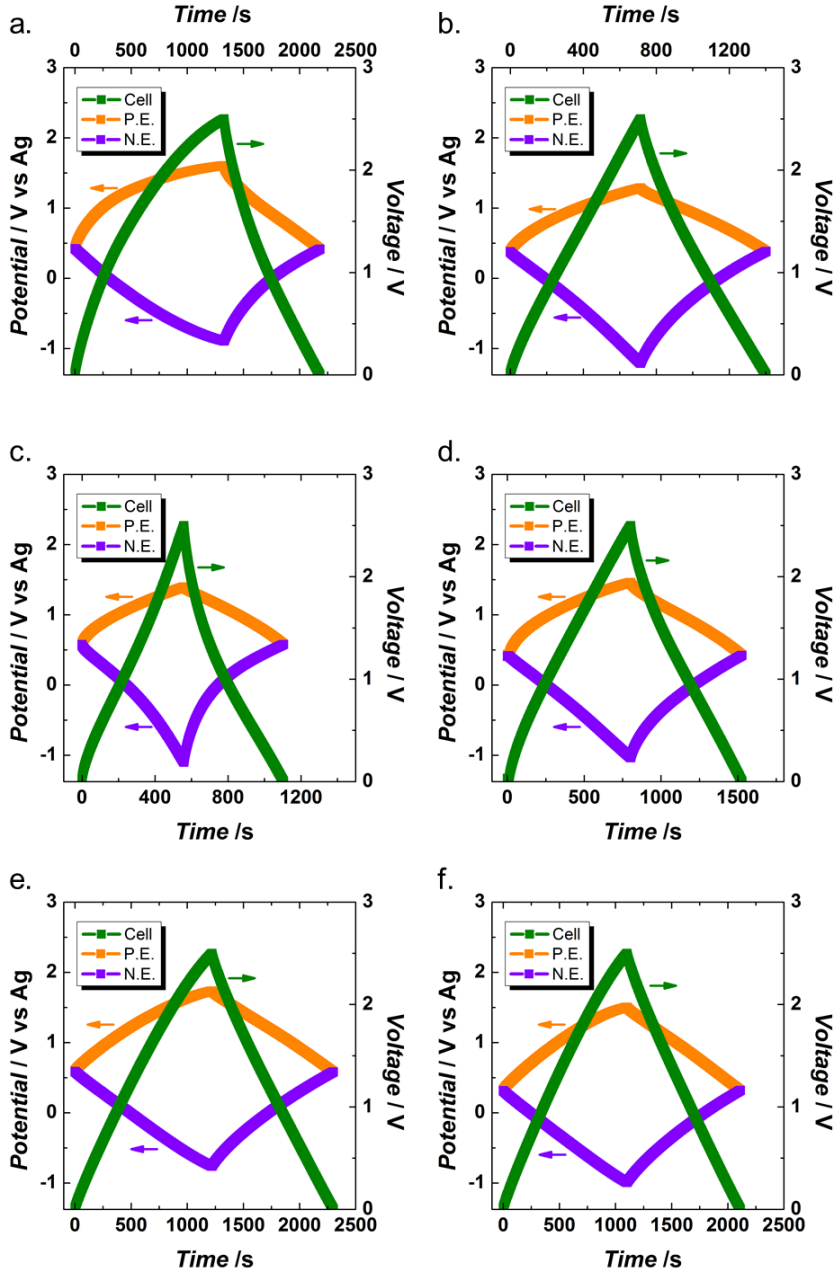

Figure 2-27. Charge/discharge curves at 0.1 A.g^{-1} in a two-electrode cell configuration (green line) using a Ag pseudo-reference electrode. The orange line indicates the contribution of the positive electrode whereas the violet line shows the contribution of the negative electrode. Samples BL_900_2_900 (a), BL_900_3_900 (b), BL_900_4_900 (c), BL_900_5_900 (d), BL_900_6_900 (e), and BL_900_7_900 (f).

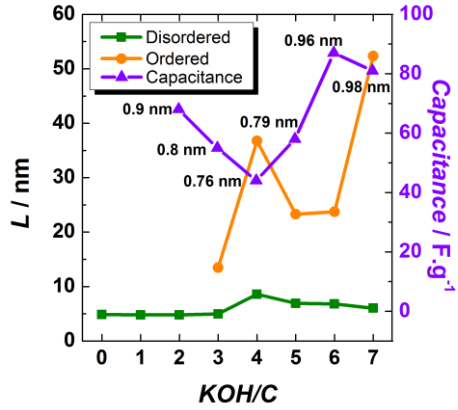

Figure 2-28. Changes in the crystallite size of graphene domains in disordered (green squares) and ordered (orange dots) regions along with the gravimetric capacitance ($F.g^{-1}$) (violet triangles) versus KOH/C ratio. The values shown along the capacitance line refer to the average micropore size calculated by the NLDFT method. Gravimetric capacitance was calculated from the galvanostatic curves at a current density of 0.1 $A.g^{-1}$ in Et_4NBF_4/ACN.

2.4 Conclusions and Perspectives

A series of nanoporous carbons were prepared by chemical activation of natural lignin and tested as electrode materials for electrical double-layer capacitors.

The pore development in lignin-derived carbons depended strongly on the carbonization temperature. Two sets of samples were carbonized at 400 °C and 900 °C. A carbonization temperature of 900 °C yielded carbons with higher micropore volume than those carbonized at 400 °C, this difference was probably caused by the release of methane above 350 °C. Carbons with high micropore volume proved to be better materials for aqueous supercapacitors because of their small micropore size (*i.e.* samples BL_400_4_900 and BL_900_4_700 achieved 200 $F.g^{-1}$ in 6 M KOH) while carbons with some mesoporosity achieved higher capacitance values in organic electrolytes thanks to a better interaction between average pore and ion sizes (*i.e.* sample BL_400_4_700 achieved 97 $F.g^{-1}$ in 1.5 M Et_4NBF_4/ACN).

The effect of the KOH/C ratio used during the activation step on the in-plane crystal size of FLG and the pore size of the resulting carbons and, ultimately, its impact on

the final capacitive properties were assessed. Generally, an increase in the in-plane crystal size of FLG in this carbon was related to a decrease on the average micropore size and, therefore, the capacitance values. Using the carbon activated with KOH/C ratio equal to 6, 144 $F.g^{-1}$ and 87 $F.g^{-1}$ were achieved in 6 M KOH and 1.5 M Et_4NBF_4/ACN, respectively, indicating that the presence of ordered zones in activated carbons was counterproductive to achieve high capacitance.

The operational voltage window of organic electrolytes was also maintained in systems based on lignin-derived carbon, which confirmed the suitability of this material for industry-standard organic electrolytes.

In general, lignin-based activated carbon exhibits a highly disordered microstructure with a high number of defects resulting in a complex porous network. This material is a good example proving that advanced nanoporous materials with tuneable pore size and partially ordered microstructure can be achieved by using natural and affordable precursors, such as lignin, thereby enhancing electrochemical performance when used as electrodes in energy storage applications.

2.5 References

(1) Pandolfo, A. G.; Hollenkamp, A. F. *J. Power Sources* **2006**, *157* (1), 11–27.

(2) Gosselink, R. J. A.; De Jong, E.; Guran, B.; Abächerli, A. *Ind. Crops Prod.* **2004**, *20*, 121–129.

(3) Johnson, D. J.; Tomizuka, I.; Watanabe, O. *Carbon N. Y.* **1975**, *13* (4), 321–325.

(4) Baker, D. A.; Rials, T. G. *J. Appl. Polym. Sci.* **2013**, *130* (2), 713–728.

(5) Rodríguez-Mirasol, J.; Cordero, T.; Rodríguez, J. J. *Carbon N. Y.* **1996**, *34* (1), 43–52.

(6) Saha, D.; Li, Y.; Bi, Z.; Chen, J.; Keum, J. K.; Hensley, D. K.; Grappe, H. A.; Meyer, H. M.; Dai, S.; Paranthaman, M. P.; Naskar, A. K. *Langmuir* **2014**, *30* (3), 900–910.

(7) Stoller, M. D.; Park, S.; Zhu, Y.; An, J.; Ruoff, R. S.; Stoller, M. D.; Park, S.; Zhu, Y.; An, J.; Ruoff, R. S. *Nano Lett.* **2008**, *8* (10), 3498–3502.

(8) Huang, Y.; Liang, J.; Chen, Y. *Small* **2012**, *8* (12), 1805–1834.

(9) Song, Y.; Yang, J.; Wang, K.; Haller, S.; Wang, Y.; Wang, C.; Xia, Y. *Carbon N. Y.* **2016**, *96*, 955–964.

(10) Spent liquor from alkaline pulping and bleaching containing spent inorganic process chemicals and dissolved organic substances originating from the cellulosic raw material. http://echa.europa.eu/registration-dossier/-/registered-dossier/15523.

(11) Ilavsky, J.; Jemian, P. R. *J. Appl. Crystallogr.* **2009**, *42* (2), 347–353.

(12) Porod, G. *Kolloid-Zeitschrift* **1953**, *133* (1), 51–51.

(13) Porod, G. *Small Angle X-Ray Scattering*; O. Glatter and O. Kratky, Ed.; Academic Press: London, 1982.

(14) Ferrari, A. C.; Robertson, J. *Phys. Rev. B* **2000**, *61* (20), 14095–14107.

(15) Largeot, C.; Portet, C.; Chmiola, J.; Taberna, P. L.; Gogotsi, Y.; Simon, P. *J. Am. Chem. Soc.* **2008**, *130* (9), 2730–2731.

(16) Akbar, D.; Ümmugül E. Güngörb. *Surf. Coatings Technol.* **2014**, *240*, 233–242.

(17) Wei, L.; Yushin, G. *Nano Energy* **2012**, *1* (4), 552–565.

(18) Marsh, H.; Yan, D. S.; O'Grady, T. M.; Wennerberg, A. *Carbon N. Y.* **1984**, *22* (6), 603–611.

(19) *The SAXS Guide*, 2nd ed.; Schnablegger, H., Singh, Y., Eds.; Paar, Anton: Graz, 2011.

(20) Winslow, F. H.; Baker, W. O.; Yager, W. A. *Proc. Conf. Carbon* **1954**, *7* (2), 93–102.

(21) Dresselhaus, M. S.; Jorio, A.; Hofmann, M.; Dresselhaus, G.; Saito, R. *Nano Lett.* **2010**, *10* (3), 751–758.

(22) Zhu, Y.; Murali, S.; Stoller, M. D.; Ganesh, K. J.; Cai, W.; Ferreira, P. J.; Pirkle, A.; Wallace, R. M.; Cychosz, K. A.; Thommes, M.; Su, D.; Stach, E. A.; Rodney S. Ruoff. *Science (80-.).* **2011**, *332* (6037), 1537–1541.

(23) Lin, R.; Taberna, P. L.; Chmiola, J.; Guay, D.; Gogotsi, Y.; Simon, P. *J. Electrochem. Soc.* **2009**, *156* (1), A7–A12.

(24) Salitra, G.; Soffer, A.; Eliad, L.; Cohen, Y.; Aurbach, D. *J. Electrochem. Soc.* **2000**, *147* (7), 2486.

(25) Eliad, L.; Salitra, G.; Soffer, A.; Aurbach, D. *J. Phys. Chem. B* **2001**, *105* (29), 6880–6887.

(26) Mysyk, R.; Raymundo-Piñero, E.; Pernak, J.; Béguin, F. *J. Phys. Chem. C* **2009**, *113* (30), 13443–13449.

(27) Chmiola, J.; Largeot, C.; Taberna, P. L.; Simon, P.; Gogotsi, Y. *Angew. Chemie - Int. Ed.* **2008**, *47* (18), 3392–3395.

(28) Weingarth, D.; Foelske-Schmitz, A.; Kötz, R. *J. Power Sources* **2013**, *225*, 84–88.

(29) Hantel, M. M.; Weingarth, D.; Kötz, R. *Carbon N. Y.* **2014**, *69*, 275–286.

(30) Everett, D. H. *Pure Appl. Chem.* **1972**, *31* (4), 577–638.

(31) Haul, R. *Berichte der Bunsengesellschaft für Phys. Chemie* **1982**, *86* (10), 957–957.

(32) Sing, K. S. W. *Pure Appl.Chem* **1982**, *54* (11), 22–22.

(33) Lillo-Ródenas, M. A.; Juan-Juan, J.; Cazorla-Amorós, D.; Linares-Solano, A. *Carbon N. Y.* **2004**, *42* (7), 1365–1369.

(34) Shimada, T.; Sugai, T.; Fantini, C.; Souza, M.; Cançado, L. G.; Jorio, A.; Pimenta, M. A.; Saito, R.; Grüneis, A.; Dresselhaus, G.; Dresselhaus, M. S.; Ohno, Y.; Mizutani, T.; Shinohara, H. *Carbon N. Y.* **2005**, *43* (5), 1049–1054.

(35) Ferrari, A. C. *Solid State Commun.* **2007**, *143* (1–2), 47–57.

(36) Bianco, A.; Cheng, H. M.; Enoki, T.; Gogotsi, Y.; Hurt, R. H.; Koratkar, N.; Kyotani, T.; Monthioux, M.; Park, C. R.; Tascon, J. M. D.; Zhang, J. *Carbon N. Y.* **2013**, *65*, 1–6.

(37) Zhang, S.; Song, H.; Zhang, J.; Zhu, L.; Chen, X.; Zhang, H.; Zhou, J. *RSC Adv.* **2013**, *3* (17), 6117.

(38) Yoon, S. H.; Lim, S.; Song, Y.; Ota, Y.; Qiao, W.; Tanaka, A.; Mochida, I. *Carbon N. Y.* **2004**, *42* (8–9), 1723–1729.

(39) Khomenko, V.; Raymundo-Piñero, E.; Béguin, F. *J. Power Sources* **2006**, *153* (1), 183–190.

(40) Khomenko, V.; Raymundo-Piñero, E.; Béguin, F. *J. Power Sources* **2010**, *195* (13), 4234–4241.

(41) Pimenta, M. A.; Dresselhaus, G.; Dresselhaus, M. S.; Cançado, L. G.; Jorio, A.; Saito, R. *Phys. Chem. Chem. Phys.* **2007**, *9* (11), 1276–1291.

MULTI-REDOX PARTIALLY REDUCED GRAPHITE OXIDE/BIOPOLYMER ELECTRODES FOR SUPERCAPACITORS

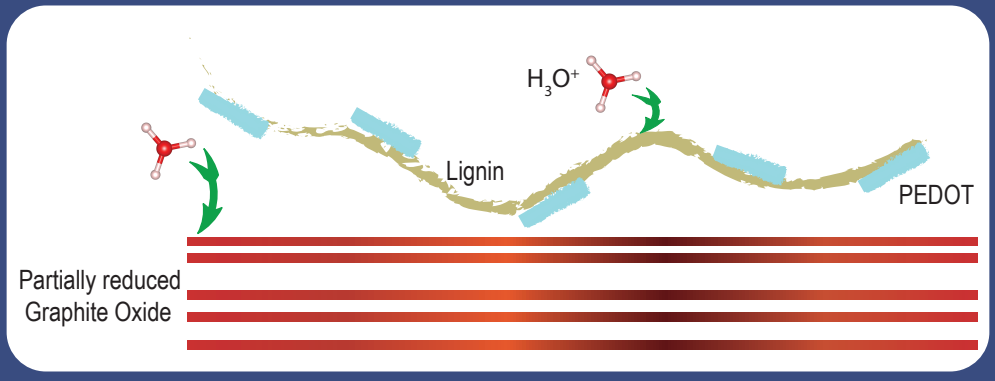

3 MULTI-REDOX PARTIALLY REDUCED GRAPHITE OXIDE/BIOPOLYMER ELECTRODES FOR SUPERCAPACITORS

3.1 Introduction

The introduction of redox active moieties into the electrode material is a well-positioned strategy to enhance capacitance through reversible Faradaic reactions.[1–3] Electroactive organic compounds and polymers involving reversible redox reactions are considered promising candidates to introduce these moieties. Even though there is a large number of suitable organic molecules, those containing quinones have received the greatest attention, since they have high theoretical capacity, high electron transfer kinetics, excellent redox reversibility and low cost.[4–6] In those molecules containing quinone/hydroquinone (Q/QH_2) moieties, two electrons and protons are stored in a structure of 6 carbon and 2 oxygen atoms, an electronic charge density of 2 Farads per 108 g, 1787 $C.g^{-1}$, or

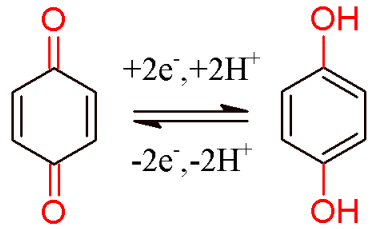

Reaction 3-1. Quinone/Hydroquinone Redox reaction.

496 mAh.g^{-1} (Reaction 3-1).

Phenol and quinone compounds are found in plants and wood. Black liquor, a by-product of paper processing, incorporates lignin rich in phenol groups, which can be further converted to quinones through oxidation processes (Reaction 3-2). However, lignin is a poor electron conductor. Accordingly, it is necessary to combine lignin with an electron conducting material, in order to allow charge transport.[7,8] The electron conductor may then facilitate the transport of electrons and ions to the lignin moiety where charge can be stored in a reversible redox reaction between the hydroquinone and quinone forms (Reaction 3-2). The use of electron conducting polymers is attractive as their properties can be modified by variations in polymer structure.[9,10] The first example of this approach utilized a combination of lignin and polypyrrole.[9] In addition, various combinations of lignin and another electron conductors such as reduced graphene oxide[11] or carbon nanotubes[12] have been investigated.

More recently, poly(3,4-ethylenedioxythiophene) (PEDOT) was used to facilitate the electron transfer to the lignin. The lignin/PEDOT biopolymer was studied as supercapacitor and higher capacitance retention (83 % after 1000 cycles) was achieved than with the lignin/polypyrrole blend, in which strong degradation after cycling was observed.[13]

However, lignin has not been tested in a two-electrode configuration yet, as the

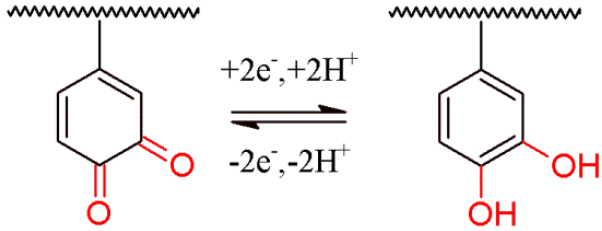

Reaction 3-2. Lignin Redox reaction.

previous studies have focused on the electrochemical characterization of the material. Here, to develop a full cell we have used a partially reduced Graphite Oxide (prGrO) synthesized by the Marcano-Tour method[14] which yields a material with majority of quinone groups.[15] The electrochemistry of a quinone group is determined by its neighbours;[16] therefore, different peak potentials are expected for the lignin/PEDOT and the prGrO. By having another peak in the CV curve, higher values of capacitance than the ones reported in the literature[17–22] are foreseen.

The goals of the chemical approach delineated herein are the following:

i) The use of low cost electrodes is of utmost importance and with that objective in mind, the lignin used in these experiments is separated from an industrial by product and the prGrO is partially reduced at low temperatures avoiding any additional step and the use of hazardous chemicals.

ii) Synergize both features of the electroactive Lignin/PEDOT blend and the electron-conducting partially reduced Graphite Oxide for renewable energy-storage materials. For that, two strategies are explored: an asymmetric cell with Lignin/PEDOT and prGrO as negative and positive electrode, respectively and development of a composite between Lignin/PEDOT and prGrO, tested in a symmetric cell.

3.2 Methodology

3.2.1 Materials Synthesis

3.2.1.1 Lignin/PEDOT Polymerization

The natural lignin is isolated from Black Liquor with sulfuric following a process explained in section 2.3.1. Lignin/PEDOT biopolymers are synthesized via chemical oxidative polymerization of EDOT monomer in the presence of lignin, by using Iron (III) Chloride as catalyst and Sodium Persulfate as primary oxidant at room temperature during 8 hours, as explained elsewhere.[13] In this case, as lignin is not sulfonated, the mixture containing lignin and oxidant is left stirring in water for 8 hours in order to partially solubilise the lignin. Then, EDOT monomer is added and the mixture is left stirring at room temperature for 8 more hours. Finally, Lignin/PEDOT dispersions are dialyzed with deionized water in 12000-14000 Da molecular weight cut-off membranes for 2 days. After freeze-drying the Lig/PEDOT polymers, are obtained as dark bluish powders. The initial

Scheme 3-1. Chemical oxidative polymerization of Lig/PEDOT blends.

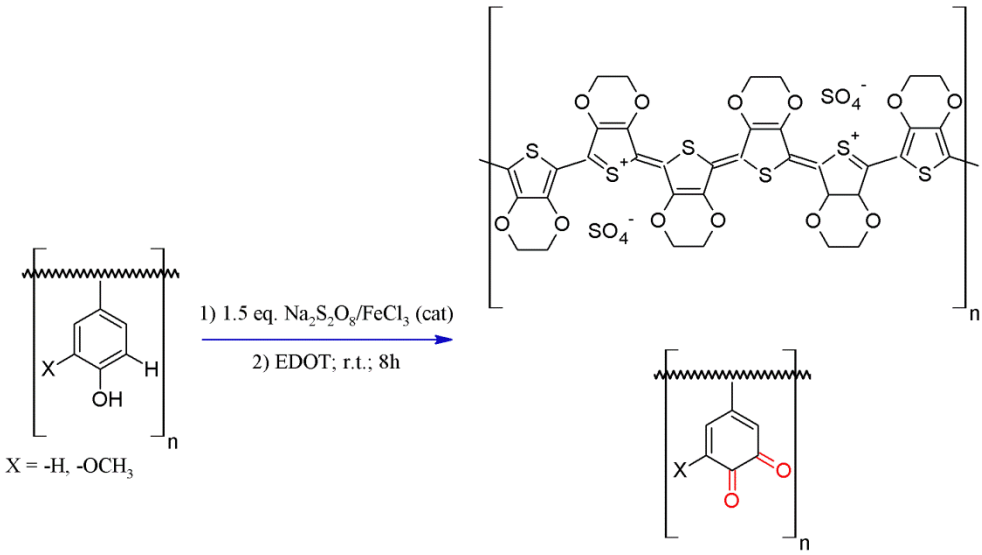

Lignin:EDOT mass ratios used are 0:100, 20:80, 40:60 and 60:40 yielding the as called PEDOT, Lig/PEDOT 20/80, Lig/PEDOT 40/60 and Lig/PEDOT 60/40 polymers, respectively. These polymers are also tested as cathodes in Na-ion and Li-ion batteries as can be seen in Appendix II.

3.2.1.2 Partially Reduced Graphite Oxide Synthesis

Graphite powder (Sigma Aldrich, particle size < 20 µm, cat#282863) is oxidized by a modified Hummers' method described elsewhere.[14] Briefly, a 9:1 mixture of concentrated H_2SO_4/H_3PO_4 (360:40 mL) is added to a mixture of graphite powder (3.0 g, 1 wt. equiv.) and $KMnO_4$ (18.0 g, 6 wt. equiv.). The reaction is then heated to 50 °C and stirred overnight. The reaction is cooled down to room temperature and poured onto ice (~400 mL) with 30 % H_2O_2 (3 mL). The solution is centrifuged (10000 rpm for 30 min), and the supernatant is decanted away. The remaining solid material is then washed in succession with 200 mL of water, 200 mL of 30 % HCl, and then water until neutral pH; for each wash, the mixture is centrifuged (10000 rpm for 30 min) and the supernatant decanted away. The solid recovered, Graphite Oxide (GrO), is vacuum-dried overnight at 60 ºC. GrO is then heated, under argon flow, at a heating rate of 5 ºC.min^{-1} up to 160 ºC, followed by an isothermal step of 1 hour. The solid obtained is referred as prGrO (partially reduced Graphite Oxide).

3.2.2 Characterization Methods

Lignin/PEDOT and prGrO are a polymer and a carbon, respectively. This means that different characterization methods should be used for each one of them.

3.2.2.1 Lignin/PEDOT Characterization

The different functional groups in the polymer are studied by Fourier Transform Infrared Spectroscopy (FTIR) measurements. These are acquired at room temperature using a Thermo scientific model Nicolet 6700 FT-IR spectrometer, applying 10 scans in transmission mode using KBr pellets.

The thermal stability of the polymers is investigated through thermo-gravimetric analysis (TGA) performed on a TGA Q500 from TA Instruments. Measurements are carried out by heating around 3 mg of the sample at 10 °C.min^{-1}, under nitrogen atmosphere, from room temperature to 800 °C.

3.2.2.2 prGrO Characterization

The carbon and oxygen content of prGrO is quantified by X-Ray Photoelectron Spectra (XPS). The spectra are recorded on a KRATOS AXIC 165 equipped with Mg K_α radiation and hemispherical analyser Phoibos 150 with 3D-DLD detector (SPECS). The binding energy (BE) of all the samples are tested as referenced to C 1*s* at 284.8 eV. The assignment of C 1*s* and O 1*s* components are based on theoretical predictions of core level shifts and on reported spectra containing the particular oxygen functional groups.[23,24] The XPS peaks are fitted to pseudo-Voigt functions having 80 % Gaussian and 20 % Lorentzian character, after performing a Shirley background subtraction.

The changes from GrO to prGrO are followed with Fourier Transform Infrared Spectroscopy, N_2 gas sorption, X-Ray Diffraction. These techniques are explained in Appendix I.

3.2.3 Electrochemical Testing

3.2.3.1 Qualitative Methods

To determine the capacitive contributions to the current of each material, initial voltammetric measurements are made in a cavity micro-electrode (CME), in which the electrochemical interface area is around a fraction of mm^2 and the ohmic drop coming from the bulk of the electrolyte can be neglected, allowing the use of high

scan rates.[25] The lignin/PEDOT and prGrO are studied in a 3-electrode configuration in a 0.1 M perchloric acid ($HClO_4$, sigma Aldrich) solution with a platinum wire as counter electrode and Ag/AgCl as reference electrode. Given the electronically insulating character of lignin, a composite made out of lignin and Multi-Walled Carbon Nanotubes (MWCNT) is physically mixed in a proportion (80:20) and its electrochemical properties are measured with the CME. The microcavity is filled with active material by pressure of the carbon powders against a glass plate. The cavity is cleaned by immersing the electrode in ethanol in an ultrasonic bath between experiments. A study of the charge/discharge mechanism of the prGrO electrode in different aqueous-based electrolytes is performed by means of the cavity microelectrode and X-Ray Diffraction as it will be explained in Appendix III.

3.2.3.2 Quantitative Methods

Lignin/PEDOT and Lignin/PEDOT/prGrO electrodes are prepared by drop-casting on a Platinum mesh from an aqueous solution. The electrodes are left to dry at room temperature under air for 8 h before testing.

Initially, to study the electrochemical properties of the prGrO three strategies are used: a pellet prepared with 1 Ton pressure, a slurry with 10 % PTFE and a film prepared by vacuum-assisted filtration. This latter method is selected for the symmetric and asymmetric cells. The preparation is as follows, the prGrO is suspended in ethanol and filtered under vacuum by using polytetrafluoroethylene membranes (Sartorius, pore size 0.45 µm and 4.5 cm diameter) and dried in a vacuum oven at 60 °C for 8 h, resulting in a prGrO film that detaches easily from the membrane and can be further used as a free-standing electrode.

To quantify the amount of charge stored by these materials, Swagelok cells are assembled and the materials are electrochemically tested as follows.

The cells are electrochemically studied by using a 0.1 M $HClO_4$ solution and Ag/AgCl as reference electrode. For those tests carried out by using a 3-electrode cell, a platinum mesh is used as counter electrode. Details about the electrochemical measurements can be found in Appendix 1.

3.3 Results and Discussion

3.3.1 Lignin/PEDOT Characterization

In order to confirm the EDOT polymerization in the presence of lignin and their blending, FTIR and TGA experiments are performed on the lignin, the PEDOT and the Lig/PEDOT 20/80, Lig/PEDOT 40/60 and Lig/PEDOT 60/40 polymers.

3.3.1.1 Fourier Transform Infrared

Lignin Fourier Transform Infrared Spectrum (Figure 3-1) shows peaks at 1600, 1510 cm^{-1} (vibrations of aromatic ring), 1460, 1428 cm^{-1} (aromatic ring vibrations combined with methyl and methylene C-H deformations), 1212 cm^{-1} (C-C and C-O stretching vibrations) and 1040 cm^{-1} (C-O-C stretching vibrations). Conversely, PEDOT shows peaks at 1200, 1090, 1060 cm^{-1} (C-O-C stretching of ethylenedioxy group), 980, 840 cm^{-1} (C-S stretching) and 685 cm^{-1}.[13] All the Lig/PEDOT polymers exhibit vibration bands related to lignin and PEDOT structures and the intensity of the bands depend on the composition of the polymer. For instance, the peak at 1600 cm^{-1} attributed to the C=C stretching of the aromatic ring in lignin decreases as the percentage of PEDOT increases in the polymer. On the contrary, the broad C-S stretching peak at 840 cm^{-1} decreases as the percentage of Lignin is increased. This peak is characteristic of PEDOT and its decrease is associated with the decrease of the conductive polymer proportion on the biopolymer.

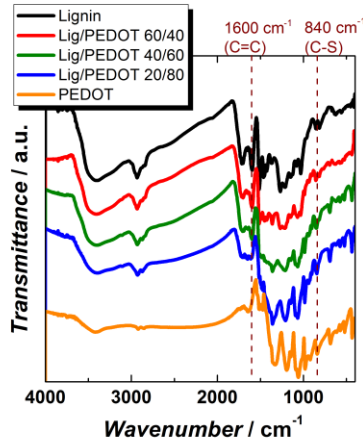

Figure 3-1. FTIR spectra of lignin, Lig/PEDOT 60/40, Lig/PEDOT 40/60, Lig/PEDOT 20/80 and PEDOT.

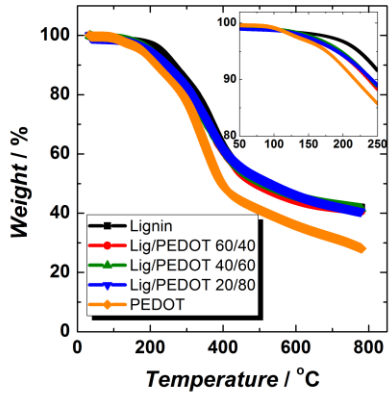

Figure 3-2. TGA curves obtained for lignin, Lig/PEDOT 60/40, Lig/PEDOT 40/60, Lig/PEDOT 20/80 and PEDOT at a heating rate of 10 °C.min^{-1} under Nitrogen atmosphere.

3.3.1.2 Thermogravimetric Analysis

The lignin and Lig/PEDOT polymers show high thermal stability as shown in the TGA curves in Figure 3-2. All the Lig/PEDOT polymers are stable up to 190 ºC. Then, a continuous degradation occurs, corresponding to the elimination of absorbed water, and then a major decomposition in the region between 300 ºC and 450 ºC is observed, which is attributed to the decomposition of PEDOT main chains.[26] Finally, at 800 °C, PEDOT shows a residual trace of 28 %, while lignin and Lig/PEDOT polymers exhibit residual traces of 41 % of the total mass; this value agrees with the results achieved under Argon atmosphere in the previous chapter (Figure 2-2).

3.3.2 prGrO Characterization

In order to determine the functional groups, present in the prGrO synthesized, the material in powder is analysed by XPS and FTIR. Graphite Oxide (GrO) is also analysed as comparison.

3.3.2.1 X-Ray Photoelectron Spectroscopy

The significant surface charging effect due to the electrically insulating nature of GrO is reflected in the presence of XPS bands towards high binding energies (Figure 3-3 (a – b)). The C 1*s* spectrum of GrO on the top of Figure 3-3 (a) has two main peaks at 285.5 eV and 287.3 eV. These can be fit to peaks at 284.5,

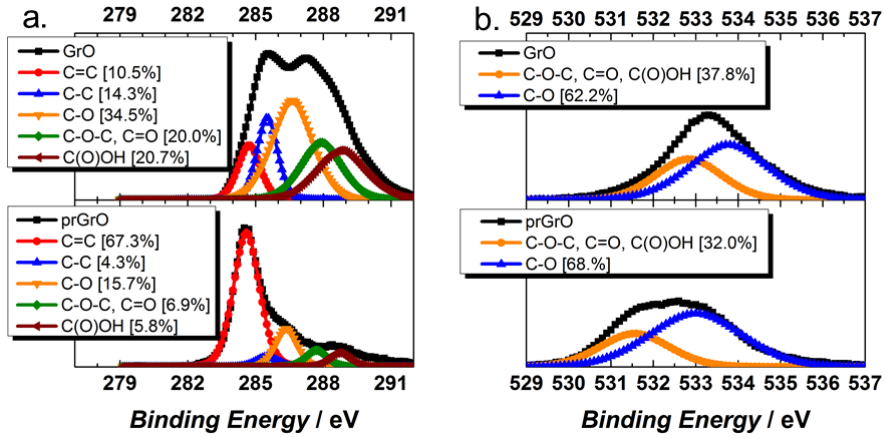

Figure 3-3. C 1*s* (a) and O 1*s* (b) survey by X-Ray Photoelectron Spectroscopy of the Graphite Oxide (top) and the partially reduced Graphite Oxide (bottom).

285.5, 286.5, 287.7 and 288.7 eV and thus assigned to C=C, C-C, C-O, C-O-C and C=O, and C(O)OH respectively. Upon heating under Argon flow, the C 1*s* spectrum exhibits a transformation from a double peak at room temperature to a single peak (~284.6 eV) at 160 °C, being indicative of a tendency to restore the sp^2 bonding graphene character. This affirmation can be confirmed by the intensity increase of the peak at 284.5 eV, related to C=C bonds, from 10.5 % to 67.3 % and the decrease of the peaks related to Carbon directly attached to an Oxygen atom, from 75.2 % to 28.4 %. A clear shift of peak-maxima to lower BE with increasing temperature signifies the transformation from electrically insulated GO to the conducting nature of graphite. Comparing the C/O atomic ratio of GrO with prGrO, there is an increase in C-content and an associated decrease of the O groups, from 1.5 to 2.5.

Information provided by analysis of the O 1*s* spectra (Figure 3-3 (b)) can complement the information provided by analysis of C 1*s* spectra. As the O 1*s* photoelectron kinetic energies are lower than those of the C 1*s*, the O 1*s* sampling depth is smaller, and therefore the O 1*s* spectra are slightly more surface specific. The peak corresponding to the C-O bonds increases from 62.2 % to 68.0 % during the thermal reduction, this could be explained by the formation of phenol (or aromatic diol) groups during deoxygenation because of the close proximity of C-OC and C-OH on the basal plane.[27]

3.3.2.2 Fourier Transform Infrared Spectroscopy

Five main absorption bands are identified in the FTIR spectra (Figure 3-4), centred

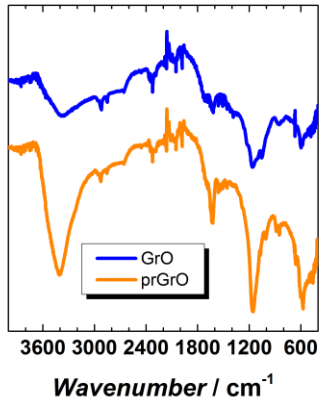

Figure 3-4. FTIR of the Graphite Oxide and the partially reduced Graphite Oxide.

at 3400 cm^{-1} (O-H stretching vibrations), 1714 cm^{-1} (C=O stretching vibrations), 1620 cm^{-1} (skeletal vibrations from unoxidized graphitic domains), 1230 cm^{-1} (C-OH stretching vibrations) and 1160 cm^{-1} (C-O stretching vibrations).[28] The decrease in the C=O band, when comparing prGrO with GrO, and the increase in all the other bands, agrees with the results from XPS and reinforces the hypothesis of phenol and/or aromatic diols as the main functional groups in the prGrO. These observations are consistent with the ones made by Pumera *et al.*, who noticed that quinone/hydroquinone functionalities are the likely source of the redox reactions observed in graphene oxide prepared by Marcano-Tour's method.[15]

The textural properties (average pore size, pore size distribution, surface area) as well as the change of the basal distance between the individual graphene layers before and after oxidation, were determined by N_2 gas sorption, Raman and XRD.

3.3.2.3 N_2 Adsorption/Desorption

The N_2 isotherms of the two samples are shown in Figure 3-5 (a). On the one hand, GrO presents a type I isotherm indicating that is a microporous material; while, the hysteresis loop at high relative pressure is associated with capillary condensation in mesoporosity. On the other hand, prGrO presents a type IV isotherm indicating a wide distribution of pore sizes.

Comparing GrO and prGrO textural properties (Table 3-1), a slight increment in the Specific Surface Area is observed after thermal reduction. This increase seems to be caused by the development of mesopores in the structure (Figure 3-5

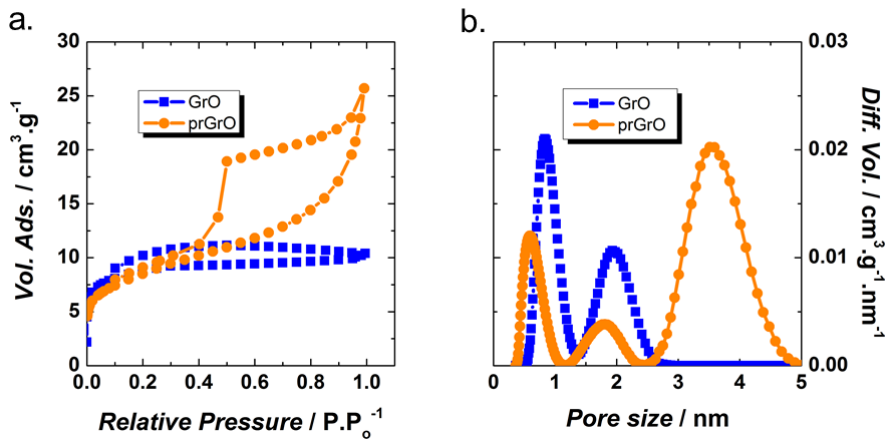

Figure 3-5. N_2 isotherm (a), and Pore size distribution (b) of the Graphite Oxide (GrO) and the partially reduced Graphite Oxide (prGrO).

(b)), which could be explained by the removal of functional groups during the deoxygenation process.

3.3.2.4 Raman Spectroscopy

Raman spectra of GrO and prGrO (Figure 3-6 (a)) yield the G and D peaks at 1587 and 1347 cm^{-1}, respectively. The G peak is due to the bond stretching of all pairs of sp^2 atoms in both rings and chains. The D peak is attributed to the breathing modes of sp^2 atoms in rings.[29] The I_D/I_G ratio, provides a measure of the disorder in the sample. In this case the ratio in both, the GrO and the prGrO, is 0.87. Other thermally reduced graphene oxides have been reported to have I_D/I_G ratio above 1.5,[30] indicating that our method yields a less disordered rGO.

Table 3-1. Textural properties of the Graphite Oxide and the partially reduced Graphite Oxide.

Sample	S_{NLDFT} ($m^2.g^{-1}$)	$S_{micro\text{-}NLDFT}$ ($m^2.g^{-1}$)	$S_{meso\text{-}NLDFT}$ ($m^2.g^{-1}$)	$L_{micro\text{-}NLDFT}$ (nm)
GrO	27	24	3	1.19
prGrO	30	16	14	0.99

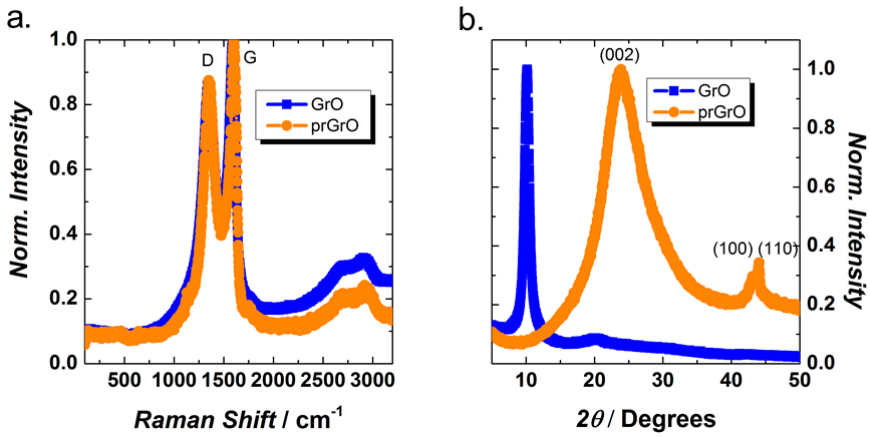

Figure 3-6. Raman (a) and XRD (b) of the Graphite Oxide (GrO) and the partially reduced Graphite Oxide (prGrO).

3.3.2.5 X-Ray Diffraction

The X-Ray Diffraction patterns of Graphite Oxide (GrO) and partially reduced Graphite Oxide (prGrO) can be seen in Figure 3-6 (b). The interlayer distance range calculated from the (002) peak is 6.86 – 11.53 Å in GrO. After thermal reduction, a heterogeneous material with interlayer distances ranging from 2.60 to 5.32 Å is achieved; prGrO also exhibits the (100) and (110) Bragg reflections indicating a turbostratic structure.[31] A turbostratic structure indicates a stacking disorder in which different layers have no regular rotational or translational relationship.[32]

3.3.3 Electrochemical Testing

3.3.3.1 Qualitative Methods

Lignin, Lig/PEDOT 40/60 (as example) and prGrO are tested electrochemically in a 3-electrode configuration with a microcavity as working electrode. Two separate mechanisms, surface capacitive effects and diffusion-controlled processes, can be discriminated by relating the current response to the voltammetric sweep rate according to the following equation:

$$\frac{i}{v^{1/2}} = k_1 v^{1/2} + k_2 \qquad \textbf{Equation 3-1}$$

where i is the measured current, v is the sweep rate, and k_1 and k_2 are related to

the current contributions from the surface capacitive effects and the diffusion-controlled process, respectively. Figure 3-7 shows the cyclic voltammetry curves at 100 mV.s^{-1} of lignin, Lig/PEDOT 40/60 and prGrO. By plotting $\boldsymbol{i/v^{1/2}}$ vs $\boldsymbol{v^{1/2}}$, according to Equation 3-1, the values of $\boldsymbol{k_1}$ and $\boldsymbol{k_2}$ are calculated in the whole potential window and therefore we are able to quantify the fraction of the current due to each of these contributions.

The comparison of Figure 3-7 (a) and Figure 3-7 (b), will give us important information about the electrochemical properties of lignin and how these characteristics change by polymerizing EDOT in the presence of lignin. In Figure 3-7 (a), Lignin-MWCNT presents a narrow peak around 0.5 V and its potential window is constricted between 0 and 0.9 V vs Ag/AgCl. When analysing the capacitive contributions, a small peak appears at 0.5 V, indicating that both capacitive and diffusion-controlled processes cause this peak. This peak might correspond to the redox process of the quinones present in the lignin,[9] and is present in both curves as result of the reaction taking place in both the surface of the material (pseudocapacitive process) and the bulk of the electrode. The total capacitive contribution was of 42 % at 100 mV.s^{-1}.

When EDOT is polymerized in the presence of lignin, the CV shape changes dramatically (Figure 3-7 (b)). First, the potential window is increased in 0.20 V, going from -0.2 to 0.9 V vs Ag/AgCl. Second, the peaks attributed to the Reaction 3-2 in lignin-MWCNT are now broader and more separated, indicating a more

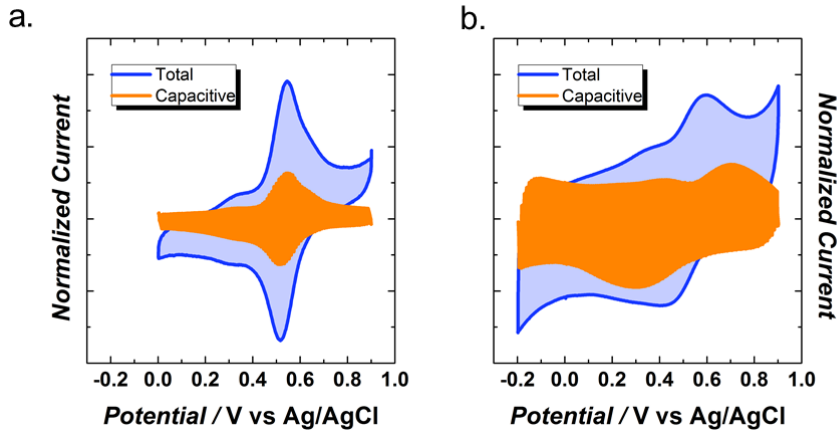

Figure 3-7. Total (blue area) and capacitive contributions (orange area) to charge storage in 0.1 M $HClO_4$ of lignin-MWCNT (a) and Lig/PEDOT 40/60 (b).

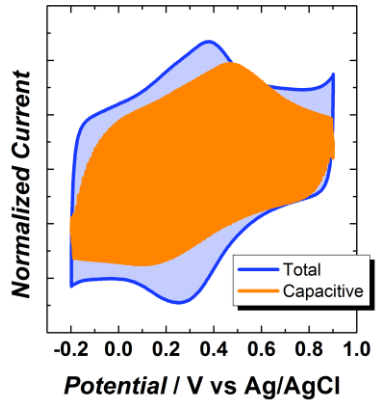

Figure 3-8. Total (blue area) and capacitive contributions (orange area) to charge storage in 0.1 M $HClO_4$ of prGrO.

pseudo-capacitive process. Third, the shape of the cyclic voltammetry looks more rectangular indicating a more capacitive process than in the lignin-MWCNT composite. These two last points are confirmed by the more rectangular shape of the capacitive contributions to the current of the Lig/PEDOT 40/60 polymer and the increase of the contribution up to 66 % at 100 $mV.s^{-1}$. These results prove that PEDOT is an adequate facilitator for transferring electrons to the lignin and the Lig/PEDOT biopolymer is ideal for supercapacitor applications thanks to its high capacitive contributions at high scan rates.

In the case of the prGrO (Figure 3-8), the redox peaks observed at ~0.3 V, correspond to the redox reactions involving the quinone/hydroquinone functionalities (Reaction 3-1). The capacitive charge storage corresponds to 75 % of the total charge at 100 $mV.s^{-1}$ and might be caused by double-layer and pseudo capacitive processes. However, given the low Specific Surface Area presented by the prGrO, most of this capacitance should be caused by redox pseudocapacitance involving again the quinone/hydroquinone functionalities (Reaction 3-1) or fast intercalation of the ions inside the material. This surface-confined charge-transfer process is confirmed by the broad peak in the capacitive curve of the material.

3.3.3.2 Quantitative Methods

As the quantity of material inserted in a cavity micro-electrode is unknown, Swagelok cells were assembled to quantify the capacitance achieved by the

materials.

3.3.3.2.1 Optimization of the Lignin/PEDOT Ratio

Figure 3-9 shows the rate capability of the different Lig/PEDOT proportions. In Figure 3-9 (a) the differences in capacitance between the different proportions can be observed. These differences can be explained by the effect the lignin and PEDOT proportions have on the electrochemical conductivity of the film. On the one hand, in Lig/PEDOT 20/80, as the percentage of lignin is low, there is probably not enough quinone moieties for Reaction 3-2. On the other hand, in Lig/PEDOT 60/40, the percentage of PEDOT might be too low, making it difficult for the electrons to transfer to the lignin. The highest capacitance value, 97 $F.g^{-1}$, is achieved by Lig/PEDOT 40/60.

Figure 3-9 (b) relates the capacitance retention with the current density of the Lig/PEDOT biopolymers. The increment of the lignin proportion on the polymer increases the capacitance retention with the current density. This might seem counterintuitive, as the PEDOT should be increasing the conductivity of the material. However, as explained by Ajjan *et al.*, Lignin acts in the polymer as both dopant and dispersing agent,[13] therefore its decrease might cause a charge unbalance that reflects on a more difficult charge transport, hence a drop in the capacitance with the current density.

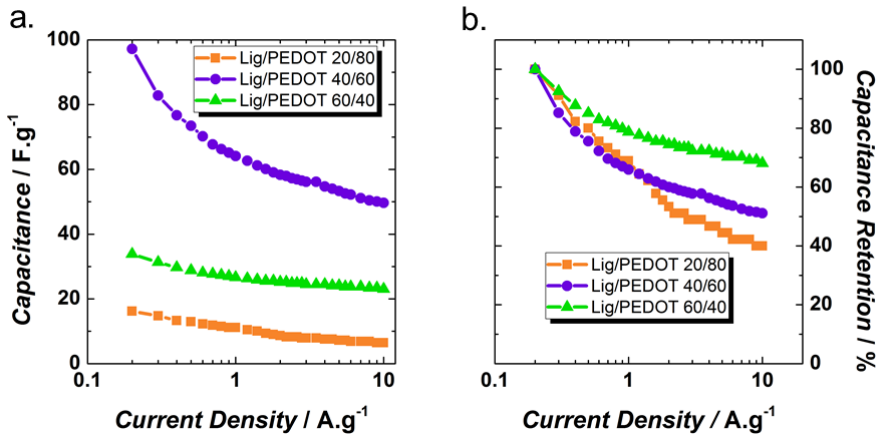

Figure 3-9. Rate capability (a) and capacitance retention (b) of the Lig/PEDOT different proportions in 0.1 M $HClO_4$.

3.3.3.2.2 Optimization of the prGrO Electrode

In the case of the prGrO, the development of an electrode that could retain its capacitance with the current density was the key challenge. The quinone groups in the prGrO should yield high capacitance values because of the redox reactions in the surface and bulk of the material, as explained in the previous section. However, as they are involved in the electrochemical process a depletion of the quinone group with increase of the current density or cycling is expected.[33] Figure 3-10 shows the rate capability of the three different electrodes of prGrO in $HClO_4$, *i.e.* pellet, slurry and film.

The pellet achieves 221 $F.g^{-1}$ at 0.1 $A.g^{-1}$ (Figure 3-10 (a)) but is rapidly diminished when the current density is increased (Figure 3-10 (b)). This might be caused by the high resistance present in a pellet caused by the thickness of the electrode. In order to prepare thinner films, a slurry with PTFE and a vacuum-assisted film are tested.

At low current densities, the prGrO slurry shows lower capacitance at 0.1 $A.g^{-1}$ than the pellet, *i.e.* 148 $F.g^{-1}$; however, after 0.5 $A.g^{-1}$ the prGrO slurry maintains larger values than the pellet. In fact, as can be seen in Figure 3-10 (b) the preparation of thinner electrodes improves the capacitance retention of the prGrO. The prGrO film achieves the highest capacitance, 248 $F.g^{-1}$, of the three preparation methods and keeps a capacitance retention similar to the slurry up to 3 $A.g^{-1}$. At higher current densities, the slurry's capacitance drops faster than the film's.

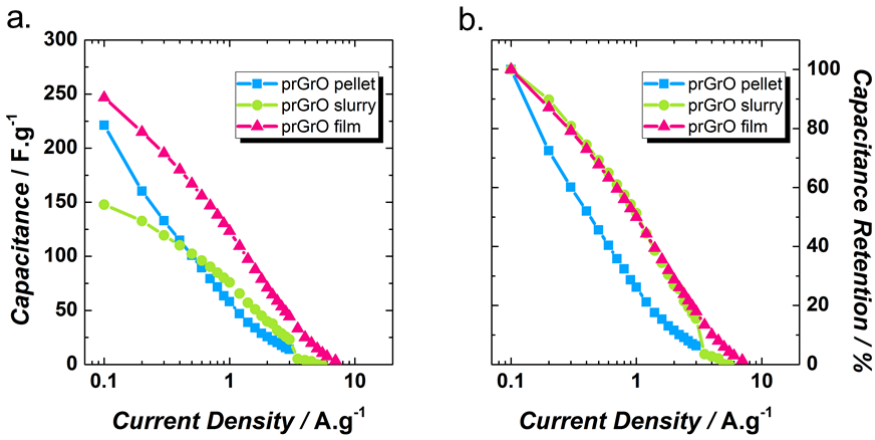

Figure 3-10. Rate capability (a) and capacitance retention (b) of prGrO in 0.1 M $HClO_4$.

3.3.3.2.3 Symmetric Cells of Lig/PEDOT 40/60 and prGrO

Lig/PEDOT 40/60 and the prGrO film are selected as the optimum electrode materials for this study. Therefore, they are tested in different symmetric cells and the electrochemical results are shown in . (a – b), show the rate performance of the symmetric cells. As expected from the 3-electrode measurements, the symmetric prGrO exhibits a higher capacitance (130 $F.g^{-1}$) than the symmetric Lig/PEDOT 40/60 (44 $F.g^{-1}$). Nevertheless, symmetric Lig/PEDOT 40/60 maintains 77 % of its capacitance at 10 $A.g^{-1}$, while symmetric prGrO only retains 15 % at 3 $A.g^{-1}$. This is caused by the balance between Lignin and PEDOT that provides an optimum charge transport. Lig/PEDOT's electron conductivity proceeds from

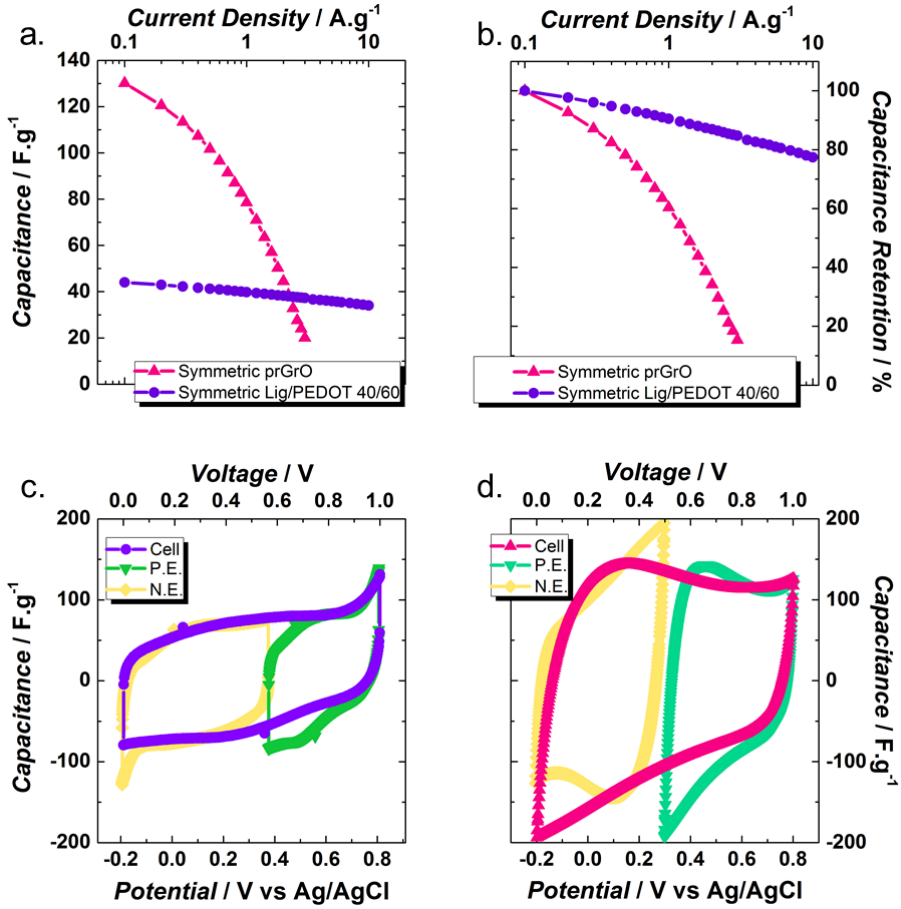

Figure 3-11. Rate capability (a) and capacitance retention (b) of the symmetric cells of prGrO and Lig/PEDOT 40/60 in 0.1 M $HClO_4$. Cyclic Voltammetry in a symmetric cell configuration at 5 $mV.s^{-1}$ of Lig/PEDOT 40/60 (c) and prGrO (d).

tunnelling between small conducting grains separated by insulating barriers[34] while prGrO has a lower conductivity given that it is caused by delocalization of the electrons.[35]

Both, Lig/PEDOT 40/60 ((c)) and prGrO ((d)) show rectangular CVs which evidence a capacitor behaviour. In the case of the Lig/PEDOT 40/60 cells, the potential window of each electrode is slightly different, being 0.6 V for the negative electrode and 0.4 V for the positive electrode. The difference in the potential window is caused by the redox reaction of the quinones (Reaction 3-2) in the positive electrode increasing the capacitance of this electrode.

By principle, the charge ($\boldsymbol{q}$) stored at the positive and negative electrode is equivalent ($\boldsymbol{q_+ = q_-}$). This charge depends on the specific capacitance ($\boldsymbol{C}$), the potential window ($\Delta\boldsymbol{E}$) and the mass ($\boldsymbol{m}$) of each electrode following the equation below:[36]

$$\boldsymbol{q = C \times \Delta E \times m} \qquad \textbf{Equation 3-2}$$

In the case of the Lig/PEDOT 40/60 electrode, the redox reaction related to the quinone moieties occurs at the positive electrode; therefore, its capacitance is larger than the one exhibited by the negative electrode, and as $\boldsymbol{q_+ = q_-}$, then $\boldsymbol{\Delta E_+ < \Delta E_-}$. These results indicate that the supercapacitor performance is limited by the negative electrode.

For the prGrO film, the potential windows and capacitance values of each electrode are equal.

3.3.3.2.4 Asymmetric Device

An asymmetric device based on Lig/PEDOT 40/60 as positive electrode and prGrO as negative electrode is assembled. This device will take advantage of the redox reactions taking place at the positive electrode in the Lig/PEDOT polymer and its high capacitance retention, and the large capacitance values exhibited by the prGrO. As both electrode materials have the same potential window, we assume that the whole potential will be divided equally in between the materials. Therefore, their masses are balanced based on their capacitance values at 0.1 mAh.g^{-1}, as follows:

$$\boldsymbol{C_+ \times m_+ = C_- \times m_-} \qquad \textbf{Equation 3-3}$$

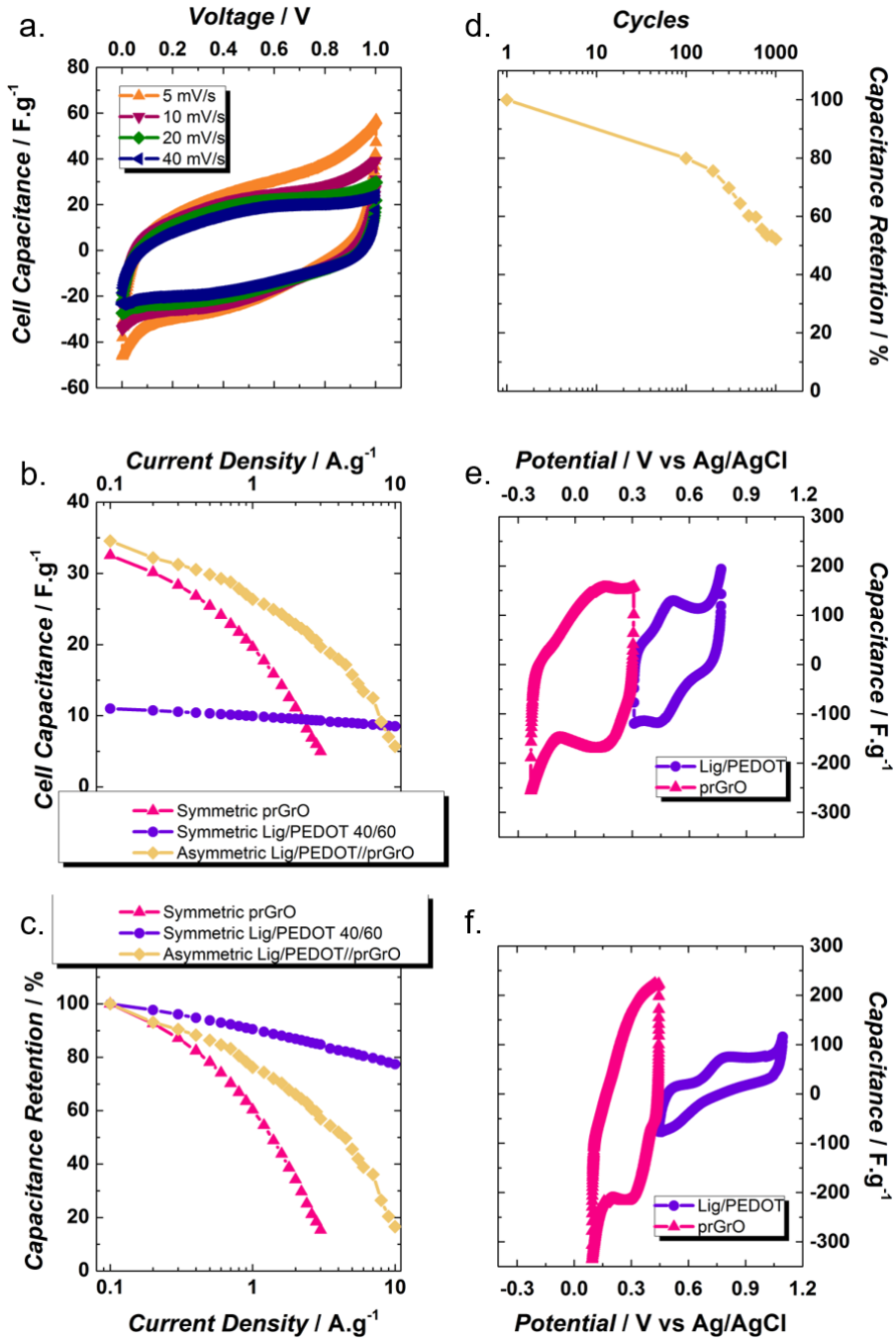

Figure 3-12. Results of the asymmetric Lig/PEDOT//prGrO device. Cyclic voltammetry (a), rate capability (b) and capacitance retention with current density (c) Capacitance retention after 1000 cycles at 5 mV.s^{-1} (d), 2nd cycle CV at 5 mV.s^{-1} (e) and 1000th cycle CV at 5 mV.s^{-1} (f).

$$\frac{\boldsymbol{m_+}}{\boldsymbol{m_-}} = \frac{\boldsymbol{C_-}}{\boldsymbol{C_+}} = \frac{\mathbf{248}}{\mathbf{97}} = \mathbf{2.6} \qquad \textbf{Equation 3-4}$$

Figure 3-12 shows the main electrochemical results of the asymmetric Lig/PEDOT//prGrO device with $\boldsymbol{m_+/m_-}$= 2.6. To compare the results from the asymmetric and symmetric devices, the capacitance values here reported correspond to the cell capacitance. The CVs of the asymmetric device in Figure 3-12 (a), show that even having two diffusion-limited processes, the total effect is an almost rectangular CV, similar to the ones exhibited by double-layer capacitors. This behaviour is kept at different scan rates, demonstrating appropriate electronic conductivity in the material. By using an asymmetric device, the capacitance is increased to 140 $F.g^{-1}$, 7 % and 69 % higher than the symmetric cells of prGrO and Lig/PEDOT 40/60, respectively. Then, Figure 3-12 (c) shows that at 10 $A.g^{-1}$, the asymmetric device still maintains 17 % of its initial capacitance. These effects, large capacitance and intermediate capacitance retention, are caused by a synergistic effect between Lig/PEDOT and prGrO. The former provides capacitance retention while the latter delivers high capacitance values.

In real life applications, supercapacitors are cycled thousands of times; herein, we cycled the Lig/PEDOT//prGrO asymmetric device at 5 $mV.s^{-1}$ during 1000 times. Figure 3-12 (d) shows the capacitance retention of the device every 100 cycles. The results show that the device keeps 52.2 % of its initial capacitance after 1000 cycles. In order to understand the reason for this loss of capacitance, a pseudo-reference electrode is introduced to study the electrochemical processes in each electrode. Cycles number 2 and 1000 are shown as example.

Figure 3-12 (e) shows the 2nd cycle of the cycling life test of the asymmetric device. The positive electrode, Lig/PEDOT 40/60, shows the redox peaks characteristic of the quinone/hydroquinone process (Reaction 3-2). The negative electrode, prGrO, presents wider peaks product of the pseudocapacitive processes. The potential windows are 0.46 V and 0.54 V for the positive and negative electrode, respectively, showing that the initial mass balance is appropriate for this device.

After 1000 cycles (Figure 3-12 (f)), the positive electrode expands its potential window to 0.65 V, leaving the negative electrode to work in a total electrochemical window equal to 0.35 V. This effect is caused by the decrease in capacitance in the Lig/PEDOT 40/60 electrode, which might be induced by depletion of quinone groups in the material.[33] This can be confirmed by the diminishing in the intensity of the redox peaks in the CV curve of the positive electrode.

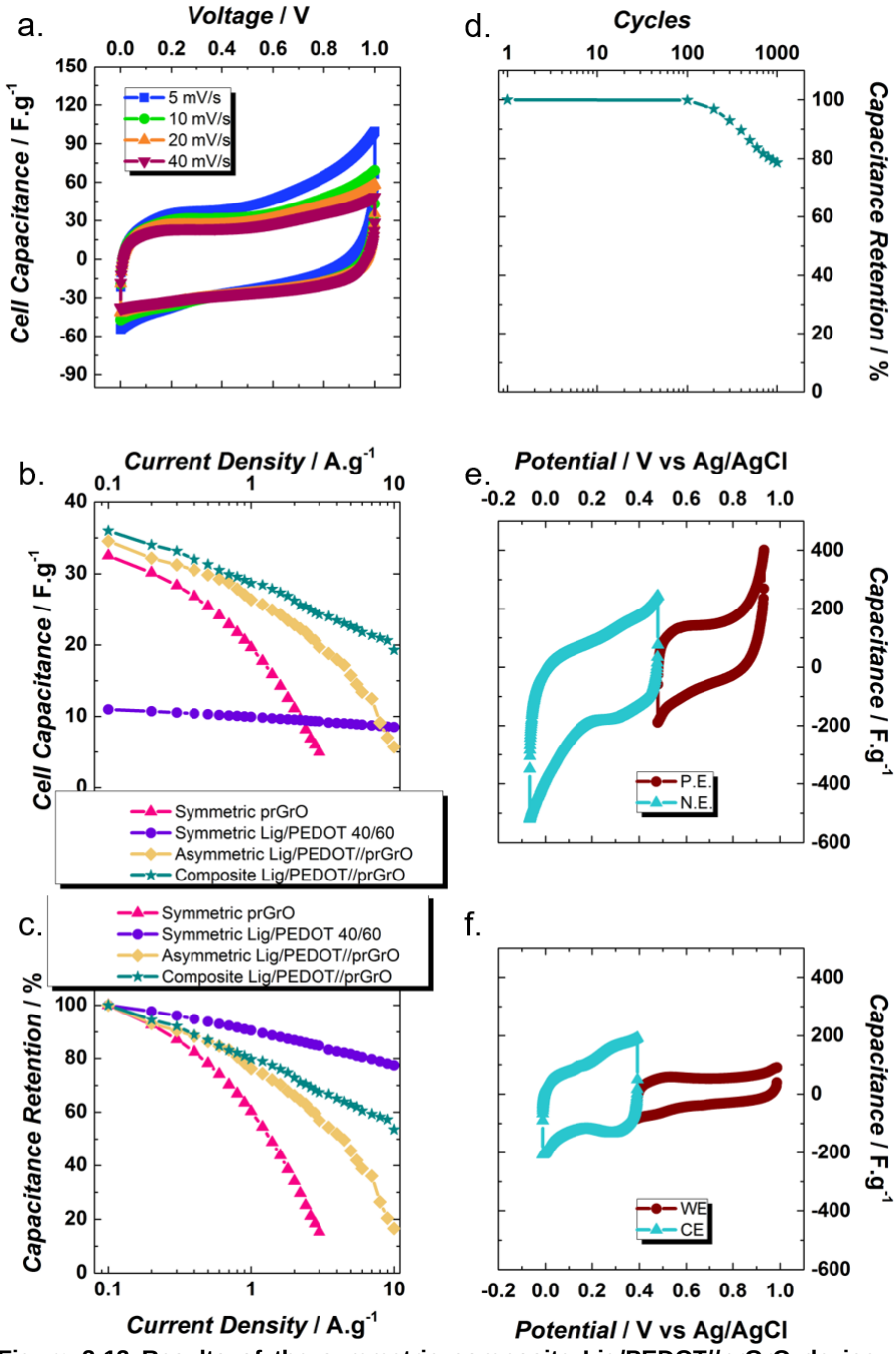

Figure 3-13 Results of the symmetric composite Lig/PEDOT//prGrO device. Cyclic voltammetry (a), rate capability (b) and capacitance retention with current density (c) Capacitance retention after 1000 cycles at 5 mV.s^{-1} (d), 2nd cycle CV at 5 mV.s^{-1} (e) and 1000th cycle CV at 5 mV.s^{-1} (f).

3.3.3.2.5 Composite Lig/PEDOT//prGrO

In order to maximize the capacitance values and capacitance retention, Lig/PEDOT 40/60 and prGrO are dispersed in water in a 50/50 ratio and then drop-cast in a platinum mesh, which acts as current collector. Figure 3-13 shows the main results of the electrochemical test of the composite in a symmetric cell configuration. The cyclic voltammetry curves of the composite (Figure 3-13 (a)) are rectangular, a behaviour usually seen when charging the electric double layer. In Figure 3-13 (b), can be seen that the distribution of an equal pseudocapacitive effect in both electrodes, is traduced in a capacitance slightly higher than the one exhibited by the asymmetric device, *i.e.* 144 $F.g^{-1}$ for the composite and 140 $F.g^{-1}$ for the asymmetric device. This effect is also caused by the similarity of the electrodes' masses, as there is not additional weight on any side in this configuration. When the current density increases, Figure 3-13 (c), the capacitance retention of the composite (54 %) is superior to the one exhibited by the asymmetric device (17 %), as a result of a more appropriate charge transfer in the electrodes. These devices cannot achieve the high capacitance retention of the symmetric Lig/PEDOT 40/60; however, in these cases, cycle life is sacrificed for the sake of large capacitance values.

The symmetric composite cell is also tested at 5 $mV.s^{-1}$ during 1000 cycles, the main results are shown in Figure 3-13 (d-f). After 1000 cycles, the composite Lig/PEDOT 40/60//prGrO retains 79 % of its initial capacitance (Figure 3-13 (d)). This is an exciting result, as the composite not only achieves larger capacitance values, and higher capacitance retention but also a better cycling life when compared to the asymmetric device.

Moreover, the analysis of each electrode, in Figure 3-13 (e – f), shows more rectangular CVs than in the asymmetric device. During the second cycle, the negative and positive electrode works in a potential window of 0.55 and 0.45 V, respectively. After 1000 cycles, the new potential window is 0.40 and 0.60 V for the negative and positive electrode, respectively. This increase in the potential window of the positive electrode potential is caused by the higher capacitance of the negative electrode.

3.4 Conclusions and Perspectives

EDOT was polymerized in presence of Lignin, a biopolymer rich in quinone moieties, to enhance the electron conductivity of the material and transport charge to the active sites of the polymer. Lig/PEDOT polymers with different Lignin/PEDOT ratios were characterized by means of FTIR and TGA to confirm

the polymerization of EDOT and the blending with Lignin. These polymers were studied in a 3-electrode configuration, being Lig/PEDOT 40/60 the material with the largest capacitance.

Graphite Oxide was partially reduced at 160 °C to improve electron conductivity while maintaining a high concentration of quinone/hydroquinone groups. The obtained prGrO was characterized by means of XPS, FTIR, N_2 gas sorption and XRD techniques.

The capacitive contributions to the charge storage of the materials was studied with a cavity microelectrode. This technique proved that the PEDOT enhanced the lignin's capacitive contribution to the current by 22 %. The capacitive contributions were equal to 66 % and 75 % in the Lig/PEDOT 40/60 and the prGrO respectively.

Asymmetric supercapacitors were assembled using Lig/PEDOT 40/60 as positive electrode and prGrO as negative electrode. The electrochemical results showed that the asymmetric device achieved high capacitance values, 140 $F.g^{-1}$ at 0.1 $A.g^{-1}$, and intermediate capacitance retention when compared to symmetric cells of Lig/PEDOT 40/60, and prGrO. When cycled 1000 times at 5 $mV.s^{-1}$, the device kept 52.2 % of its initial capacitance due to depletion of the quinone groups in the positive electrode, *i.e.* Lig/PEDOT 40/60.

A composite between the Lig/PEDOT 40/60 and the prGrO in a ratio 50/50 was prepared by physical mixture. Due to the distribution of the pseudocapacitive and faradaic processes between the two electrodes high capacitance values, 144 $F.g^{-1}$ at 1 $A.g^{-1}$, and high capacitance retention, 54 % at 10 $A.g^{-1}$, is achieved. A long cycle life was also accomplished by this method, maintaining 79 % of its capacitance after 1000 cycles.

There is still plenty of room to improve the electrochemical performance of Lignin and prGrO. Changing the composite ratio, improving the conductivity in the prGrO or by polymerizing the lignin with other conductive polymers might be solutions in the outlook for these materials.

3.5 References

(1) Chen, X.; Wang, H.; Yi, H.; Wang, X.; Yan, X.; Guo, Z. *J. Phys. Chem. C* **2014**, *118* (16), 8262–8270.

(2) Le Comte, A.; Chhin, D.; Gagnon, A.; Retoux, R.; Brousse, T.; Bélanger, D. *J. Mater. Chem. A* **2015**, *3* (11), 6146–6156.

(3) Casado, N.; Hernández, G.; Sardon, H.; Mecerreyes, D. *Prog. Polym. Sci.*

2016, *52*, 107–135.

(4) Song, Z.; Zhou, H. *Energy Environ. Sci.* **2013**, *6* (8), 2280–2301.

(5) Gracia, R.; Mecerreyes, D. *Polym. Chem.* **2013**, *4* (7), 2206–2214.

(6) Vonlanthen, D.; Lazarev, P.; See, K. A.; Wudl, F.; Heeger, A. J. *Adv. Mater.* **2014**, *26* (30), 5095–5100.

(7) Huskinson, B.; Marshak, M. P.; Suh, C.; Er, S.; Gerhardt, M. R.; Galvin, C. J.; Chen, X.; Aspuru-Guzik, A.; Gordon, R. G.; Aziz, M. J. *Nature* **2014**, *505*, 195–198.

(8) Kim, Y. J.; Wu, W.; Chun, S.-E.; Whitacre, J. F.; Bettinger, C. J. *Adv. Mater.* **2014**, *26* (38), 6572–6579.

(9) Milczarek, G.; Inganas, O. *Science (80-.).* **2012**, *335* (6075), 1468–1471.

(10) Ajjan, F. N.; Jafari, M. J.; Rębiś, T.; Ederth, T.; Inganäs, O. *J. Mater. Chem. A* **2015**, *3* (24), 12927–12937.

(11) Kim, S. K.; Kim, Y. K.; Lee, H.; Lee, S. B.; Park, H. S. *ChemSusChem* **2014**, *7* (4), 1094–1101.

(12) Milczarek, G.; Nowicki, M. *Mater. Res. Bull.* **2013**, *48* (10), 4032–4038.

(13) Ajjan, F. N.; Casado, N.; Rębiś, T.; Elfwing, A.; Solin, N.; Mecerreyes, D.; Inganäs, O. *J. Mater. Chem. A* **2016**, *4* (5), 1838–1847.

(14) Marcano, D. C.; Kosynkin, D. V.; Berlin, J. M.; Sinitskii, A.; Sun, Z.; Slesarev, A.; Alemany, L. B.; Lu, W.; Tour, J. M. *ACS Nano* **2010**, *4* (8), 4806–4814.

(15) Eng, A. Y. S.; Ambrosi, A.; Chua, C. K.; Šaněk, F.; Sofer, Z.; Pumera, M. *Chem. - A Eur. J.* **2013**, *19* (38), 12673–12683.

(16) Biilmann, E. *Trans. Faraday Soc.* **1924**, *19*, 676–691.

(17) Rębiś, T.; Nilsson, T. Y.; Inganäs, O. *J. Mater. Chem. A* **2016**, *4* (5), 1931–1940.

(18) Leguizamon, S.; Díaz-Orellana, K. P.; Velez, J.; Thies, M. C.; Roberts, M. E. *J. Mater. Chem. A* **2015**, *3* (21), 11330–11339.

(19) Admassie, S. *Bull. Chem. Soc. Ethiop.* **2016**, *30* (1), 153–160.

(20) Admassie, S.; Elfwing, A.; Jager, E. W. H.; Bao, Q.; Inganas, O. *J. Mater. Chem. A* **2014**, *2* (207890), 1974–1979.

(21) Nagaraju, D. H.; Rebis, T.; Gabrielsson, R.; Elfwing, A.; Milczarek, G.; Inganäs, O. *Adv. Energy Mater.* **2014**, *4* (1), 1–7.

(22) Admassie, S.; Nilsson, T. Y.; Inganäs, O. *Phys. Chem. Chem. Phys.* **2014**, *16* (45), 24681–24684.

(23) Deng, D.; Pan, X.; Yu, L.; Cui, Y.; Jiang, Y.; Qi, J.; Li, W. X.; Fu, Q.; Ma, X.; Xue, Q.; Sun, G.; Bao, X. *Chem. Mater.* **2011**, *23* (5), 1188–1193.

(24) Yang, D.; Velamakanni, A.; Bozoklu, G.; Park, S.; Stoller, M.; Piner, R. D.; Stankovich, S.; Jung, I.; Field, D. A.; Ventrice, C. A.; Ruoff, R. S. *Carbon N. Y.* **2009**, *47* (1), 145–152.

(25) Cachet-Vivier, C.; Vivier, V.; Cha, C. S.; Nedelec, J. Y.; Yu, L. T. *Electrochim. Acta* **2001**, *47* (1), 181–189.

(26) Shin, H.-J.; Jeon, S. S.; Im, S. S. *Synth. Met.* **2011**, *161* (13), 1284–1288.

(27) Ganguly, A.; Sharma, S.; Papakonstantinou, P.; Hamilton, J. *J. Phys. Chem.* **2011**, 17009–17019.

(28) Choi, E.-Y.; Han, T. H.; Hong, J.; Kim, J. E.; Lee, S. H.; Kim, H. W.; Kim, S. O. *J. Mater. Chem.* **2010**, *20* (10), 1907–1912.

(29) Ferrari, A. C. *Solid State Commun.* **2007**, *143* (1–2), 47–57.

(30) Huh, S. H. In *Physics and Applications of Graphene - Experiments*; Mikhailov, S., Ed.; InTech, 2010; pp 73–90.

(31) Li, Z. Q.; Lu, C. J.; Xia, Z. P.; Zhou, Y.; Luo, Z. *Carbon N. Y.* **2007**, *45* (8), 1686–1695.

(32) Lutterotti, L.; Voltolini, M.; Wenk, H.-R.; Bandyopadhyay, K.; Vanorio, T. *Am. Mineral.* **2010**, *95*, 98–103.

(33) Oh, Y. J.; Yoo, J. J.; Kim, Y. Il; Yoon, J. K.; Yoon, H. N.; Kim, J. H.; Park, S. Bin. *Electrochim. Acta* **2014**, *116*, 118–128.

(34) Tjong, S. C.; Mai, Y. W. *Physical properties and applications of polymer nanocomposites*; Woodhead Pub, 2010.

(35) Hwang, E. H.; Adam, S.; Sarma, S. Das. *Phys. Rev. Lett.* **2007**, *98* (18), 186806–186811.

(36) Khomenko, V.; Raymundo-Piñero, E.; Béguin, F. *J. Power Sources* **2010**, *195* (13), 4234–4241.

STUDY OF REDOX ACTIVE QUINONE-AMINE POLYMERS FOR ENERGY STORAGE DEVICES

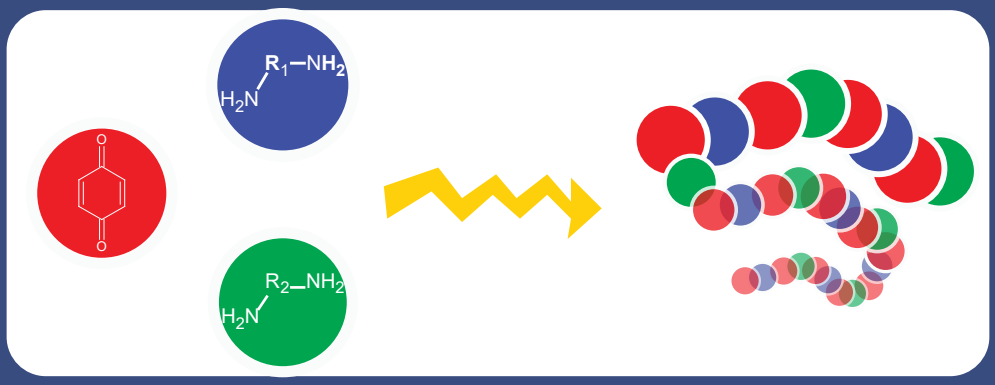

4 Study of Redox Active Quinone-Amine Polymers for Energy Storage Devices

4.1 Introduction

As mentioned before in this thesis, introducing redox active moieties in the surface of the materials will enhance the capacitive contributions to the total current by moving from an exclusive double-layer capacitor to a pseudocapacitor.[1,2]

Among the surface functional groups, oxygen- and nitrogen-containing groups have been well-studied for years.[3] Several functions of nitrogen have been proposed, such as being an electron donor to attract protons or enhance charge density of space charge layer,[4–6] strengthening oxidation/reduction of quinone,[7] and introducing redox reactions of amine groups.[8]

Herein, the nanostructuring process of a redox active polymer electrode with different types of nanocarbon are studied. Two kinds of diamine, linear and aromatic, are polymerized with benzoquinone to favour the development of

pseudo-faradaic charge transfer processes, (linear diamine) and to introduce a redox reaction of amine groups (aromatic diamine). A straightforward strategy to improve the electron conductivity of a polymer is the addition of conductive fillers. As the electronic properties of a carbon are expected to depend on its crystal structure and C-C bonding connectivity, carbons with different dimensionalities like carbon black nanoparticles (3D), graphene (2D) and carbon nanotubes (1D) are evaluated as conductive fillers.

The aim of this work is to develop low cost and easy to process electrodes for applications in batteries or supercapacitors. The approach is to copolymerize a monomer with quinone/hydroquinone functional groups with a second monomer based on diamines. The impact of the linearity/aromaticity of the second monomer on the electrochemical properties is assessed. In order to improve processability in solution, a third monomer based on polyethylene oxide is used as a linker. Polymerizations of the copolymers are also studied in the presence of carbons with different dimensionalities to improve their conductivity. The optimum synthesis conditions are determined to provide the best match between the electrochemical properties of the redox active polymer and the dimensionality of the nanocarbon. The polymers are characterized by X-Ray Diffraction, Fourier Transform Infrared, Raman Spectroscopy, Thermogravimetric Analysis, Scanning Electron Microscopy, cyclic voltammetry and galvanostatic measurements.

4.2 Methodology

4.2.1 Materials Synthesis

4.2.1.1 Synthesis of Benzoquinone-Diamine Bipolymers

3 mmol of p-benzoquinone (Sigma Aldrich, 98 %) are dissolved in 25 ml of ethanol (EtOH, Scharlau, 96 %) or Dimethylformamide (DMF, Fisher scientific, 99.97 %) to which 1 mmol of p-phenylenediamine (Sigma Aldrich, 98 %) or hexamethylenediamine (Sigma Aldrich, 98 %), previously dissolved in 25 ml of EtOH or DMF, is added. Polymerization is allowed to complete within 14 hours at room temperature. Scheme 4-1 and Table 4-1 shows the polymerization conditions. After completion of reaction, the product is removed from the reaction solution by centrifugation at 10000 rpm for 15 minutes in a Sorvall legend X1 centrifuge (Thermo Scientific, Germany). The solid obtained is dried at 60 °C under vacuum. When the polymerization takes place with the conductive filler, (*in situ* polymerization), the Graphene Oxide (GO), the multi walled carbon nanotubes, or the carbon black nanoparticles (C65) are sonicated for one hour in

Scheme 4-1. Conditions of the bipolymer formation.

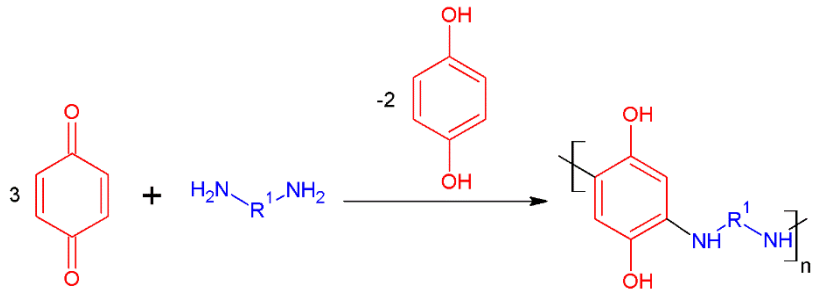

EtOH previous to each polymerization. The graphite is oxidized by the Marcano-Tour method[9] as explained in section 3.3.1.2. After sonication, the GrO is delaminated and Graphene Oxide (GO) is obtained. In order to thermally reduce the GO, the *in situ* bipolymer is heated under argon flow at a heating rate of 5 °C.min^{-1} up to 140 °C and kept for 6 hours, cooled down and stored for later utilization.

The benzoquinone is the limiting reagent, given that 2 mmoles are converted into hydroquinone and these do not make part of the final polymer structure.

4.2.1.2 Synthesis of Benzoquinone-PEO-Diamine Terpolymers

For the preparation of the terpolymer, five different PEO molecules are tested as linkers for the terpolymers. They were 1,10-Diamino-4,7-dioxadecane (Acros

Table 4-1. Reaction conditions of the bipolymer formation.

Entry	$H_2N-R^1-NH_2$	Product (Copolymer)	Time (h)	Conditions
1		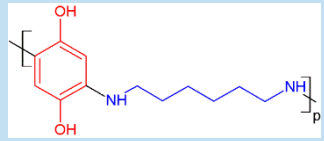	14	1a. EtOH 1b. DMF 1c. C65/DMF 1d. C65/EtOH 1e. MWCNT/EtOH 1f. GrO/EtOH
2	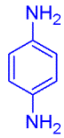	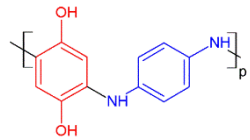	14	2a. EtOH 2b. DMF 2c. C65/DMF 2d. C65/EtOH 2e. MWCNT/EtOH 1f. GrO/EtOH

Table 4-2. List of PEO molecules used as linkers.

Structure	Name	Acronym
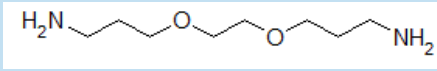	1,10-Diamino-4,7-dioxadecane	Dioxa
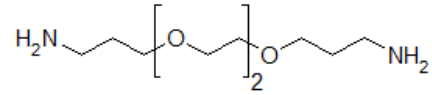	4,7,10-Trioxa-1,13-tridecanediamine	Trioxa
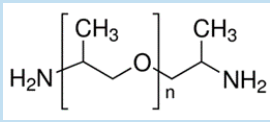 **n ≈ 6.1**	(Poly(propylene glycol) bis(2-aminopropyl ether)	D-400
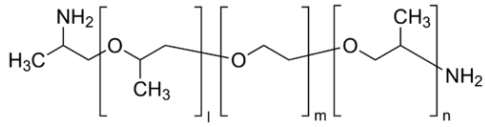 **m ≈ 9; (l+n) ≈ 3.6**	O,O′-Bis(2-aminopropyl) polypropylene glycol-block-polyethylene glycol-block-polypropylene glycol 500	ED-600
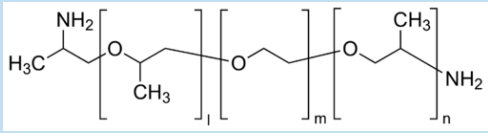 **m ≈ 12.5; (l+n) ≈ 6**	O,O′-Bis(2-aminopropyl) polypropylene glycol-block-polyethylene glycol-block-polypropylene glycol 800	ED-900

Organics CAS nº 2997-01-5), 4,7,10-Trioxa-1,13-tridecanediamine (also known as O,O′-Bis(3-aminopropyl)diethylene glycol, Sigma-Aldrich 369519), Poly(propylene glycol) bis(2-aminopropyl ether) (Mn ~ 400 Sigma-Aldrich, 406678), O,O′-Bis(2-aminopropyl) polypropylene glycol-block-polyethylene glycol-block-polypropylene glycol 500 (also known as Jeffamine-ED600, Sigma-Aldrich 14526) and O,O′-Bis(2-aminopropyl) polypropylene glycol-block-polyethylene glycol-block-polypropylene glycol 800 (also known as Jeffamine-ED900, Sigma-Aldrich 14527). Their structures and the short names used for them in this manuscript are shown in Table 4-2.

The synthesis is carry out by dissolving 1 mmol of PEO linker is dissolved in 25 ml of EtOH to which 6 mmol of p-benzoquinone, previously dissolved in 25 ml of

Scheme 4-2. Synthesis conditions of the terpolymer formation.

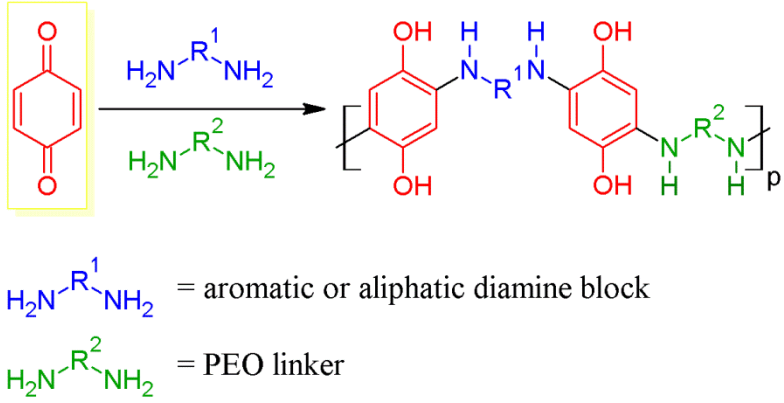

EtOH, are added. Polymerization is allowed to complete within 48 hours at room temperature and then 1 mmol of p-phenylene diamine or hexamethylene diamine, is added to the solution. The reaction is left for another 48 hours. The reaction conditions are summarized in Scheme 4-2. After completion of reaction, the product is removed from the reaction solution by centrifugation at 10000 rpm for 15 minutes in a centrifuge. The solid obtained is dried at 60 °C under vacuum. When the polymerization takes place with the conductive filler, (*in situ* polymerization), the GO or the MWCNT is sonicated for one hour in EtOH previous to be added to the reaction mixture to each polymerization. For the *in situ* polymerization by using GO, the graphite is oxidized by the Marcano-Tour method[9] as explained in section 3.3.1.2. After sonication, the GrO gets delaminated and Graphene Oxide (GO) is obtained. In order to thermally reduce the GO, the *in situ* terpolymer is heated under argon flow at a heating rate of 5 °C.min^{-1} up to 140 °C and kept for 6 hours, cooled down and stored for later utilization.

During the synthesis of the terpolymer, the benzoquinone reacts with two different diamines; therefore, each structural unit of the polymer will contain two hydroquinone molecules and four other will be by-products of the reaction.

4.2.2 Preparation of the Electrodes

4.2.2.1 Benzoquinone-Diamine Bipolymers

Bipolymer pellets of 11 mm diameter and with a thickness between 150 – 200 μm are pressed under a pressure of 2 Tons for 1 minute. The pellets are directly used as working electrodes and assembled in an asymmetric cell (Swagelok type) with a platinum mesh as counter electrode, in a 0.1 M $HClO_4$ solution for potential between -0.2 and 0.9 V and silver/silver chloride (Ag/AgCl) is used as reference electrode. Details on the electrochemical characterization are described in Appendix I.

4.2.2.2 Benzoquinone-PEO-Diamine Terpolymers

For the processing of the terpolymer-based electrodes by drop casting, a screening of different solvent media was explored. Among the different solvent used are the following: deionized water, perchloric acid (Sigma Aldrich, 70 %), N-methyl-2-pyrrolidone (Sigma Aldrich, 99.5 %), dichloromethane (Sigma Aldrich, > 99.8 %), tetrahydrofuran (Acros, 99.9 %), chloromethane (Sigma Aldrich, > 99.5 %), 1,4-dioxane (Sigma Aldrich, 99.8 %), dimethyl sulfoxide (Sigma Aldrich, 99,9 %), acetonitrile (Sigma Aldrich, 99.8 %), ethyl acetate (Panreac, 100 %), diethyl ether (Sigma Aldrich, 100 %), isopropyl alcohol (Sigma Aldrich, 99.8 %).

As it will be seen, N-methyl pyrrolidone shows the best solvent properties for the processing of the terpolymer electrodes. Then, 60 mg of each terpolymer are dissolved in 3 ml of N-methyl-2-pyrrolidone. In order to create porosity in the electrode, to enhance the electroactive surface area, 20 % of sodium chloride (NaCl, Fisher Scientific, 99.5 %) is also added. The mix was drop-cast on a Stainless-Steel disk. The electrodes are left to dry at room temperature in the vacuum fume hood for 8 h. Then, the electrodes are washed with water to remove the NaCl and left to dry again for 8 h before testing.

All the materials are first characterized electrochemically to select the optimum electrochemical parameters and then, these materials are physicochemically characterized by X-Ray Diffraction, Fourier Transform Infrared, Raman Spectroscopy, and Thermogravimetric Analysis as explained in Appendix I.

4.3 Results and Discussion

4.3.1 Benzoquinone-Diamine Bipolymers

Theoretically, poly[benzoquinone-co-hexamethylenediamine] (herein referred as BQhMdA) and poly[benzoquinone-co-(p-phenylenediamine)] (herein referred as BQpPhdA) should undergo a 2 e^- and 4 e^- redox process per structural unit, respectively, as indicated in Reactions 4-1 and 4-2:

Based on these reactions, poly[benzoquinone-co-hexamethylenediamine] and poly[benzoquinone-co-(p-phenylenediamine)] should deliver 239 $mAh.g^{-1}$ (717 $F.g^{-1}$) and 496 $mAh.g^{-1}$ (1487 $F.g^{-1}$), respectively, which makes these polymers attractive for energy storage applications.

The electrochemical properties of the electroactive polymers herein developed are affected by different parameters during the synthesis. In order to maximize the capacity values achieved with these compounds, the following parameters are studied and optimized: Reaction medium, inclusion of the conductive filler and dimensionality of the conductive filler.

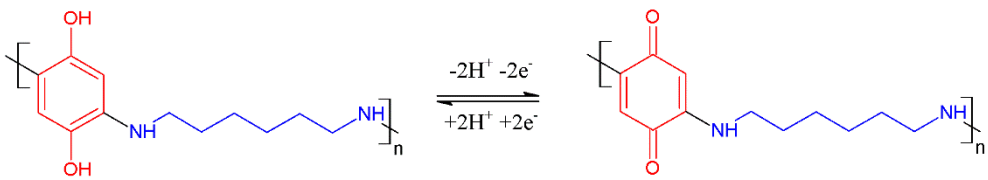

Reaction 4-1. Redox process of poly[benzoquinone-co-(hexamethylene diamine)]

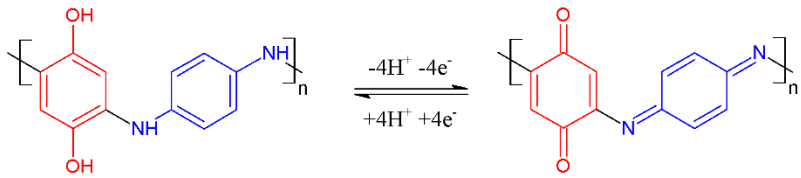

Reaction 4-2. Redox reaction of poly[benzoquinone-co-(p-phenylenediamine)]

4.3.1.1 Poly[benzoquinone-co-hexamethylenediamine]

Poly[benzoquinone-co-hexamethylenediamine] is first synthesized in EtOH and DMF to find those conditions in which the electrochemical capacity is the highest. Figure 4-1 shows the galvanostatic charge/discharge of the bipolymers synthesized in DMF and EtOH. In order to improve conductivity, the bipolymers are physically mixed with C65 (Figure 4-1 (a.I and b.I)) or the polymerization takes place in the presence of C65 (Figure 4-1 (a.II and b.II)) to achieve their maximum capacity. The ratio for all the mixtures of BQhMdA:C65 is 50:50.

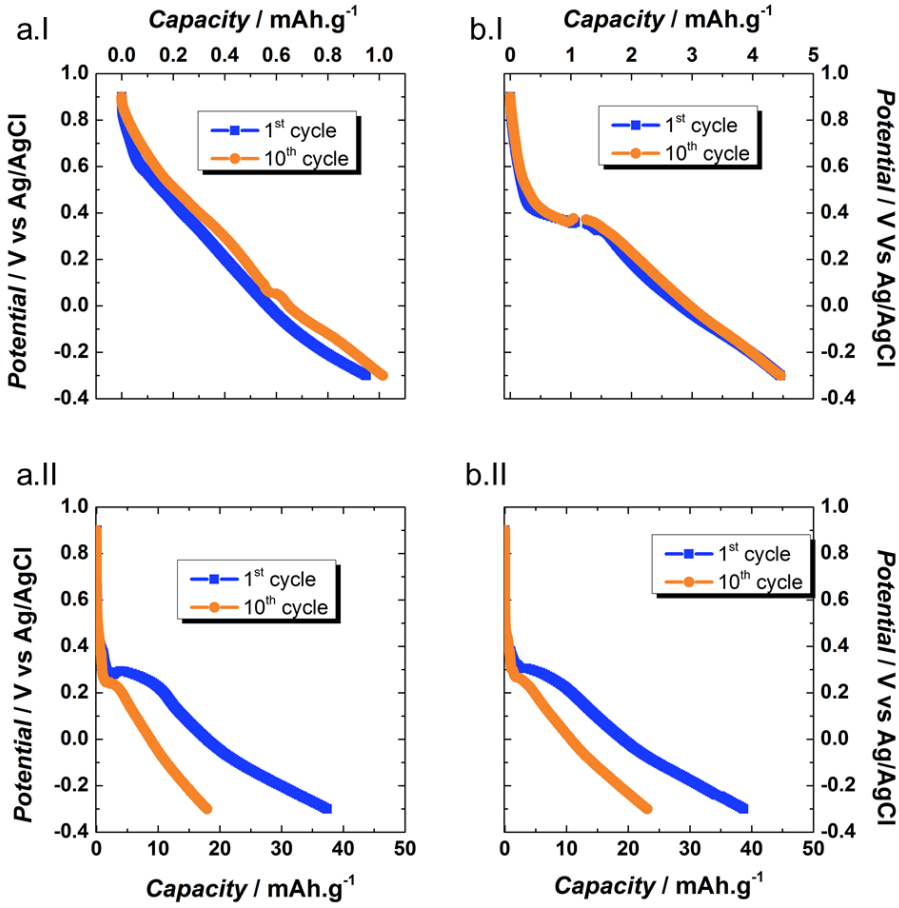

Figure 4-1. Galvanostatic discharge at 0.08 A.g^{-1} of the poly[benzoquinone-co-hexamethylenediamine] synthesized in DMF (a) and in EtOH (b). Inclusion of the C65 after polymerization (I) and before polymerization (II).

The bipolymer synthesized in DMF and then mixed with C65 shows a discharge with a linear slope similar to the ones yielded by double-layer capacitors (Figure 4-1 (a.I)). This might imply that the charge being stored is just in the surface of the polymer and no redox reactions are taking place. This hypothesis would agree with the low capacity value yielded by the bipolymer, 1 $mAh.g^{-1}$. The synthesis developed in EtOH improves 4.5 times the capacity achieved (Figure 4-1 (b.I)) thanks to a plateau at 0.4 V, probably caused by Reaction 4.1. These results indicate that when the BQhMdA is synthesized in EtOH, its redox reaction is favoured.

To confirm that all the possible capacity of the polymer is being attained, the polymerization is repeated in EtOH and DMF but the C65 is added at the beginning of the reaction. The galvanostatic results are shown in Figure 4-1 (a.II and b.II). When the polymerization occurs in the presence of C65 particles, both products show a plateau around 0.3 V, and the slope between 0.2 V and -0.4 V is increased. These phenomena enhance the capacity values up to 37 $mAh.g^{-1}$ and 39 $mAh.g^{-1}$, in DMF and EtOH, respectively. After 10 cycles, the BQhMdA synthesized in DMF, has retained 49 % of its capacity while the one synthesized in EtOH still preserves 59 % of it. To achieve the maximum capacity and capacity retention, in the following experiments regarding hexamethylenediamine, the polymerizations will be carried out *in situ* in the presence of the conductive filler and in EtOH.

Afterwards, the effect of the nanodimensionality of the conductive filler is studied. Herein, C65, rGO, and MWCNT are used as 3-D, 2-D, and 1-D carbons, respectively. Figure 4-2 shows the galvanostatic discharges of the polymers with C65, rGO and MWCNT. When polymerizing BQhMdA with C65 and MWCNT, the monomers are attracted towards the carbons by non-covalent interactions and therefore the carbon nanomaterials do not interfere with the redox moieties.

However, GO has a large number of highly reactive oxygen-containing functional groups that might be creating covalent bonds with the monomers[10] and therefore causing a change in the redox potential of the polymers as can be seen in Figure 4-2 (b). The only composite that shows a clear plateau around 0.4 V is the one prepared with C65 (Figure 4-2 (a)). MWCNTs, show only a change in the slope at 0.4. Probably, the polymerization with the 1-D material enhance the capacitive abilities of this material in such a way that the redox peaks get concealed. Because of these reasons, the rGO composite presents the lowest capacity (1.9 $mAh.g^{-1}$) from the three samples and MWCNT the highest (109 $mAh.g^{-1}$). To achieve the maximum capacity deliverable by BQhMdA, the reaction must be made in EtOH with previous addition of MWCNT.

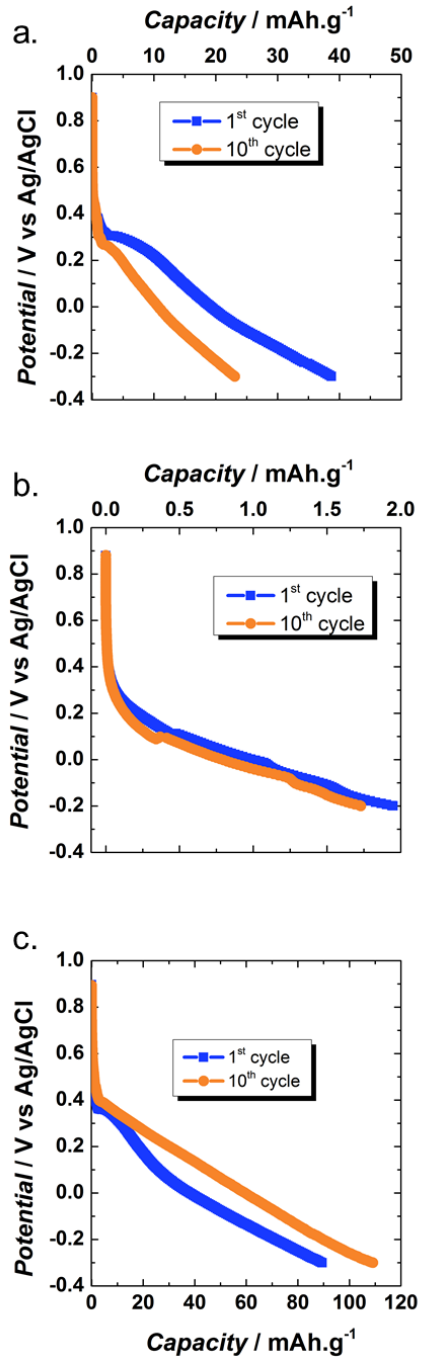

Figure 4-2. Electrochemical comparison at 0.08 A.g^{-1} of the poly[benzoquinone-co-hexamethylenediamine] synthesized in EtOH *in situ* with C65 (a) rGO (b) and MWCNT (c).

The changes caused in the material by *in situ* polymerization with MWCNT are followed by XRD and TGA as can be seen in Figure 4-3. The XRD pattern of the MWCNTs (Figure 4-3) shows an intense peak at 2θ = 25.8 ° corresponding to the (002) reflection. Compared to the normal graphite, 2θ = 26.5 °, this peak shows a downward shift; which is attributed to an increase in the number of sp^2 bonds, C=C layers spacing.[11] The polymer without conductive filler presents a broad peak, indicating an amorphous structure.[12] When the polymerization takes place around the MWNCTs, the peak at 25.8 ° is broaden but still an intense peak is observed. This pattern indicates a microcrystallinity, meaning that the polymer has regions of aligned chains in small crystallites that diffract and that the remaining chains have no order and contribute to an incoherent scatter.[13]

In order to know the real content (compared to the nominal content) of BQhMdA in the composite, a TGA is performed. Figure 4-3 (b) shows the TGA of the MWCNTs, BQhMdA and their composite. The MWCNTs have an initial weight loss temperature at 542 °C and an oxidation temperature at 621 °C. At 900 °C a residual mass of 12 % is found, product of the metal catalyst used to manufacture the nanotubes.[14] The BQhMdA undergoes thermal degradation beginning at 250 °C and with a total mass loss of 97 %. The BQhMdA-CNT undergoes thermal degradation beginning at 250 °C with a mass loss of 30 %. At 900 °C, the residual mass is 15 %. As 30 % of the composite is active material, Figure 4-2 (c) is recalculated and the new values are shown in Figure 4-3 (c). The capacity delivered by BQhMdA-MWCNT is 364 $mAh.g^{-1}$, 1.5 times higher than the theoretical one. This extra stored charge might be due to capacitive effects between the polymer and the ions.

Herein, Raman, XRD and FTIR are used to follow the reactions taking place during the galvanostatic cycling of the BQhMdA-MWCNT. To decrease the signal coming from the MWCNTs in the previous techniques, the ratio BQhMdA:MWCNT is modified to 95:5. The results are shown in Figure 4-4.

The structure of the bipolymer is obviously affected by the insertion of the conductive filler before polymerization as can be seen by comparing Figure 4-3 (a) and Figure 4-3 (b). By decreasing the proportion of MWCNTs in the composite, BQhMdA-MWCNTs goes from having a microcrystalline structure to a more amorphous structure. Still, the polymer has some regions of aligned chains that are the cause of the small peaks in the broad feature. After charge and discharge, these aligned regions are not observable anymore.

Figure 4-4 (b) shows the Raman spectra of the sample before cycling and after charge and discharge. The only appreciable peaks are at ≈ 1601 cm^{-1} and ≈ 1337 cm^{-1} and might correspond to the G and D band of the MWCNTs, respectively.

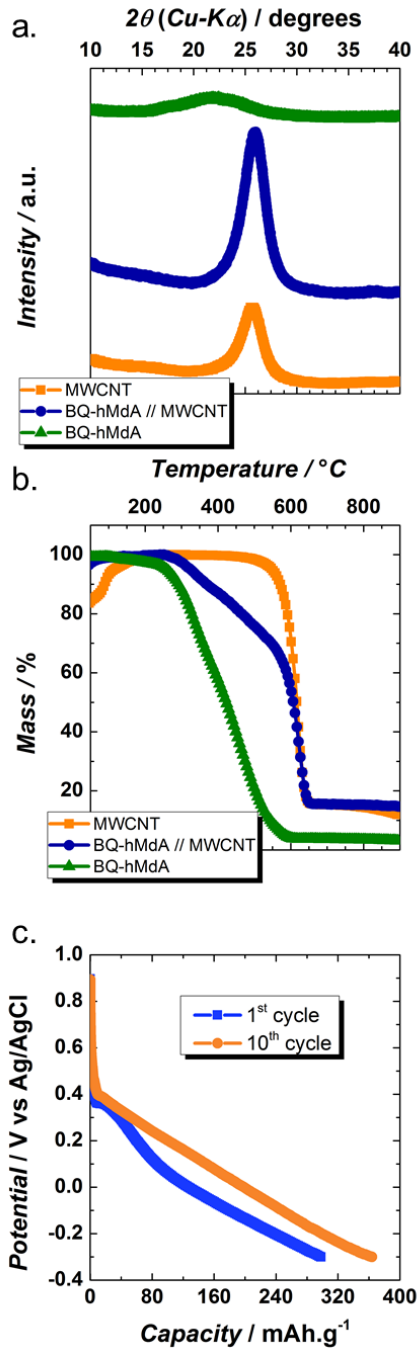

Figure 4-3. XRD (a) and TGA (b) of the BQhMdA, MWCNT and their composite. Galvanostatic discharge at 0.08 A.g^{-1} of the BQhMdA-MWCNT per active material (c).

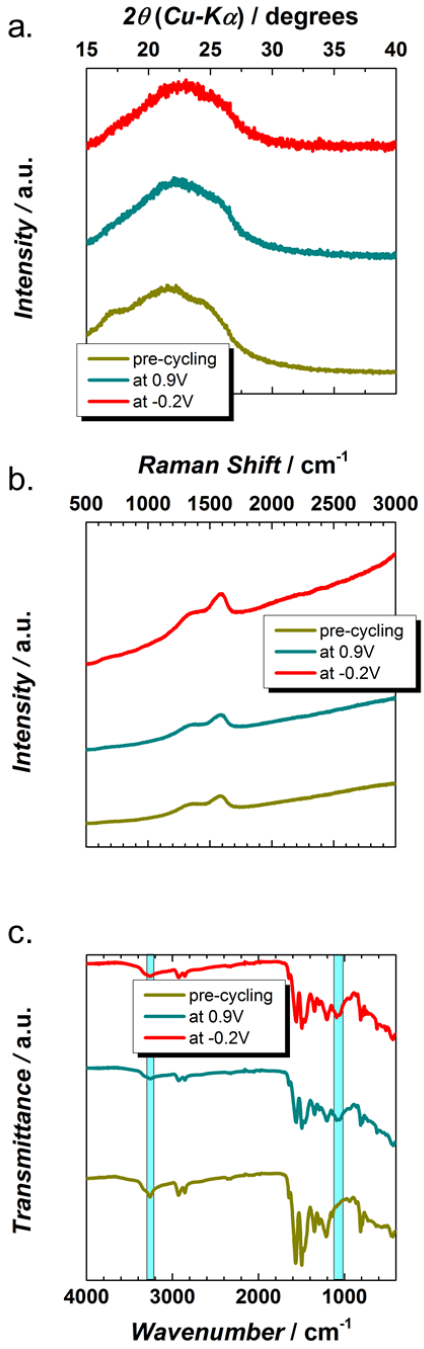

Figure 4-4. XRD (a), Raman (b) and FTIR (c) plots of the BQhMdA-MWCNT before cycling, and after charge and discharge.

The G peak corresponds to the E_{2g} phonon at the Brillouin zone centre. The D peak is due to the breathing modes of sp^2 rings and requires a defect for its activation.[15] These defects that activate the D band might be caused by the polymer surrounding the MWCNT. These bands are not affected by the cycling of the polymer, meaning no more defects are included in the material with cycling. However, these peaks are also overlapped with the typical Raman shifts from the hydroquinone molecules. In this case, the peaks at ~1601 cm^{-1} and ~1337 cm^{-1}, would correspond to the C=C and C-C vibrations, respectively.[16] These vibrations do not change with cycling; therefore, the bands do not change either.

Figure 4-4 (c) shows the FTIR of the BQhMdA before cycling and after charge and discharge. BQhMdA shows peaks at 3338 cm^{-1} (amine N-H stretch), 3261 cm^{-1} (Phenol O-H stretch), 2933, 2851 cm^{-1} (alkyl C-H stretch), 1643, 1566, 1495, 1470 cm^{-1} (aromatic C=C bending), 1346, 1209 cm^{-1} (Aromatic C-N) and 810 cm^{-1} (aromatic C-H bending). After charging and discharging, the strong peak at 1690 cm^{-1}, typical of Aromatic C=O does not appear, which indicates that is not the reaction indicated as Reaction 4.1 as expected but instead a new mechanism is occurring. The changes in the spectra (shadowed in light blue) are instead a diminishing of the peaks at 3261, 1346, and 1209 cm^{-1} and the appearance of a new feature at 1054 cm^{-1}. In fact, all these characteristics are interrelated and can be explained by an intramolecular hydrogen bonding in the molecules as can be seen in Reaction 4.3. [17–19]

The formation of intramolecular hydrogen bonds would be benefited by the formation of a 5-atom ring, which is stable and energetically favoured. The $2e^-$ and $2H^+$ transfer would still occur, explaining the high capacity. Still, the Fourier Transform Infrared fingerprint would not change as much as expected but for a slight diminish of the Phenol O-H stretch and a red-shift of the aromatic C-N from 1209 cm^{-1} to 1054 cm^{-1}.

As proved in this section, BQhMdA-MWCNT is a promising polymer for energy

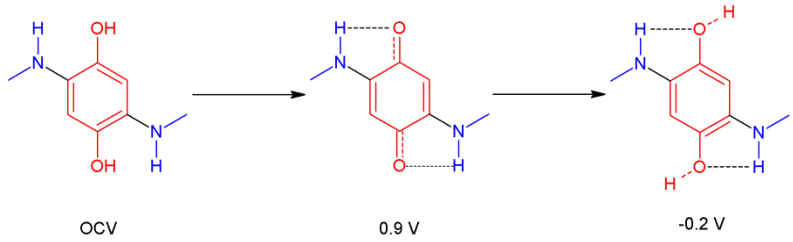

Reaction 4-3. Intramolecular hydrogen bonding in of poly[benzoquinone-co-(hexamethylene diamine)] during cycling.

storage devices. Preparation of thinner electrode films has proven to be beneficial for increasing the pseudo-capacitance behaviour of a material.[20] A method to process the poly[benzoquinone-co-(hexamethylene diamine)] electrode will be studied in Section 4.4.2.1.

4.3.1.2 Poly[benzoquinone-co-(p-phenylenediamine)]

The same parameters from the previous section are studied with the BQpPhdA: Reaction medium, inclusion of the conductive filler and dimensionality of the conductive filler.

Figure 4-5 shows the electrochemical results of the polymers synthesized in DMF and EtOH, with ex situ and *in situ* addition of the C65. When the reaction takes place in DMF and the C65 is physically mixed, Figure 4-5 (a.I), the galvanostatic discharge plateau appears around 0.4 V but also more features are observed. This might indicate presence of oligomers or hydroquinone in the sample. In EtOH, there is no well-defined plateau but the presence of different slopes is also observed. Besides, in both solvents, the capacity increases after 10 cycles, this might be related to these oligomers reacting with each other and making longer chains that yield higher capacity values than the smaller molecules, because of the increase in conjugation.

When the polymerization occurs in the presence of C65 and in DMF, the BQpPhdA's discharge curve presents again several changes in the slope but the capacity is doubled compared to the *ex situ* process in the same solvent (Figure 4-5 (a.II)). The polymer synthesized by *in situ* process in EtOH, presents one slope change at 0.4 V and its capacity retention after 10 cycles is 100 %, indicating that there is no presence of oligomers or another species contributing to an extra capacitance. These studies confirm that for BQpPhdA, the conductive filler must be added before polymerization and the reaction should be made in EtOH.

Figure 4-6 shows the galvanostatic discharges of the BQpPhdA synthesized in EtOH, *in situ* with C65 (Figure 4-6 (a)), rGO (Figure 4-6 (b)), and MWCNT (Figure 4-6 (c)). Compared to the results from the linear polymer in Figure 4-2, all the composites achieve higher capacity values. This is most probably due to the $4e^-$ transfer of the aromatic polymer compared to the $2e^-$ transfer in the linear one. The electrode containing C65, as explained above, achieves 102 $mAh.g^{-1}$ without loss of capacity with cycling. When the polymerization takes place in the presence of GO (Figure 4-6 (b)), the same effect than with the BQhMdA occurs. The change of slope takes place around 0 V and the capacity achieved is the lowest of the three composites, *i.e.* 11 $mAh.g^{-1}$. Following, when the MWCNTs are used as

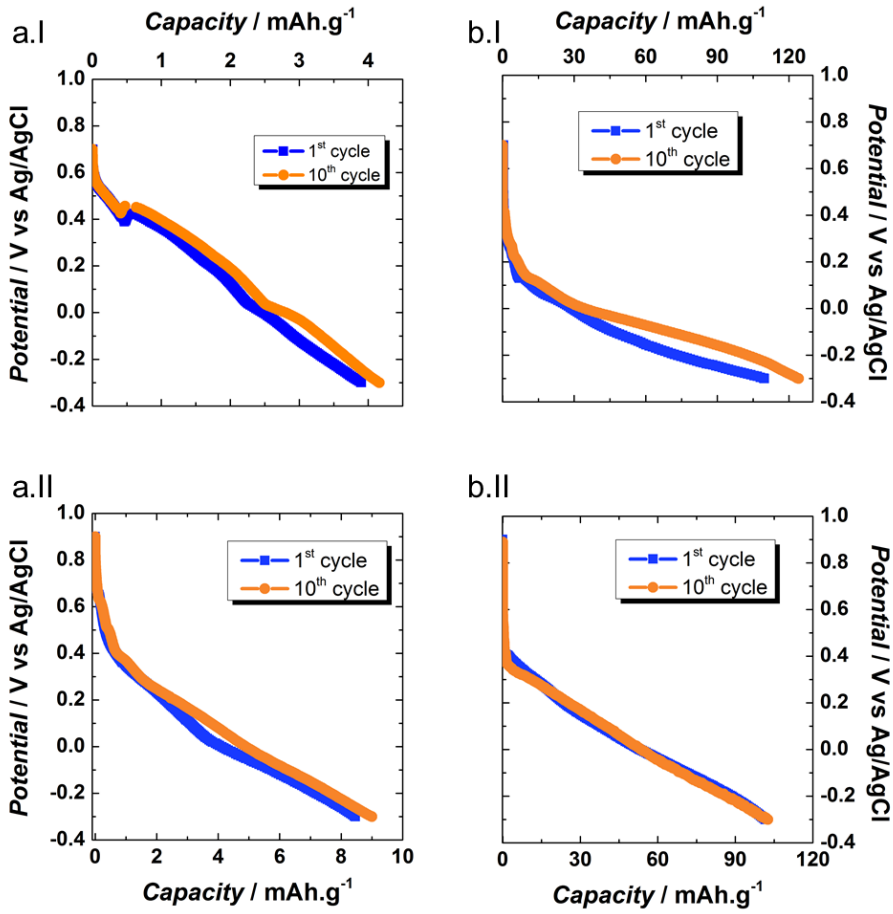

Figure 4-5. Galvanostatic discharge at 0.08 A.g^{-1} of the poly[benzoquinone-co-(p-phenylenediamine)] synthesized in DMF (a) and in EtOH (b). Inclusion of the C65 after polymerization (I) and before polymerization (II).

conductive fillers, the change of slope occurs at 0.4 V, the capacity achieved during the first cycle is equal to 151 mAh.g^{-1} and 64 % of it is maintained after 10 cycles. Even though the capacity retention with C65 is better than with MWCNT, herein we will continue the studies with the latter as the capacity achieved is higher and the retention might be improved by engineering of the electrode. This optimization will be studied in Section 4.4.2.2.

The structure and thermal properties of the bipolymer containing MWCNTs are studied by XRD and TGA. Figure 4-7 (a) shows the XRD of the MWCNT, the BQpPhdA and the composite BQpPhdA-MWCNT. As explained in the previous section, MWCNTs show an intense peak at 2θ = 25.8 ° corresponding to the (002)

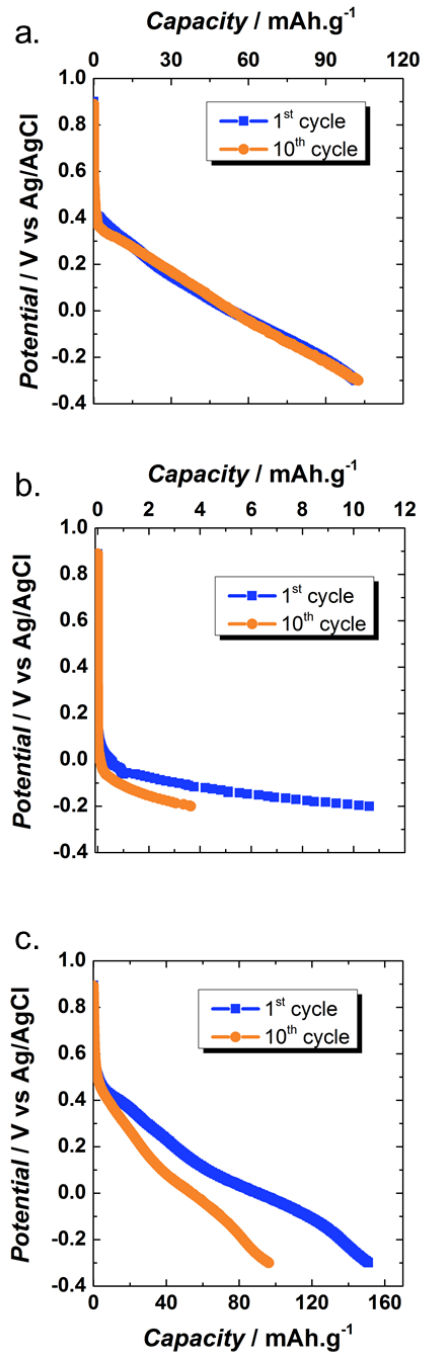

Figure 4-6. Electrochemical comparison at 0.08 A.g^{-1} of the poly[benzoquinone-co-(p-phenylenediamine)] synthesized in EtOH *in situ* with C65 (a) rGO (b) and MWCNT (c).

diffraction. Yet, the aromatic polymer still contain crystalline domains due to the π - π stacking between the chains after *in situ* polymerization.[12]

The experimental composition of the composite is found by TGA. Figure 4-7 (b) shows the TGA of the MWCNTs, BQpPhdA and their composite. The MWCNTs start losing mass at a temperature of 542 °C and have an oxidation temperature in air at 621 °C. The BQpPhdA losses 10 % of its mass below 200 ºC, due to loss of moisture. Then, the bipolymer undergoes thermal degradation at 310 °C with a total mass loss of 93 %. The absorbance of water seems less drastic in the BQpPhdA-CNT as only 1 % of mass is loss below 200 °C. The thermal degradation of the composite starts at 310 °C with a mass loss of 32 %. At 900 °C, the residual mass is 15 %. As 32 % of the composite is active material, the actual capacity delivered by the active material is calculated and shown in Figure 4-7 (c). The capacity delivered by BQpPhdA-MWCNT is 472 $mAh.g^{-1}$ in its first cycle, 95 % of the theoretical. The stability of the capacity as mentioned before will be improved by optimizing the design of the electrode in Section 4.4.2.2.

The changes in the BQpPhdA by cycling were studied by XRD, Raman and FTIR. The potentials at which these studies were performed are 0.9 V and at -0.2 V vs Ag/AgCl. The proportion of BQpPhdA: MWCNTs is diminished to 95:5 in order to follow these changes easily. Figure 4-8 (a) shows the XRD spectra of the composite at different potentials. Before cycling, the aromatic composite presents a semi-crystalline structure, caused by the presence of MWCNTs. After charge and discharge, the broad features of the amorphous regions overshadow the crystalline peaks, still, some microcrystallinity is observed.

The Raman spectra of BQpPhdA-MWCNT (Figure 4-8 (b)) shows several peaks that correspond to the p-phenylenediamine structure. Badawi *et al.*[21] have reported these peaks might be: 1598 cm^{-1} (ring deformation), 1489 cm^{-1} (ring stretch deformation), 1470 cm^{-1} (ring stretch deformation and p-CH in plane bending), 1320 cm^{-1} (ring-N stretch and ring breathing), and 1168 cm^{-1} (p-CH in plane bending). As the redox processes of the BQpPhda involve the active moieties of the p-phenylenediamine, changes in the spectra are expected; however, the reaction is difficult to follow because of the vicinity of all the bands.

Figure 4-8 (c) shows the FTIR spectrum of the BQpPhdA. BQpPhdA shows peaks at 3219 cm^{-1} (Phenol O-H stretch), 1629, 1562, 1514, 1481 cm^{-1} (aromatic C=C bending), 1350, 1275, 1206 cm^{-1} (Aromatic C-N) and 827 cm^{-1} (aromatic C-H bending). This bipolymer features changes in its structure with cycling as can be highlighted in light blue in the FTIR spectrum. The first feature to notice is the lack of appearance of the aromatic C=O at 1690 cm^{-1}, indicating that the mechanism is

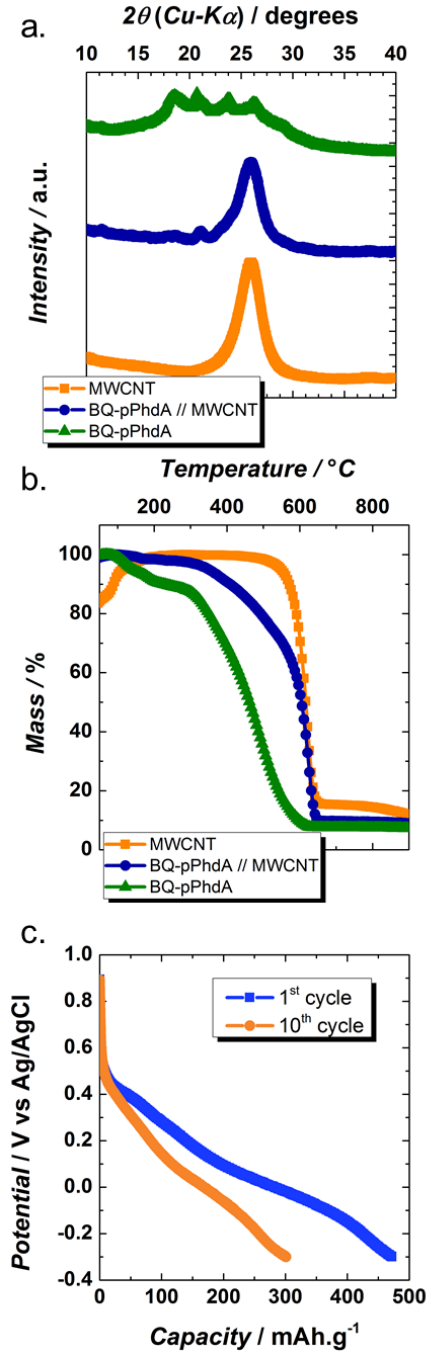

Figure 4-7. XRD (a) and TGA (b) of the BQpPhdA, MWCNT and their composite. Galvanostatic discharge at 0.08 A.g^{-1} of the BQpPhdA-MWCNT per active material (c).

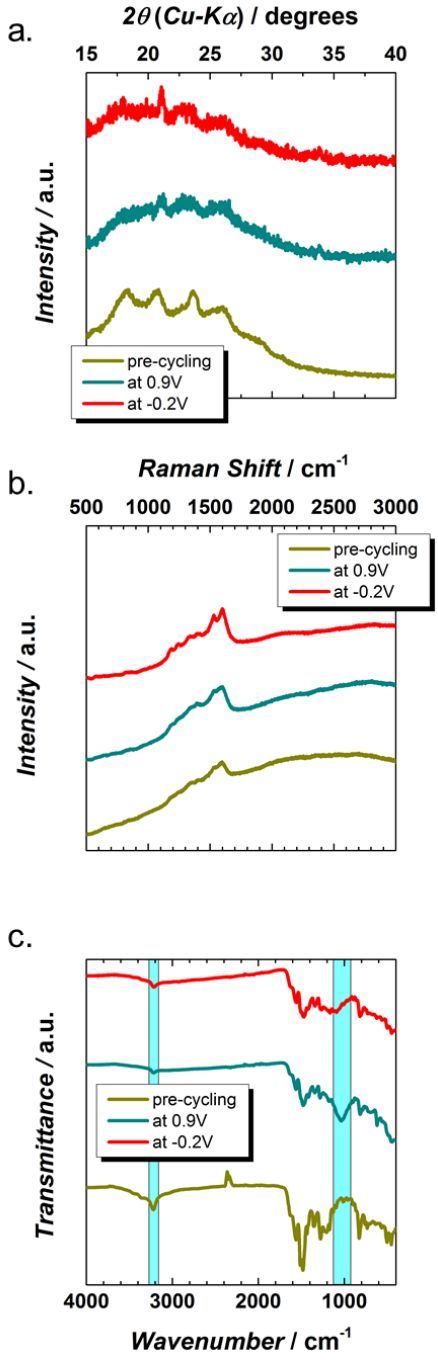

Figure 4-8. XRD (a), Raman (b) and FTIR (c) plots of the BQpPhdA-MWCNT before cycling (mustard line), and after charge (green line) and discharge (red line).

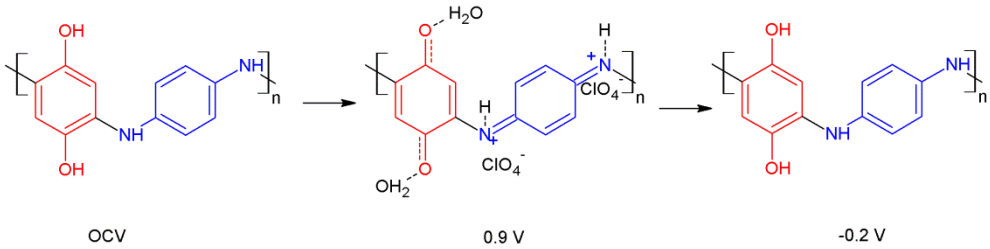

Reaction 4-4. Electrochemical process during cycling of poly[benzoquinone-co-(p-phenylenediamine)], proposed in this work.

different from Reaction 4.2. Then, the peak at 3219 cm^{-1} is decreased but does not disappear indicating the presence of the Phenol O-H bond during cycling. The most significant change is the appearance of a broad peak at 1033 cm^{-1} at 0.9 V. This peak is caused by the asymmetric stretching band of ClO_4^-.[22] The presence of this anion suggests a possible mechanism that is depicted in Reaction 4-4.

Because of the aromatic ring connected to the nitrogen, BqpPhdA is more likely to have a second redox process than BQhMdA as the p-orbitals of the system will be connected and the electrons will be delocalized. The structure of the BQpPhdA does not allow forming intramolecular hydrogen bonds because of steric interference. Still, the hydrogen bonds are formed with the water in the electrolyte and a doped state in perchloric acid, similar to the one presented by polyaniline is found.[23] The presence of a benzoquinone in between the p-phenylenediamine molecules would stop the dissociation of the bipolaron.[24] The doping of polyaniline with perchlorate is beneficial for its conductivity,[23] so it will be interesting to see if with a better electrode design, the capacity achieved will be higher than expected.

4.3.2 Benzoquinone-PEO-Diamine Terpolymers

4.3.2.1 Poly[benzoquinone-co-hexamethylenediamine-co-PEO]

In order to develop processable electrodes, benzoquinone and hexamethylenediamine are copolymerized with PEO derivatives. The polymers formed are depicted in Scheme 4-3. Table 4-3 relates the PEO linkers with the terpolymers shown in Scheme 4-3 as well as their theoretical capacity.

Each structural unit of the terpolymer comprises two benzoquinone molecules that will have a redox process. Hence, the theoretical capacity of the terpolymers should be higher than the one calculated by the poly[benzoquinone-co-hexamethylenediamine] (239 $mAh.g^{-1}$). However, as more weight is being added to the electrode material a decrease is observed.

Scheme 4-3. Polymerization of Poly[benzoquinone-co-hexamethylenediamine-co-PEO].

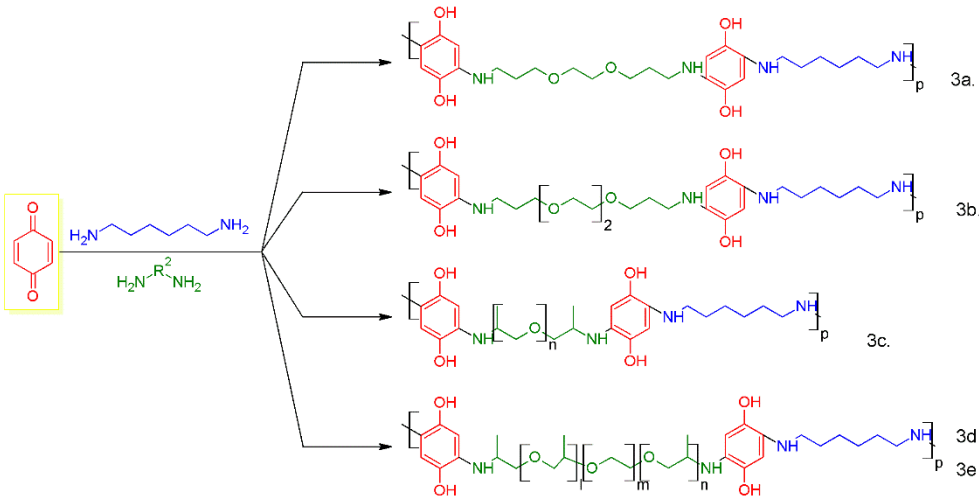

To develop processable electrodes, these materials should be soluble in a solvent whit low evaporation temperature so it can be easily eliminated after casting. In addition, the terpolymers cannot be soluble in perchloric acid as this is the electrolyte in which they are going to be electrochemically tested. The results of these tests are summarized in Table 4-4.

Most of the terpolymers are insoluble or partially soluble in the solvents tested. Only poly[benzoquinone-co-hexamethylenediamine-co-poly(propylene glycol) bis(2-aminopropyl ether)] (herein referred as BQhMdA400) is soluble in NMP while still being insoluble in perchloric acid.

Table 4-3. Poly[benzoquinone-co-hexamethylenediamine-co-PEO] theoretical capacity related to the PEO linker.

Entry	Remarks	PEO Acronym	Terpolymer Theoretical Capacity $mAh.g^{-1}$
3a	--	Dioxa	211
3b	--	Trioxa	194
3c	n ≈ 6.1	D-400	146
3d	m ≈ 9; (l+n) ≈ 3.6	ED-600	115
3e	m ≈ 12.5; (l+n) ≈ 6	ED-900	87

Table 4-4. Solubility tests of the Poly[benzoquinone-co-hexamethylenediamine-co-PEO].

Solvent	3a	3b	3c	3d	3e
Water	No	No	No	No	No
$HClO_4$	No	No	No	No	No
NMP	Partially	Partially	Yes	No	No
CH_2Cl_2	Partially	Partially	Partially	No	No
THF	Partially	Partially	Partially	No	No
CH_3Cl	Partially	Partially	Partially	No	No
Dioxane	Partially	Partially	Partially	No	No
DMSO	Partially	Partially	Partially	No	No
ACN	Partially	Partially	Partially	No	No
Ethyl Acetate	Partially	Partially	Partially	No	No
Diethyl Ether	Partially	Partially	Partially	No	No
Isopropanol	Partially	Partially	Partially	No	No

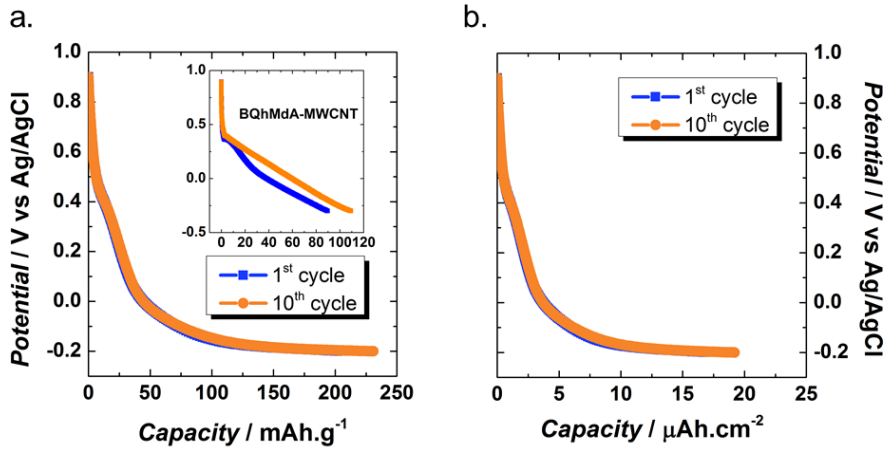

Figure 4-9. Galvanostatic discharge at 0.08 $A.g^{-1}$ of the BQhMdA400 synthesized *in situ* with MWCNT. Gravimetric (a) and areal (b) capacity. Inset in (a) corresponding to the galvanostatic discharge of BQhMdA-MWCNT.

Figure 4-9 shows the galvanostatic discharge of the BQpPhdA400 at 0.08 $A.g^{-1}$. When comparing the discharge of BQpPhdA (Inset in Figure 4-9 (a)) and BQpPhdA400 (Figure 4-9 (a)), a decrease in the initial resistance drop is observed. Moreover, the capacity value is doubled in the terpolymer (230 $mAh.g^{-1}$ at 0.08 $A.g^{-1}$ for BQpPhdA400), even though the mass of the polymer has increased because of the PEO linker. This is caused by the development of a film electrode instead of a pellet. Another advantage of engineering the electrodes is that areal capacities can be calculated. BQpPhdA400 achieves 20 $\mu Ah.cm^{-2}$ (Figure 4-9 (b)), a value comparable with the one exhibited by activated carbons in double-layer capacitors.[25]

4.3.2.2 Poly[benzoquinone-co-(p-phenylenediamine)-co-PEO]

The processability of the Poly[benzoquinone-co-(p-phenylenediamine)] is improved by co-polymerization with PEO linkers, following Scheme 4-4.

As with the previous terpolymer, the increase of mass in the structure decreases the capacity (Table 4-5) when comparing to the poly[benzoquinone-co-(p-phenylenediamine)] (496 $mAh.g^{-1}$).

In order to choose an adequate solvent for the preparation of the electrode, solubility tests of the Poly[benzoquinone-co-(p-phenylenediamine)-co-PEO] in different solvents are performed. The results of these tests are shown in Table 4-6.

Scheme 4-4. Polymerization of Poly[benzoquinone-co-(p-phenylenediamine)-co-PEO]

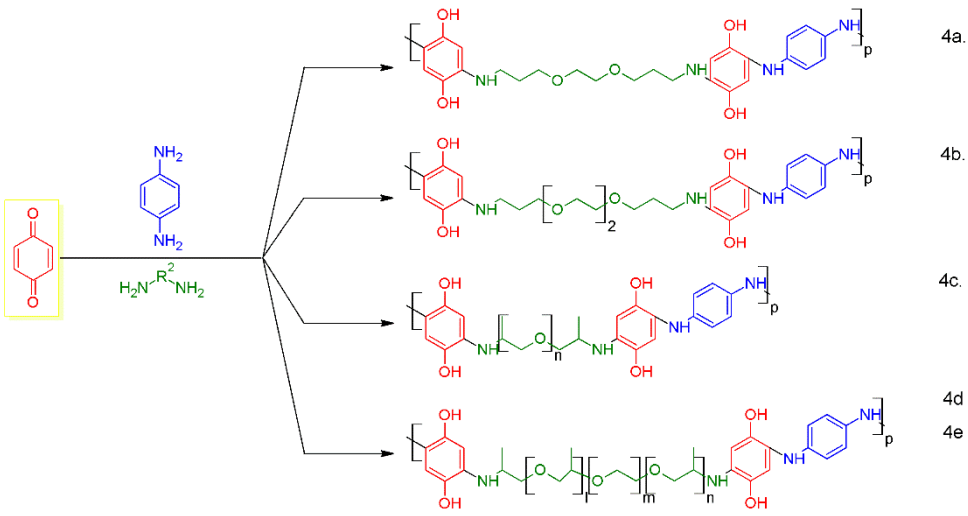

Table 4-5. Poly[benzoquinone-co-(p-phenylenediamine)-co-PEO] theoretical capacity related to the PEO linker.

Entry	Remarks	PEO Acronym	Terpolymer Theoretical Capacity $mAh.g^{-1}$
4a	--	Dioxa	321
4b	--	Trioxa	295
4c	n ≈ 6.1	D-400	222
4d	m ≈ 9; (l+n) ≈ 3.6	ED-600	174
4e	m ≈ 12.5; (l+n) ≈ 6	ED-900	131

The only material that is completely soluble in NMP is the Poly[benzoquinone-co-(p-phenylenediamine)-co-(O,O′-Bis(2-aminopropyl) polypropylene glycol-block-polyethylene glycol-block-polypropylene glycol 800)] (herein referred as BQpPhdA900). Therefore, the electrochemical tests are performed in BQpPhdA900 electrodes drop-casted from a NMP slurry.

Table 4-6. Solubility tests of the Poly[benzoquinone-co-(p-phenylenediamine)-co-PEO].

Solvent	4a	4b	4c	4d	4e
Water	No	No	No	No	No
$HClO_4$	No	No	No	No	No
NMP	Partially	Partially	Partially	No	Yes
CH_2Cl_2	Partially	Partially	Partially	No	Partially
THF	Partially	Partially	Partially	No	Partially
CH_3Cl	Partially	Partially	Partially	No	Partially
Dioxane	Partially	Partially	Partially	No	Partially
DMSO	Partially	Partially	Partially	No	Partially
ACN	Partially	Partially	Partially	No	Partially
Ethyl Acetate	Partially	Partially	Partially	No	Partially
Diethyl Ether	Partially	Partially	Partially	No	Partially
Isopropanol	Partially	Partially	Partially	No	Partially

To see if the rate capability of the material is improved by the inclusion of the PEO linker, the electrochemical properties of the BQpPhdA900 are studied. As mentioned on Section 4.4.1.2, the polymers are synthesized *in situ* with the conductive filler and in EtOH. MWCNTs or rGO are used as conductive fillers, the former because of the superior properties shown in section 4.4.1.2. While the latter to study if the behaviour previously observed is affected by the PEO linker.

Figure 4-10 (a.I) shows the galvanostatic discharges at 0.08 $A.g^{-1}$ of the BQpPhdA900 *in situ* with MWCNT. When comparing the bipolymer (Figure 4-6 (c) and Inset in Figure 4-10 (a.I)) with the terpolymer (Figure 4-10 (a.I)) a decrease in

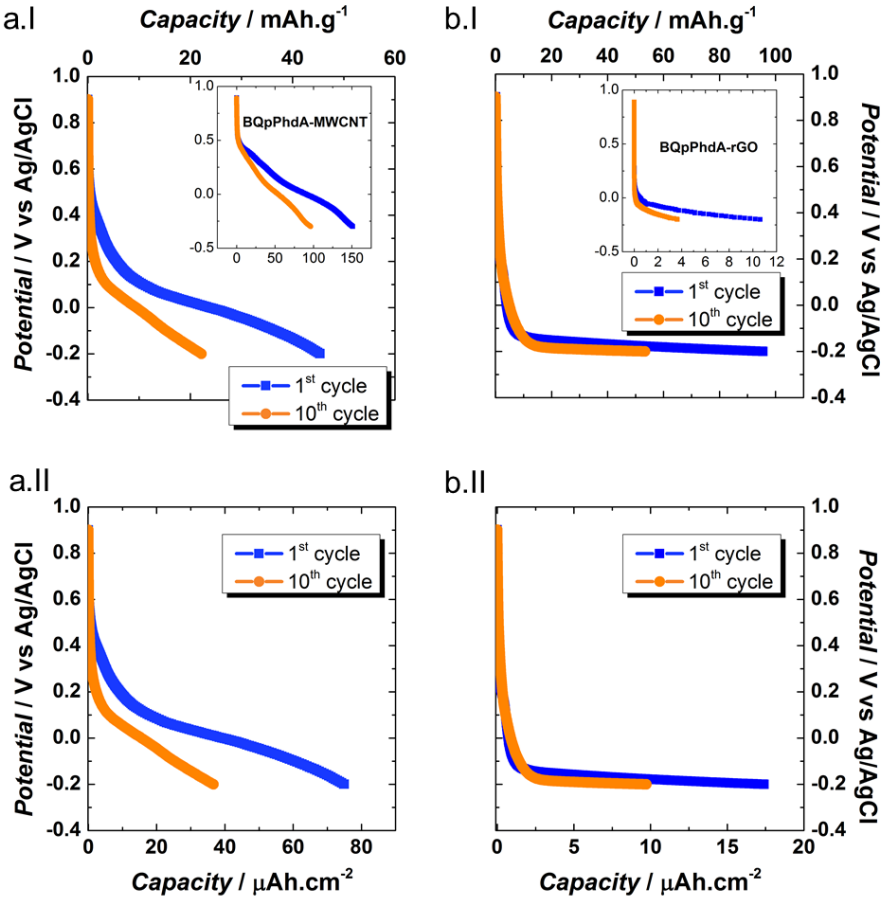

Figure 4-10. Galvanostatic discharge at 0.08 $A.g^{-1}$ of the BQpPhdA900 synthesized *in situ* with MWCNT (a) and rGO (b). Gravimetric (I) and areal (II) capacity. Insets in a.I and b.I corresponding to the galvanostatic discharge of BQpPhdA-MWCNT and BQpPhdA-rGO, respectively.

the capacity values can be observed. While BQpPhdA-MWCNT achieves 151 – 96 $mAh.g^{-1}$, BQpPhdA900-MWCNT only exhibits 45 – 22 $mAh.g^{-1}$.

The electrochemical plateau of BQpPhdA900-rGO is observed below 0 V (Figure 4-10 (b)), following the same trend as BQpPhdArGO. However, an increase in the electrode capacity of one order of magnitude is observed in this terpolymer when compared to the bipolymer. The shape of the discharge curve is similar to the one exhibited by materials used as catalysts in the Hydrogen Evolution Reaction (HER).[26]

BQpPhdA900-MWCNT shows areal capacitance values up to 75 $\mu Ah.cm^{-2}$ in Figure 4-10 (a.II). This value is four times higher than the one achieved by the linear terpolymer. Indicating that BQhMdA400-MWCNT can be used in applications where gravimetric capacity is required, while BQpPhdA900-MWCNT can be used for portable electronics - thin film technology.

4.4 Conclusions and Perspectives

Two bipolymers with quinone-amine functional groups were synthesized and their electrochemical properties were tested in an aqueous-based electrolyte. The poly[benzoquinone-co-(hexamethylene diamine)] presented a redox process involving 2 e^- and 2 H^+, while the poly[benzoquinone-co-(p-phenylenediamine)] one consisted of $4e^-$ and $4H^+$.

Different parameters during the synthesis steps were optimised in order to achieve the highest capacity values possible. *In situ* polymerization with multi-walled carbon nanotubes in EtOH was chosen as the optimum synthesis condition.

An intramolecular hydrogen bonding in of poly[benzoquinone-co-(hexamethylene diamine)] was confirmed by Fourier Transform Infrared during cycling. The structure of the poly[benzoquinone-co-(p-phenylenediamine)] does not allow forming intramolecular hydrogen bonds, yet hydrogen bonds were formed with the water in the electrolyte and a doped state in perchloric acid, similar to the one observed in electroactive polymers was found.

A PEO linker was introduced during the polymerization step, in order to process thin film electrodes. The mass of this PEO linker played an important role in the final achieved capacity as the terpolymer with the lowest molecular weight achieved the highest capacity values.

The excellent performance observed by poly[benzoquinone-co-

hexamethylenediamine-co-PEO] and poly[benzoquinone-co-(p-phenylenediamine)-co-PEO], makes them interesting for thin film technology and grid energy storage. On the one hand, poly[benzoquinone-co-hexamethylenediamine-co-PEO] achieved up to 230 $mAh.g^{-1}$ at 0.08 $A.g^{-1}$. On the other hand, poly[benzoquinone-co-(p-phenylenediamine)-co-PEO] shows areal capacitance values up to 75 $\mu Ah.cm^{-2}$.

These high-quality materials showed significant improvement of processability by introducing linkers during the polymerization, proving that development of these electrode materials can be scaled up for real-life applications.

4.5 References

(1) Chen, X.; Wang, H.; Yi, H.; Wang, X.; Yan, X.; Guo, Z. *J. Phys. Chem. C* **2014**, *118* (16), 8262–8270.

(2) Le Comte, A.; Chhin, D.; Gagnon, A.; Retoux, R.; Brousse, T.; Bélanger, D. *J. Mater. Chem. A* **2015**, *3* (11), 6146–6156.

(3) Liu, C.; Li, F.; Ma, L.-P.; Cheng, H.-M. *Adv. Mater.* **2010**, *22* (8), E28–E62.

(4) Hulicova, D.; Kodama, M.; Hatori, H. *Chem. Mater.* **2006**, *18* (9), 2318–2326.

(5) Hulicova, D.; Junya Yamashita; Yasushi Soneda; Hatori, H.; Kodama, M. *Chem. Mater.* **2005**, *17* (5), 1241–1247.

(6) Lota, G.; Lota, K.; Frackowiak, E. *Electrochem. commun.* **2007**, *9* (7), 1828–1832.

(7) Ania, C. O.; Khomenko, V.; Raymundo-Piñero, E.; Parra, J. B.; Béguin, F. *Adv. Funct. Mater.* **2007**, *17* (11), 1828–1836.

(8) Li, W.; Chen, D.; Li, Z.; Shi, Y.; Wan, Y.; Huang, J.; Yang, J.; Zhao, D.; Jiang, Z. *Electrochem. commun.* **2007**, *9* (4), 569–573.

(9) Marcano, D. C.; Kosynkin, D. V.; Berlin, J. M.; Sinitskii, A.; Sun, Z.; Slesarev, A.; Alemany, L. B.; Lu, W.; Tour, J. M. *ACS Nano* **2010**, *4* (8), 4806–4814.

(10) Wang, M.; Duan, X.; Xu, Y.; Duan, X. *ACS Nano* **2016**, *10* (8), 7231–7247.

(11) Zhang, H.-B.; Lin, G.-D.; Zhou, Z.-H.; Dong, X.; Chen, T. *Carbon N. Y.* **2002**, *40* (13), 2429–2436.

(12) Klug, H. P. (Harold P.; Alexander, L. E. (Leroy E. *X-ray diffraction procedures for polycrystalline and amorphous materials*, 2nd ed.; John Wiley & Sons, 1974.

(13) Lee, T. H.; Boey, F. Y. C.; Khor, K. A. *Polym. Compos.* **1995**, *16* (6), 481–488.

(14) Lehman, J. H.; Terrones, M.; Mansfield, E.; Hurst, K. E.; Meunier, V. *Carbon N. Y.* **2011**, *49*, 2581–2602.

(15) Casiraghi, C.; Hartschuh, A.; Qian, H.; Pliscanec, S.; Georgia, C.; Fasoli, A.; Novoselov, K. S.; Basko, D. M.; Ferrari, A. C. *Nano Lett.* **2009**, *9* (4), 1433–1441.

(16) Stammreich, H.; Teixeira Sans, T. *J. Chem. Phys.* **1965**, *42* (3), 920–931.

(17) Gupta, N.; Linschitz, H. *J. Am. Chem. Soc.* **1997**, *119* (27), 6384–6391.

(18) Joseph, J.; Jemmis, E. D. *J. Am. Chem. Soc.* **2007**, *129*, 4620–4632.

(19) Gilli, P.; Bertolasi, V.; Ferretti, V.; Gilli, G. *J. Am. Chem. Soc.* **2000**, *122* (42), 10405–10417.

(20) Simon, P.; Gogotsi, Y.; Dunn, B. *Science (80-.).* **2014**, *343* (6176), 1210–1211.

(21) Badawi, H. M.; Förner, W.; Ali, S. A. *Spectrochim. Acta Part A Mol. Biomol. Spectrosc.* **2013**, *112*, 388–396.

(22) Chen, Y.; Zhang, Y.-H.; Zhao, L.-J. *Phys. Chem. Chem. Phys.* **2004**, *6*, 537–542.

(23) Catedral, M. D.; Tapia, A. K. G.; Sarmago, R. V; Tamayo, J. P.; Del Rosario, E. J. *Sci. Diliman* **2004**, *16* (2), 41–46.

(24) Deibel, C.; Strobel, T.; Dyakonov, V. *Phys. Rev. Lett.* **2009**, *103* (3), 36402.

(25) Marsh, H.; Rodríguez-Reinoso, F. *Activated Carbon*; Elsevier, 2006.

(26) Li, Y.; Wang, H.; Xie, L.; Liang, Y.; Hong, G.; Dai, H. *J. Am. Chem. Soc.* **2011**, *133* (19), 7296–7299.

DEVELOPMENT OF ASYMMETRIC SUPERCAPACITORS USING TITANIUM CARBIDE-REDUCED GRAPHENE OXIDE COUPLES AS ELECTRODES

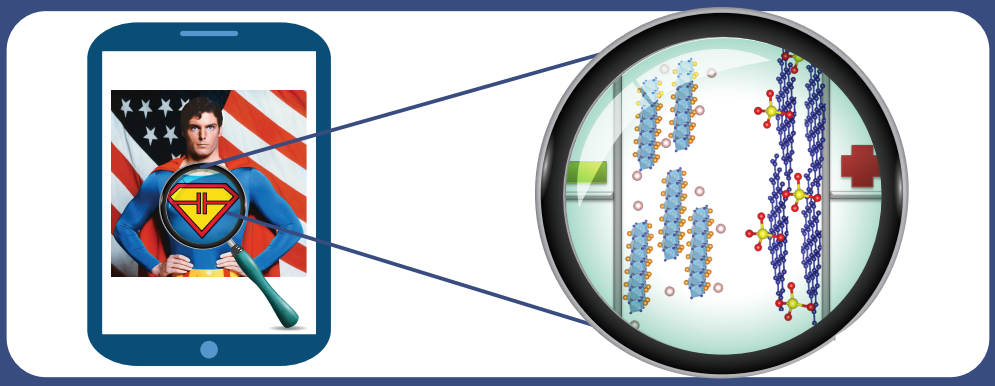

5 DEVELOPMENT OF ASYMMETRIC SUPERCAPACITORS USING TITANIUM CARBIDE-REDUCED GRAPHENE OXIDE COUPLES AS ELECTRODES

5.1 Introduction

In this thesis, we have been focused on the development of electrode materials for supercapacitor devices showing a rapid electrochemical charge/discharge and long cycle life. However, the incorporation of supercapacitors in high energy density applications demands improvement on the density of the electrode materials.[1] Moreover, developing miniaturized supercapacitors for applications such as microchip technology, wearable electronics, etc., demands high volumetric capacitances for light, small and flexible devices.[2]

Two-dimensional (2D) materials are inherently flexible, have a high surface

reactivity, high electrical conductivity, and large surface area, which are fundamental characteristics for energy storage devices.[3] The exfoliation of graphite into single layers of graphene and the discovery of their astonishing properties, in 2004, resulted in a new field of interest based on two-dimensional materials.[4] The latest addition to the single layered materials is MXene, a two-dimensional transition metal carbide family discovered in 2011.[5]

MXenes are produced by the etching out of the A layers from *"MAX"* phases. The latter are so-called because of their composition, $M_{n+1}AX_n$, where M is an early transition metal (*e.g.* Ti, Nb), A is an element of group 13 or 14 (*e.g.* Al, Si), X can be Carbon or Nitrogen, and n might be equal to 1, 2 or 3. The strong $M-X$ bond has a mixed covalent/metallic/ionic character, whereas the $M-A$ bond is metallic.[6] Taking advantage of the differences in character and relative strengths of the $M-A$ compared with the $M-X$ bonds, the A layers can be selectively etched by chemical routes without disrupting the $M-X$ bonds. After etching, MXene has a general formula of $M_{n+1}X_n$.

MXenes have shown a great potential as electrode materials in supercapacitors.[7–15] Pristine d-Ti_3C_2, the most studied MXene, has achieved capacitance values up to 238 F.g^{-1}, and 900 F.cm^{-3} in 1 M H_2SO_4.[8,15] The main drawback of d-Ti_3C_2 is that its potential window in aqueous electrolytes is narrow (-0.2 to 0.35 V vs Ag/AgCl). This translates in lower energy and power densities when compared to other carbon materials.[16]

Herein, we will develop a full cell using d-Ti_3C_2 and rGO as negative and positive electrode, respectively, in aqueous and organic electrolytes. The goals of the preparation and study of an asymmetric capacitor delineated within this chapter are the following:

i) By using an asymmetric device, the electrochemical window of the d-Ti_3C_2 will be enlarged and higher energy and power densities than those exhibited by pure d-Ti_3C_2 will be achieved.
ii) rGO and d-Ti_3C_2 are both conductive materials with high surface area and ion intercalation capability. Because of these properties, high gravimetric and volumetric capacitance, and a long cycle life are expected from the asymmetric device.
iii) Preparation of the electrode materials as a thin film, will open the path for flexible energy storage devices.

5.2 Methodology

5.2.1 Materials Synthesis

5.2.1.1 2D Titanium Carbide MXene

The synthesis method is described elsewhere.[8] Briefly, to synthesize Ti_3C_2, 20 mL of 9 M hydrochloric acid (HCl, Fisher Scientific) are added to 7.5 molar equivalents (2 g) of lithium fluoride (LiF, Alfa Aesar). The mixture is stirred until the salt is dissolved. Then, two grams of the ternary Titanium Aluminium Carbide in powder (Ti_3AlC_2, < 38 µm particle size) are slowly added to this solution. The reaction mixture is held at 35 °C for 24 h while stirring at 200 rpm. After 24 h, the mixture is washed by adding deionized water, separated by centrifugation at 3500 rpm for two minutes and the supernatant is collected. The washing process is repeated until pH above 5 is achieved. In order to increase the surface area, the Ti_3C_2 solution is delaminated (d-Ti_3C_2) by bath sonication for one hour under argon flow. Then, we centrifuge for another hour at 3500 rpm. Finally, the supernatant containing the d-Ti_3C_2 is collected. In order to prepare a d-Ti_3C_2 film, the d-Ti_3C_2 is filtered using a polypropylene membrane (3501 Coated PP, Celgard LLC) and dried under vacuum.

To increase the interlayer distance of the d-Ti_3C_2 for organic-based supercapacitors, a d-Ti_3C_2/Multi-walled Carbon Nanotube (MWCNT) composite is prepared as described elsewhere.[17] First, an aqueous 1 mg.ml^{-1} d-Ti_3C_2 suspension is prepared as well as an aqueous solution of 0.1 mg.ml^{-1} MWCNT in 8 mg.ml^{-1} aqueous solution of sodium dodecyl sulphate (SDS, Sigma Aldrich). Sandwich-like MXene/MWCNT films are prepared using an alternating filtration method. Specifically, 1 ml of the d-Ti_3C_2 dispersion is filtered through a polypropylene membrane to yield a thin d-Ti_3C_2 layer. Then, 1 mL of the MWCNT-SDS dispersion is filtered on top of the d-Ti_3C_2 layer. This alternate filtration is repeated several times to yield composite films composed of 5 and 4 alternating d-Ti_3C_2 and MWCNTs layers, respectively. Afterwards, the film is washed with 200 millilitres of deionized water. The composite film is vacuum dried under argon flow.

5.2.1.2 Reduced Graphene Oxide Synthesis

The Graphite Oxide is prepared following the Marcano-Tour method,[18] as it was explained in Section 3.2.1.2, using $KMnO_4$, H_2SO_4, and H_3PO_4. The Graphite Oxide (GrO) is then sonicated in water for 1 hour and the exfoliated Graphene Oxide (GO) is collected. Then, two different reduction methods are used. The first one, is a

chemical method that yields rGO with carboxylic acid groups.[19] These groups can be beneficial for pseudocapacitance in aqueous electrolytes.[20] In the second method, the rGO is reduced thermally, eliminating the oxygen functional groups.[21] These groups are known for being detrimental to capacitance in organic-based supercapacitors.[22]

5.2.1.2.1 Hydrazine Method

Graphene Oxide (GO) was reduced following the Li-Wallace method. [23] Briefly, 30 ml of GO in water (7 $mg.ml^{-1}$) are heated at 85 °C, then 2 ml of hydrazine hydrate (98 %, TCI America) and 1 ml of ammonium hydroxide (Fischer Scientific) are added to the GO. The reaction is kept under reflux during one hour, after which the solution is left to cool down, centrifuged for half an hour and the reduced Graphene-Oxide (rGO_H) is re-dispersed in ethanol (Decon Labs, Inc). In this case, hydrazine monohydrate acts as reducing agent and ammonium hydroxide is used to promote the colloidal stability of the Graphene Oxide sheets through electrostatic repulsion.[24] In order to prepare a film, the rGO_H is filtered using a polypropylene membrane (3501 Coated PP, Celgard LLC) and dried under vacuum.

5.2.1.2.2 Thermal Method

The GO solution is freeze dried producing a GO aerogel. Then, 200 mg of the freeze dried-GO is heated under argon flow at a heating rate of 10 $°C.min^{-1}$ up to 900 °C and kept for 2 h. After cooling down, the reduced Graphene-Oxide (rGO_T) is re-dispersed in ethanol. The, the rGO_T is filtered using a polypropylene membrane (3501 Coated PP, Celgard LLC) and dried under vacuum.

5.2.2 Characterization Methods

The characterization of the d-Ti_3C_2, d-Ti_3C_2-MWCNT, and rGO films morphologies is carried out using Scanning Electron Microscopy (SEM, Zeiss Supra 50VP, Germany).

The vibration frequencies of the materials are studied by Raman Spectroscopy. The Raman spectra are recorded on Renishaw inVia spectrometer with a 632 nm laser as an excitation source (5 % laser power).

The interlayer distance of the d-Ti_3C_2, d-Ti_3C_2-MWCNT, and rGO films is calculated from the X-Ray Diffractions. XRD is carried out on a Rigaku Smart Lab (Japan) diffractometer using Cu-Kα radiation (40 kV and 44 mA) and step scan 0.02 °, the

2θ range is 5 – 50 ° and step time of 0.5 s.

5.2.3 Electrochemical Testing

To quantify the amount of charge stored by these materials, all tested films are cut with the same thickness and weight and assembled in Swagelok type cells. The materials are evaluated in a 3-electrode configuration to evaluate their capacitance and electrochemical window. Then, symmetric and asymmetric devices are assembled. The cells are electrochemically studied by using a 1 M sulfuric acid (H_2SO_4, Sigma Aldrich) solution with Ag/AgCl as reference or pseudo-reference electrode. For organic electrolyte, 1 M tetraethyl ammonium tetrafluoroborate ($Et_4N^+BF_4^-$, Sigma Aldrich) in acetonitrile (ACN, Fischer) is used as electrolyte and Ag wire as reference or pseudo-reference electrode. For those tests carried out by using a 3-electrode cell, activated carbon (YP-50, Kuraray) is used as counter electrode. Electrochemical cyclic voltammetry (CV) measurements at different scan rates ranging from 2 to 100 $mV.s^{-1}$, as well as impedance measurements are performed at ambient conditions in a multichannel potentiostat/galvanostat (Biologic VMP3, France). The cycling performance of the asymmetric devices is tested at 20 $mV.s^{-1}$ over 1000 cycles in 1 M H_2SO_4 and 1 M Et_4NBF_4/ACN from 0 V to 1.1 V and from 0 V to 2 V, respectively. Before and after the cycling testing, electrochemical impedance spectroscopy is measured within the ac frequency region from 10 mHz to 200 kHz at different fixed ΔV with ac voltage amplitude of 10 mV.

5.3 Results and Discussion

5.3.1 Materials for Aqueous-Based Supercapacitors

5.3.1.1 2D Titanium Carbide MXene

Scheme 5-1 shows the approach to the synthesis of d-Ti_3C_2 from Ti_3AlC_2. After dissociation of HCl and LiF, H^+ and F^- ions weaken the Ti-Al bonds. Consequent opening of interlayer gap allows further insertion that leads to the formation of AlF_3 and H_2. The 2D Ti_3C_2 layers possess two exposed Ti atoms per unit formula that have as ligands hydroxyl and fluorine (not shown in Scheme 5-1), which are present in the reaction media.[25] The synthetic process is summarized by Reaction 5-1.

In order to confirm the synthesis of d-Ti_3C_2 and to study its structure, a d-Ti_3C_2 film is studied by Scanning Electron Microscopy, Raman, and X-Ray Diffraction.

Scheme 5-1. Illustration of the Ti_3C_2 MXene formation process.

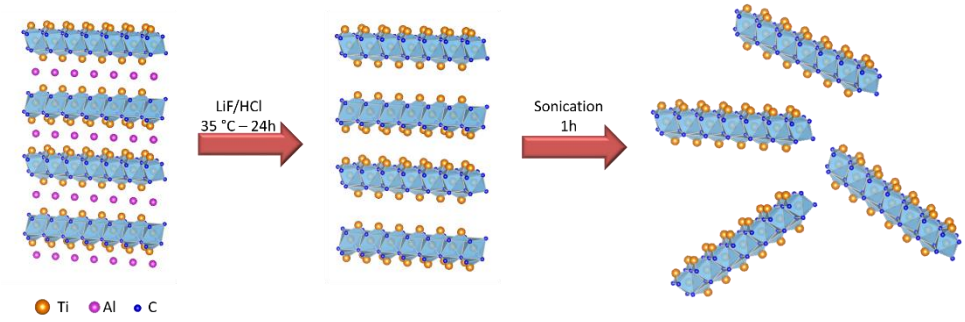

$$2Ti_3AlC_2 + 6HCl + 6LiF \rightarrow 2Ti_3C_2 + 3H_2 + 2AlF_3 + 6LiCl$$

Reaction 5-1. Formation of MXene from MAX phase.

5.3.1.1.1 2D Titanium Carbide MXene Characterization

Figure 5-1 shows the cross-sectional Scanning Electron Microscopy (SEM) image of a binder-free d-Ti_3C_2 film. This image proves that the entire film is composed of well-aligned stacked Ti_3C_2 MXene sheets. This layered morphology resembles expanded graphite, as the nanolayers are clearly separated from each other. This shearing of the 2-dimensional particles allows the material to be a flexible standing film.

Figure 5-2 (a) shows the Raman spectrum of the d-Ti_3C_2 film. All the vibration bands are consistent with the reported ones.[26] The four broad Raman peaks centred around 199.5, 369, 628.5 and 716.3 cm^{-1} are attributed to the vibrations from non-stoichiometric titanium carbide.[27]

The XRD pattern of the d-Ti_3C_2 (Figure 5-2 (b)) shows a sharp, intense peak (002) and higher-order (00*l*) peaks ascribed to restacking of Ti_3C_2 flakes. Pristine MXene has been reported to have a hexagonal structure with a = b = 3.0505(5) Å. The (002)

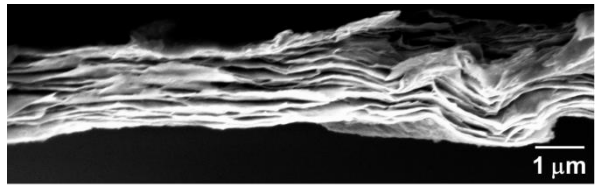

Figure 5-1. Cross-sectional SEM image of d-Ti_3C_2 film.

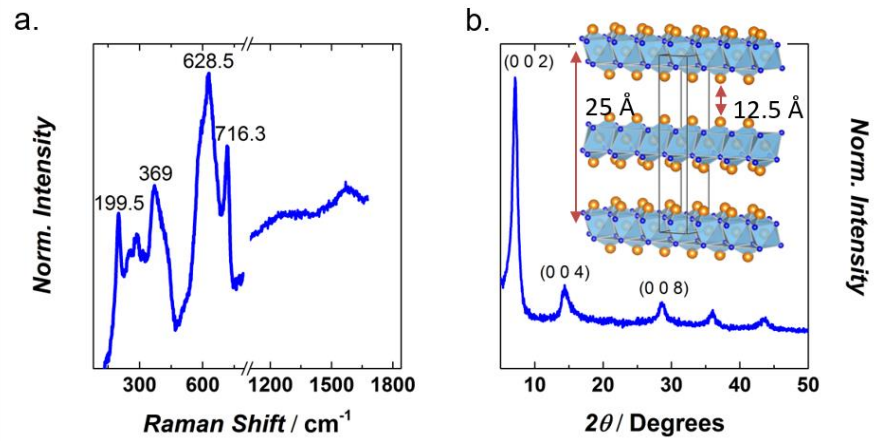

Figure 5-2. Raman (a), XRD (b) of the d-Ti_3C_2. Numbers in the Raman spectrum denote the vibration frequency while in the XRD pattern indicates the miller indices related to the diffraction peaks. Inset in (b) shows the crystallographic structure of the d-Ti_3C_2.

peak around 7.1 ° corresponds to a *c*-lattice parameter of 25 Å and an interlayer distance of 12.5 Å (Inset in Figure 5-2 (b)). This separation is caused by the presence of water between the d-Ti_3C_2 flakes.[14] It has been shown previously that vacuum drying at above 100 °C is needed to remove the water between MXene flakes.[28]

5.3.1.1.2 2D Titanium Carbide MXene Electrochemistry

The d-Ti_3C_2 binder-free film is electrochemically characterized in a 3-electrode configuration. Figure 5-3 shows the main results of the electrochemical characterization of the film. The CV curves of d-Ti_3C_2, shown in Figure 5-3 (a) keep a rectangular shape even at a fast scan rate of 100 $mV.s^{-1}$, confirming ion diffusion in between the layers. The maximum capacitance achieved by d-Ti_3C_2 is 230 $F.g^{-1}$ at 2 $mV.s^{-1}$. The specific capacitance of the material decreases gradually with the scan rate (Figure 5-3 (b)) to 167 $F.g^{-1}$ at 100 $mV.s^{-1}$, showing acceptable capacitance retention with scan rate. Because of the high density of d-Ti_3C_2 films (4.07 $g.cm^{-3}$) an outstanding volumetric capacitance of 934 $F.cm^{-3}$ is achieved. The excellent performance of d-Ti_3C_2 as supercapacitor electrode has been ascribed to the smaller size of H^+ compared to other intercalating cations, surface redox processes, and good accessibility of interlayer spacing because of the pre-intercalated water.[14]

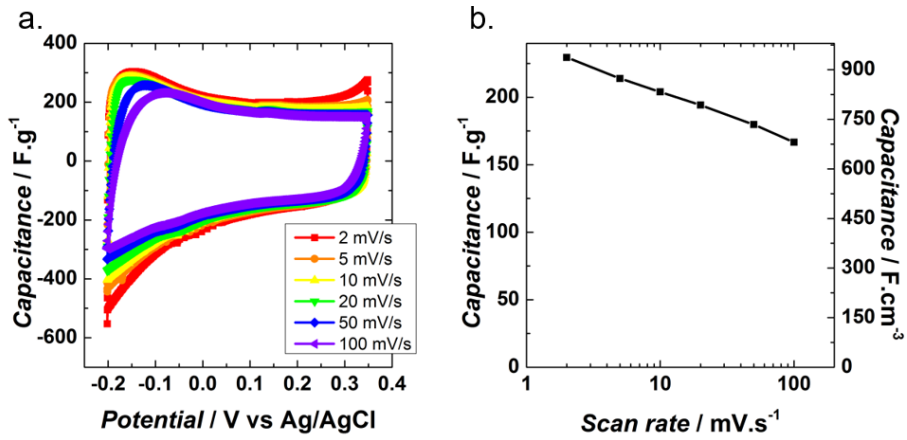

Figure 5-3. Cyclic voltammetry (a) and rate capability (b) of the d-Ti_3C_2 in 1 M H_2SO_4.

By combining two d-Ti_3C_2 electrodes, a full device might be assembled and as result, the performance of the material in a real environment can be tested. Figure 5-4 shows the results of the cyclic voltammetry tests at different scan rates for the symmetric cell. As the potential window of d-Ti_3C_2 is constricted from -0.2 to 0.35 V vs Ag/AgCl (Figure 5-3 (a)), the electrochemical window of the symmetric device is only 0.55 V (Figure 5-4 (a)). At 2 $mV.s^{-1}$, the gravimetric and volumetric values of capacitance are 216 $F.g^{-1}$ and 880 $F.cm^{-3}$, respectively. The symmetric cells exhibit 94 % of the capacitance expected from the 3-electrode measurement, showing

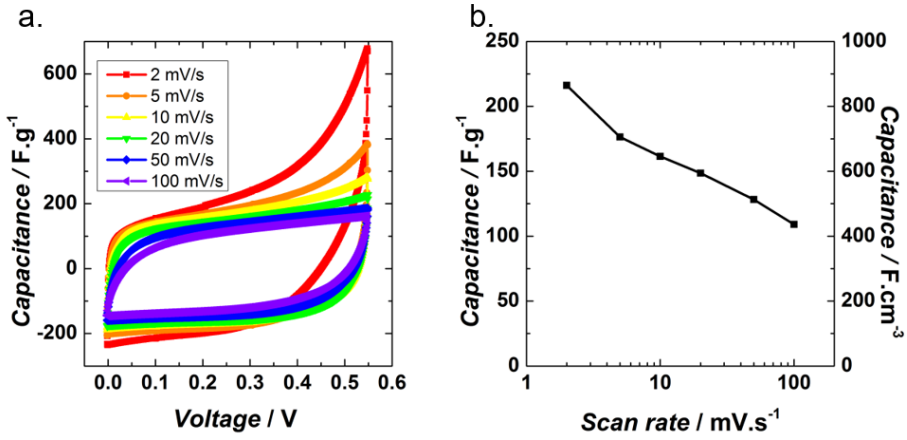

Figure 5-4. Cyclic voltammetry (a) and rate capability (b) of d-Ti_3C_2 in a symmetric configuration in 1 M H_2SO_4.

Scheme 5-2. Approach to synthesize reduced Graphene Oxide, where the blue points denote Carbon and the red ones oxygen groups.

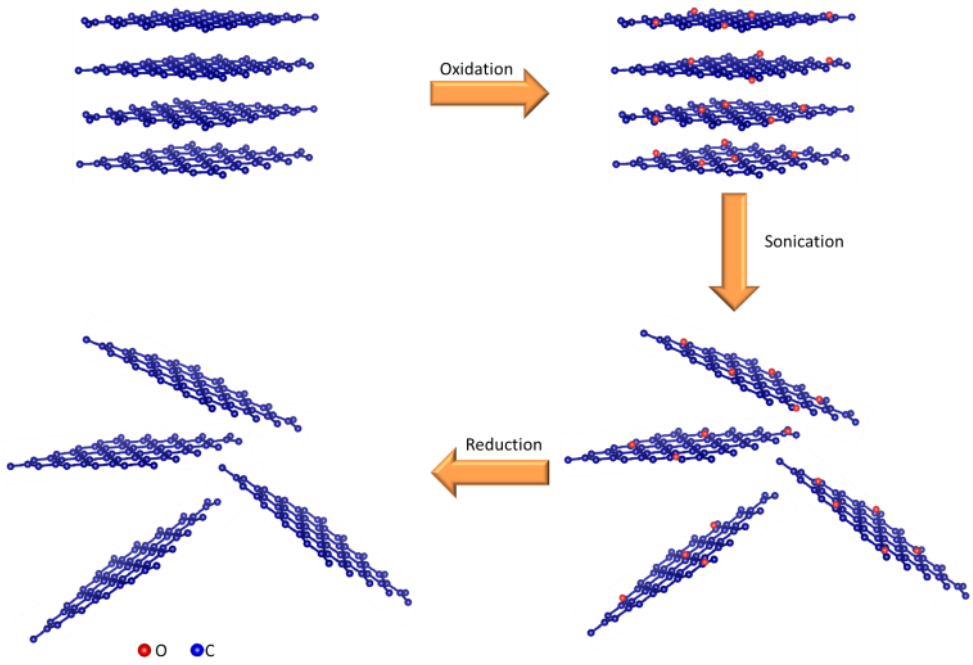

optimum electronic conductivity of the electrolyte between the electrodes. The rate capability of the material is studied in Figure 5-4 (b). The capacitance decrease is more marked in the symmetric device than in the 3-electrode configuration owing to the presence of having two capacitors in series. At 100 $mV.s^{-1}$ the gravimetric and volumetric capacitances are 110 $F.g^{-1}$ and 444 $F.cm^{-3}$, respectively.

5.3.1.2 Chemically Reduced Graphene Oxide

The synthesis of the reduced Graphene Oxide is summarized on Scheme 5-2. By comparing Scheme 5-1 and Scheme 5-2, can be observed that both materials present a 2-dimensional structure.

To confirm the 2-dimensional structure of the rGO_H film, the material is analysed by Scanning Electron Microscopy, Raman, and X-Ray Diffraction.

5.3.1.2.1 Chemically Reduced Graphene Oxide Characterization

A cross section image of the rGO_H film by SEM is shown in Figure 5-5. As with d-

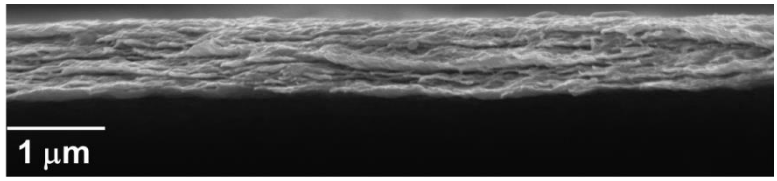

Figure 5-5. Cross section of the rGO_H film analysed by Scanning Electron Microscopy.

Ti_3C_2, the structure is layered.

Figure 5-6 shows the Raman and XRD results of the analysis of the rGO_H film. The Raman spectrum (Figure 5-6 (a)) shows the typical D and G bands explained before in this thesis. Briefly, the G band (1595 cm^{-1}) is the only band coming from a normal first order Raman scattering process in graphene, while the D band (1331 cm^{-1}) is originated from a second-order process, involving one phonon and one defect.[29] The I_D/I_G ratio is 1.4 indicating a disordered structure. [30]

Figure 5-6 (b) shows the X-Ray Diffraction of the rGO_H film. The material shows interlayer distances ranging from 2.2 to 4.4 Å.

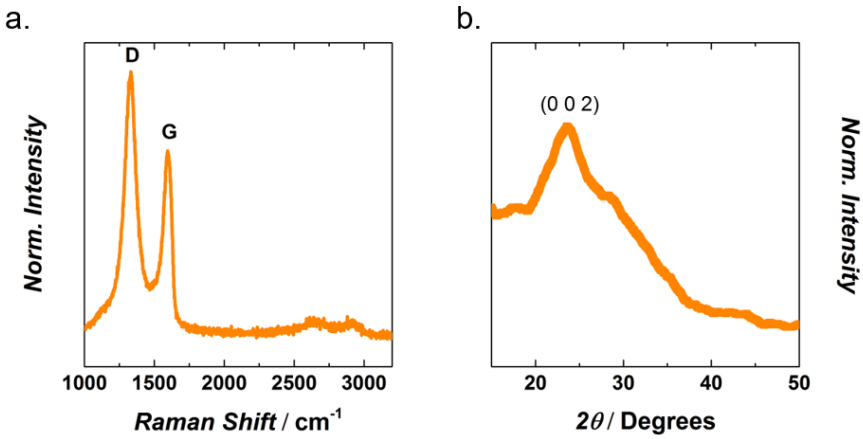

Figure 5-6. Raman (a) and XRD (b) of the rGO_H. The number in the XRD pattern indicates the miller index of the maximum peak.

5.3.1.2.2 Chemically Reduced Graphene Oxide Electrochemistry

Figure 5-7 shows the results from cycling the rGO_H binder-free film in a 3-electrode configuration at different scan rates. The cyclic voltammetry curves (Figure 5-7 (a)) show an almost rectangular shape with a wide peak around 0.4 V vs Ag/AgCl. This redox process is due to residual functional groups in rGO_H. The maximum capacitance achieved is 251 $F.g^{-1}$ at 2 $mV.s^{-1}$. The capacitance of the material has a rapid decrease when the scan rate is increased (Figure 5-7 (b)), reaching 129 $F.g^{-1}$ at 100 $mV.s^{-1}$ (51 % of the initial one). This decrease is caused, in principle, because of the depletion of functional groups in the material.[20] The volumetric capacitance value is similar to the gravimetric one, given that the density of the film is 0.99 $g.cm^{-3}$.

The rGO_H film is tested in a symmetric configuration to evaluate its potential in real life applications. These results are shown in Figure 5-8. When the electrodes are tested in a symmetric configuration, the CV curves (Figure 5-8 (a)) are more rectangular than in a 3-electrode configuration. However, at high scan rates the capacitance becomes more dependent on the voltage. The maximum capacitance value of the symmetric device is 167 $F.g^{-1}$ at 2 $mV.s^{-1}$, which is 66 % of the one achieved with the 3-electrode configuration. At high scan rates, the rGO_H film only exhibits 33 % of the capacitance achieved at low scan rates.

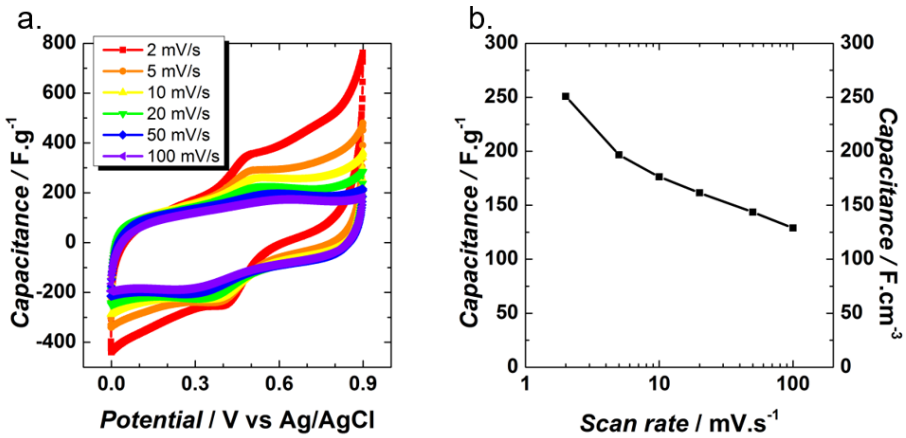

Figure 5-7. Electrochemical characterization of the rGO_H in 1 M H_2SO_4. Cyclic voltammetry (a) and rate capability (b).

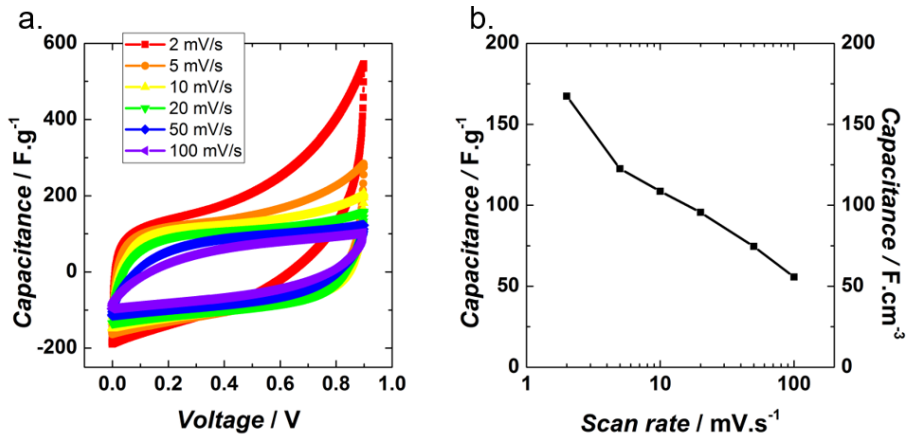

Figure 5-8. Cyclic voltammetry (a) and rate capability (b) of rGO_H in a symmetric configuration in 1 M H_2SO_4.

The electrochemical studies of the d-Ti_3C_2 and the rGO_H films can be summarized as it follows: On the one hand, the d-Ti_3C_2 film has a high volumetric and gravimetric capacitance and excellent capacitance retention. On the other hand, the rGO_H film achieves a high gravimetric capacitance but its volumetric capacitance and capacitance retention need to be improved. As these materials have complementary potential windows (from -0.2 to 0.35 V for d-Ti_3C_2 and from 0.0 to 0.9 V for rGO_H), herein an asymmetric device is proposed.

5.3.1.3 Aqueous-Based Asymmetric Device

In order to assemble the asymmetric capacitor, the d-Ti_3C_2 film is used as negative electrode (CE) and the rGO_H film as positive electrode (WE). The mass balance is calculated using Equation 1-13, taking into account the maximum capacitance of each material in three electrodes and the same potential window. Then,

$$\frac{m_{rGO_H}}{m_{d-Ti_3C_2}} = \frac{C_{d-Ti_3C_2} \times \Delta E_{d-Ti_3C_2}}{C_{rGO_H} \times \Delta E_{rGO_H}} = \frac{230}{251} = 0.9 \qquad \textbf{Equation 5-1}$$

In an asymmetric device, the electrodes have dissimilar charge storage capacities; therefore, in this section the capacitance reported will be the one corresponding to the cell. Figure 5-9 (a) shows the evolution of the cell capacitance with voltage at different scan rates of the asymmetric device with $m_{rGO_H}/m_{d-Ti_3C_2} = 0.9$. The capacitive behaviour (rectangular shape) is maintained at different scan rates proving optimum electrical conductivity and ion diffusion inside the pores. In the

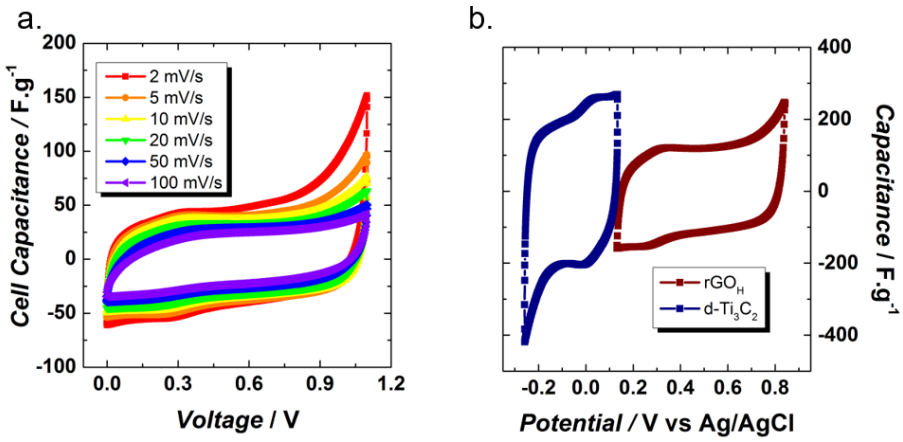

Figure 5-9. Cyclic voltammetry at different scan rates (a) and at 10 mV.s^{-1} (b) of the asymmetric device in 1 M H_2SO_4.

asymmetric device, the electrochemical window is expanded to 1.1 V as the electrodes have complementary potential working windows. This increment in voltage window will affect positively the energy and power delivered by the device. Figure 5-9 (b) shows the contributions from each electrode when the cell is cycled at 10 mV.s^{-1}. The potential window corresponding to the rGO_H and d-Ti_3C_2 is 0.71 and 0.39 V, respectively. To equilibrate the charges, other mass balance proportions are tried (not shown) but the d-Ti_3C_2 potential window always is constricted to less than 0.4 V. The capacitance achieved by the d-Ti_3C_2 electrode, and the rGO_H electrode at 10 mV.s^{-1} are 195 and 114 F.g^{-1}, respectively.

The cell gravimetric capacitance and Ragone plot (calculated for the active material) of the asymmetric and symmetric devices are shown in Figure 5-10 (I). The asymmetric device exhibits intermediate capacitance retention in between the symmetric cells of d-Ti_3C_2 and rGO_H (Figure 5-10 (a.I)). The maximum cell capacitance achieved by the asymmetric device is 48 F.g^{-1} (78 F.cm^{-3}). The use of d-Ti_3C_2 as counterpart to rGO_H in an asymmetric cell, improves the capacitance retention (44 % at 10 A.g^{-1}) compared to the symmetric rGO_H (33 % at 10 A.g^{-1}). However, the value is lower than the one achieved by the symmetric d-Ti_3C_2 device.

The advantage of using rGO_H as counterpart of d-Ti_3C_2 is, as explained before, the increment of the voltage window of the MXene electrode. In the Ragone plot observed in Figure 5-10 (b) can be seen that because of its small voltage window, the symmetric d-Ti_3C_2 device presents the lowest gravimetric energy values of the three devices. The symmetric rGO_H device exhibits a larger energy density than the

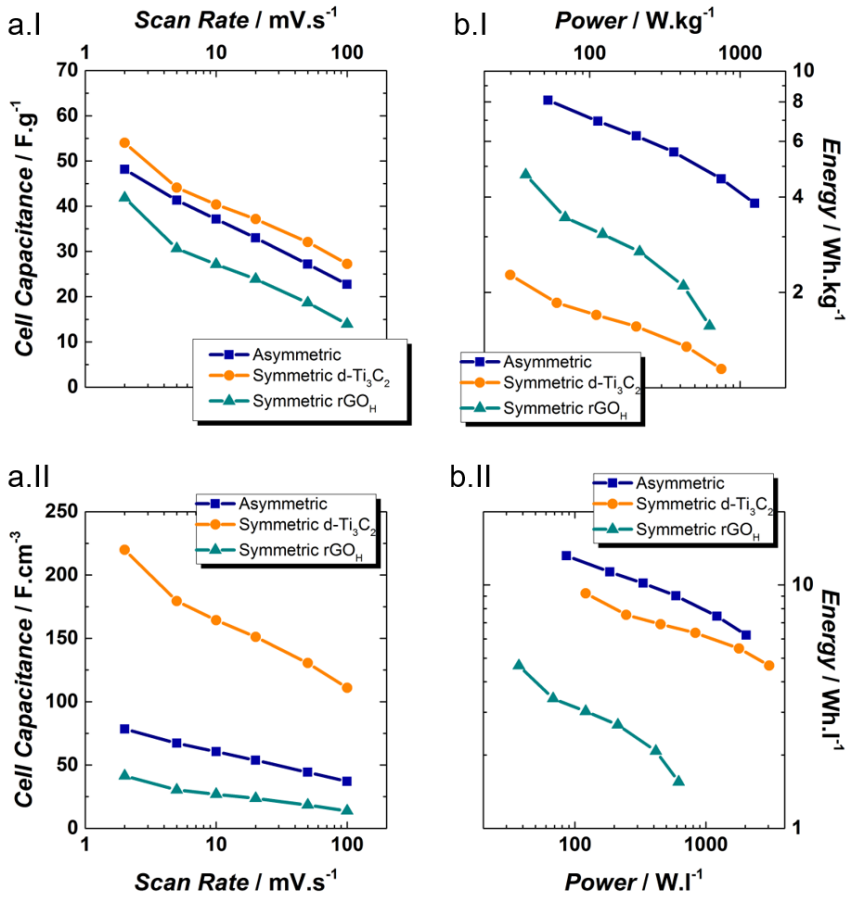

Figure 5-10. Comparison of the capacitance retention (a) and Ragone plot (b) calculated gravimetrically (I) and volumetrically (II) of the asymmetric device with the symmetric ones in 1 M H_2SO_4.

symmetric d-Ti_3C_2 device, but drops quickly as the power increases. As expected, the asymmetric device achieves the highest energy density, because of its voltage window, and the most stable energy density of the three devices. The asymmetric d-Ti_3C_2//rGO_H achieves up to 8 Wh.kg^{-1}, this value is comparable to the ones exhibited by carbon-based active materials.[31]

The influence of the density of the materials can be observed in Figure 5-10 (II). As explained before, d-Ti_3C_2 is a denser material than rGO_H, then, when comparing their volumetric capacitance retention, d-Ti_3C_2 exhibits the highest values, rGO_H the lowest and the asymmetric device, intermediate values. This behaviour is translated

Table 5-1. Summary of the performance of d-Ti_3C_2 and rGO_H in aqueous-based supercapacitors.

Aqueous-based supercaps	C_{Cell} $F.g^{-1}$	C_{Cell} $F.cm^{-3}$	Ret at 100 mV/s %	Energy Density $Wh.kg^{-1}$
Symmetric d-Ti_3C_2	54	220	50	2
Symmetric rGO_H	42	41	33	5
Asymmetric d-Ti_3C_2//rGO_H	48	78	48	8

to the Ragone plot, where as in the gravimetric plot, the asymmetric device achieves the highest energy values. Nevertheless, in contrast to the gravimetric plot, d-Ti_3C_2 achieves larger energy values than rGO_H, as its film density is 4 times higher. Table 5-1 summarizes the main results of the electrochemical testing of d-Ti_3C_2 and rGO_H in aqueous-based electrolytes in symmetric and asymmetric configurations.

One of the advantages of supercapacitors is their long-term cycling behaviour.[32] Therefore, the asymmetric device is tested for 1000 cycles and the evolution of its capacitance is plotted on Figure 5-11 (a). After 1000 cycles at 20 $mV.s^{-1}$, the capacitance retained is 76 % of the initial one. The decrease in capacitance might be caused by the lower conductivity of the rGO_H, as it has been proven that d-Ti_3C_2 can be cycled up to 10000 cycles without capacitance losses.[15] Coulombic

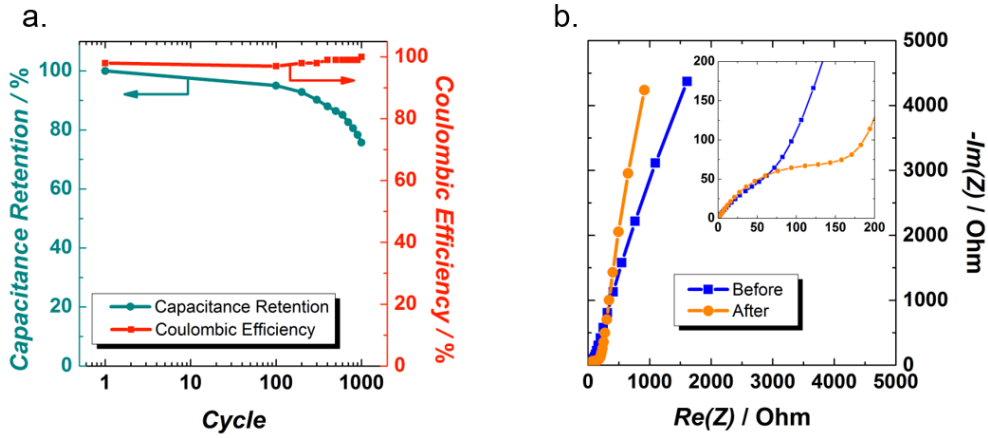

Figure 5-11. Capacitance retention during 1000 cycles at 20 $mV.s^{-1}$ (a) and Electrochemical Impedance spectroscopy before and after cycling (b) of the asymmetrical device in 1 M H_2SO_4.

efficiency is close to 100 % confirming that the process does not involve parasitic reactions.

The asymmetric device is analysed by Electrochemical Impedance Spectroscopy before and after cycling as shown in Figure 5-11 (b). The Nyquist plot of the asymmetric device, before cycling, shows a straight line in the low frequency region and no presence of a semicircle at high frequencies. This behaviour indicates low electronic resistance between the electrolyte and the electrodes. The electronic resistance increases with cycling as can be observed by the appearance of a semicircle after the cycle test. The slope of the 45 º portion of the curve is called Warburg resistance.[33] The increment on the Warburg resistance after cycling, describes an increment in the ion diffusion path between the electrode and the electrolyte.

For the first time, we have found a matching positive electrode for MXene in aqueous-based electrodes. Thus, this work opens up exciting possibilities of using d-Ti3C2 and rGO_H as couples in asymmetric aqueous-based supercapacitors.

5.3.2 Materials for Organic- and Ionic Liquid-Based Supercapacitors

In order to increase the energy density delivered by the asymmetric device, the materials are also tested in an organic electrolyte. The materials are slightly modified to improve their performance in organic electrolytes and are characterized as the ones used for aqueous electrolytes.

5.3.2.1 2D Titanium Carbide MXene-MWCNT Composite

Recently, Dall'Agnese *et al.* proved that the addition of MWCNT improves the performance of d-Ti_3C_2 in organic electrolytes.[11] After delamination of the MXene, the MWCNT are added following the procedure explained elsewhere.[12] In this case, the proportion d-Ti_3C_2:MWCNT of the film is 92:8. The insertion of MWCNT between

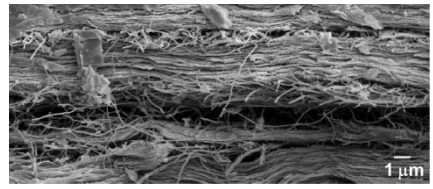

Figure 5-12. Cross section image of d-Ti_3C_2/MWCNT film.

the layers of d-Ti_3C_2 decreases the density of the film from 4.07 in the MXene to 2.44 g.cm^{-3} in the composite. The influence of the MWCNT on the d-Ti_3C_2 is studied by Scanning Electron Microscopy, Raman and X-Ray Diffraction.

5.3.2.1.1 2D Titanium Carbide MXene-MWCNT Composite Characterization

Figure 5-12 shows the cross-sectional Scanning Electron Microscopy image of a d-Ti_3C_2/MWCNT composite. The anticipated increase in spacing between the Ti_3C_2 layers after the incorporation of the MWCNTs is evident in the image.

Figure 5-13 shows the characterization of d-Ti_3C_2/MWCNT film by Raman Spectroscopy and X-Ray Diffraction. The spectrum combines the features of both d-Ti_3C_2 and MWCNT. The peaks observed at low frequencies in Figure 5-13 (a) correspond to the peaks attributed to d-Ti_3C_2 and are in agreement with the values of the MXene by itself (Figure 5-2 (a)). d-Ti_3C_2 does not present observable peaks at high frequencies; yet, the d-Ti_3C_2/MWCNT film does. The peak at 1141.4 cm^{-1} corresponds to C-H vibration of the surfactant.[34] Then, the peaks at 1295 and 1538.4 cm^{-1} correspond to the D and G band of the MWCNT, respectively. The D band can be understood as a measurement of structural disorder coming from amorphous carbon and any defects. The G band originates from the tangential in-plane stretching vibrations of the carbon–carbon bonds.[35]

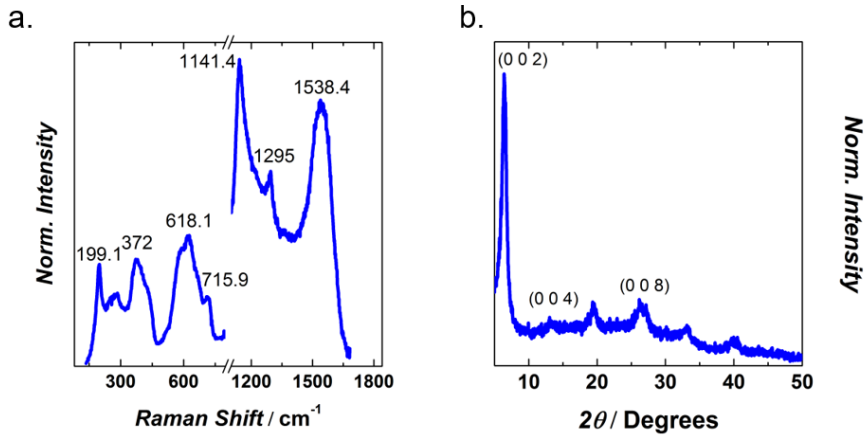

Figure 5-13.Raman (a) and XRD (b) of the d-Ti_3C_2/MWCNT film. Numbers in the Raman spectrum denote the vibration frequency while in the XRD pattern indicate the distance between the layers of the material.

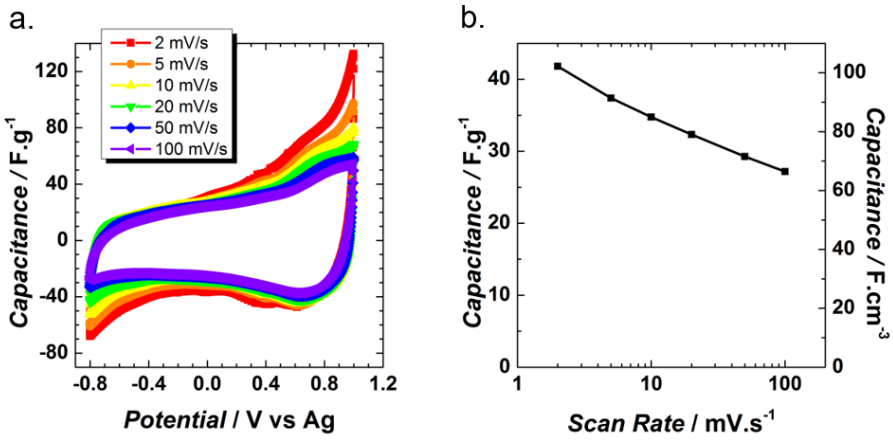

Figure 5-14. Electrochemical characterization of the d-Ti_3C_2/MWCNT in 1 M Et_4NBF_4. Cyclic voltammetry (a) and rate capability (b).

The XRD pattern of the d-Ti_3C_2/MWCNT (Figure 5-13 (b)) shows a sharp, intense peak corresponding to the (002) reflection of d-Ti_3C_2. The (002) peak in the XRD pattern of d-Ti_3C_2 shifted from 7.1 ° to 6.4 ° for the sandwich-like d-Ti_3C_2/MWCNT film. This shift translates in an increase in the interlayer distance from 12.5 Å in d-Ti_3C_2 to 13.8 Å in d-Ti_3C_2/MWCNT.

5.3.2.1.2 2D Titanium Carbide MXene-MWCNT Composite Electrochemistry

The electrochemical stability of the d-Ti_3C_2/MWCNT binder-free film in 1 M Et_4NBF_4/ACN is investigated by studying the material in a 3-electrode configuration. It is important to mention that other MWCNTs addition methods and other proportions were tried but the Sandwich-like d-Ti_3C_2/MWCNT in a 92:8 proportion delivers the highest capacitance values and the best capacitance retention from all the methods. The main results of the testing of this material are shown in Figure 5-14. The electrochemical signature of the d-Ti_3C_2/MWCNT film is characterized by a capacitive envelope and broad peaks typical of intercalation.[31]

This behaviour is maintained at high scan rates. The potential range (1.8 V) is narrower than expected from this electrolyte, but can been explained by water trapped between d-Ti_3C_2 layers. The intercalated water is responsible for electrolyte reaction at the extrema of the potential range visible at low scan rates.[11] At low scan rates, the d-Ti_3C_2/MWCNT film achieves 42 F.g^{-1} (102 F.cm^{-3}) and maintains 65 %

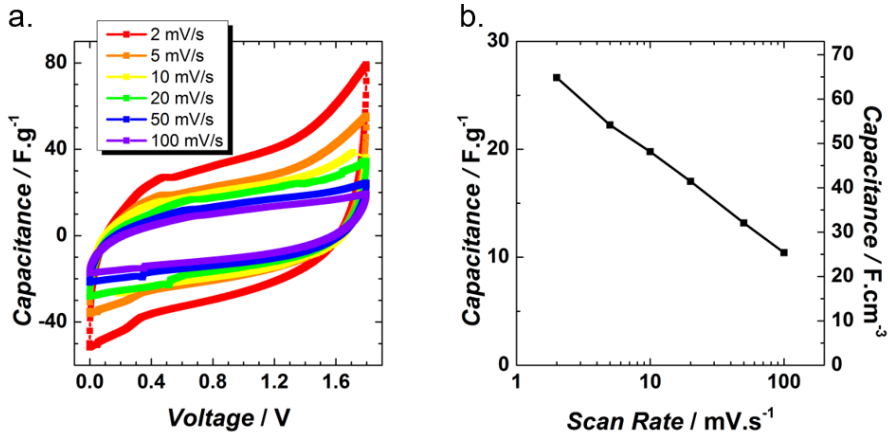

Figure 5-15. Cyclic voltammetry (a) and rate capability (b) of d-Ti_3C_2/MWCNT in a symmetric configuration in 1 M Et_4NBF_4/ACN.

of this capacitance at 100 $mV.s^{-1}$.

The electrochemical performance of two d-Ti_3C_2/MWCNT films is evaluated in a symmetric cell in 1 M Et_4NBF_4/ACN and shown in Figure 5-15. The shape of the CVs (Figure 5-15 (a)), at different scan rates, is rectangular indicating a capacitive behaviour. Moreover, an intercalation process seems to occur below 0.4 V. The maximum capacitance achieved by the symmetric cell in the organic electrolyte is 27 $F.g^{-1}$ (65 $F.cm^{-3}$). Comparing the electrochemical results of the 3-electrode and symmetric configurations, the latter shows 64 % of the maximum capacitance achieved by the former. At 100 $mV.s^{-1}$, only 39 % of the capacitance exhibited at 2 $mV.s^{-1}$ is maintained. The intercalated water in the MXene layers might cause this phenomenon.

5.3.2.2 Thermally Reduced Graphene Oxide

The presence of surface functionalities, water or impurities in the active material are the main causes of ageing in organic-based supercapacitors.[22] The hydrazine reduction of Graphene Oxide does not remove epoxide groups from the edges of the aromatic domains,[21] making of the rGO_H a weak candidate for organic-based supercapacitors. Thermal annealing of the Graphene Oxide above 700 °C eliminates hydroxyl and carboxyl groups from the material.[21] Herein, the Graphene Oxide is thermally reduced at 900 °C (labelled in here as rGO_T) in order to use it as electrode material for organic-based supercapacitors. rGO_T is characterized by Scanning Electron Microscopy, Raman Spectroscopy, and X-Ray Diffraction.

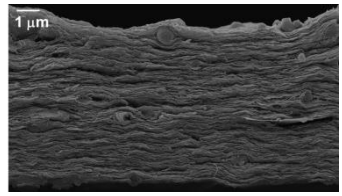

Figure 5-16. Cross-sectional SEM image of rGO_T film.

5.3.2.2.1 Thermally Reduced Graphene Oxide Characterization

A cross section image of the rGO_T film by SEM is shown in Figure 5-16. This image confirms the layered nanostructure of the material.

Figure 5-17 shows the Raman and XRD results of the analysis of the rGO_T. The Raman spectrum (Figure 5-17 (a)) shows the typical fingerprint of carbon materials. The D band is around 1323 cm^{-1} while the G band is at 1598 cm^{-1}, with an I_D/I_G ratio of 1.3. rGO_T and rGO_H have similar I_D/I_G ratios indicating that the two reduction methods achieve similar reduced Graphene Oxides in terms of ordering of the material.

Figure 5-17 (b) shows the XRD pattern of rGO_T. The (002) peak of the material is at 25.4 °, 1.7 ° to the right of the (002) peak of the rGO_H. This shift towards higher angles indicates that rGO_T is less oxidized than rGO_H.

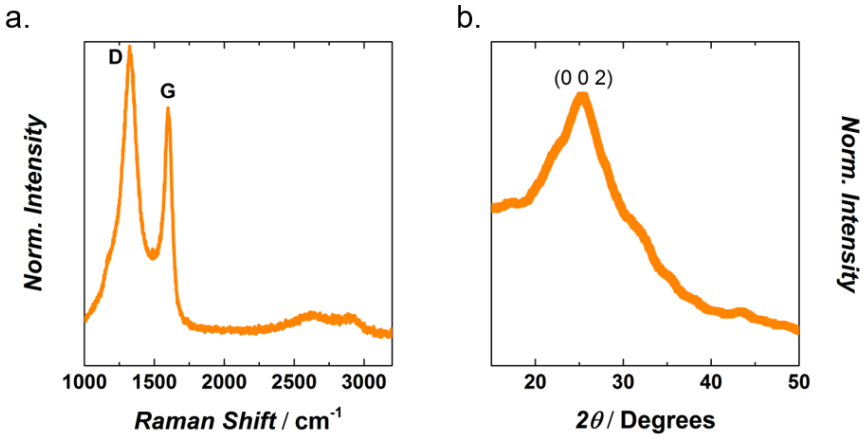

Figure 5-17. Raman (a) and XRD (b) of the rGO_T. The number in the XRD pattern indicates interlayer distance.

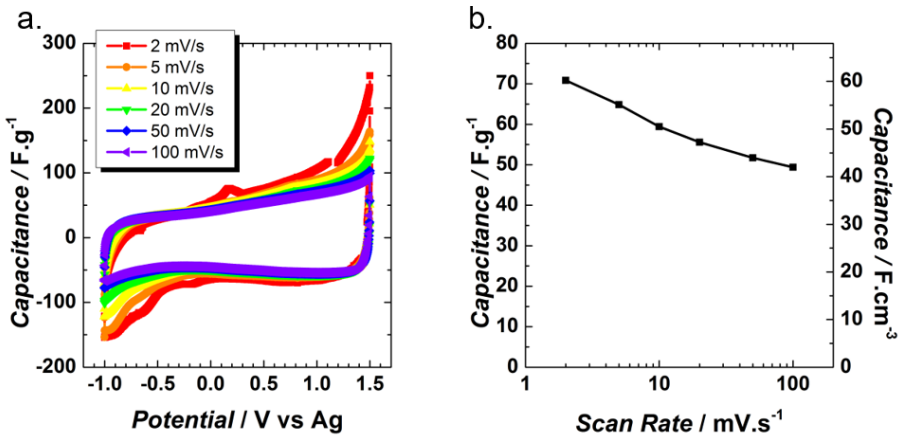

Figure 5-18. Electrochemical characterization of the rGO_T in 1 M Et_4NBF_4/ACN. Cyclic voltammetry (a) and rate capability (b).

5.3.2.2.2 Thermally Reduced Graphene Oxide Electrochemistry

Figure 5-18 shows the results from cycling the rGO_T binder-free electrode in organic electrolyte in a 3-electrode configuration. The cyclic voltammetry curves (Figure 5-18 (a)) have a capacitive envelope with some broad peaks, caused by intercalation, at low scan rates. The evaluation of the capacitance at different scan rates shows that the maximum capacitance achieved is 71 $F.g^{-1}$ at 2 $A.g^{-1}$. 70 % of this capacitance is maintained at 100 $A.g^{-1}$ showing acceptable capacitance retention with scan rate. The density of rGO_T is 0.84 $g.cm^{-3}$, making of this film, 15 % less dense than rGO_H.

Figure 5-19 shows the main results of the testing of rGO_T in a symmetric configuration in 1 M Et_4NBF_4/ACN. The voltage window for the cyclic voltammetry measurements in Figure 5-19 (a) is equal to the maximum potential window in the 3-electrode configuration *i.e.* 2.5 V. At 2 $mV.s^{-1}$, the capacitance is 75 $F.g^{-1}$ and at 100 $mV.s^{-1}$, 50 % of it is retained. At low scan rates, the electrolyte reaction at the right extreme of the voltage is more pronounced. This electrolyte decomposition affects the capacitance calculation, making it larger than it probably is.

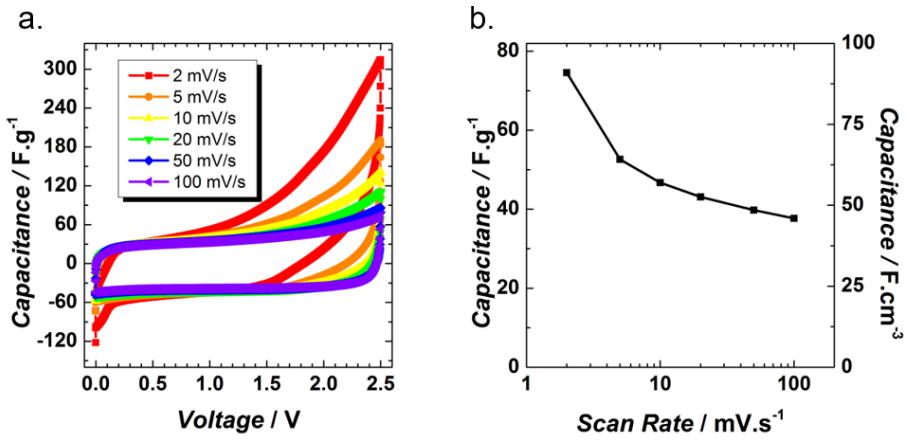

Figure 5-19. Cyclic voltammetry (a) and rate capability (b) of rGO_T in a symmetric configuration in 1 M Et_4NBF_4/ACN.

5.3.2.3 Organic-Based Asymmetric Device

The assembling of an asymmetric organic-based supercapacitor, is not as straightforward as the aqueous-based one. The potential windows of the d-Ti_3C_2/MWCNT and rGO_T are not complementary and rGO_T has a better electrochemical performance in 1 M Et_4NBF_4/ACN than the composite. Nevertheless, the asymmetric supercapacitor is assembled to see if the performance of the d-Ti_3C_2/MWCNT can be improved by using rGO_T as positive electrode. rGO_T is chosen as positive electrode as it has a larger potential window. d-Ti_3C_2/MWCNT is chosen as negative electrode as its interlayer distance is larger and can fit better the Et_4N^+ ions. The mass balance is calculated using Equation 1-13, and taking into account the maximum capacitance values showed by each material in the 3-electrode configuration. Then,

$$\frac{m_{rGO_T}}{m_{d-Ti_3C_2/MWCNT}} = \frac{C_{d-Ti_3C_2/MWCNT}}{C_{rGO_T}} = \frac{42}{71} = 0.6 \qquad \textbf{Equation 5-2}$$

Figure 5-20 shows the cyclic voltammetry analysis of the asymmetric d-Ti_3C_2/MWCNT and rGO_T device using $m_{rGO_T}/m_{d-Ti_3C_2/MWCNT} = 0.6$. The cell can reach up to 2.3 V but the cell capacitance drops drastically when the scan rate is increased, therefore the asymmetric cells in this study are run up to 2 V (Figure 5-20 (a). The performance of each electrode is studied with a pseudo-reference

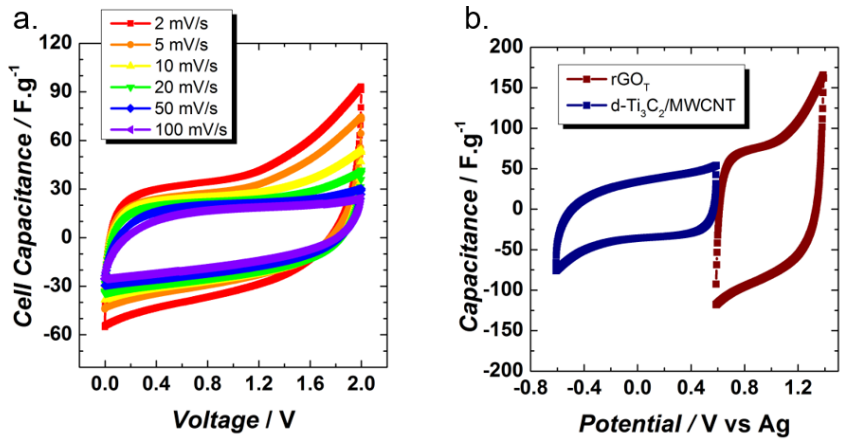

Figure 5-20. Cyclic voltammetry of the asymmetric device in 1 M Et_4NBF_4/ACN. Cell capacitance variation with voltage at different scan rates (a) and behaviour of each electrode with potential at 10 mV.s^{-1} (b).

electrode. On the one hand, the potential window of rGO_T is equal to 0.8 V and shows a capacitance of 83 F.g^{-1}. On the other hand, d-Ti_3C_2/MWCNT exhibits a potential window of 1.2 F and achieves 35 F.g^{-1}.

Figure 5-21 (a) shows the cell capacitance values of the asymmetric device and the symmetric cells of d-Ti_3C_2/MWCNT and rGO_T. Surprisingly, the cell capacitance value of the asymmetric device is the highest one, this is caused by the matching of the interlayer distance with the ion sizes. The XRD pattern indicated an interlayer distance for d-Ti_3C_2/MWCNT of 1.38 nm and the size of the Et_4N^+ bare cation is 0.67 nm and solvated is 1.3 nm,[36] the similarity in size allows the insertion of ions in between the layers of the material. Then, rGOT has an interlayer distance ranging between 0.23 and 0.44 nm which matches perfectly the BF_4^- ion size which is 0.33 nm.[37]

When taking into account the density of the materials (Figure 5-21 (a.II)), the symmetric cells achieve similar capacitance values at 2 mV.s^{-1}. After increasing the scan rate above 5 mV.s^{-1} the symmetric rGO_T retains 71 % of its initial capacitance while the symmetric d-Ti_3C_2/MWCNT maintains 84 %. Figure 5-21 (b) shows the gravimetric (I) and volumetric (II) Ragone plot of the asymmetric devices in aqueous and organic electrolytes. As expected, the increase in voltage window is reflected on a higher energy density for the cell. Nevertheless, the aqueous-based supercapacitor exhibits a better energy retention as there is no decomposition of electrolyte caused by the water in between the layers. Table 5-2 summarizes the

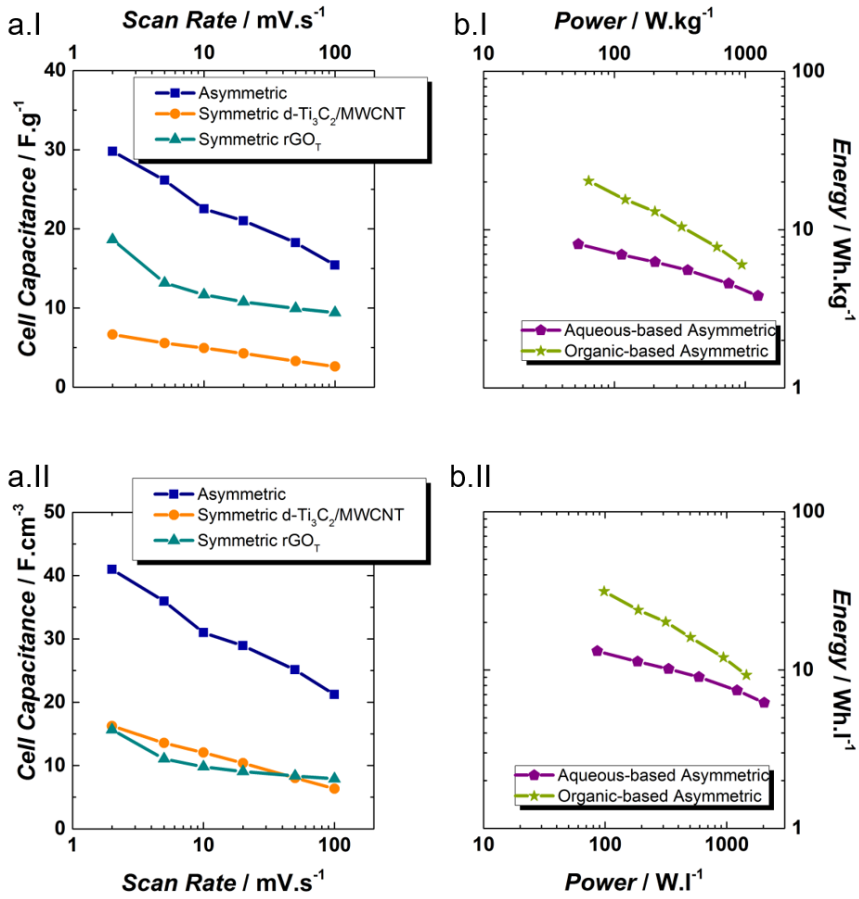

Figure 5-21. Comparison of the capacitance retention of the asymmetric device with the symmetric ones in 1 M EtN_4BF_4 (a). Ragone plot comparing the aqueous- with the organic-based supercapacitor (b). Values calculated gravimetrically (I) and volumetrically (II).

Table 5-2. Summary of the performance of d-Ti_3C_2-CNT and rGO_T in organic-based supercapacitors.

Organic-based supercaps	C_{Cell} $F.g^{-1}$	C_{Cell} $F.cm^{-3}$	Ret at 100 mV/s %	Energy Density $Wh.kg^{-1}$
Symmetric d-Ti_3C_2-CNT	7	16	37	3
Symmetric rGO_T	19	16	47	16
Asymmetric d-Ti_3C_2-CNT//rGO_T	30	41	50	20

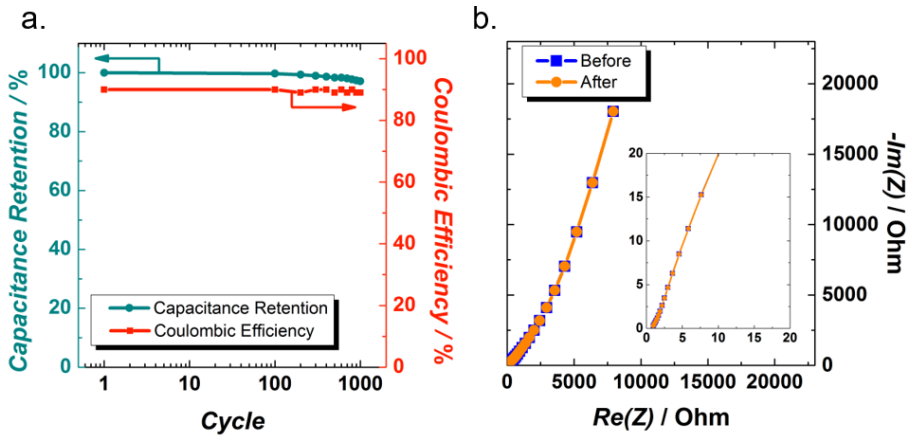

Figure 5-22. Capacitance retention during 1000 cycles at 20 mV.s^{-1} (a) and Electrochemical Impedance spectroscopy before and after cycling (b) of the asymmetrical device in 1 M Et_4NBF_4/ACN.

performance of d-Ti_3C_2-CNT and rGO_T as electrodes for supercapacitors in organic-based electrolytes.

The asymmetric d-Ti_3C_2/MWCNT//rGO_T device is cycled 1000 times at 20 mV.s^{-1} and the main results are shown in Figure 5-22. As it can be seen in Figure 5-22 (a), the cell maintains 97% of its initial capacitance after 1000 cycles showing a good long-term cycling performance. The Coulombic efficiency during the cycling is maintained around 90%. This indicates that the charge storage process is not caused entirely by capacitive processes but some diffusion-limited processes might be involved as well. In fact, Dall'Agnese *et al.*[11] have already proven that d-Ti_3C_2/MWCNT presents some redox peaks in organic electrolytes. Herein, these peaks might be overshadowed by the high capacitance of the material. Figure 5-22 (b) shows the electrochemical impedance spectrum before and after the cycling test. There is no appreciable change in the spectrum confirming the long-term stability at high rates of this device.

There is only one report on the performance of d-Ti_3C_2/MWCNT in organic based supercapacitors. Electrochemical testing of d-Ti_3C_2/MWCNT in ET_4NBF_4/ACN in a 3-electrode configuration has been previously reported.[11] Capacitance values (reported for the electrode) are around 40 F.g^{-1}. By multiplying our cell capacitance by four, we can give an approximate electrode capacitance for comparison. This means that our organic-based asymmetric device delivers up to 120 F.g^{-1}, a value

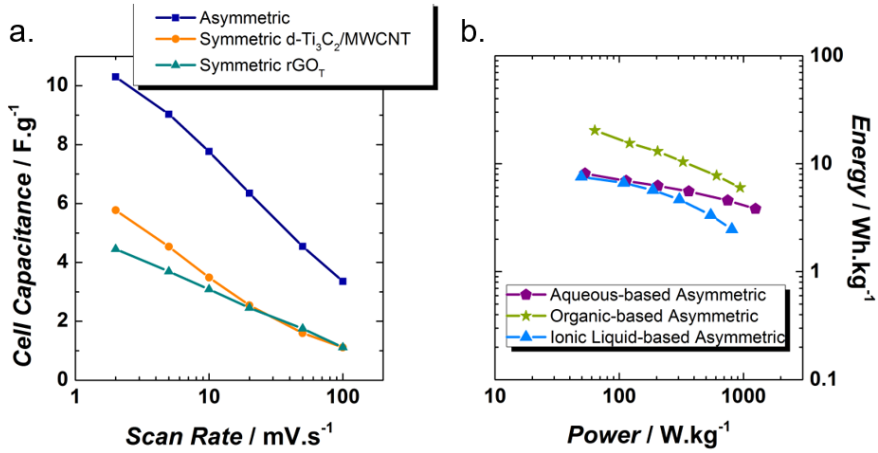

Figure 5-23. Comparison of the capacitance retention of the asymmetric device with the symmetric ones in $C_8H_{11}F_6N_3O_4S_2$ (a). Ragone plot comparing the different electrolytes (b).

three times higher than the previous report.

5.3.2.4 Ionic Liquid Asymmetric Supercapacitor

d-Ti_3C_2/MWCNT and rGO_T electrodes are electrochemically characterized in a 3-electrode and symmetric configurations in an ionic liquid electrolyte (results not shown). d-Ti_3C_2/MWCNT and rGO_T electrodes are used as negative and positive electrodes, respectively, in an ionic liquid-based supercapacitor. A summary of the asymmetric device results is shown in Figure 5-23. A decrease in the capacitance of the materials when compared to organic electrolyte is expected. The maximum cell capacitance achieved by the asymmetric device in ionic liquid is 10 $F.g^{-1}$, three times lower than the maximum capacitance exhibited by the asymmetric device in an organic electrolyte. Moreover, the presence of water in between the layers of d-

Ti_3C_2/MWCNT also causes a decrease in its maximum potential window (1.6 V). These two parameters, greatly affect the energy and power delivered by the device and values even lower than for aqueous electrolyte are achieved (Figure 5-23 (b)). Recently, Lin *et al.*[9] have shown that a pre-intercalation of the ionic liquid is necessary to increase the capacitance, energy and power delivered.

5.4 Conclusions and Perspectives

Pure d-Ti_3C_2 and a composite made out of d-Ti_3C_2 and MWCNT were tested as counterparts of chemically and thermally reduced Graphene Oxide electrodes in asymmetric supercapacitor devices in aqueous-, organic- and ionic liquid electrolytes. SEM images of the materials proved that they presented layered morphologies.

The aqueous-based asymmetric supercapacitor achieved cell capacitances of 48 $F.g^{-1}$ (78 $F.cm^{-3}$). These values were lower than those achieved by a symmetric d-Ti_3C_2 cell. However, the increase in the potential window of the asymmetric when compared to the symmetric cell rendered an increase of the energy density.

The organic-based asymmetric supercapacitor exhibited larger gravimetric and volumetric cell capacitances (30 $F.g^{-1}$ and 41 $F.cm^{-3}$, respectively) when compared to the symmetric cells of d-Ti_3C_2 and rGO_T. The increase in the voltage window of the device caused an increase in the energy density of the organic-based device when compared to the aqueous one.

The great performance of the asymmetric devices could not be maintained in an ionic liquid electrolyte. Further experiments on displacement of the intercalated water by ionic liquid ions are required. This problem might be solved by pre-incorporating electrolytes in between 2-Dimensional nanosheets.

5.5 References

(1) Faggioli, E.; Rena, P.; Danel, V.; Andrieu, X.; Mallant, R.; Kahlen, H. *J. Power Sources* **1999**, *84* (2), 261–269.

(2) Beidaghi, M.; Gogotsi, Y. *Energy Environ. Sci.* **2014**, *7*, 867–884.

(3) Mendoza-Sanchez, B.; Gogotsi, Y. *Adv. Mater.* **2016**, *28* (29), 6104–6135.

(4) Nicolosi, V.; Chhowalla, M.; Kanatzidis, M. G.; Strano, M. S.; Coleman, J. N. *Science (80-.).* **2013**, *340* (6139), 1420–1438.

(5) Naguib, M.; Kurtoglu, M.; Presser, V.; Lu, J.; Niu, J.; Heon, M.; Hultman, L.; Gogotsi, Y.; Barsoum, M. W. *Adv. Mater.* **2011**, *23* (37), 4248–4253.

(6) Sun, Z.; Music, D.; Ahuja, R.; Li, S.; Schneider, J. M. *Phys. Rev. B* **2004**, *70* (9), 92102.

(7) Mashtalir, O.; Lukatskaya, M. R.; Kolesnikov, A. I.; Raymundo-Piñero, E.; Naguib, M.; Barsoum, M. W.; Gogotsi, Y. *Nanoscale* **2016**, *8* (17), 9128–9133.

(8) Boota, M.; Anasori, B.; Voigt, C.; Zhao, M. Q.; Barsoum, M. W.; Gogotsi, Y. *Adv. Mater.* **2016**, *28* (7), 1517–1522.

(9) Lin, Z.; Barbara, D.; Taberna, P. L.; Van Aken, K. L.; Anasori, B.; Gogotsi, Y.; Simon, P. *J. Power Sources* **2016**, 2–6.

(10) Come, J.; Xie, Y.; Naguib, M.; Jesse, S.; Kalinin, S. V.; Gogotsi, Y.; Kent, P. R. C.; Balke, N. *Adv. Energy Mater.* **2016**, *6* (9), 1–9.

(11) Dall'Agnese, Y.; Rozier, P.; Taberna, P. L.; Gogotsi, Y.; Simon, P. *J. Power Sources* **2016**, *306*, 510–515.

(12) Zhao, M. Q.; Ren, C. E.; Ling, Z.; Lukatskaya, M. R.; Zhang, C.; Van Aken, K. L.; Barsoum, M. W.; Gogotsi, Y. *Adv. Mater.* **2015**, *27* (2), 339–345.

(13) Tang, Y.; Zhu, J.; Yang, C.; Wang, F. *J. Alloys Compd.* **2016**, *685*, 194–201.

(14) Ghidiu, M.; Lukatskaya, M. R.; Zhao, M.-Q.; Gogotsi, Y.; Barsoum, M. W. *Nature* **2014**, *516* (7529), 78–81.

(15) Lukatskaya, M. R.; Mashtalir, O.; Ren, C. E.; Dall'Agnese; Rozier, P.; Taberna, P. L.; Naguib, M.; Simon, P.; Barsoum, M. W.; Gogotsi, Y. *Science (80-.).* **2013**, *341* (6153), 1502–1505.

(16) Gogotsi, Y.; Simon, P. *Science (80-.).* **2011**, *334* (6058), 917–918.

(17) Zhao, M.-Q.; Ren, C. E.; Ling, Z.; Lukatskaya, M. R.; Zhang, C.; Van Aken, K. L.; Barsoum, M. W.; Gogotsi, Y. *Adv. Mater.* **2015**, *27* (2), 339–345.

(18) Marcano, D. C.; Kosynkin, D. V.; Berlin, J. M.; Sinitskii, A.; Sun, Z.; Slesarev, A.; Alemany, L. B.; Lu, W.; Tour, J. M. *ACS Nano* **2010**, *4* (8), 4806–4814.

(19) Yang, X.; Cheng, C.; Wang, Y.; Qiu, L.; Li, D. *Science (80-.).* **2013**, *341* (August), 534–537.

(20) Oh, Y. J.; Yoo, J. J.; Kim, Y. Il; Yoon, J. K.; Yoon, H. N.; Kim, J. H.; Park, S. Bin. *Electrochim. Acta* **2014**, *116*, 118–128.

(21) Gao, X.; Jang, J.; Nagase, S. *J. Phys. Chem. C* **2010**, *114*, 832–842.

(22) Azaïs, P.; Duclaux, L.; Florian, P.; Massiot, D.; Lillo-Rodenas, M.-A.; Linares-Solano, A.; Peres, J.-P.; Jehoulet, C.; Béguin, F. *J. Power Sources* **2007**, *171* (2), 1046–1053.

(23) Li, D.; Müller, M. B.; Gilje, S.; Kaner, R. B.; Wallace, G. G. *Nat. Nanotechnol.* **2008**, *3* (2), 101–105.

(24) Fernández-Merino, M. J.; Guardia, L.; Paredes, J. I.; Villar-Rodil, S.; Solís-Fernández, P.; Martínez-Alonso, A.; Tascón, J. M. D. *J. Phys. Chem. C* **2010**, *114* (14), 6426–6432.

(25) Srivastava, P.; Mishra, A.; Mizuseki, H.; Lee, K.-R.; Singh, A. K. *ACS Appl. Mater. Interfaces* **2016**, *8* (36), 24256–24264.

(26) Naguib, M.; Mashtalir, O.; Lukatskaya, M. R.; Dyatkin, B.; Zhang, C.;

Presser, V.; Gogotsi, Y.; Barsoum, M. W. *Chem. Commun.* **2014**, *50* (56), 7420–7423.

(27) Cai, K. J.; Zheng, Y.; Shen, P.; Chen, S. Y. *CrystEngComm* **2014**, *16* (24), 5466–5474.

(28) Hope, M. A.; Forse, A. C.; Griffith, K. J.; Lukatskaya, M. R.; Ghidiu, M.; Gogotsi, Y.; Grey, C. P. *Phys. Chem. Chem. Phys.* **2016**, *18* (7), 5099–5102.

(29) Malard, L. M.; Pimenta, M. A.; Dresselhaus, G.; Dresselhaus, M. S. *Phys. Rep.* **2009**, *473* (5–6), 51–87.

(30) Cançado, L. G.; Jorio, A.; Martins Ferreira, E. H.; Stavale, F.; Achete, C. A.; Capaz, R. B.; Moutinho, M. V. O.; Lombardo, A.; Kulmala, T. S.; Ferrari, A. C. *Nano Lett.* **2011**, *11*, 3190–3196.

(31) Simon, P.; Gogotsi, Y. *Nat. Mater.* **2008**, *7* (11), 845–854.

(32) Brousse, T.; Taberna, P.-L.; Crosnier, O.; Dugas, R.; Guillemet, P.; Scudeller, Y.; Zhou, Y.; Favier, F.; Bélanger, D.; Simon, P. *J. Power Sources* **2007**, *173* (1), 633–641.

(33) Taberna, P. L.; Simon, P.; Fauvarque, J. F. *J. Electrochem. Soc.* **2003**, *150* (3), A292–A300.

(34) Valmalette, J.-C.; Tan, Z.; Abe, H.; Ohara, S. *Sci. Rep.* **2014**, *4*, 436–441.

(35) Osswald, S.; Havel, M.; Gogotsi, Y. *J. Raman Spectrosc* **2007**, *38*, 728–736.

(36) Chmiola, J.; Largeot, C.; Taberna, P. L.; Simon, P.; Gogotsi, Y. *Angew. Chemie - Int. Ed.* **2008**, *47* (18), 3392–3395.

(37) Chmiola, J.; Yushin, G.; Gogotsi, Y.; Portet, C.; Simon, P.; Taberna, P.-L. *Science (80-.).* **2006**, *313* (5794), 1760–1763.

Conclusions & Outlook

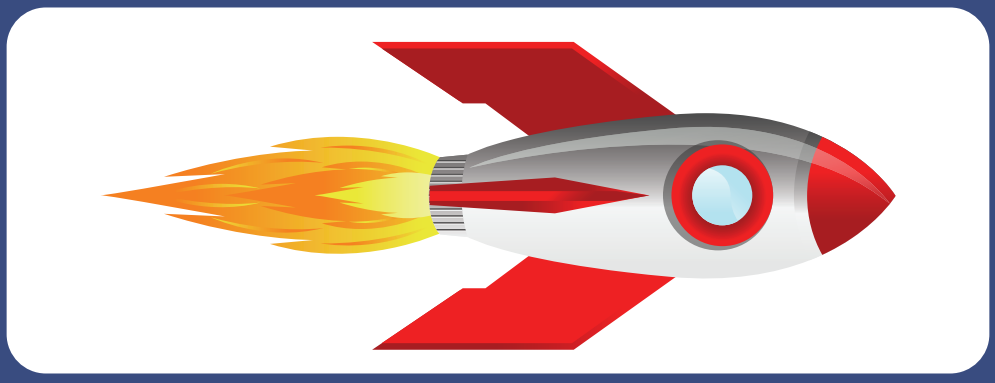

6 CONCLUSIONS & OUTLOOK

6.1 Conclusions

From the evaluation of graphene-based materials as electrodes for electrochemical capacitors can be concluded the following:

- An activated carbon with tuneable porosity and microstructure can be synthesized from lignin by chemical activation with KOH at different temperatures and ratios.
- Tuneable porosity is achievable by changing the carbonization temperature of the precursor.
- Graphene-like zones can be introduced in the activated carbon by adjusting the KOH/C ratio.

- Increment on the capacitive contribution of lignin is achievable by copolymerizing the biopolymer with PEDOT.
- A pseudocapacitive behaviour can be introduced in the reduced graphite oxide by selecting the appropriate oxidation and reduction method.
- The preparation of a composite made out of Lignin/PEDOT and partially reduced Graphite Oxide enhances the electrochemical performance of each material.

- Quinone-amine polymers present optimum characteristics for applications in energy storage devices.
- Processability of the material is achieved by introducing a PEO linker.
- Notable electrochemical performance is achieved by introducing nanostructured materials, *i.e.* multiwalled carbon nanotubes, during polymerization.

- Outstanding volumetric capacitance values are achievable by assembling an aqueous-based asymmetric device using chemically reduced graphene oxide and d-Ti_3C_2 MXene.
- Enhancement of the energy density is attainable by increasing the interlayer distance in between the MXene layers and thermally reducing the graphene oxide and using them as electrodes in organic-based supercapacitors.

6.2 Outlook

Based on the results achieved in this thesis the following further experiments are recommended:

6.2.1 Lignin-Derived Carbons for Supercapacitors

- Carbonization of the material at different temperatures to further study the development of the internal microporosity.
- Doping of the activated carbons with heteroatoms to increase the charge carrier density, and therefore, increase the capacitance values of the supercapacitor.
- Assembling of asymmetric EDLC by using lignin-derived carbons which porosity matches perfectly either the cations or anions present in the electrolyte used.

6.2.2 Multi-Redox Electrodes for Supercapacitors

- Improvement of the conductivity of the prGrO by mixing the material with conductive filler.
- Copolymerization of the lignin with other conductive polymers.
- Variation of the ratios Lig/PEDOT//prGrO in the composite to achieve optimal distribution of the pseudocapacitive and faradaic processes.

6.2.3 Quinone-Amine Polymers for Energy Storage Devices

- Replacing the PEDOT linkers with other Jeff Amines of lower molecular weight to increase the capacity offered by the terpolymer.
- Studies of solubility of the terpolymer in other solvents in order to replace the NMP by a less harmful solvent.
- Utilization of the polymers in a full cell assembly.

6.2.4 Titanium Carbide-Reduced Graphene Oxide for Supercapacitors

- Preparation of a Titanium carbide-reduced graphene oxide composite to optimize the distribution of charges.
- Pre-intercalation of organic and ionic liquid electrolytes in the layers to displace the water molecules.
- Testing of other MXenes as counterparts to the reduced graphene oxide in asymmetric configurations.

As concluding remark, the general research direction of supercapacitors would be greatly benefitted from theoretical studies to analyse nanostructured materials with well-defined surface chemistry and their performance as electrode materials for energy storage devices.

Appendices

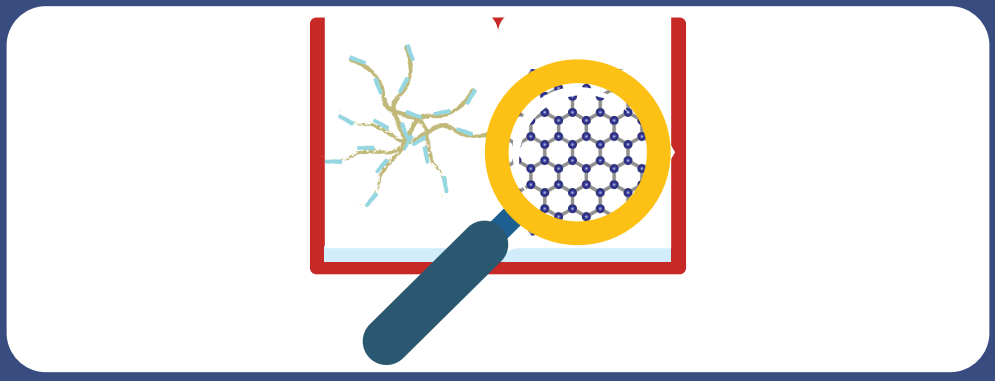

7 APPENDICES

CONTENTS

APPENDIX I: Characterization Methods

Scanning Electron Microscopy and Energy-Dispersive X-Ray Spectroscopy

The SEM technique utilizes electron beams to scan the surface of a sample specimen. The specimen is irradiated by a focused electron beam and the signals produced create useful images describing the surface morphology of the specimen. Samples must be electronically conductive to prevent charging effects that can blur image quality at higher resolutions. To avoid this, some insulating samples are gold sputtered to provide a nanometre-thick conductive surface layer.

When the incident electron strikes the specimen surface, instead of bouncing off immediately, it penetrates for some distance before it collides with a surface atom and a region of primary excitation where signals are produced is created.[1] The most common signals used for imaging are secondary electrons, backscattered electrons, and characteristic X-rays. In normal conditions, the secondary electrons created from inelastic surface scattering can reach the detector in greater numbers, depending on incidence angle, and generate topographic information.

The backscattered electrons are higher energy electrons deflected elastically or scattered back to the detector. This backscattering provides specimen composition data because heavier elements produce greater backscattering intensity, resulting in brighter images than those produced by lighter elements.[1,2] Characteristic X-rays can reveal the distribution of chemical elements. Drawbacks of SEM include the requirement for a sample to be in a solid state and stable inside a vacuum. Normally, materials saturated with hydrocarbons, wet samples, and moisture-containing organic materials and clays are not compatible with SEM until they are lyophilized.[3]

In the study of supercapacitors, SEM can provide important information about the material surface morphologies of cell components, specifically when analysing separator membrane porosity and electrode morphology.[4] Images of the material surface can be collected before and after certain chemical or physical modifications or treatments to investigate their effects on material phases and morphologies

EDX is commonly used as an addition to SEM, utilizing an electron gun and imaging equipment to locate the desired sample position. To perform EDX analysis of a sample, the electron imaging detector is replaced by an X-ray detector system. As previously noted, an electron beam that hits a sample produces a variety of signals

including characteristic X-rays.

The X-rays are created when the incident electrons cause ejection of an electron in the inner shell. An outer shell electron fills the hole and releases the energy difference as an X-ray.[5] The X-ray energy is characteristic of the atomic structure and the difference between the electron shells.

EDX is a useful tool for ECs research, for example, for determining the atomic dispersion of a sample surface. However, EDX loses measurement accuracy because of (1) overlapping peaks, (2) detector resolution, and (3) emission of X-rays in all directions—they must escape the sample before being reabsorbed to be detected. The third factor can mean lower energy X-rays are collected with lower intensity than is actually present and rough morphology can mask elements resulting in inaccurate atomic composition descriptions.[6]

In this thesis, the morphological characterization of the materials is conducted by scanning electron microscopy (SEM) in a Quanta 200 FEG (FEI) microscope. The chemical composition is studied by energy dispersive X-rays (EDX).

Transmission Electron Microscopy

Similar to SEM, transmission electron microscopy (TEM) also utilizes a highly focused electron beam. However, TEM imaging requires a very thin specimen to achieve good image quality. This means that sample preparation is extremely important. A sample layer must be thin enough to allow electrons to pass through.[7] An electron gun emits high energy beams that can penetrate several microns into a solid. The electrons can penetrate through a thin specimen.

The essential components of a TEM instrument consist of an electron gun, lenses, detectors, and a specimen holder. [3] A three- or four-stage condenser system will control variation of the illuminating aperture and the area of the specimen illuminated. The electrons that pass through the specimen then go through an imaging detection system and the image is displayed.[8] TEM is essential for material tomography or examining crystalline defects. However, TEM analysis is two-dimensional and it may be difficult to distinguish some features of an image. Further, the combination of ultrahigh voltage beam and high power electron sources makes the technique destructive for many sample types.[7]

In electrochemical supercapacitors, TEM is used to collect and examine the microstructures of electrode materials, providing information about pore arrangements.[4] If a specimen is crystalline, the electrons will diffract or scatter off

atomic planes inside the material, enabling the resolution of the crystal lattice structure down to atomic scale.[9] Similar to SEM, TEM can also show changes in pore structures or arrangements after a material undergoes certain chemical or physical changes.[10,11]

Images taken by transmission electron microscopy (TEM) through this thesis are performed in a Tecnai G2 (FEI) operated at 200 kV field emission gun (FEG).

N_2 sorption

N_2 sorption provides precise specific area measurements of a material by analysing the absorption isotherm of nitrogen gas compared to a reference cell. Initially the sample is degassed fully to remove all the gas within the sample volume. During testing, a film of the test gas will form on the surface of the sample area, penetrating the pores. The gas desorption is also measured during a final degas as well. The analysis of the absorption and desorption isotherms provides total specific surface area (usually m^2/g^{-1}). It also allows determination of pore size distribution.[3]

N_2 sorption is an important tool for ECs characterization because surface area and pore size are both important parameters in determining material capacitance.[12]. Pore size measurements enable the estimation of electrochemical effectiveness of an active material when matched to a specific electrolyte. Pore size and surface area are also good indicators of structural changes after chemical or heat treatment

Textural properties of the materials prepared are studied using a Micromeritics (ASAP 2020) surface analyser by adsorption/desorption of N_2 gas at 77 K. Before the analysis, the samples are outgassed for 8 hours at 200 °C. The specific surface area (S_{NLDFT}) and the micro- ($S_{micro\text{-}NLDFT}$) and mesopores ($S_{meso\text{-}NLDFT}$) contributions to the total surface area, average pore size (L_{micro}-NLDFT) and the pore size distribution are determined by 2D Non-Local Density Functional Theory (NLDFT).[13] For comparison, the average micropore size ($L_{o\text{-}DR}$), is determined from the adsorption data using the Dubinin–Radushkevich and Stoeckli equations.[14]

Raman Spectroscopy

Raman is a spectroscopic technique based on inelastic or Raman scattering of a monochromatic light source on a sample. A typical Raman spectroscopy instrument should have an excitation source (laser generation), sample illumination and light collection optic system, spectrophotometer (for filtering and selecting wavelength), and a detector.[3] The technique measures weak inelastic scattering that occurs when photons interact with the electron cloud (Raman effect). The molecules absorb the

photons, becoming excited, and then re-emit photons of different wavelengths, returning the molecule to a different rotational or vibrational state than its original ground state.[15]

A filter removes all the elastically scattered light that retains the same wavelength as the incident photons. Energy shifting information collected over the spectrum of wavelengths is used to study vibrational, rotational, and other low-frequency transitions in molecules. Raman Spectroscopy gives results on most molecular samples and is flexible for testing solids, gases, and aqueous states. It can also identify mixtures through characteristic peaks that fingerprint certain functional groups in a molecule.

Raman is used as a complementary tool with TEM and XPS to examine structures and chemical composition changes of ECs electrode materials that have undergone chemical or physical alterations.

The spectra of the materials here developed are recorded with a Renishaw spectrometer (Nanonics multiview 2000) operating with an excitation wavelength of 532 nm. The spectrum is acquired after 10 seconds of exposition time of the laser beam to the sample.

X-Ray Diffraction

XRD is a non-destructive method of bombarding a sample with an X-ray beam to analyse the transmitted and diffracted beams.[3] The three basic components of an XRD instrument are the X-ray production unit arm, sample holder, and detector arm. The detector can rotate around the sample to measure the intensity of the diffracted X-rays at different angles. The angles, intensity, and peak widths of the resulting spectrum are keys for analysing the sample against a materials database and calculating information about the sample. XRD performs best when a sample is homogeneous or single-phase. For non-isometric crystalline structures, indexing of patterns can be very difficult and amorphous materials cannot be identified.

The method is widely used for characterizing and identifying unknown crystalline materials, determining the structures and orientations of single crystals or grains, and measuring average spacing between layers or rows of atoms. XRD can also measure sample purity or texture.[3] In ES research, XRD is usually used to gather information about structure arrangements, crystallite size, defects, and alterations of materials after they undergo certain processes.[3]

The interlayer distance of the materials synthesized during this thesis are studied

by X-Ray Diffraction performed in a D8 X-Ray diffractometer (Bruker).

Fourier Transform Infrared Spectroscopy

FTIR is an analytical spectroscopy method that utilizes the infrared light spectrum to probe sample interactions. In principle, a sample is irradiated with infrared radiation (IR) and some of the IR light is absorbed by the material and some is transmitted through it.[3] The absorbed IR photons will excite molecules into a higher vibrational energy state and the wavelength absorbed is unique to the sample's molecular structure. The result is a unique profile of a material. FTIR fingerprints can be used quantitatively to determine concentration down to a few parts per million. Qualitatively, FTIR can be used to identify quality of a material.

Changes in the functional groups of the materials developed in this work are followed with Fourier transform Infrared spectroscopy. This analysis is performed in a Hyperion 1000 FT-IR spectrometer, using about 5% of the material to be analysed grinded with KBr.

Electrochemical Cell Preparation

Electrochemical tests are performed in a Swagelok cell using a glass fibre membrane (Whatman® glass microfiber filters, grade GF/B) of 12.7 mm diameter as separator and placed in direct contact with polished stainless steel or titanium plungers. To confirm the reproducibility of the measurements at least three electrochemical cells are assembled for each type of material described in the present work. For the electrochemical studies in organic electrolyte, the cells are assembled inside an argon glove box with O_2 and H_2O concentration levels below 5 ppm.

Electrochemical Analysis Conditions

Capacitance ($F.g^{-1}$ and $F.cm^{-3}$) and energy/power density ($Wh.kg^{-1}$ and $W.kg^{-1}$), tested at a specific current density ($A.g^{-1}$), are generally used to evaluate the electrochemical performance of an electrode material or a supercapacitor device. Several typical electrochemical measurements for the evaluation of supercapacitors, such as cyclic voltammetry, galvanostatic charge/discharge, and electrochemical impedance spectrometry are briefly summarized in here. Electrochemical cyclic voltammetry (CV) measurements at different scan rates, as well as rate capability measurements in galvanostatic mode at different current densities are performed at ambient conditions in a multichannel

potentiostat/galvanostat (Biologic VMP3, France). To analyse independently the behaviour and to determine the capacitance and the real working potential range of each electrode,[16,17] a silver rod (Ag) is used as a pseudo-reference electrode in the organic electrolyte. When aqueous-based electrolytes are used, an Ag/AgCl electrode is used as reference.

The specific capacitance is evaluated per active mass of a single electrode after a minimum of 20 cycles at each scan rate. The volumetric capacitance is calculated by considering the density of a single electrode. The specific capacitance (C_{grav}) is calculated from the CVs using the following equation:

$$C_{Grav} = \frac{2I}{\frac{dv}{dt}m} \qquad \textbf{Equation 7-1}$$

where I is the current, m the mass of the active material and dv/dt is the scan rate. The CV measurement can be directly used to evaluate the average capacitance for an EDLC behaviour and/or a typical pseudocapacitance behaviour that exhibits a rectangular CV curve. However, the faradaic behaviour of a battery type electrode or the intercalation pseudocapacitive behaviour displays obvious redox peaks in the CV curves, and thus the corresponding average capacitance cannot be directly calculated from CV measurements.[18] In those cases, Equation 7-2 should be used:

$$C = \frac{1}{2m\Delta V}[Q_a + Q_c] \qquad \textbf{Equation 7-2}$$

where, m is the is the mass of the active material, ΔV the working potential window of the electrode (V) and Q_a and Q_c the anodic and cathodic charge in one cycle of potential sweep, respectively.[19]

A charge/discharge test is the most efficient measurement for capacitance evaluation. It is also well known that the capacitance of electrode materials can be calculated on the basis of:

$$C = \frac{i \times t}{\Delta V} \qquad \textbf{Equation 7-3}$$

where, t is the charging/discharging time (s).[18]

Coulombic Efficiency is defined as the ratio of discharging time and charging time and it can be calculated by the following equation

$$\eta = \frac{t_D}{t_C} \times 100 \qquad \textbf{Equation 7-4}$$

where, η is the coulombic efficiency, t_D is discharging time (s), t_C is charging time (s). The coulombic efficiency is calculated by comparing the first and the end cycle after hundreds or thousands galvanostatic charge/discharge cycles. [19]

Electrochemical Impedance Spectroscopy (EIS) measurements are usually performed by collecting the supercapacitor impedance data at a specific potential, with small voltage amplitude of 5 or 10 mV over a wide range of frequencies, 0.01 Hz to 100 kHz. The EIS can be expressed as a Nyquist plot. From this plot, a charge transfer resistance can be obtained from the diameter of the semicircle. At high frequency (larger than 10^4 Hz), the impedance implies the conductivity of both active materials and electrolyte. The high-to-medium frequency region (10^4 to 1 Hz) shows pseudocharge transfer resistance, which is associated with the porous structure of the electrodes. At low frequency ranges (less than 1 Hz), the impedance plot is the characteristic feature of pure capacitive behavior.[20] The relationship between the imaginary part of the impedance $-Im(Z)$ and the frequency f can be obtained from EIS measurements. The capacitance can be calculated using Equation 7-5.

$$C = \frac{1}{2\pi f[-Im(Z)]} \qquad \textbf{Equation 7-5}$$

The impedance results can also be visualized in a Bode plot, that shows how the capacitance decreases with increasing frequency by plotting $log(-Im(Z))$ vs $log(f)$.

Ragone plots are calculated from the galvanostatic charge–discharge curves. The gravimetric energy (E_{grav}) and power (P_{grav}) corresponding to the mass of the active material per electrode are estimated by using the following equations respectively:

$$E_{Grav} = \frac{C_{Grav}\Delta V^2}{8} \qquad \textbf{Equation 7-6}$$

$$P_{Grav} = \frac{E_{Grav}}{t} \qquad \textbf{Equation 7-7}$$

where ΔV is the voltage drop of the galvanostatic discharge curve after ohmic drop subtraction and t is the discharge time.

In order to compare the capacitance values of asymmetric and symmetric devices, capacitance of the cells is calculated using Equation 7-4, where m_+ and m_- corresponds to the mass of the positive and negative electrode, respectively.

$$C_{Cell} = \frac{I}{\frac{dv}{dt}(m_+ + m_-)} \qquad \textbf{Equation 7-8}$$

Then, Equation 7-2 becomes:

$$E_{Grav} = \frac{C_{Cell}\Delta V^2}{2} \qquad \textbf{Equation 7-9}$$

References

(1) *Scanning Microscopy for Nanotechnology*; Zhou, W., Wang, Z. L., Eds.; Springer New York: New York, NY, 2007.

(2) Wells, O. C. *Scanning electron microscopy*; McGraw-Hill, 1974.

(3) Yu, A.; Chabot, V.; Zhang, J. *Electrochemical supercapacitors for energy storage and delivery : fundamentals and applications*; CRC Press, 2013.

(4) Frackowiak, E. *Phys. Chem. Chem. Phys.* **2007**, *9* (15), 1774–1785.

(5) Garratt-Reed, A. J.; Bell, D. C. *Energy-dispersive X-ray analysis in the electron microscope*; BIOS, 2003.

(6) Goldstein, J. I.; Newbury, D. E.; Echlin, P.; Joy, D. C.; Lyman, C. E.; Lifshin, E.; Sawyer, L.; Michael, J. R. *Scanning Electron Microscopy and X-ray Microanalysis*, 3rd ed.; Springer US: Boston, MA, 2003.

(7) Williams, D. B.; Carter, C. B. *Transmission Electron Microscopy*; Springer US: Boston, MA, 2009.

(8) Ludwig Reimer; Helmut Kohl. *Transmission Electron Microscopy*; Springer Series in Optical Sciences; Springer New York: New York, NY, 2008; Vol. 36.

(9) Egerton, R. F. *Physical Principles of Electron Microscopy*; Springer US: Boston, MA, 2005.

(10) Yoon, S.; Kang, E.; Kim, J. K.; Lee, C. W.; Lee, J. *Chem. Commun.* **2011**, *47* (3), 1021–1023.

(11) Miller, J. M.; Dunn, B.; Tran, T. D.; Pekala, R. W. *J. Electrochem. Soc.* **1997**, *144* (12), L309–L311.

(12) Zhu, Y.; Murali, S.; Stoller, M. D.; Ganesh, K. J.; Cai, W.; Ferreira, P. J.; Pirkle, A.; Wallace, R. M.; Cychosz, K. A.; Thommes, M.; Su, D.; Stach, E.

A.; Rodney S. Ruoff. *Science (80-.).* **2011**, *332* (6037), 1537–1541.

(13) Jagiello, J.; Olivier, J. P. *Carbon N. Y.* **2013**, *55* (2), 70–80.

(14) Stoeckli, F.; Daguerre, E.; Guillot, A. *Carbon*. 1999, pp 2075–2077.

(15) Derek J. Gardiner; Pierre R. Graves. *Practical Raman Spectroscopy*; Gardiner, D. J., Graves, P. R., Eds.; Springer Berlin Heidelberg: Berlin, Heidelberg, 1989.

(16) Khomenko, V.; Raymundo-Piñero, E.; Béguin, F. *J. Power Sources* **2006**, *153* (1), 183–190.

(17) Khomenko, V.; Raymundo-Piñero, E.; Béguin, F. *J. Power Sources* **2010**, *195* (13), 4234–4241.

(18) Wang, Y.; Song, Y.; Xia, Y. *Chem. Soc. Rev.* **2016**, *451*, 652–657.

(19) Chen, S. M.; Ramachandran, R.; Mani, V.; Saraswathi, R. *Int. J. Electrochem. Sci.* **2014**, *9* (8), 4072–4085.

(20) Sun, W.; Zheng, R.; Chen, X. *J. Power Sources* **2010**, *195* (20), 7120–7125.

APPENDIX II: Lignin/PEDOT as Cathode Material for Sodium- and Lithium-Ion Batteries

The use of earth abundant and renewable materials is encouraging for the future development of environmentally clean, safe and affordable batteries. Herein, we use the Lignin/PEDOT polymers synthesized on Chapter 3 (Table 7-1) as cathodes for battery applications.

Electrochemical tests are conducted in 2032 coin cells, which are assembled in an argon filled dry box, with Sodium or Lithium foil as anode and Lignin/PEDOT blends as cathode. In order to test the lignin by itself, the powder is mixed with 20 wt.% of Timcal Super C65 Conductive Carbon Black. Four different electrolytes are used and are shown in Table 7-12 in a 50/50 vol.% mixture of ethylene carbonate and dimethyl carbonate (EC/DMC). The cathode materials re kept under vacuum at 80 ºC overnight prior to each experiment, while the anode and electrolyte are maintained at the dry box.

The theoretical capacity of Lignin/polypyrrole is 80 $mAh.g^{-1}$.[1] Then, the cells are cycled at C/20 (4 $mA.g^{-1}$), C/10 (8 $mA.g^{-1}$), C/2 (40 $mA.g^{-1}$) for five cycles each one, and finally C/20 (4 $mA.g^{-1}$) for 25 cycles. Results of this cycling testing are shown in Figure 7-1.

Figure 7-1 (a.I) shows the results of the cycling in $LiClO_4$ (EC:DMC). It can be seen that in this electrolyte, Lig/PEDOT 20:80 presents the most favourable combination of total capacity (62 $mAh.g^{-1}$ at C/20) and capacity retention (44 % after 25 cycles at C/20). Lignin mixed with C65 shows a similar performance, yet the capacity

Table 7-1. Lignin/PEDOT ratios synthesized.

Acronym	Lignin wt.%	PEDOT wt.%
PEDOT	0	100
Lig/PEDOT 20/80	20	80
Lig/PEDOT 40/60	40	60
Lig/PEDOT 60/40	60	40
Lignin	100	0

Table 7-2. Electrolytes used in the evaluation of Lig/PEDOT for battery applications.

Salt	Acronym electrolyte (Salt Chemical Formula)
Lithium Hexafluorophosphate	$LiPF_6$
Lithium Perchlorate	$LiClO_4$
Sodium Hexafluorophosphate	$NaPF_6$
Sodium Perchlorate	$NaClO_4$

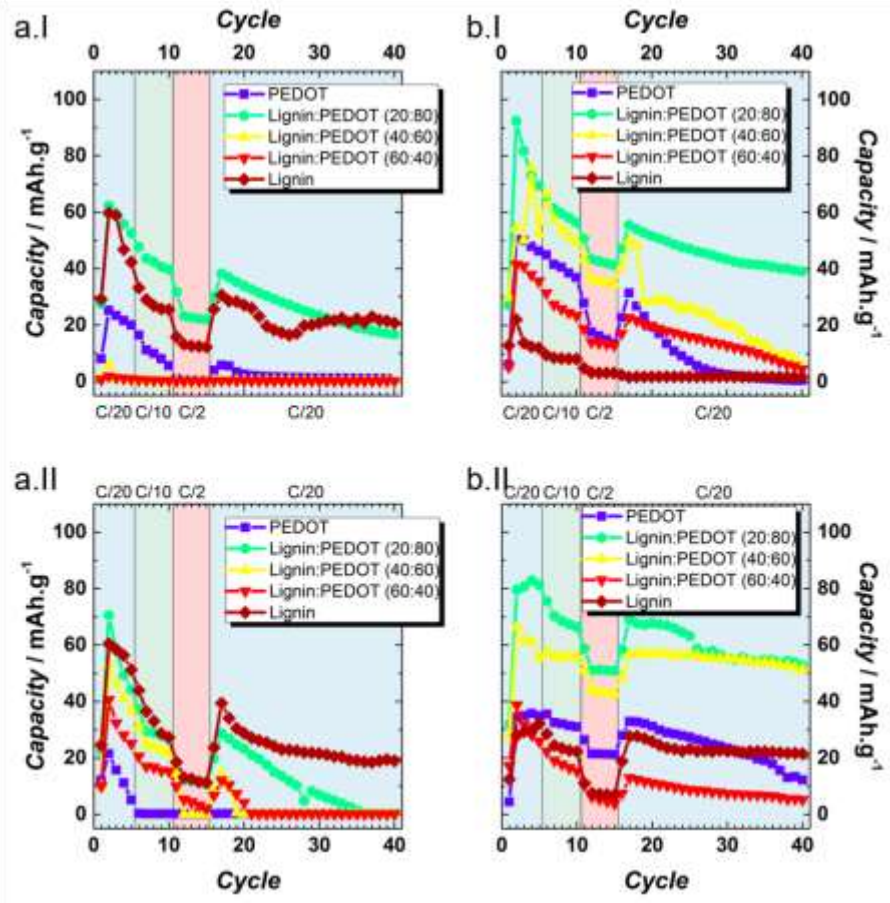

Figure 7-1. Discharge capacity retention at different current densities in $LiClO_4$ (a.I), $LiPF_6$ (b.I), $NaClO_4$ (a.II), and $NaPF_6$ (b.II).

values are lower and less stable. The other Lig/PEDOT proportions do not intercalate lithium ions. This behaviour proves that in this electrolyte, lignin requires either a conductive filler (C65) or a high proportion (80 %) of electron conductor polymer.

The cycle-life data in $LiPF_6$ (EC:DMC) is shown in Figure 7-1 (b.I). Lig/PEDOT 20:80 exhibits the highest capacity of all the materials and shows an improvement in comparison to the same material in $LiClO_4$. Capacity values up to 92 $mAh.g^{-1}$ at C/20 and capacity retention of 70 % after 25 cycles at C/20 are achieved with this material. In contrast to the performance in $LiClO_4$, all the other proportions insert lithium ion in the cathode, showing an improvement in the intercalation properties of lignin.

Results of the cycling evaluation in $NaClO_4$ (EC:DMC) are shown in Figure 7-1 (a.II). In this case, the conductive filler allows the continuous insertion of ions in the lignin cathode, maintaining 48 % of its initial capacity. Lig/PEDOT 20:80 achieves the highest capacity during the second discharge, but the material saturates and ceases inserting Na^+. The co-polymerization of Lignin and PEDOT worsens the Na^+ intercalation abilities in $NaClO_4$.

A contrasting effect is observed in $NaPF_6$ (EC:DMC) (Figure 7-1 (b.II)), where all the Lignin-derived material present intercalation abilities even after 40 cycles. The increment on the PEDOT proportion enhances the insertion abilities of the lignin, achieving the highest capacity value, 83 $mAh.g^{-1}$ at C/20, with Lig/PEDOT 20/80.

The behaviour of these cathode materials seems to be dependent on the salt anion. By comparing Figure 7-1 (a) and Figure 7-1 (b), it is evident that the intercalation phenomenon is enhanced in the Lig/PEDOT blends when PF_6^- is the anion accompanying the metal.

Nor Lignin, nor Lignin/PEDOT blends have been studied for sodium battery applications. Hydrolysis lignin has been studied as cathode for Li-ion batteries at low-rate, achieving up to 185 $mAh.g^{-1}$ at 75 $\mu A.cm^{-2}$.[2] As our experiments are performed in powder, a comparison between the two materials cannot be drawn.

As concluding remark, lignin, a renewable and inexpensive material, can be used as sustainable organic electrode with highly efficient electrochemical energy storage for Lithium- and Sodium-ion batteries. Surface and interface engineering is essential to improve the electrochemical performance of Lignin/PEDOT materials for Lithium- and Sodium-ion batteries.

References

(1) Milczarek, G.; Inganas, O. *Science (80-.).* **2012**, *335* (6075), 1468–1471.

(2) Gnedenkov, S. V.; Opra, D. P.; Sinebryukhov, S. L.; Tsvetnikov, A. K.; Ustinov, A. Y.; Sergienko, V. I. *J. Solid State Electrochem.* **2013**, *17* (10), 2611–2621.

APPENDIX III: Partially Reduced Graphite Oxide: A Close Examination of the Capacitive Contributions to its Storage Capacity

Batteries and supercapacitors have proven to be of crucial importance for advanced and highly efficient energy storage and management. The nature of their electrochemical processes is directly correlated to their charge-storage mechanisms and understanding them is crucial to optimize both their energy and power densities. Graphene-derived materials have been used both in batteries and supercaps because of their high electronic conductivity, intercalation properties and large surface area.[1] This study provides insight into the role of the diffusion- and surface controlled processes during the voltammetry cycling of a partially reduced graphite oxide.

prGrO synthesized in Chapter 3 is electrochemically analysed with a cavity micro electrode (CME), in which the electrochemical interface area is around a fraction of mm^2 and the ohmic drop coming from the bulk of the electrolyte can be neglected, allowing the use of high scan rates.[2] The prGrO is studied in a 3-electrode configuration with a platinum wire as counter electrode and $Hg/HgSO_4$ as reference electrode for the sulphuric acid, and sodium sulphate, and Ag/AgCl for the potassium hydroxide solution. The microcavity is filled with active material by pressure of the carbon powders against a glass plate. The cavity is cleaned by immersing the electrode in ethanol in an ultrasonic bath between experiments. Two separate mechanisms, surface capacitive effects and diffusion-controlled insertion processes, can be discriminated by relating the current response to the voltammetric sweep rate according to equation 7-10:[3]

$$\frac{\boldsymbol{i}}{\boldsymbol{v}^{1/2}} = \boldsymbol{k_1 v}^{1/2} + \boldsymbol{k_2} \qquad \textbf{Equation 7-1}$$

where $\boldsymbol{i}$ is the measured current, $\boldsymbol{v}$ is the sweep rate, and $\boldsymbol{k_1}$ and $\boldsymbol{k_2}$ are related to the current contributions from the surface capacitive effects and the diffusion-controlled intercalation process, respectively. Figure 7-2 (a to c) shows the cyclic voltammetry curves at 100 $mV.s^{-1}$, in the three different electrolytes. By plotting $\frac{\boldsymbol{i}}{\boldsymbol{v}^{1/2}}$ vs $\boldsymbol{v}^{1/2}$, according to Equation7-10, the values of $\boldsymbol{k_1}$ and$\boldsymbol{k_2}$ are calculated in the whole potential window and therefore we are able to quantify the fraction of the current due to each of these contributions (Figure 7-2 (d)).

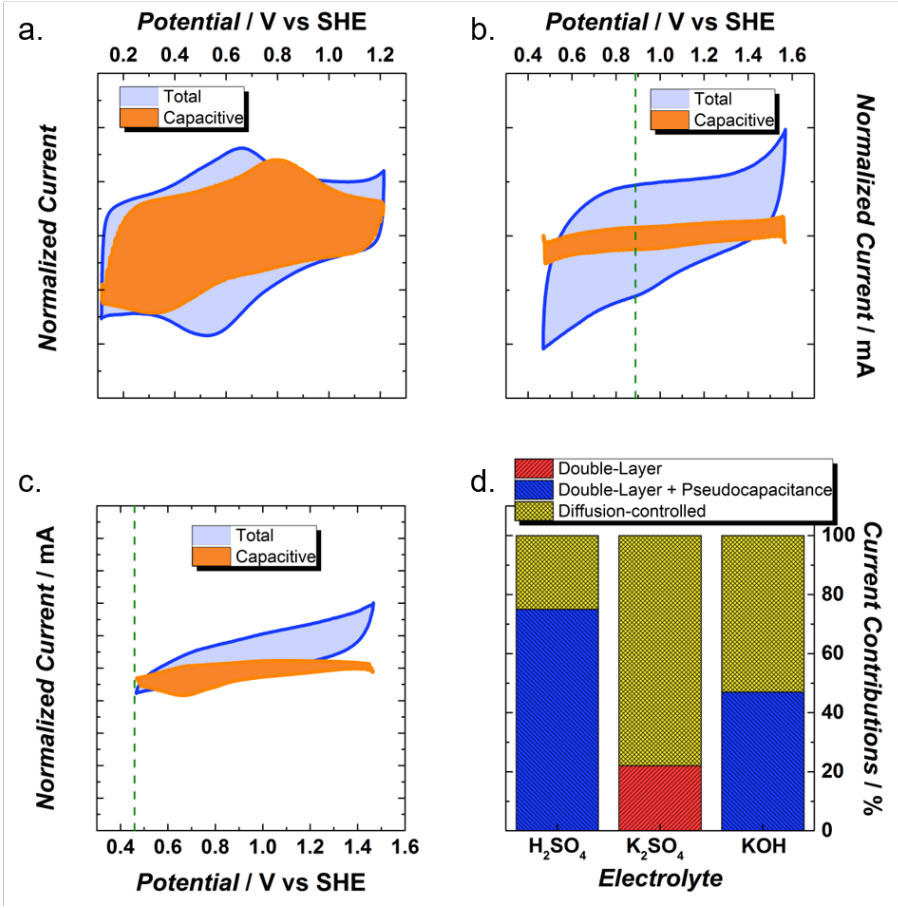

Figure 7-1. Total (blue area) and capacitive (orange area) contributions to charge storage in prGrO, cycled in 0.1M H_2SO_4 (a), 0.1M K_2SO_4 (b), and 0.1M KOH (c) at 100 mV.s^{-1}. The dotted green lines indicate the oxygen evolution potential. Summary of the contributions in each one of the electrolytes (d).

The cycling of the material in H_2SO_4 (Figure 7-2 (a)), yields redox peaks at ~0.6V that correspond to the redox reactions involving the quinone/hydroquinone functionalities confirmed by the XPS and FTIR experiments (Section 3.3.1.2). The capacitive charge storage, in both cases, corresponds to 75% of the total current and is caused by double-layer and pseudo capacitive processes. However, given the low Specific Surface Area presented by the prGrO, most of this capacitance might be caused by redox pseudocapacitance, involving again the quinone/hydroquinone functionalities, or intercalation pseudocapacitance. This surface-confined charge-transfer process is confirmed by the broad peak in the capacitive curves of both electrolytes.

In the case of the K_2SO_4 (Figure 7-2 (b)), the capacitive contribution is diminished to 22%. The rectangular shape of the capacitive contribution for K_2SO_4 indicates a double-layer process.

When prGrO is tested in KOH, the capacitive contribution increases to 47%, and the presence of peaks at ~0.66 V in the capacitive charge storage indicates that the quinone/hydroquinone functionalities are involved in a redox process. The reactions occurring in acidic, neutral and basic media are shown in Scheme 7-1.[4]

Pseudocapacitance can be due to monolayer adsorption of ions at an electrode surface, surface redox reactions or ion intercalation that does not result in a phase change.[5] Intercalation processes occurring in the prGrO might be confirmed by changes in the interlayer distance of the prGrO, for this X-ray diffractions of the prGrO at the OCV in the different electrolytes are measured (Figure 7-3). X-ray diffraction pattern of the material in water is shown for comparison.

Scheme 7-1. Quinone Redox Reactions at different pH.

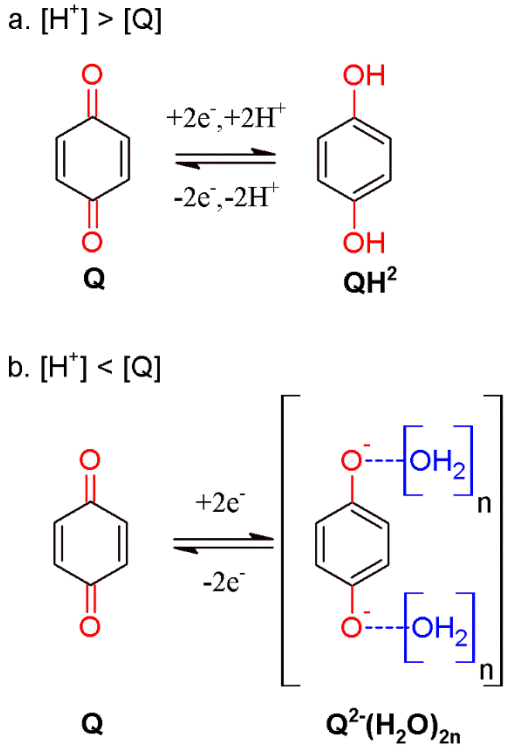

The first thing to notice is that all the spectra have three broad peaks at 2θ equal to 13°, 30° and 43° (Figure 7-3 (b-d)). The peak at 2θ equal to 43° corresponds to the (100) and (110) Bragg reflections and it is also observed in the original prGrO (Figure 7-3 (a)). The peaks at 13° and 30° correspond to the intercalation of the ions inside the material layers. The presence of these peaks evinces spontaneous intercalation and the presence of several intercalation stages. These results are particularly exciting in the case of H_2SO_4, as this is the first time that a sulfuric acid graphite intercalation compound is observed without anodic or chemical oxidation.[6]

To study the intercalation stages during cycling, thick electrodes (~100 μm) are charged and discharged, following the same and opposite scan direction than with

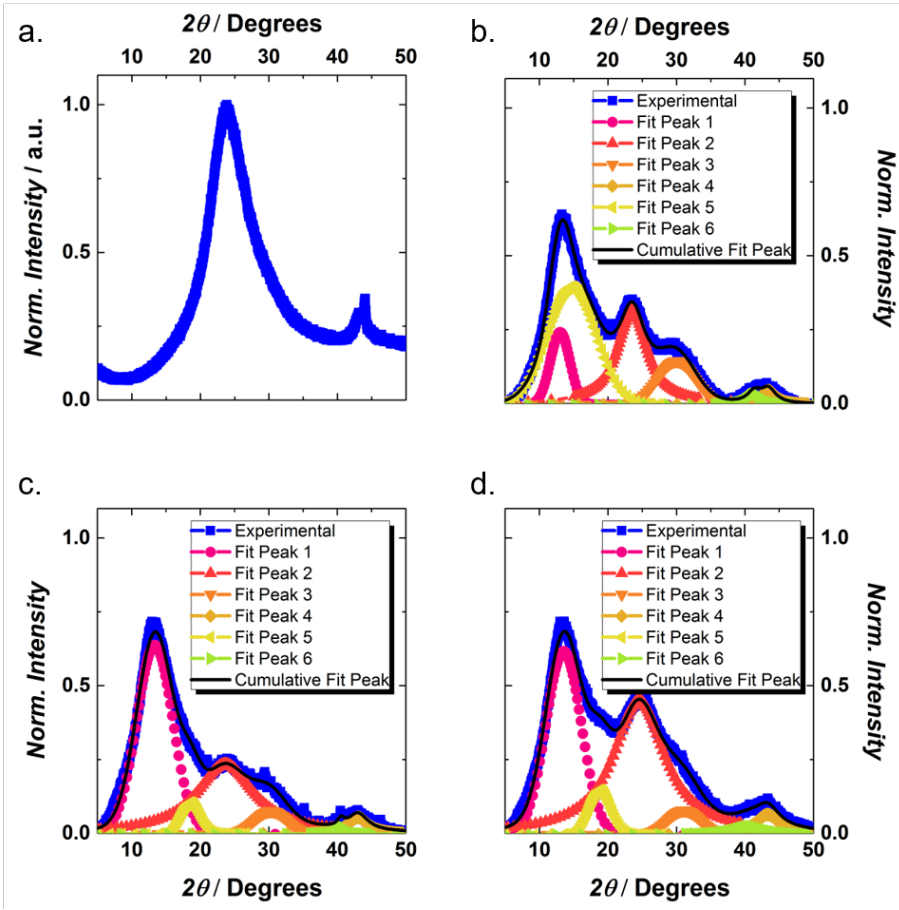

Figure 7-2. X-ray diffraction of prGrO at OCV after being immersed in water (a), H_2SO_4 (b), K_2SO_4 (c) and KOH (d).

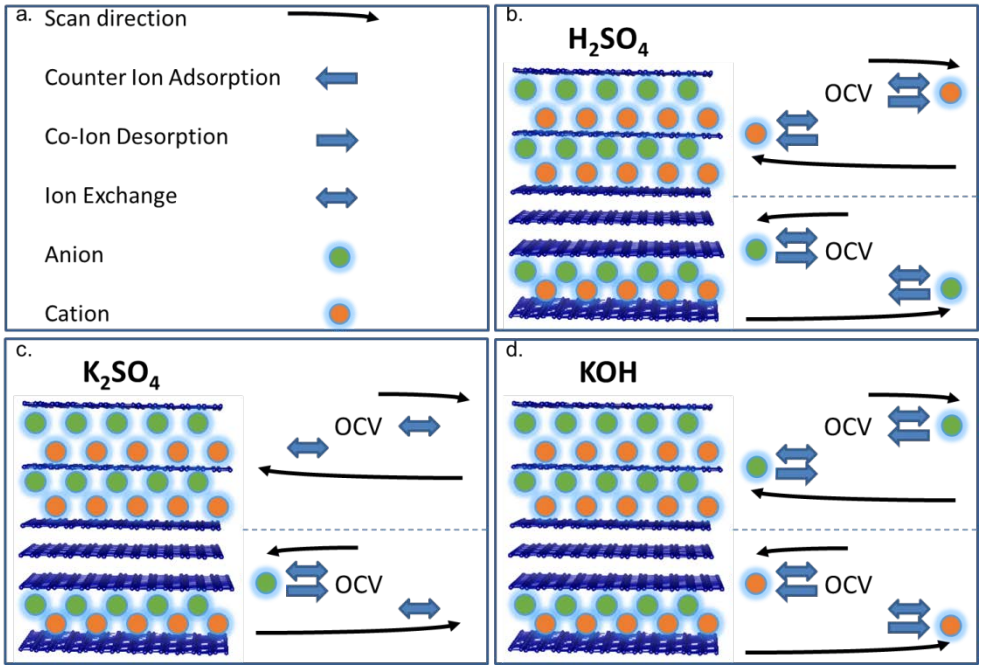

Figure 7-3. Schematic description of the symbols (a) and proposed charging mechanism in H_2SO_4 (b), K_2SO_4 (c), and KOH (d).

the microcavity electrode. X-ray diffraction patterns are taken in different stages of charge/discharge (not shown). The analysis of these patterns and the charging mechanisms proposed by Forse *et al*[7] allow us to formulate a schematic illustration of the process occurring in each electrolyte in Figure 7-4.

The charge storage mechanism depends on initial scan direction and pH of the electrolyte. While cycling prGrO in H_2SO_4 (Figure 7-4 (b)) an inverse mechanism, to the one observed in KOH (Figure 7-4 (d)), is discern. From OCV (open circuit voltage) towards positive potentials in H_2SO_4, the cation is the mainly ion involved in the movement into (or out) of the carbon pores. From OCV towards negative potentials, is the anion that becomes mainly involved in the adsorption/desorption process.

Figure 7-4 (c) shows the charging mechanism of the material in K_2SO_4. In this case, counter-ion adsorption is accompanied by simultaneous co-ion desorption from the pores, *i.e.* ion exchange.

In situ characterization by techniques such as Raman, NMR and XRD are fundamental to confirm the method herein proposed. Nevertheless, this work opens

up the path to deeper studies of the charging mechanisms of graphene-related materials in aqueous electrolytes.

References

(1) Wassei, J. K.; Kaner, R. B. *Acc. Chem. Res.* **2013**, *46* (10), 2244–2253.

(2) Cachet-Vivier, C.; Vivier, V.; Cha, C. S.; Nedelec, J. Y.; Yu, L. T. *Electrochim. Acta* **2001**, *47* (1), 181–189.

(3) Wang, J.; Polleux, J.; Lim, J.; Dunn, B. *J. Phys. Chem. C* **2007**, *111* (40), 14925–14931.

(4) Quan, M.; Sanchez, D.; Wasylkiw, M. F.; Smith, D. K. *J. Am. Chem. Soc.* **2007**, *129* (42), 12847–12856.

(5) Conway, B. E. *Electrochemical Supercapacitors*; Springer US: Boston, MA, 1999.

(6) Dimiev, A. M.; Ceriotti, G.; Behabtu, N.; Zakhidov, D.; Pasquali, M.; Saito, R.; Tour, J. M. *ACS Nano* **2013**, *7* (3), 2773–2780.

(7) Forse, A. C.; Merlet, C.; Griffin, J. M.; Grey, C. P. *J. Am. Chem. Soc.* **2016**, jacs.6b02115.

APPENDIX IV: List of Publications

Adriana M. Navarro-Suárez, Javier Carretero-González, Teófilo Rojo, and Michel Armand "Benzoquinone-Diamine Bi- and Ter-Polymers for Energy Storage." To be submitted.

Adriana M. Navarro-Suárez, Katherine L. Van Aken, Thyler Mathis, Taron Makaryan, Jun Yan, Javier Carretero-González, Teófilo Rojo, and Yury Gogotsi "Development of asymmetric supercapacitors using Titanium Carbide-reduced Graphene Oxide couples as electrodes". Submitted to *Nano Energy*.

Adriana M. Navarro-Suárez, Nerea Casado, Javier Carretero-González, David Mecerreyes, and Teófilo Rojo "Partially reduced Graphite Oxide/Biopolymer Full-Cell Supercapacitor". Submitted to *ChemSusChem*.

Adriana M. Navarro-Suárez, Paula Sánchez, Damien Saurel, Elizabeth Castillo, Javier Carretero-González, and Teófilo Rojo, "Effect of the carbonization and activation temperatures on the porosity and electrochemical performance of lignin-derived carbons". Submitted to *ACS Applied Materials & Interfaces*.

Adriana M. Navarro-Suárez, Javier Carretero-González, Vladimir Roddatis, Eider Goikolea, Julie Ségalini, Edurne Redondo, Teófilo Rojo and Roman Mysyk, "Nanoporous carbons from natural lignin: study of structural-textural properties and application to organic-based supercapacitors", *RSC Advances*, 2014, **4**, pp 48336-48343.

APPENDIX IV: List of Presentations

1. 229th ECS meeting, San Diego, USA, 29th May – 2nd June 2016.
   Oral presentation: "Partially Reduced Graphite Oxide: A close examination of the contributions to its storage capacity". Adriana M. Navarro-Suárez; Javier Carretero-González; Teófilo Rojo.

2. European Materials Research Society (E-MRS), Warsaw, Poland, 15th – 18th September 2015.
   Oral presentation: "Lignin as hard carbon precursor for anodes of sodium ion batteries". Paula Sánchez-Fontecoba; Damien Saurel; Adriana M. Navarro-Suárez; Javier Carretero-González; Elizabeth Castillo-Martínez, Teófilo Rojo.

3. XXXV Biannual Congress of the Spanish Royal Society of Chemistry, A Coruña, Spain, 19th – 23rd July 2015.
   Oral presentation: "Microporous Lignin-derived carbons for electric double-layer capacitors". Adriana M. Navarro-Suárez; Damien Saurel; Javier Carretero-González; Teófilo Rojo.

4. XXXV Biannual Congress of the Spanish Royal Society of Chemistry, A Coruña, Spain, 19th – 23rd July 2015.
   Poster presentation: "Lignin derived hard carbons as anodes for sodium ion batteries". Paula Sánchez-Fontecoba; Damien Saurel; Adriana M. Navarro-Suárez; Javier Carretero-González; Elizabeth Castillo-Martínez, Teófilo Rojo.

5. Carbon 2015, Dresden, Germany, 12th – 17th July 2015.
   Poster presentation: "Multilayered Graphene-Biopolymer Supercapacitor". Adriana M. Navarro-Suárez; Javier Carretero-González; Teófilo Rojo.

6. 7th European Summer School on Electrochemical Engineering, Leeuwarden, Netherlands, 22nd – 26th June 2015.
   Poster presentation: "Synthesis and electrochemical characterization of nanoporous carbon materials". Adriana M. Navarro-Suárez; Javier Carretero-González; Teófilo Rojo.

7. 2015 MRS Spring meeting and exhibit, San Francisco, USA, 6th – 10th April 2015.
   Oral presentation: "Nanostructured carbons for Energy Storage Applications". Javier Carretero-González; Adriana M. Navarro-Suárez.

8. The XIII Brazilian MRS meeting, Rio de Janeiro, Brazil, 28th September – 2nd October 2014.
   Oral presentation: "Nanocarbons derived from renewable sources for supercapacitors". Javier Carretero-González; Adriana M. Navarro-Suárez; Edurne Redondo; Eider Goikolea; Roman Mysyk.

9. The XIII Brazilian MRS meeting, Rio de Janeiro, Brazil, 28th September – 2nd October 2014.
   Poster presentation: "Lignin-derived carbon with graphene–like structure for supercapacitors". Javier Carretero-González; Adriana M. Navarro-Suárez; Eider Goikolea; Edurne Redondo; Vladimir Roddatis; Julie Ségalini; Roman Mysyk; Teófilo Rojo.

10. 65th Annual Meetingof the International Society of Electrochemistry, Lausanne, Switzerland, 31st August – 5th September 2014.
    Oral presentation: "Supercapacitor Electrode Materials from Abundant Lignocellulose Biomass: fine-tuning porosity to specific electrolytes". Roman Mysyk; Edurne Redondo; Adriana M. Navarro-Suárez; Javier Carretero-González; Eider Goikolea; Julie Ségalini.

11. World Conference on Carbon (Carbon 2014), Jeju, Korea, 29th June – 4th July 2014.
    Oral presentation: "Impact of textural-structural properties on capacitive behavior of microporous carbons derived from renewable biomass sources". Javier Carretero-González; Adriana M. Navarro-Suárez; Edurne Redondo; Julie Ségalini; Vladimir Roddatis; Eider Goikolea; Roman Mysyk.

12. 225th ECS meeting, Orlando, U.S.A., 11th – 15th May, 2014.
    Poster presentation: "Fine-Tuned Nanoporous Supercapacitor Electrode Materials from Renewable Natural Precursors". Edurne Redondo; Eider Goikolea; Javier Carretero-González; Julie Ségalini; Adriana M. Navarro-Suárez; Roman Mysyk.

13. Graphene International Conference, Toulouse, France, 6th – 9th May, 2014.
    Poster presentation: "Nanoporous carbon electrodes with graphene–like structure for supercapacitors". Adriana M. Navarro-Suárez; Javier

Carretero-González; Eider Goikolea; Edurne Redondo; Vladimir Roddatis; Julie Ségalini; Roman Mysyk; Teófilo Rojo.

14. Power Our Future 2014, Vitoria-Gasteiz, Spain, 2nd – 4th April, 2014.
    Poster presentation: "Microporous carbons from natural lignin for electric double-layer capacitors" Adriana M. Navarro-Suárez; Javier Carretero-González; Vladimir Roddatis; Julie Ségalini; Eider Goikolea; Edurne Redondo; Roman Mysyk; Teófilo Rojo.

15. Power Our Future 2014, Vitoria-Gasteiz, Spain, 2nd – 4th April, 2014.
    Oral presentation: "Fine-tuning nanoporous supercapacitor electrode materials from selected lignocellulose precursors". Edurne Redondo; Adriana Navarro Suárez; Javier Carretero González; Eider Goikolea; Julie Ségalini; Roman Mysyk.

16. Graphene study 2014, Obergurgl, Austria, 2nd – 7th February, 2014.
    Poster presentation: "Graphene-based electrode materials for electrical double-layer capacitor applications". Adriana M. Navarro-Suárez

17. 5th International Conference on Carbon for Energy Storage/Conversion and Environment Protection, Mülheim a.d. Ruhr, Germany, 23rd – 26th September, 2013.
    Poster presentation: "Sustainable supercapacitor electrode materials through activation of natural precursors". Javier Carretero-González; Eider Goikolea; Edurne Redondo; Julie Ségalini; Adriana M. Navarro-Suárez; Roman Mysyk.

Adriana M. Navarro-Suárez

anavarrosuarez@gmail.com

https://www.researchgate.net/profile/Adriana_Navarro-Suarez2

Calle 84 # 24A-74 Diamante II
Bucaramanga, Colombia

Research Summary

My research during the past years has intertwined Chemistry, Electrochemistry, and Materials Science. I have synthesized nanoporous carbons, conductive polymers, and 2D nanomaterials and tested their application as electrodes for Energy Storage Devices.

Education

Ph.D. in Materials Science and Technology, *Euskal Herriko Unibertsitatea,* Expected 18th November 2016

M.Sc. in Materials for Energy Storage and Conversion, *Université de Picardie Jules Verne, Université Paul Sabatier, Aix-Marseille Université, Warsaw University of Technology, Universidad de Córdoba.* 12th September 2013

B.Sc. in Chemistry, *Universidad Nacional de Colombia,* 6th October 2011

Additional Education

7th European Summer School on Electrochemical Engineering, *Wetsus, centre of excellence for sustainable water technology,* 22nd - 26th June 2015.

Tutorial on Electrochemical Capacitors, *Université Montpellier II,* 8th June 2015.

Supercaps and Batteries Tutorial, *CIC energiGUNE,* 1st April 2014.

Graphene Study 2014, *Graphene Flagship,* 2nd - 7th February 2014.

Solid State NMR: Principles and Applications, *Euskal Herriko Unibertsitatea,* 25th – 28th November 2013.

Research Experience

Doctoral Researcher at CIC energiGUNE. *Research advisers: Dr. Javier Carretero-González & Pr. Teófilo Rojo.* Oct 2013 - Dec 2016.

Visiting PhD Student at Drexel Nanomaterials Institute. *Research adviser: Pr. Yury Gogotsi.* Feb 2016 - Aug 2016.

Internship at CIC energiGUNE. *Research adviser: Dr. Javier Carretero-González* Feb 2013 – Sep 2013.

Visiting Scientist at National Institute of Chemistry. *Research adviser: Dr. Robert Dominko.* Jul 2012 – Sep 2012.

Internship at Electrochemistry Lab – Universidad Nacional de Colombia. *Research adviser: Dr. Marco Fidel Suárez-Herrera.* Jun 2010 – Jun 2011.

Participation in Projects

Etortek (ENERGIGUNE12). *Energigune'12: L2. Supercapacitadores: Desarrollo de materiales para electrodos de alto rendimiento para condensadores electroquímicos*. 2013-2014

GRAPHENE Flagship: Graphene-Based Revolutions in ICT and Beyond. *Grant agreement No: 604391. Call: FP7-ICT-2013-FET-F.* 2013-2017

Grants & Fellowships

Basque Government Short Stay Grant EGONLABUR for a 3-month stay at Drexel University. May – Aug, 2016.

Scholarship for young researchers to attend the XXXV Biennial Congress of the Spanish Royal Society of Chemistry. July, 2015.

Basque Government Scholarship for pre-doctoral formation. 2015 - 2017.

PhD fellowship at CIC energiGUNE. 2013-2016.

Erasmus Mundus Scholarship for MESC Master. 2011-2013.

Establishment and Research Call of the DIB (Universidad Nacional de Colombia). 2010.

Enrolment of honor granted by the Science Faculty's Council (Universidad Nacional de Colombia). 2007.

Published Papers

Pedro González-García, Adriana M. Navarro-Suárez, Javier Carretero-González, Esteban Urones-Garrote, Luis Carlos Otero-Díaz and David Ávila-Brande, "Nanostructure, porosity and electrochemical performance of chromium carbide derived carbons", ***Carbon***, 2015, **85**, pp 38-49.

Adriana M. Navarro-Suárez, Javier Carretero-González, Vladimir Roddatis, Eider Goikolea, Julie Ségalini, Edurne Redondo, Teófilo Rojo and Roman Mysyk, "Nanoporous carbons from natural lignin: study of structural-textural properties and application to organic-based supercapacitors", ***RSC Advances***, 2014, **4**, pp 48336-48343.

Adriana M. Navarro-Suárez, Jonnathan C. Hidalgo-Acosta, Luca Fadini, Juan M. Feliu and Marco F. Suárez-Herrera, "Electrochemical Oxidation of Hydrogen on Basal Plane Platinum Electrodes in Imidazolium Ionic Liquids", ***Journal of Physical Chemistry C***, 2011, **115 (22)**, pp 11147–11155.

Conference Presentations

229th ECS meeting, *San Diego, USA,* 29th May – 2nd June 2016.
Oral presentation: "Partially Reduced Graphite Oxide: A close examination of the contributions to its storage capacity". Adriana M. Navarro-Suárez; Javier Carretero-González; Teófilo Rojo.

XXXV Biannual Congress of the Spanish Royal Society of Chemistry, *A Coruña, Spain,* 19th – 23rd July 2015.
Oral presentation: "Microporous Lignin-derived carbons for electric double-layer capacitors". Adriana M. Navarro-Suárez; Damien Saurel; Javier Carretero-González; Teófilo Rojo.

6 Poster and 11 co-authored presentations.

1 Oral and 2 poster presentations at outreach events.

Skills and Qualifications

Synthesis of materials: Nanoporous carbons, Graphene, Graphene Oxide, Polymers, 2D Transition metal carbides.
Materials characterization: Raman Spectroscopy, Fourier Transform Infrared Spectroscopy, Nitrogen adsorption/desorption, Small Angle X-ray Scattering, X-Ray Diffraction, Ultraviolet-Visible Spectroscopy.
Electrochemical testing: Galvanostatic Charge/Discharge, Cyclic Voltammetry, Electrochemical Impedance Spectroscopy, Alternating Current Voltammetry, Floating tests.
Technical/Computer: Excel, Origin, EC Lab, μ-Autolab II, SAIEUS, Igor/IRENA, MIMS Client, Diffrac.EVA, ChemSketch, Vesta (3D visualization program), Adobe Creative Cloud.
Technology applications: Energy Storage, Supercapacitors, Batteries, Hybrid Devices.
Languages: Spanish (Native); English (TOEFL 110/120); French, German and Basque language (Beginner).

Peer-Review Experience

ACS Nano since 2016
RSC Advances since 2014

Affiliations

The Electrochemical Society

References

Prof. Yury GOGOTSI
Director
A.J. Drexel Nanomaterials Institute, USA
Phone: + 1 215 895 6446
E-mail: **yg36@drexel.edu**

Prof. Teófilo ROJO
Scientific Director
CIC energiGUNE, Spain
Phone: + 34 94 529 71 08
E-mail: **trojo@cicenergigune.com**

Dr. Javier CARRETERO-GONZÁLEZ
Post-doc Researcher
Cambridge University, United Kingdom
Phone: +44 (0)1223 336300
E-mail: **jabenzo@hotmail.com**

Dr. Robert DOMINKO
Research Associate
National Institute of Chemistry, Slovenia
Phone: +386 31 348 888
E-mail: **robert.dominko@ki.si**

Dr. Rer. Nat. Marco F. SUÁREZ-HERRERA
Associate Professor
Universidad Nacional de Colombia
Phone: +571 4846632
E-mail: **mfsuarezh@unal.edu.co**